LAWRENCE TECHNOLOGICAL UNIVERSITY

EVALUATION OF 0.7 INCH DIAMETER CARBON FIBER REINFORCED POLYMER PRETENSIONING STRANDS IN PRESTRESSED BEAMS

Submitted to

By

Nabil F. Grace, PhD, P.E., Project Investigator
Mena Bebawy, PhD, P.E., Co-Project Investigator

Department of Civil and Architectural Engineering
Lawrence Technological University
Southfield, MI 48075-1058, U.S.A.

Mar. 31st, 2022

TECHNICAL REPORT DOCUMENTATION PAGE

1. Report No. **SPR-1707**	2. Government Accession No. N/A	3. Recipient's Catalog No.	
4. Title and Subtitle Evaluation of 0.7 Inch Diameter Carbon Fiber Reinforced Polymer Pretensioning Strands in Prestressed Beams		**5. Report Date** March 31, 2022	
		6. Performing Organization Code N/A	
7. Author(s) Nabil Grace, PhD, P.E.; Mena Bebawy, PhD, P.E., Mohamed Mohamed, P.E., Marc Kasabasic, Ezekiel Ababio, & Peter Kornyoh		**8. Performing Organization Report No.** N/A	
9. Performing Organization Name and Address Center for Innovative Material Research (CIMR) Lawrence Technological University (LTU) University Advancement Office 21,000 West Ten Mile Road, Southfield, MI 48075		**10. Work Unit No.** N/A	
		11. Contract or Grant No. 2016-0065 Z3	
12. Sponsoring Agency Name and Address Michigan Department of Transportation (MDOT) Research Administration 8885 Ricks Road P.O. Box 33049 Lansing, Michigan 48909		**13. Type of Report and Period Covered** Final Report, 12/5/2017 – 03/31/2022	
		14. Sponsoring Agency Code N/A	

15. Supplementary Notes

Conducted in cooperation with the U.S. Department of Transportation, Federal Highway Administration. MDOT research reports are available at www.michigan.gov/mdotresearch.

16. Abstract

A comprehensive investigation was conducted to evaluate the short and long-term performance of large-diameter (0.70 in. (17.8 mm)) CFRP strands and the potential for use in precast prestressed highway bridge beam construction. The investigation extended to address parameters such as creep rupture strength, relaxation, prestress losses, and strength under extreme events such as a fire event and after extended exposure to environmental cycles such as freeze-and-thaw cycles. The experimental investigation included testing and evaluating unbonded prestressed CFRP strands, half-scale and full-scale pretensioned bridge beams, and a half-scale decked bulb T-beam bridge model. Various test protocols were adopted including testing and evaluating bonded and unbonded CFRP specimens: (1) at ambient temperature and controlled laboratory conditions, (2) under combined fire/loading events, (3) after exposure to cycles of freezing and thawing, (4) inside an environmental chamber and simulating extremely hot and cold weather conditions, and (5) after exposure to elevated temperatures, with and without loading. The results from the experimental investigation were implemented in the development of an extensive analytical investigation that addressed the flexural design of full-scale highway bridge beams. Test results were deployed to establish benchmark design criteria, design guidelines, and recommendations in a similar presentation as AASHTO LRFD to facilitate and promote the design and construction of highway bridges with CFRP components.

17. Key Words CFRP; Prestressed Highway Bridges; Creep Rupture, Relaxation; Fire; Environmental Conditions; Freeze-Thaw.		18. Distribution Statement No restrictions. This document is also available to the public through the Michigan Department of Transportation.	
19. Security Classif. (of this report) Unclassified	20. Security Classif. (of this page) Unclassified	21. No. of Pages 392	22. Price N/A

Form DOT F 1700.7 (8-72)   Reproduction of completed page authorized

ACKNOWLEDGEMENTS AND DISCLAIMER

TABLE OF CONTENT

LIST OF FIGURES

viii

xiii

xv

xvii

xviii

xix

xxvii

LIST OF TABLES

xxx

EXECUTIVE SUMMARY

Successful deployment of 0.6 in. (15.2 mm) diameter CFRP strands in pretensioning bridge beams motivated the bridge industry and designers to explore options to further optimize the design using CRFP and produce cost-competitive long-lasting highway bridge beams. One option is to increase the size of the CFRP strands to a larger diameter (0.7 in. (17.8 mm)). The deployment of 0.7 in. (17.8 mm) CFRP strands in bridge beam construction will increase the prestressing force per strand and consequently reduce the number of strands per beam. This creates potential for the use of CFRP technology in longer spans, beams with shallower depths, and in bridges with wider beam spacing. In addition, the use of 0.7 in. (17.8 mm) CFRP prestressing strands is expected to facilitate and expedite beam construction by reducing the number of anchorage devices and will also improve the design by lowering the center of gravity of the strands. Nevertheless, a larger prestressing force per strand could also lead to stress concentrations and unfavorable conditions, particularly at beam ends at the time of prestress release. Therefore, careful evaluations for parameters such as bond strength, transfer length, and strand spacings are mandatory to ensure a proper design for the section and eliminate potential cracking.

This report presents the details and results of comprehensive experimental and analytical investigations that were executed with the main objective of establishing a design criteria of bridge beams prestressed with large diameter CFRP strands. The investigations evaluated the short and long-term performance of 0.7 in. (17.8 mm) CFRP under various environmental and loading conditions. The experimental investigations started by evaluating and optimizing the performance of different anchorage devices and selecting a device that was adequate for executing other tasks of the investigation. Second, the mechanical properties of the selected CFRP material, such as average tensile strength, maximum strain, elastic modulus, and guaranteed strength were established through testing 64-in. (1626-mm) long CFRP specimens. Third, long-term properties of CFRP strands such as relaxation and creep rupture strength were evaluated by testing sets of CFRP specimens that were loaded and monitored at ambient temperature and controlled laboratory conditions. In addition, multiple sets of test specimens with the same configuration were evaluated for strength and prestress loss under severe exposure conditions. For instance, two sets of test specimens were subjected to elevated temperatures and loads under two different test protocols.

Two sets were prestressed and exposed to 150 and 300 cycles of freezing and thawing in a special environmental chamber, and then loaded to failure in a uniaxial test setup.

The test program included establishing the bond strength between large diameter CFRP strands and concrete and evaluating the transfer and development lengths. Pullout specimens were prepared and tested under static tensile loads as well as cyclic loading. In addition, multiple sets of test specimens were constructed and instrumented to evaluate the transfer and development lengths.

The experimental investigation also included testing and evaluating half-scale and full-scale bridge beams prestressed with bonded CFRP strands. Three full-scale 28-in. (711-mm) deep AASHTO I-beams were designed, constructed, and tested to failure under four-point flexural loading. The first beam served as a control beam and was reinforced and prestressed with steel strands with a diameter of 0.6 in. (15.2 mm). The second beam was prestressed with carbon fiber composite cable (CFCC) strands with a diameter of 0.6 in. (15.2 mm). The third beam was prestressed with CFCC strands with a diameter of 0.7 in. (17.8 mm). All beams had a span of 40 ft (12.2 m) and were provided with a 9.0-in. (229-mm) thick reinforced concrete deck slab. All three beams had identical cross-sectional dimensions and were designed to support the same level of factored moment calculated according to AASHTO LRFD as an interior beam of a bridge superstructure. In order to evaluate test results for other cross sections, an additional full-scale bulb T beam with a depth of 36 in. (914 mm) and a span of 40 ft (12.2 m) was constructed with 0.7 in. (17.8 mm) CFCC strands and tested to failure under four-point loading and over a span of 39 ft (11.9 m).

After completing the full-scale testing, 16-ft (4.88-m) segments of the test beams were salvaged from the first two full-scale AASHTO beams with 0.6 in. (15.2 mm) steel and CFCC strands. In addition, two full-scale bulb T beams and two box beams were designed and prestressed with 0.7 in. (17.8 mm) CFCC strands. All the beams had a length of 16 ft (4.88 m). The salvaged beams and the new beams were split into two groups and exposed to two different fire scenarios. The first group was subjected to a fire event according to ASTM E119 combined with a service loading applied through a three-point loading setup. The test took place inside a large-scale natural-gas fire chamber, where the air temperature, beam temperature, load, and deflection were monitored during the entire test using a data acquisition system. The test ended when the test beam

failed to support the applied service load. Test results were assembled and analyzed to establish fire resistance criteria for beams prestressed with CFRP strands. The second group of beams was exposed to a similar fire/loading event that lasted for only one hour. After, the beams were allowed to cool down naturally and tested to failure under three-point loading under ambient conditions. The residual strength and the mode of failure after exposure to a one-hour fire/loading event were subsequently evaluated.

To study the effect of seasonal temperature change and the influence of freezing and thawing cycles on the performance of CFRP prestressed bridge beams, a set of half-scale CFRP prestressed decked bulb T beams was designed, constructed and tested. The set included six identical beams with a span of 16 ft (4.87 m), a depth of 16 in. (406 mm), and a top flange width of 18 in. (457 mm). The beams were constructed from the same concrete batch and were subjected to an initial prestressing force of 106 kip (471 kN) per beam. All beams were tested under three-point loading to approximately 75 % of their theoretical load carrying capacity. Two beams served as control beams and were preserved and tested in controlled laboratory conditions. Two beams were tested in hot conditions with air and beam temperatures of 176 °F (80 °C). Then the beams were allowed to cool down and that test was repeated at an ambient temperature of 68 °F (20 °C). The last two beams were tested at severe cold conditions, where the air/beam temperature was lowered to -40 °F (-40 °C). Then, the beams were allowed to warm up and the test was repeated at ambient conditions. Test results were used to back calculate the effective prestressing force in each beam during the time of the testing and were used to estimate the change of the prestressing force due to seasonal temperature change.

Testing was also conducted to evaluate the performance and residual strength of the beams after exposure to 300 cycles of freezing and thawing according to ASTM C666. The control beams were kept in controlled laboratory conditions, while the remaining four beams were subjected to the freezing and thawing cycles inside a large-scale environmental chamber. After the conclusion of the freeze-thaw cycles, all the beams, including the control beams, were loaded to failure under three-point loading. Parameters such as loss of prestressing force, mode of failure, and residual strength were examined and documented.

Parallel to the experimental investigation, a comprehensive analytical investigation was conducted to examine the test results and develop analytical models for the performance of CFRP

materials. The outcome of the analytical investigation was deployed in the development of detailed Mathcad sheets for the design of CFRP precast prestressed highway bridge beams. The Mathcad sheets were calibrated, tested, and used in the design of Cadillac Ave. Bridge and Burns Ave. Bridge over I-94 in Detroit. Test results of the investigation provided valuable information and design parameters that accurately described the short and long-term performances of unbonded and bonded CFRP strands. Those design parameters were deployed to establish benchmark design criteria, design guidelines, and recommendations.

CHAPTER 1: INTRODUCTION

1.1 Overview

The Michigan, Ohio, North Carolina, and Maine Departments of Transportation pioneer in the deployment of innovative materials such as non-corrosive CFRP to enhance the design, construction, and durability of highway bridge beams. This is influenced by the harsh weather and the overwhelming corrosion and durability issues associated with steel prestressed beam bridges (Grace et al. 2002a, 2002b, and 2004). Supported by decades of research and analysis (Grace and Abdel-Sayed 2000), the use of CFRP as a prestressing and reinforcement material started in Michigan in 2001 with the construction of the Bridge Street Bridge in Southfield, MI. Since then, several bridges have been successfully designed and built with CFRP components. For instance, in 2011, a two-span side-by-side precast prestressed box-beam bridge was constructed to carry Pembroke Rd over M-39 in Detroit, MI. The bridge is transversely post-tensioned with twelve 1.57-in. (40-mm) diameter un-bonded carbon fiber composite cable (CFCC) strands. In 2012, a three-span side-by-side box beam bridge carrying M-50 over the NSRR railroad in Jackson, MI was also constructed and transversely post-tensioned using twenty unbonded CFCC strands. In 2013 and 2014, two simply supported 45° skewed precast prestressed spread box beam bridges were constructed to carry the east and west bounds of M-102 over Plum Creek in Southfield, MI. The box beams are prestressed with 0.6 in. (15.2 mm) CFCC strands and reinforced with CFCC stirrups in the transverse direction. The cast-in-place deck slabs for both bridges are also reinforced with CFCC strands. In 2016, a 102.5-ft (31.2-m) long simply supported bulb T beam bridge was constructed to carry M-86 over Prairie River in Centreville, MI. Each of its seven bridge beams is prestressed with 59 CFCC strands with a diameter of 0.6 in. (15.2 mm). In 2017, the construction of the 137 ft (41.7 m) long I-75 highway bridge over Sexton and Kilfoil Drain in Allen Park, MI marked the construction of the world's longest bridge span prestressed with CFRP strands.

From several years of extensive research and analysis (Grace et al. 1999 to 2019), only CFRP strands with a diameter of 0.6 in. (15.2 mm) have been used in pretensioning aforementioned bridge projects, where pretenioned CFRP strands are used. The number of strands per beam is adjusted to satisfy design requirements at service and strength limit states with the prestressing force level being the prominent factor governing the design and the number of strands per beam. ACI 440.4R-04 (ACI 2004) limits the jacking strength to 65 % of the design strength of CFRP

products. The design strength of a CFRP strand is taken as 90 % of its guaranteed strength to account for any environmental effect on the strength. Using the ACI-440-4R-04 jacking limit, the jacking force of 0.6 in. (15.2 mm) strands is limited to 35.5 kip (158 kN) per strand, which explains the large number of strands that were used in existing bridge projects. Unfortunately, the larger number of CFRP strands limits the span length and the load carrying capacity of the beam and hinders the deployment of CFRP technology in several potential bridge projects.

1.2 Research Scope

The current report presents the details and results of a four-year-long extensive research investigation that has recently been completed with the main objectives of:

1. Evaluate material properties, details, and design criteria to use 0.7 in. (17.8 mm) diameter CFRP strands systems for pretensioning of prestressed AASHTO I beams, bulb T, and box-beams. Throughout the report, the strands are labeled by their diameter in inches and their material as: 0.7″ CFRP, 0.6″ CFRP, 0.7″ steel, or 0.6″ steel.
2. Evaluate the performance of 0.7″ CFRP strands for environmental conditions and extreme events.
3. Prepare design procedures and examples.
4. Prepare construction specifications for 0.7″ CFRP strands and identify fabrication concerns with the larger diameter strands.

1.3 Research Outcomes

Research outcomes for this project include the following:

1. Verify material properties of 0.7″ CFRP strands at ambient and elevated temperatures.

2. Establish differences and similarities in material properties and performance between 0.7″ and 0.6″ CFRP strands under various harsh environmental conditions.

3. Experimentally verify anchorage strength, creep rupture stress, relaxation loss, overall long-term losses, and prestress levels under harsh environmental conditions.

4. Document the interaction between 0.7″ CFRP strands and the structural concrete in pre-tensioning applications.

2

5. Evaluate the performance of 0.7″ CFRP under extreme events such as fire/loading events following ASTM E119 test standards.

6. Assess the performance of 0.7″ CFRP strands under repeated cycles of freezing and thawing on large-scale prestressed beams following appropriate test standards.

7. Document unique changes to CFRP prestressed beam design procedures when 0.7″ CFRP strands are used for longitudinal pre-tensioning.

8. Evaluate the performance of full-scale precast beams prestressed with 0.7″ CFRP strands in comparison with similar beams prestressed with 0.6″ steel or CFRP strands.

9. Develop design procedure/examples and construction specifications for 0.7″ CFRP prestressed concrete highway bridge beams.

10. Highlight fabrication concerns and provide potential solutions to the use of larger diameter CFRP strands in relation to the current stressing bed layouts.

1.4 Report Outline

This report documents the details and results of the research investigation. Each chapter summarizes the research performed for a specific objective and if applicable, provides an introduction and a brief literature review. Each chapter provides details of the research subject under consideration and provides a summary for the test results, observations, and recommendations. The final chapter of the report summarizes main findings and recommendations of the research investigation. In addition, based on the findings and recommendations of the report, Mathcad sheets for the design and construction of CFRP precast prestressed highway bridge beams were developed and are provided in the Appendix. The chapters of the report are arranged as follows:

Chapter 2:   Anchorage and tensile strength of CFRP strands

Chapter 3:   Creep rupture strength and relaxation of CFRP strands

Chapter 4:   Bond, transfer length, and development length of CFRP strands

Chapter 5:   Full-scale beam testing

Chapter 6:   Fire and heat resistance of CFRP strands

CHAPTER 2: ANCHORAGE AND TENSILE STRENGTH

2.1 Introduction

An important consideration of testing large diameter CFCC strands is to ensure that failure occurs in the test specimen, not at the anchorage. Therefore, an adequate anchorage device is mandatory to establish a successful testing protocol and a safe field deployment. Through the investigation provided in this chapter, two anchorage devices were prepared, assembled, and tested in collaboration with the manufacturer of CFCC strands. The first anchorage device is composed of a steel wedge system that was tested and verified for pre-tensioning applications in the field. Layers of buffer materials are wrapped around the CFCC strand before the steel wedge anchorage is attached to distribute the pressure from the wedges on the surface of CFCC strands. Typically, this wedge anchorage system is used as a component of a coupler system in pre-tensioning applications to attach the CFCC strands to steel strands on both the live and the dead ends of the prestressing bed. The coupler system facilitates the construction by allowing the construction crew to apply the force to the steel strands using the standard tensioning equipment and standard anchorage devices. A series of 50 ft (15.2 m) long large diameter CFCC specimens were prepared and tensioned using the coupler system and were monitored for an extended period of time to assess the safety of the coupler system and evaluate the seating losses in the system.

The second anchorage device was prepared for the purpose of conducting different tasks of the research investigation. It consisted of a sleeve anchor that was attached to large diameter CFCC strands using early tested and proven expansive grout material. To verify the anchorage device, a series of 64 in. (1626 mm) long CFCC specimens were loaded in a uniaxial test setup to failure using a sleeve anchorage device. Details of testing both anchorage systems are presented in the following sections.

2.2 Test Specimens

The CFRP strand specimens used in anchorage testing and throughout the test program were 7-wire CFCC strands, manufactured by Tokyo Rope Mfg. Co., Ltd., Japan, with a nominal diameter of 0.7 in. (17.8 mm), cross sectional area of 0.234 in.^{2} (151 mm^2), and mechanical properties per lot, reported by the manufacturer as shown in Table 2.2-1.

After installing the anchorage devices at both ends, a uniaxial tensile test was conducted in accordance with ASTM Standard D7205/7205M-06 (ASTM 2016) "Standard Test Method for Tensile Properties of Fiber Reinforced Polymer Matrix Composite Bars.".

The CFCC strands were delivered in reels, as shown in Figure 2.2-1. A reel controlling system was developed to spool the CFCC strands in both directions. The system is composed of a hand lever connected to an electric motor through a spring. The electric motor is provided with a hand controller that regulates the motion of the strands. The components of the reel controlling system are shown in Figure 2.2-2. After spooling the CFCC strand to the required length, it was cut using a power grinder.

Table 2.2-1 Mechanical properties of CFCC as provided by manufacturer, Tokyo Rope

Strand configuration & Lot No.	1 x 7, G424	1 x 7, G447	1 x 7, T007
Test date	12/8/2015	12/8/2015	8/10/2018
Diameter, in. (mm)	0.7 (17.26)	0.7 (17.32)	0.7 (17.33)
Guaranteed breaking load, kip (kN)	78.7 (350)	78.7 (350)	78.7 (350)
Effective cross-sectional area, in.^{2} (mm^2)	0.234 (151.1)	0.234 (151.1)	0.234 (151.1)
Average breaking load, kip (kN)	105.5 (469.3)	102.9 (457.5)	102.4 (456)
Max. breaking load, kip (kN)	107.1 (476.3)	107.1 (476.4)	104.8 (466)
Min. breaking load, kip (kN)	104.1 (463.1)	99.3 (441.5)	99.2 (441)
No. of test specimens	5	5	5
Average tensile strength, ksi (GPa)	451.1 (3.11)	439.5 (3.03)	438 (3.02)
Average tensile modulus, ksi (GPa)	22,626(156)	22,481 (155)	22,200 (153)
Elongation, %	2.0	2.0	1.97

Figure 2.2-1 Spool of CFCC strands with a diameter of 0.7″ (17.3 mm)
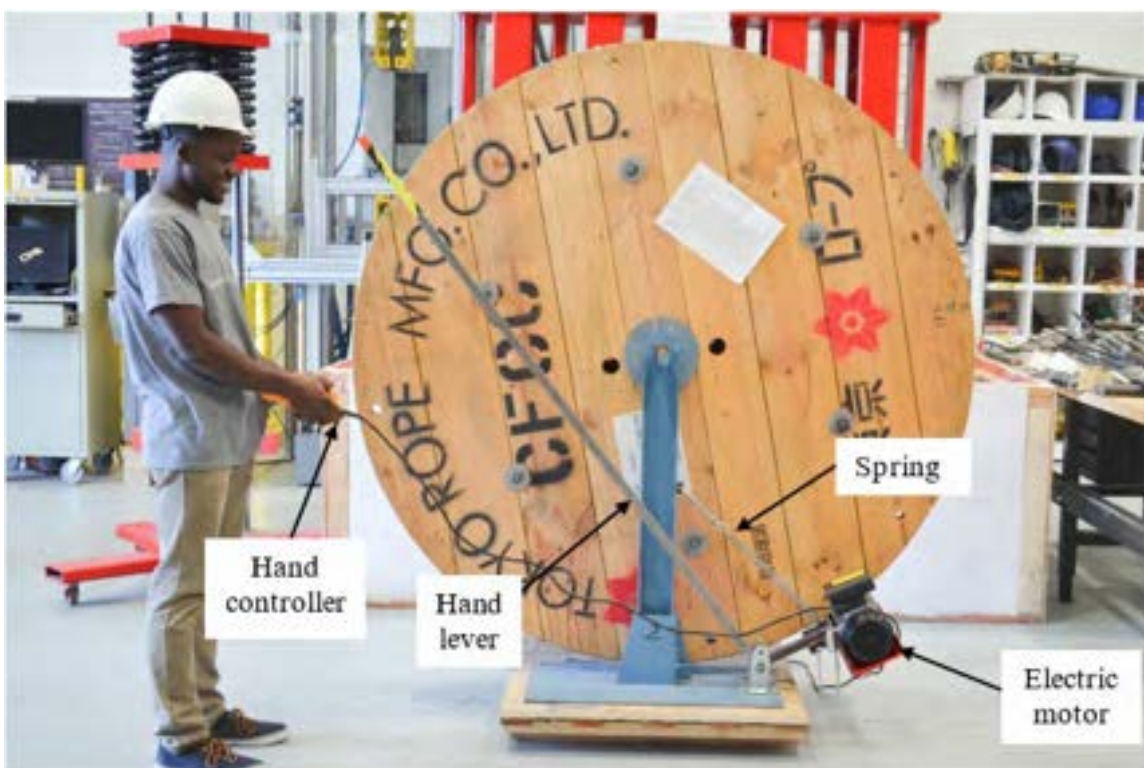
Figure 2.2-2 Components of the reel controlling system

2.3 Steel Wedge Anchorage

The steel wedge anchorage device was composed of four high-strength steel wedges that fit snuggly around the CFCC strand inside a high-strength steel barrel. As the strand is pulled, the wedges slide into the steel barrel and confines the movement of the CFCC strand. To avoid damaging the surface of the strand, the strand was wrapped with layers of buffer materials and braided wire mesh. The components of the wedge system and the buffer material are shown in Figure 2.3-1 and Figure 2.3-2 , respectively. The process of applying the buffer system and the installation of the anchorage device is shown in Figure 2.3-3.

Four CFCC test specimens were prepared and provided with the steel wedge anchorage at the ends as a part of a coupler system. The specimens were pretensioned and monitored for extended time to evaluate parameters such as rate of seating, potential for slippage over time, and initial prestress loss before concrete curing. By the end of the test program, a newly developed buffer material was developed by the manufacturer. Therefore, the test was repeated using the new buffer material and another set of four strands was prepared, pretensioned, and monitored as shown in Figure 2.3-6.

2.3.1 Wedge System with Old Buffer Material

To accommodate the larger diameter CFCC strand, the wedge system was modified from that used with 0.6″ CFCC strands. Longer wedges and thick steel barrel were manufactured and provided by the manufacturer for testing and evaluation. As shown in Figure 2.3-1 through Figure 2.3-4, the evaluation of the anchorage and coupler system was integrated into the test protocol and was conducted before the construction of full-scale box beam specimens that were used later for fire testing. The evaluation of the anchorage and coupler system included preparing, tensioning, and monitoring CFCC strands for 45 days before pouring the concrete. The time vs. force level is presented in Figure 2.3-5, while detailed force levels and prestress loss are presented in Table 2.3-1 through Table 2.3-3. As shown in the tables, seating of the steel anchors and rotation of the bulkheads during the prestressing of strands were major contributors in the overall prestress loss. This is attributed to the relatively small size of the prestressing bed (50 ft or 15.24 m). Within the first 24 hours, additional force loss was observed and was attributed to the seating of the coupler systems as well as the relaxation of CFCC strands. After the first day of prestressing, the losses seemed negligible until the end of the monitoring period before pouring the concrete.
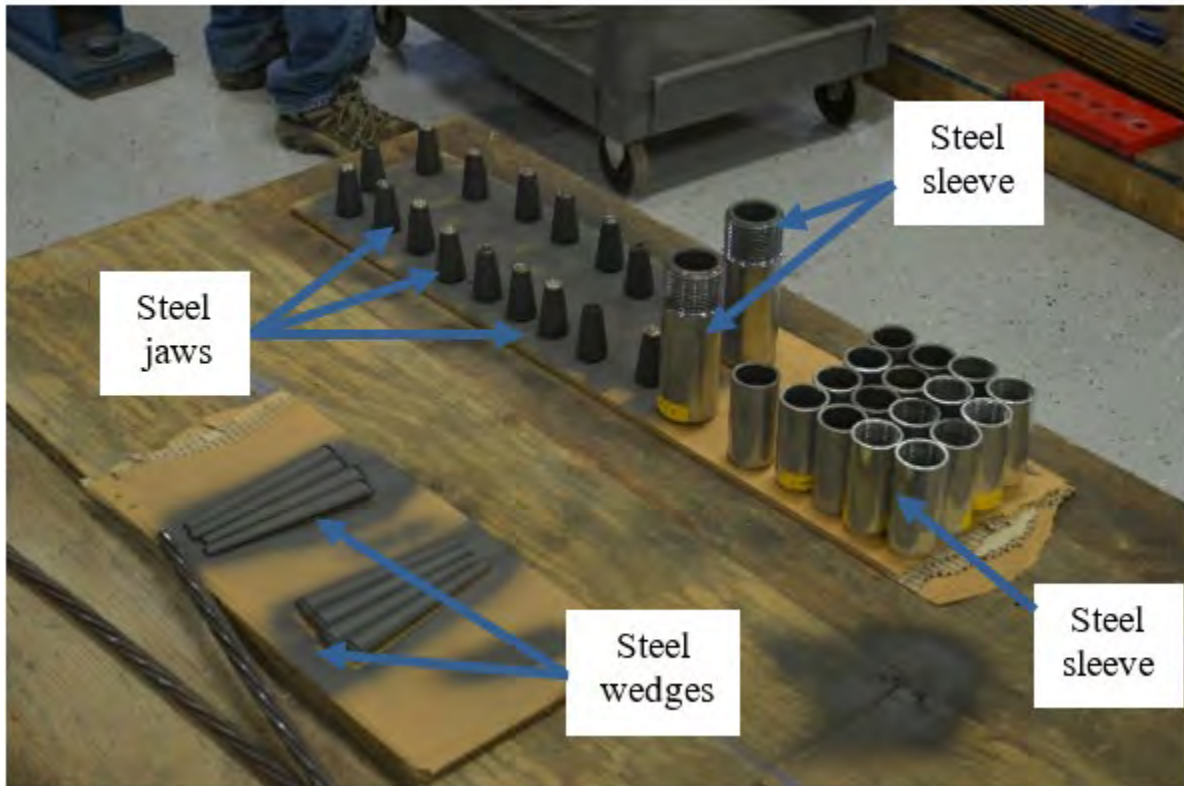
Figure 2.3-1 Components of steel wedge anchorage system
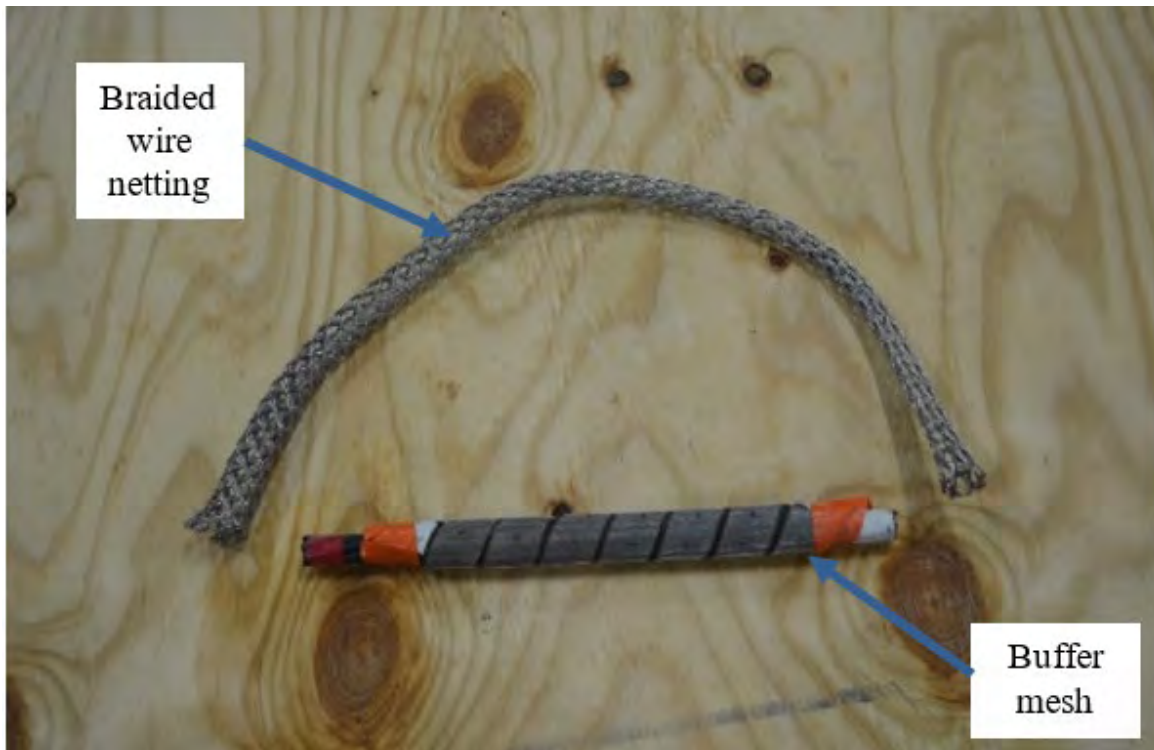
Figure 2.3-2 Buffer material (old system) wrapped around CFCC to avoid damaging the surface

(a) Wrapping buffer material around CFCC
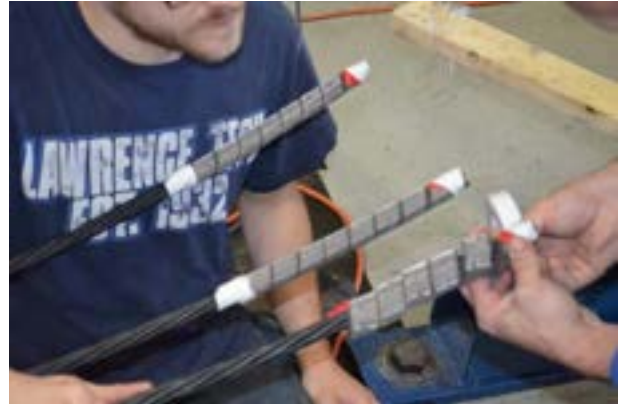
(b) Securing steel mesh in place with tape

(c) Additional braided steel wire netting

(d) Installing steel wedge system

(e) Sliding steel wedges using hand pump

(f) Completed anchorage device

Figure 2.3-3 Installing steel-wedge anchorage device on CFCC strand with buffer layer
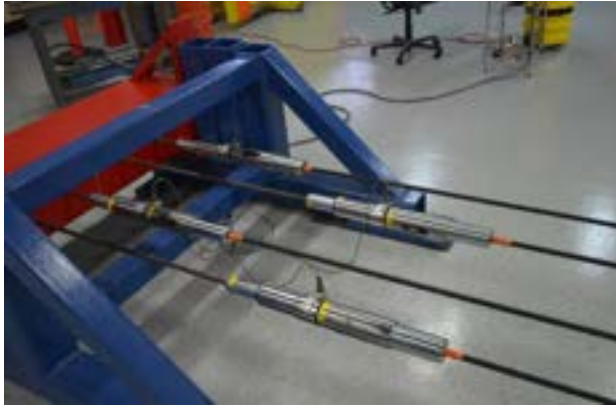
(a) Dead end anchorage with load cells

(b) Live end anchorage system

(c) Reinforcement cage of box beam section
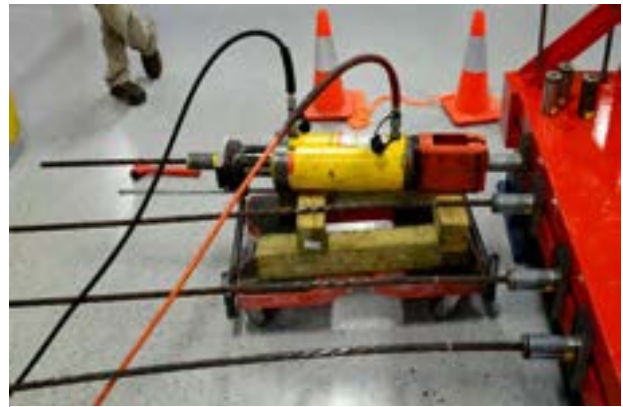
(d) Pulling CFCC strands to required force

(e) placing concrete in box beam formwork
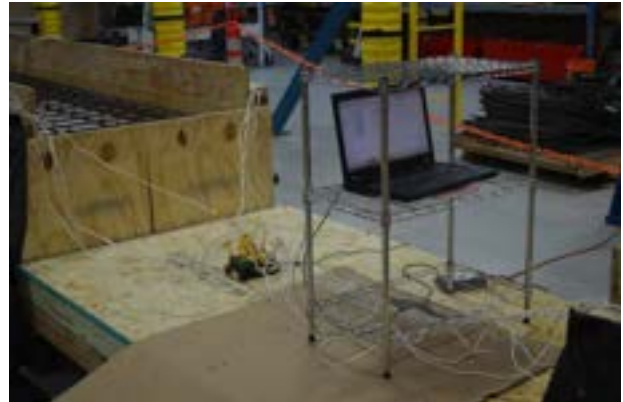
(f) Setup for monitoring of force and temp.

Figure 2.3-4 Test setup for monitoring CFCC strands during box beam construction

Figure 2.3-5 Monitoring of prestressing force in four CFCC strands from prestressing until prestress release

Table 2.3-1 Readings of load cells and prestressing force over time

	Prestress readings, kip (1.0 kip = 4.448 kN)			
Jacking	52.08	52.44	48.23	51.84
Anchor seating	48.65	49.00	45.69	48.61
After prestressing last strand	48.65	48.38	44.91	47.59
End of 2nd hour	47.85	47.74	44.64	47.17
End of 24 hrs	47.08	46.81	43.84	46.28
End of 72 hrs	46.78	46.52	43.56	45.99
End of 120 hrs	46.66	46.4	43.42	45.85
End of 168 hrs	46.58	46.28	43.33	45.73
End of 216 hrs	46.50	46.21	43.25	45.66
End of 264 hrs	46.44	46.15	43.18	45.62
End of 312 hrs	46.40	46.10	43.13	45.55
End of 360 hrs	46.35	46.06	43.08	45.52
End of 408 hrs	46.31	46.04	43.06	45.49
End of 456 hrs	46.28	46.00	43.01	45.46
End of 504 hrs	46.27	45.98	43.00	45.43
End of 552 hrs	46.24	45.94	42.97	45.4
End of 600 hrs	46.22	45.91	42.94	45.37
End of 648 hrs	46.18	45.9	42.89	45.34
End of 696 hrs	46.2	45.91	42.89	45.35
End of 744 hrs	46.18	45.87	42.88	45.34
End of 792 hrs	45.99	45.68	42.65	45.12
End of 840 hrs	46.01	45.7	42.66	45.13
End of 888 hrs	45.99	45.68	42.65	45.12
End of 936 hrs	45.97	45.68	42.65	45.12
End of 984 hrs	45.97	45.65	42.61	45.1
End of 1032 hrs	45.94	45.62	42.59	45.07
End of 1080 hrs	45.95	45.62	42.59	45.07
End of 1102 hrs, concrete casting	45.96	45.65	42.59	45.09

Table 2.3-2 Summary of prestress loss over time

Loss of prestress	Loss in prestress, kip (1.0 kip = 4.448 kN)			
	Strand 1	Strand 2	Strand 3	Strand 4
Due to anchor seating	3.43	3.44	2.54	3.23
from 0 to 2 hrs	0.80	1.26	1.05	1.44
from 2 to 24 hrs	0.77	0.93	0.80	0.89
from 24 to 72 hrs	0.30	0.29	0.28	0.29
from 72 to 120 hrs	0.12	0.12	0.14	0.14
from 120 to 168 hrs	0.08	0.12	0.09	0.12
from 168 to 216 hrs	0.08	0.07	0.08	0.07
from 216 to 264 hrs	0.06	0.06	0.07	0.04
from 264 to 312 hrs	0.04	0.05	0.05	0.07
from 312 to 360 hrs	0.05	0.04	0.05	0.03
from 360 to 408 hrs	0.04	0.02	0.02	0.03
from 408 to 456 hrs	0.03	0.04	0.05	0.03
from 456 to 504 hrs	0.01	0.02	0.01	0.03
from 504 to 552 hrs	0.03	0.04	0.03	0.03
from 552 to 600 hrs	0.02	0.03	0.03	0.03
from 600 to 648 hrs	0.04	0.01	0.05	0.03
from 648 to 696 hrs	-0.02	-0.01	0.00	-0.01
from 696 to 744 hrs	0.02	0.04	0.01	0.01
from 744 to792 hrs	0.19	0.19	0.23	0.22
from 792 to 840 hrs	-0.02	-0.02	-0.01	-0.01
from 840 to 888 hrs	0.02	0.02	0.01	0.01
from 888 to 936 hrs	0.02	0.00	0.00	0.00
from 936 to 984 hrs	0.00	0.03	0.04	0.02
from 984 to 1032 hrs	0.03	0.03	0.02	0.03
from 1032 to 1080 hrs	-0.01	0.00	0.00	0.00
from 1080 to 1102 hrs	-0.01	-0.03	0.00	-0.02

Table 2.3-3 Percentage of prestress loss with respect to total loss

Loss of prestress in	Loss in prestress, %			
First 2 hours	24.39	30.96	27.49	35.56
Rest of Day 1	23.48	22.85	20.94	21.98
Day 3	9.15	7.13	7.33	7.16
Day 5	3.66	2.95	3.66	3.46
Day 7	2.44	2.95	2.36	2.96
Day 9	2.44	1.72	2.09	1.73
Day 11	1.83	1.47	1.83	0.99
Day 13	1.22	1.23	1.31	1.73
Day 15	1.52	0.98	1.31	0.74
Day 17	1.22	0.49	0.52	0.74
Day 19	0.91	0.98	1.31	0.74
Day 21	0.30	0.49	0.26	0.74
Day 23	0.91	0.98	0.79	0.74
Day 25	0.61	0.74	0.79	0.74
Day 27	1.22	0.25	1.31	0.74
Day 29	-0.61	-0.25	0.00	-0.25
Day 31	0.61	0.98	0.26	0.25
Day 33	5.79	4.67	6.02	5.43
Day 35	-0.61	-0.49	-0.26	-0.25
Day 37	0.61	0.49	0.26	0.25
Day 39	0.61	0.00	0.00	0.00
Day 41	0.00	0.74	1.05	0.49
Day 43	0.91	0.74	0.52	0.74
Day 45	-0.30	0.00	0.00	0.00

2.3.2 Wedge System with New Buffer Material

The new buffer system eliminates the need for braided wire netting by integrating additional coarse wire mesh to the layers of the fine wire mesh in the buffer system. This facilitates the application of the buffer layer around the CFCC strand and ensures better quality control. To assess the new buffer system and calculate potential seating losses from the time of prestressing to concrete pouring, four CFCC strands were prepared and tensioned using the new buffer material as shown in Figure 2.3-6 through Figure 2.3-8. Similar to the previous monitoring test, the force level in the strands was monitored continuously until the release of the prestressing strands after 17 days from the day of prestressing as shown in Figure 2.3-9. In addition, Table 2.3-4 through Table 2.3-6 show the level of the prestressing force in each strand and loss of prestressing force each day. Since there were no plans to pour concrete, the prestressing strands were coupled with 0.7″ steel strands on the live end to facilitate prestressing and 1.5 in (38 mm) diameter high strength threaded steel bars on the dead end to facilitate prestress release by the end of the monitoring period. The length of CFCC strands was 44.07 ft (13,432 mm), while the length of the coupled steel stand on the live end was 2.77 ft (844 mm), and the length of the steel bar on the dead end was 1.91 ft (576 mm).

The average immediate loss due to seating of live end steel anchors was approximately 3.7 kip (16.5 kN). Considering an overall length of prestressing CFCC strands and the coupled steel strands/bars of 48.75 ft (14.86 m) and using the elastic modulus and cross-sectional area for each component, the estimated steel anchor seating at the live end was 0.375 in. (10 mm). It should be noted that prestress loss due to seating is adversely proportional to length of prestressing strands. For instance, in a prestressing system with a length of 300 ft (91.4 m), a seating of 0.375 in. (10 mm) yields a prestress loss of only 0.6 kip (2.7 kN) per 0.7" strand.

After anchor seating at the live end, additional seating loss was encountered due to: (1) relaxation of CFCC strands, (2) seating of the coupler system, and (3) deformation of bulkhead with subsequent strand pulling. Over the course of 17 days, the average additional prestress loss was approximately 3.23 kip (14 kN), which corresponded to an overall additional seating of the system of 0.35 in. (9 mm). By ignoring the prestress loss due to strand relaxation and rotation of the bulkheads, it can be assumed that each coupler in the system experienced a seating of 0.18 in. (5 mm). It should be noted that over 90% of additional prestress loss took place within the first 24 hours. Prestress losses in subsequent days were negligible. Similar to live end anchor seating, this

16

prestress loss is adversely proportional to the length of the prestressing strands. For a 300 ft (91.4 m) prestressing bed, the estimated prestress loss per strand, based on 0.35 in. (9 mm) of two couplers seating, is 0.58 kip (2.6 kN).

It should be noted that additional prestress loss or gain prior to concrete pouring can occur due to change in temperature and expansion/contraction of coupled steel strands. This is not applicable to the current test as temperature is controlled.

(a) New composite buffer material	(b) Spraying sleeve with lubricant
(c) Steel wedge system	(d) Sliding steel wedge system into CFCC

Figure 2.3-6 New composite buffer material as a replacement for older two-component buffer

Figure 2.3-7 Coupling CFCC strands with steel strands at the live end
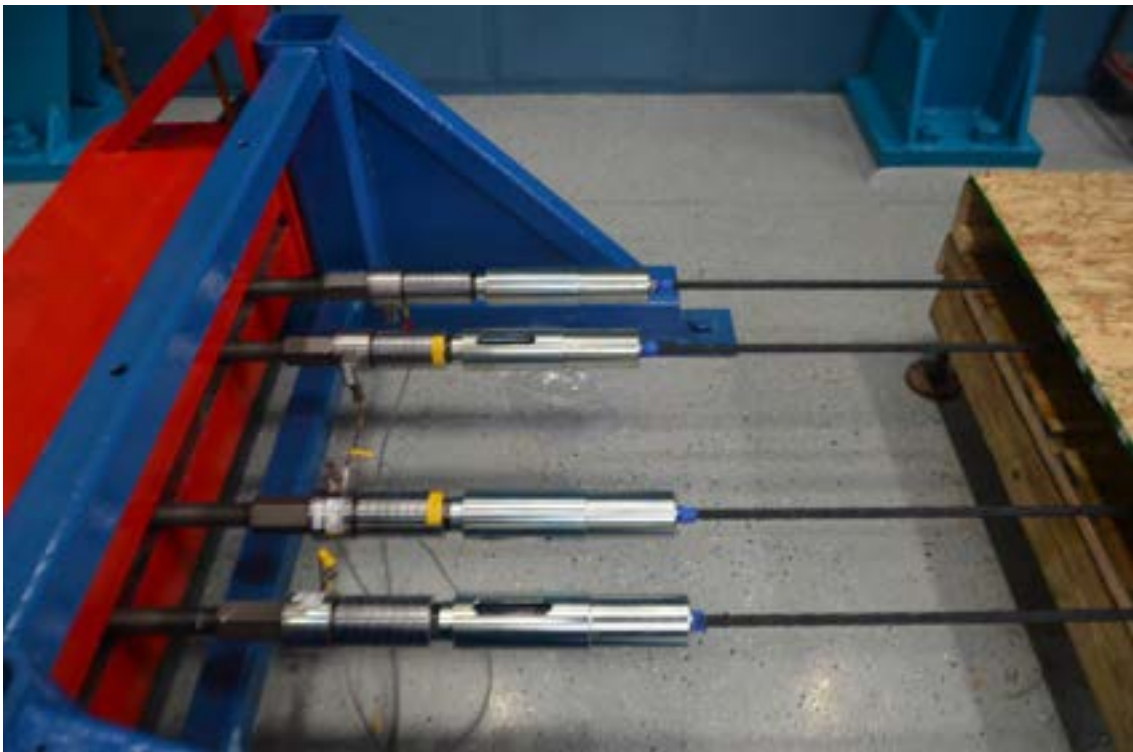
Figure 2.3-8 Coupling CFCC strands with load cells and threaded steel bars at the dead end
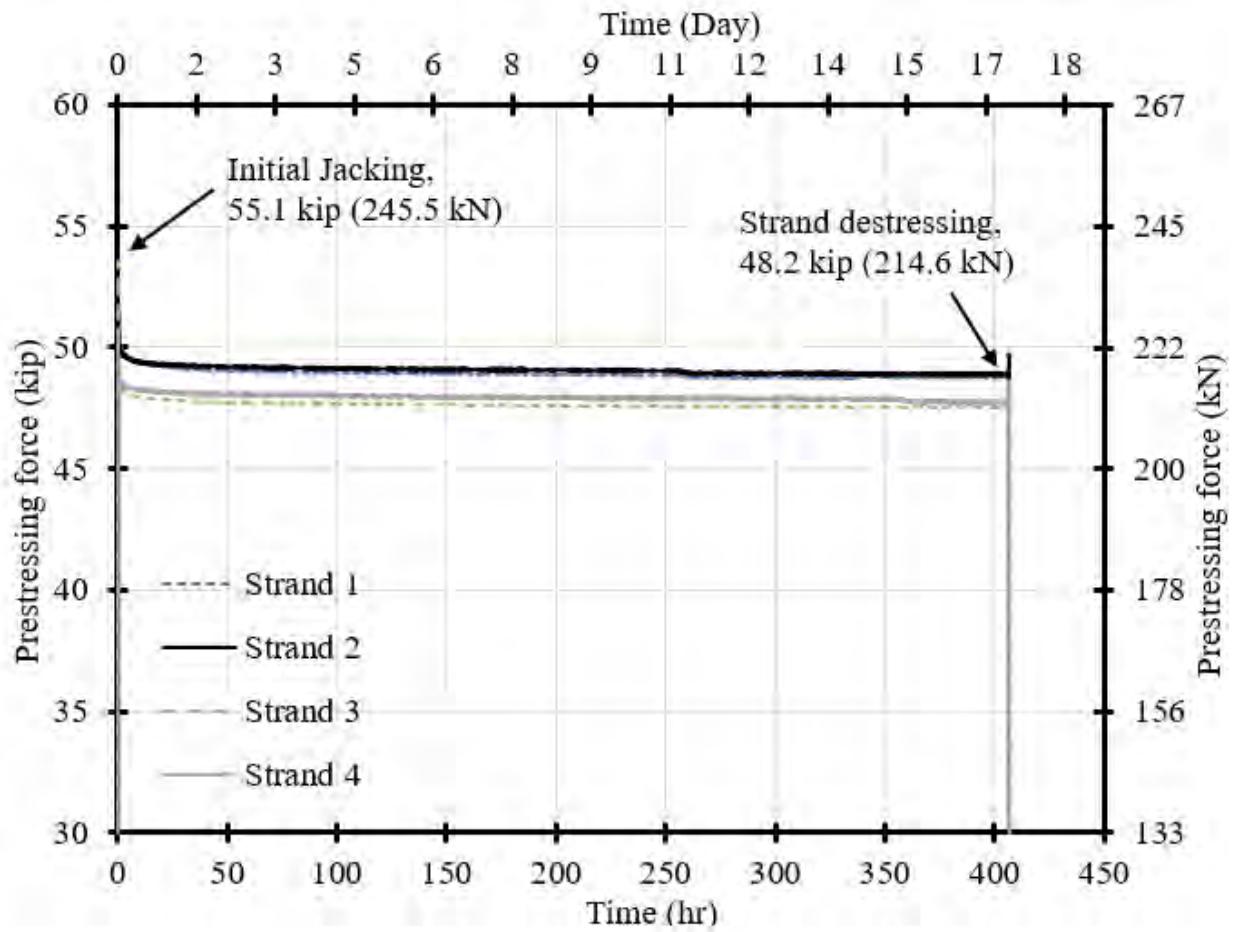
Figure 2.3-9 Monitoring of prestressing force in four CFCC strands

Table 2.3-4 Readings of load cells and prestressing force over time

	Prestress readings, kip (1.0 kip = 4.448 kN)			
Jacking	55.14	55.11	55.34	55.05
Anchor seating	51.96	52.01	50.90	51.00
After prestressing last strand	51.96	50.55	48.76	48.89
End of 1st hour	50.06	49.91	48.45	48.69
End of 24 hrs.	49.17	49.29	47.84	48.15
End of 48 hrs.	49.01	49.20	47.74	48.07
End of 72 hrs.	49.01	49.17	47.7	48.06
End of 96 hrs.	48.95	49.15	47.68	48.01
End of 120 hrs.	48.94	49.12	47.65	47.98
End of 144 hrs.	48.92	49.10	47.64	47.98
End of 168 hrs.	48.90	49.08	47.63	47.95
End of 192 hrs	48.88	49.07	47.61	47.94
End of 216 hrs	48.86	49.06	47.59	47.92
End of 240 hrs	48.75	49.04	47.58	47.92
End of 264 hrs	48.74	48.95	47.58	47.91
End of 288 hrs	48.75	48.95	47.56	47.89
End of 312 hrs	48.74	48.93	47.56	47.89
End of 336 hrs	48.76	48.90	47.55	47.87
End of 360 hrs	48.76	48.90	47.55	47.78
End of 384 hrs	48.76	48.90	47.53	47.77
Before destressing the strands	48.75	48.90	47.53	47.75

Table 2.3-5 Summary of prestress loss over time

	Loss in prestress, kip (1.0 kip = 4.448 kN)				Notes
Loss of prestress	Strand 1	Strand 2	Strand 3	Strand 4	Strand 4 was pulled first
Anchor seating	3.18	3.1	4.44	4.05	Estimated Steel anchor seating of 3/8 in.
1st hour	1.9	2.1	2.45	2.31	Includes bulkhead rotation in Strands 2, 3, 4
from 1 to 24 hrs	0.89	0.62	0.61	0.54	
from 24 to 48 hrs	0.16	0.09	0.1	0.08	
from 48 to 72 hrs	0	0.03	0.04	0.01	
from 72 to 96 hrs	0.06	0.02	0.02	0.05	
from 96 to 120 hrs	0.01	0.03	0.03	0.03	
from 120 to 144 hrs	0.02	0.02	0.01	0	
from 144 to 168 hrs	0.02	0.02	0.01	0.03	
from 168 to 192 hrs	0.02	0.01	0.02	0.01	
from 192 to 216 hrs	0.02	0.01	0.02	0.02	
from 216 to 240 hrs	0.01	0.02	0.01	0	
from 240 to 264 hrs	0.1	0.09	0	0.01	
from 264 to 288 hrs	0.01	0	0.02	0.02	
from 288 to 312 hrs	-0.01	0.02	0	0	
from 312 to 336 hrs	0.01	0.03	0.01	0.02	
from 336 to 360 hrs	-0.02	0	0	0.09	
from 360 to 384 hrs	0	0	0.02	0.01	
from 384 to release	0	0	0	0.02	
Total in 406 hrs	3.2	3.11	3.37	3.25	Not including anchor seating
movement (in.)	0.343	0.333	0.361	0.348	Seating corresponding to force loss

Table 2.3-6 Percentage of prestress loss with respect to total loss

Loss of prestress in	Loss in prestress with respect to total loss, %			
1st hour	59.37	67.52	72.7	71.08
Rest of Day 1	27.81	19.94	18.1	16.62
Day 2	5	2.89	2.97	2.46
Day 3	0	0.96	1.19	0.31
Day 4	1.87	0.64	0.59	1.54
Day 5	0.31	0.96	0.89	0.92
Day 6	0.62	0.64	0.3	0
Day 7	0.63	0.64	0.3	0.92
Day 8	0.62	0.32	0.59	0.31
Day 9	0.63	0.32	0.59	0.62
Day 10	0.31	0.64	0.3	0
Day 11	3.13	2.89	0	0.31
Day 12	0.31	0	0.59	0.62
Day 13	-0.31	0.64	0	0
Day 14	0.31	0.96	0.3	0.62
Day 15	-0.62	0	0	2.77
Day 16	0	0	0.59	0.31
Day 17	0	0	0	0.62

2.4 Sleeve Anchorage

As illustrated in Figure 2.4-1, a sleeve-type anchorage was prepared at Lawrence Technological University (LTU) in collaboration with Tokyo Rope. The anchorage device consisted of a high-strength steel socket that is threaded externally and internally. The anchorage device was attached to the CFCC strands using cementitious-based, highly expansive material (HEM). The HEM is a special grout mix that exhibits a high degree of expansion with proper curing and produces a confining pressure of approximately 5800 psi (40 MPa). The mechanical properties of the high-strength steel anchors are given in Table 2.4-1. The sockets had a length of 18 in. (457 mm) and were threaded externally for a length of 6.0 in. (152 mm) on the outer end. After cutting and threading, the sockets were cleaned with compressed air and acetone to remove debris and oil from the cutting and threading process. The strands were centered inside the sockets and were held in place using threaded acetal plastic end caps that also prevented the HEM from leaking out of the socket as shown in Figure 2.4-2. The CFCC specimen with a steel socket attached on one side was positioned and fastened by plastic ties on a wooden jig, as shown in Figure 2.4-3.

Table 2.4-1 Properties of steel pipes used in anchorage preparation

Type	A53 Grade B
Outer diameter, in. (mm)	2.0 (51)
Inner diameter, in. (mm)	1.0 (25)
Wall thickness in. (mm)	0.5 (13)
Tensile strength, ksi (MPa)	110 (758)
Yield strength, ksi (MPa)	101 (696)
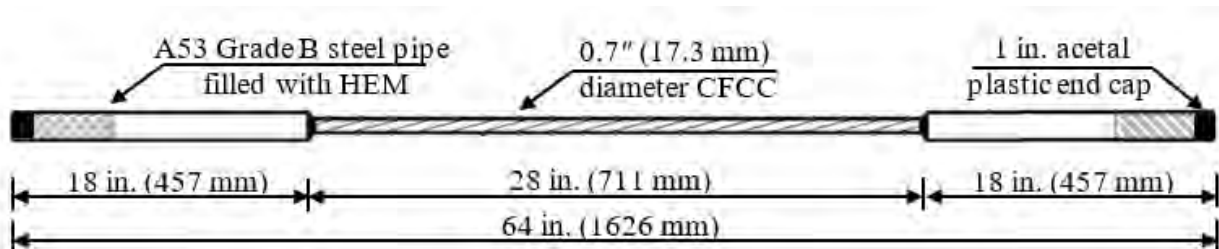
Figure 2.4-1 Schematic showing CFCC specimen with sleeve-type anchorage

<div align="center">

(a) Threading steel socket   (b) Cutting steel socket into required length

(c) Cleaning the socket   (d) Plastic end caps for holding CFCC centered

Figure 2.4-2 Manufacturing of anchorage device at LTU

</div>

HEM was mixed with distilled water, with a mix ratio of 4:1 by weight, until a uniform slurry was obtained. Then, the HEM mix was poured into the anchorage sockets with CFCC strands inside them as shown in Figure 2.4-4. A mechanical vibrator was used to tap the sockets from the outside and ensure proper compaction for the HEM mix inside the sockets. After all sockets were filled, the specimens were allowed to cure at ambient temperature (68 °F or 20 °C) for five hours and at a temperature of 140 ºF (60 ºC) in an environmental chamber for at least 15 hours. After heat curing, the specimens were allowed to gradually cool down and the specimens were released from the wooden frame. The process was repeated for the other end by rotating the specimens and attaching the anchorage devices using the same process. Figure 2.4-5 shows the CFCC specimens with sleeve anchorage devices after proper curing.

Figure 2.4-3 Placing anchors with CFCC strands in a custom-made wooden stand

(a) Measuring the HEM powder

(b) Adding water and mixing HEM

(c) Pouring HEM to the socket

(d) Tap the sockets using air vibrator

Figure 2.4-4 Mixing and placing the HEM inside the steel sockets

25

Figure 2.4-5 CFCC specimens with sleeve anchorage device after curing

2.4.1 Test Setup

A 220-kip (1000-kN) Material Test Systems (MTS®) loading actuator, supported by a four-post steel frame, was used in the testing and evaluation of the sleeve-type anchorage device (Figure 2.4-6). Tests were conducted in accordance with ASTM Standard D7205/7205M-06: "Standard Test Method for Tensile Properties of Fiber Reinforced Polymer Matrix Composite Bars". Two high-strength universal steel joints were used to accommodate the sleeve-type anchorage devices. The steel joints were designed to eliminate any possible eccentricity. For the first CFCC batch, tensile force was applied in a force control mode at a rate of 6.5 kip/min. (29 kN/min) until failure. However, it was noticed that a lower loading rate resulted in a slightly higher tensile strength. Therefore, for the rest of the batches, it was decided to maintain a lower rate of 2 kip/min (8.9 kN/min).
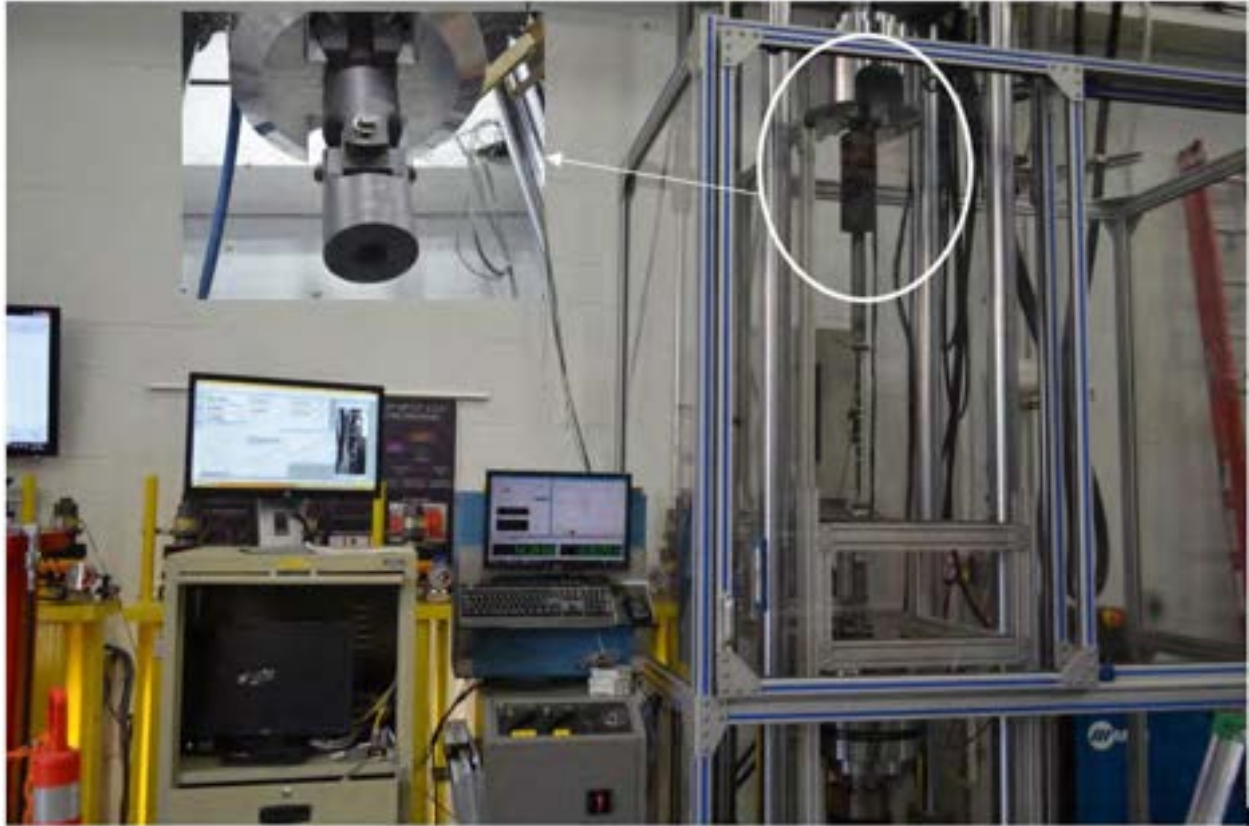
Figure 2.4-6 Uniaxial tensile test setup of CFCC specimen with sleeve-type anchorage device

2.4.2 Test Results

Testing results for CFCC specimens with sleeve anchorage are presented in Table 2.4-2. A total of 3 batches were prepared and tested. Batch 1 was prepared specifically for anchorage evaluation. Batches 2 and 3 were prepared to verify the strength for other tests included in the experimental investigation such as relaxation, creep rupture strength, and freeze-thaw tests. Before conducting any of those tests, at least two test specimens were tested under a uniaxial test setup to evaluate the tensile strength of the material and the maximum strength of the anchorage device. As shown in Table 2.4-2, all test specimens failed by rupture of CFCC strands, where rupture occurred near the anchorage device. In addition, no anchorage slippage was experienced by any of the test specimens. The strand rupture was "explosive" in that it resulted in sudden shattering of part or all of the CFCC strand as shown in Figure 2.4-7. The average tensile strength of CFCC specimens with sleeve anchorage was estimated at approximately 108.8 kip (480.6 kN), with a maximum breaking load of 114.5 kip (509.5 kN), and a minimum breaking load of 101.6 kip (452.1 kN). All specimens exceeded the guaranteed strength of 78.7 kip (350 kN) as recommended by the

27

manufacturer. The average maximum elongation for 16 CFCC test specimens was reported as approximately 2.05 %.

Figure 2.4-8 shows the load-strain curves for test specimens loaded under uniaxial tensile. Based on the test results, the average elastic modulus for 0.7″ CFCC strand was calculated as approximately 22,430 ksi (154.6 GPa). It should be noted that the wide range of strain values shown on the figure was due to the initial straightening of the CFCC specimen when it was first loaded.

Table 2.4-2 Uniaxial test results of sleeve-type anchorage

Test Group	Lot No.	Specimen No.	Loading rate, kip/min (kN/min)	Failure Load kip (kN)	Max Elongation, %	Failure Mode
Batch 1	G424	1	6.5 (29)	111.5 (496.2)	2.01	Strand rupture
		2		110.4 (491.3)	2.01	Strand rupture
		3		112.1 (499.0)	1.99	Strand rupture
		4		112.0 (498.4)	1.99	Strand rupture
		5		110.1 (489.9)	2.01	Strand rupture
		6		112.2 (499.3)	2.02	Strand rupture
		7	2 (8.9)	114.1 (507.7)	2.12	Strand rupture
		8		114.5 (509.5)	2.06	Strand rupture
		9		113.2 (503.7)	1.98	Strand rupture
Batch 2	G447	10	2 (8.9)	104.4 (464.6)	2.05	Strand rupture
		11		103.7 (461.5)	1.99	Strand rupture
Batch 3	T007	12	2 (8.9)	101.6 (452.1)	1.95	Strand rupture
		13		104.7 (465.9)	2.13	Strand rupture
		14		105.9 (471.3)	2.19	Strand rupture
		15		105.8 (470.8)	2.26	Strand rupture
		16		104.6 (465.5)	2.09	Strand rupture

Figure 2.4-7 Typical failure mode of CFCC specimens with sleeve type anchorage
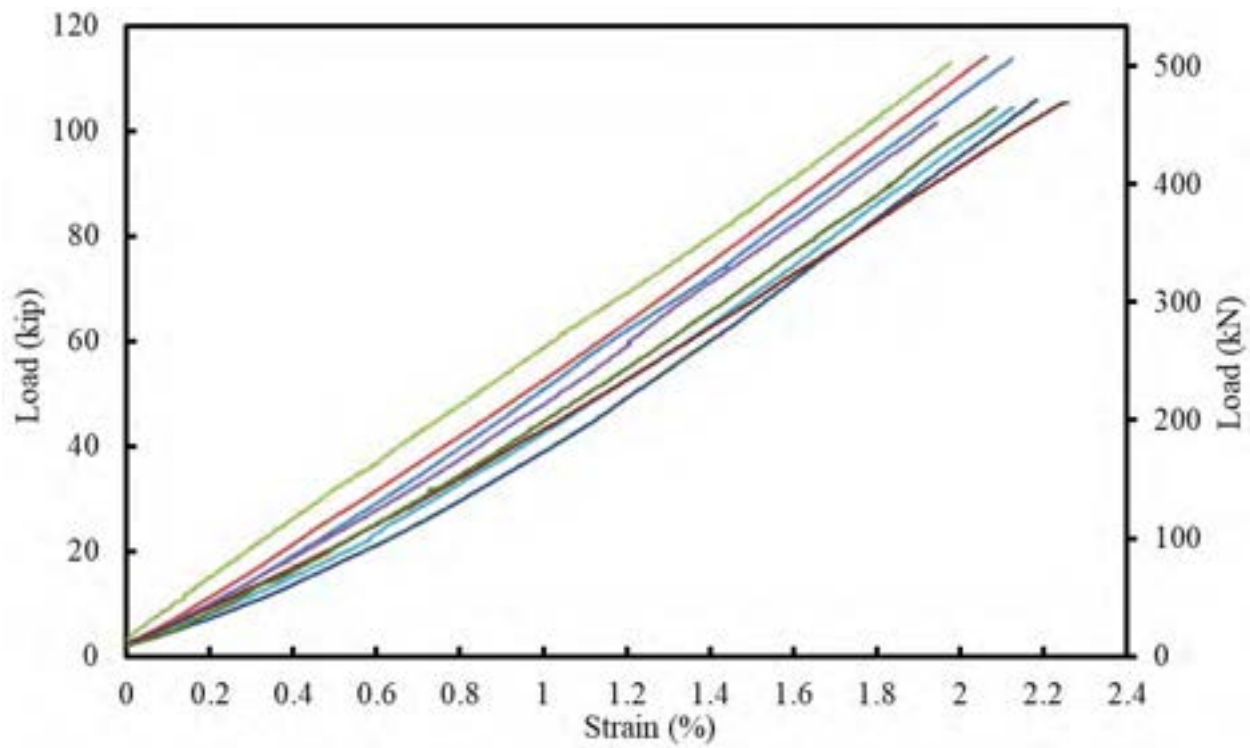
Figure 2.4-8 Load-strain curves for CFCC specimens tested under uniaxial tension

2.5 Summary

Using anchorage and couplers as discussed in the chapter, the tensile strength and strain at failure of 0.7" CFCC strands were verified for different batches. In addition, the elastic modulus of CFCC was calculated and was found to be in a good agreement with the manufacturer's established elastic modulus of 22,200 to 22,626 ksi (153 to 156 GPa). The first batch of CFCC strands achieved an average tensile strength of 113.9 kip (507 kN) with strain at failure of approximately 2 %. Subsequent batches showed an average tensile strength of 104 kip (462 kN) and nearly the same tensile strain.

   The coupler system with different buffer materials exhibited minimal seating over an extended period of monitoring. Most of the seating occurred within the first 24 hours of prestressing and was estimated as 0.18 in. (5 mm) per coupler. None of the couplers experienced any slippage or significant loss in prestressing force, even when tensioned to a force level as high as 55 kip (245 kN).

   It should be noted that based on recent development in the manufacturing process and extensive tensile test results, the manufacturer of CFCC strands updated the guaranteed breaking load of different strand diameters to reflect the current material strength and with the proper safety margin. The guaranteed breaking load of 0.6″ CFCC strands increased by approximately 10 % from 60.7 to 66.2 kip (270 to 295 kN). Similarly, the guaranteed breaking load of 0.7″ CFCC strands increased by approximately 10 % from 78.7 to 86.6 kip (350 to 385 kN)). The new guaranteed breaking loads correspond to a guaranteed strength of 370 ksi (2550 MPa) for both diameters. This increase in the guaranteed strength ensures an efficient and economical use of the material, while maintaining a consistent margin of safety for both diameters. The implications of increasing the guaranteed breaking load of CFCC strands include increasing the prestressing force per stand that may be accompanied by a slight reduction in the reinforcement ratio. Nevertheless, the current study was executed before publishing the new guaranteed strengths and the impact of the new guaranteed strength values has not been investigated.

CHAPTER 3: CREEP RUPTURE STRENGTH & RELAXATION OF CFRP

3.1 Introduction

The limits of jacking and prestressing forces are directly related to the creep rupture properties of CFRP strands. While ACI-440-4R-04 (ACI 2004) recommends that initial jacking strength of CFRP strands not exceed 65 % of their guaranteed/design strength, mainly due to concerns of creep rupture, recent test results on 0.6″ CFCC specimens showed that creep rupture strength is much higher than 65 % of the guaranteed strength. Besides the creep rupture, relaxation loss of CFRP strands is a key parameter in the design and construction of CFRP prestressed concrete highway bridge beams and needs careful evaluation. In addition, earlier test results showed that CFRP strands experienced additional relaxation when exposed to elevated temperatures.

This chapter presents test setups and test results of a comprehensive study conducted to establish the creep rupture strength and relaxation loss of 0.7″ CFCC strands at both ambient and elevated temperatures. The creep rupture test program extended to include 0.6″ CFCC test specimens. Multiple sets of CFCC specimens from both diameters were prepared, provided with sleeve anchorage, and loaded either in a four-post loading frame or in special steel frames with a closed-loop hydraulic system to establish the creep rupture strength.

The relaxation loss of 0.7" CFCC was evaluated at ambient conditions using a set of five test specimens that were loaded in a custom-made steel frame to establish the one-million-hour relaxation rate of CFCC. A similar set of test specimens was prepared and exposed to elevated temperatures to evaluate the heat-induced relaxation of CFCC strands.

Test results of this investigation showed that the one-million-hour creep rupture strength of CFCC strands is at least 86 % of their average tensile strength. In addition, the one-million-hour relaxation rate of CFCC at ambient conditions was less than 2.2 %. Furthermore, heat-induced relaxation at different temperatures was calculated and presented.

3.2 Creep Rupture Strength of CFCC Strands

3.2.1 Test Setup

Three sets of CFCC test specimens were constructed, pretensioned and are currently under continuous monitoring for creep rupture evaluation. The construction process of the specimens

followed the same procedures described earlier in Chapter 2. The creep rupture tests were conducted in accordance with JSCE-E 533-1995 (JSCE 1995), "Test Method for Creep Failure of Continuous Fiber Reinforcing Materials".

The first set consisted of five 0.6″ CFCC specimens that were tensioned in 2014 to an initial prestressing force of 55 kip (245 kN) per strand (approximately 80 % of average tensile capacity). The test setup utilizes a custom-made steel frame with high-strength steel springs to maintain the prestressing force level in the strands. The steel frames were fabricated from ASTM A500 Grade B HSS rectangular sections, while the steel springs have an outside diameter of 12.5 in. (318 mm) and a linear stiffness of 10 kip/in. (1.75 kN/mm). In-line load cells and vibrating wire displacement transducers were attached to each pre-tensioned CFCC specimen to monitor the prestressing force and the strain, respectively. All the attached sensors were connected to a data acquisition system that continuously monitors and records the prestressing force and strain in the loaded strands. Figure 3.2-1 shows the test setup for creep rupture testing of 0.6″ CFCC specimens with high strength steel springs. Partial test results from this set were presented in Grace et al. (2019), but monitoring continued under the current project.

The second set is composed of ten CFCC specimens of 6 ft (1.8 m) long; five with 0.6″ CFCC strands and five with 0.7″ CFCC strands. The specimens were tensioned in custom-made steel frames using a closed-loop constant pressure instead of the steel springs. The 0.6″ CFCC specimens were stressed to 64 kip (285 kN) per strand, which corresponds to approximately 92 % of their average tensile strength. The 0.7″ CFCC specimens were loaded to 85 % of their average tensile capacity (94 kip (418 kN) per strand). The specimens have been under continuous monitoring since 2017. The force level in the specimens is monitored through a system of pressure gages and load cells. In addition, vibrating wire strand meters are attached to the specimens to monitor the strain in the CFCC strands. Figure 3.2-2 through Figure 3.2-4 shows the creep test setup and instrumentation of CFCC specimens with the closed loop hydraulic system.

The third set consisted of fourteen 0.7″ CFCC specimens tensioned and monitored in a four-post loading frame using an MTS hydraulic actuator. This test setup was reserved for load levels higher than 95 % of the CFCC average tensile strength. In this test setup, each CFCC specimen was loaded to the assigned load level until the failure of the specimen or 1000 hours, whichever came first. The load was monitored using a load cell attached to the loading actuator, while the

strain was monitored and recorded using a high definition AVX camera that has a measurement rate of 17 Hz with a gage length of 4 in. (100 mm). Figure 3.2-5 and Figure 3.2-6 show the test setup and instrumentation for creep rupture testing of CFCC specimens with a load level higher than 95 % of the average CFCC tensile strength.

Figure 3.2-1 Creep test setup of 0.6″ CFCC specimens with steel springs

Figure 3.2-2 Creep test setup of 0.6″ CFCC specimens with closed loop hydraulic system

Figure 3.2-3 Creep test setup of 0.7″ CFCC specimens with closed loop hydraulic system

(a) Hydraulic system controller   (b) Strand-meter for strain measurement

Figure 3.2-4 Instrumentation for creep rupture testing of CFCC specimens

Figure 3.2-5 Creep rupture test setup for 0.7″ CFCC specimens with stress levels higher than 95 % of the CFCC average tensile strength

(a) AVX camera for strain monitoring   (b) Data acquisition system

Figure 3.2-6 Instrumentation for creep rupture test of CFCC specimens in four-post loading frame

3.2.2 Test Results

Figure 3.2-7 and Figure 3.2-8 show the load-time history and strain-time history, respectively, for the first set of CFCC test specimens, with 0.6″ CFCC, that were loaded with high strength steel springs (80 % load ratio). Monitoring of the specimens started 2770 days (7.5 years) ago (at the time of writing this section). As shown in the figures, a slight load loss was observed in the first 1200 days before the load plateaued over time. At the time of writing this report, the average prestressing force in those specimens was recorded as 52.7 kip (235 kN) with a corresponding average strain of 1.47 %.

Figure 3.2-9 and Figure 3.2-10 show the load-time history and strain-time history, respectively, for the second set of CFCC specimens, 0.6″ CFCC loaded with the closed-loop hydraulic system (92 % load ratio). As shown in the figures, two of the five specimens experienced a finite pressure loss in the hydraulic system that led to a slight drop in the load over time. These specimens were reloaded back to 64 kip (285 kN). The specimens have been under continuous monitoring for 1250 days (3.5 years). At the time of writing this report, the average prestressing force in those specimens was recorded as 63.8 kip (284 kN) with a corresponding average strain of 1.66 %.

Figure 3.2-11 shows the load-time history for the 0.7″ CFCC specimens, loaded and monitored with the closed-loop hydraulic setup (85 % load ratio). The strain readings over the monitoring period is presented in Figure 3.2-12. The strain-time curves show lower strain readings for one specimen in comparison to the others. This was due to slipping of the vibrating wire strand meters attached to the specimen at the time of prestressing. However, the strand meter was tightened, and the strain readings were monitored with a lower initial strain and with accurate predictions of change in strain over time. The strain in the loaded specimens displayed a linear pattern over time. After 37,522 hours (4.5 years) of monitoring the specimens, the average load was recorded as 94.8 kip (422 kN) with a corresponding average strain of 1.67 %.
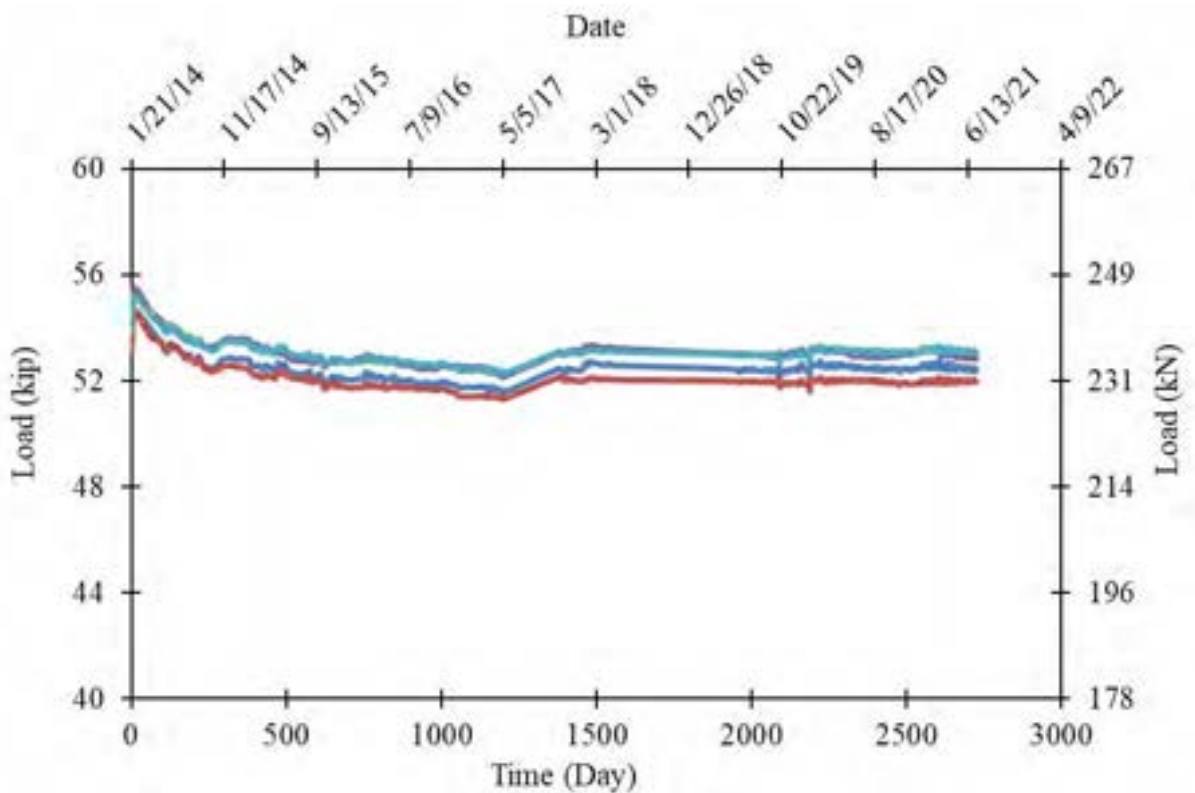
Figure 3.2-7 Force vs. time of 0.6″ (15.2 mm) CFCC specimens with 80 % load ratio
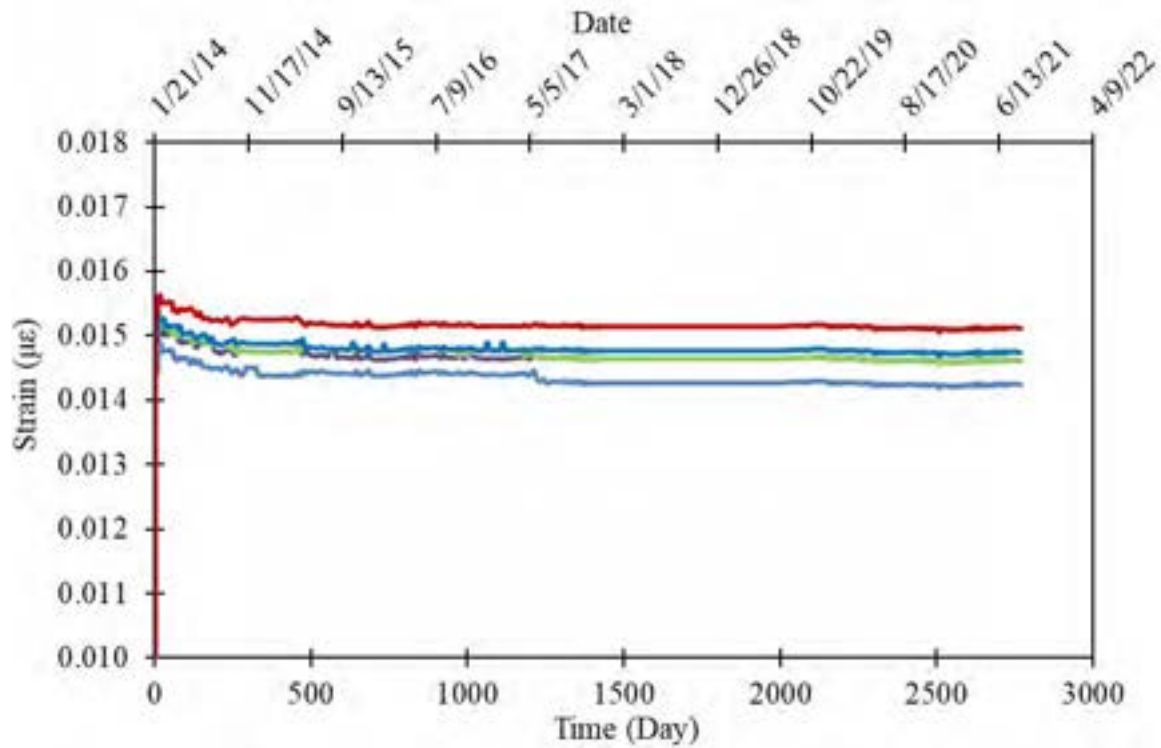
Figure 3.2-8 Strain vs. time of 0.6″ CFCC specimens with 80 % load ratio
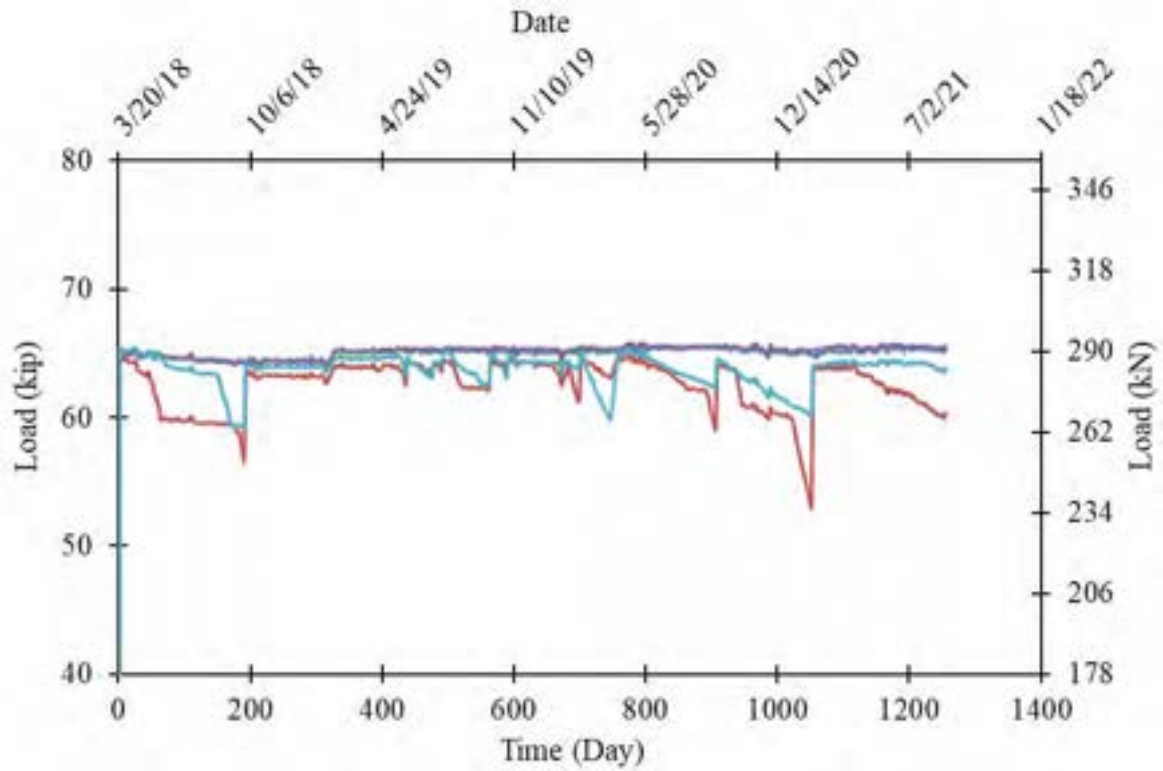
Figure 3.2-9 Force vs. time of 0.6″ CFCC specimens with 92 % load ratio

38
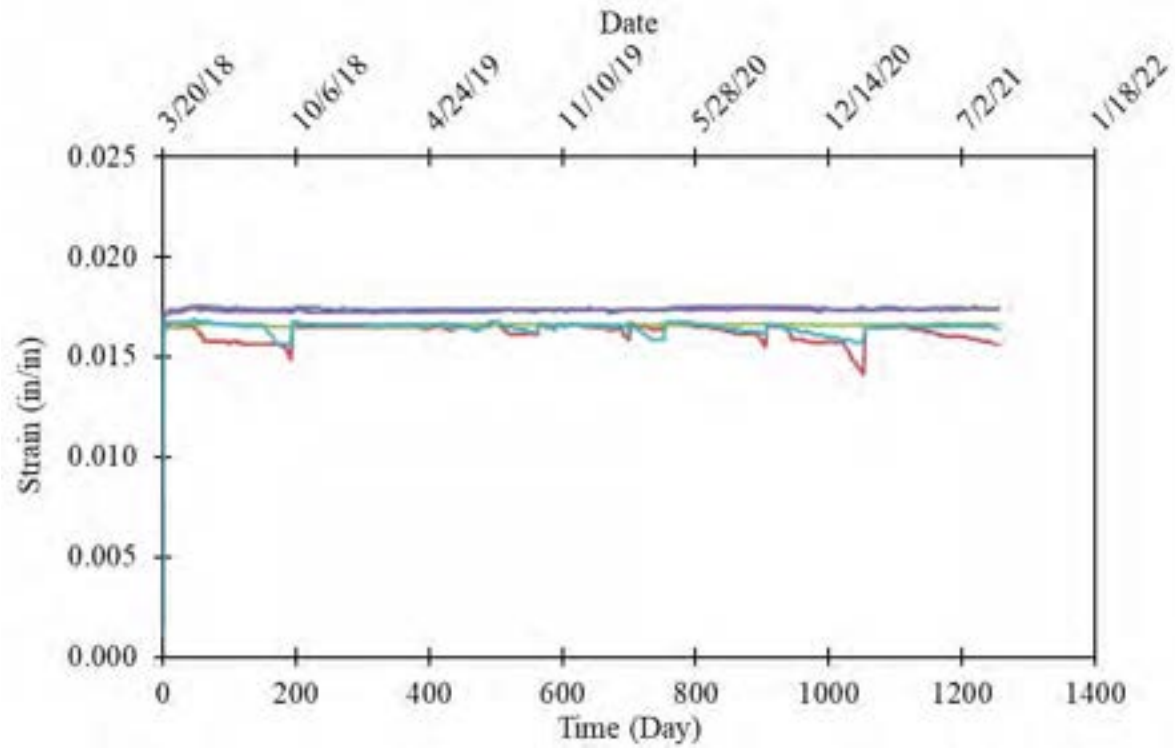
Figure 3.2-10 Strain vs. time of 0.6″ CFCC specimens with 92 % load ratio
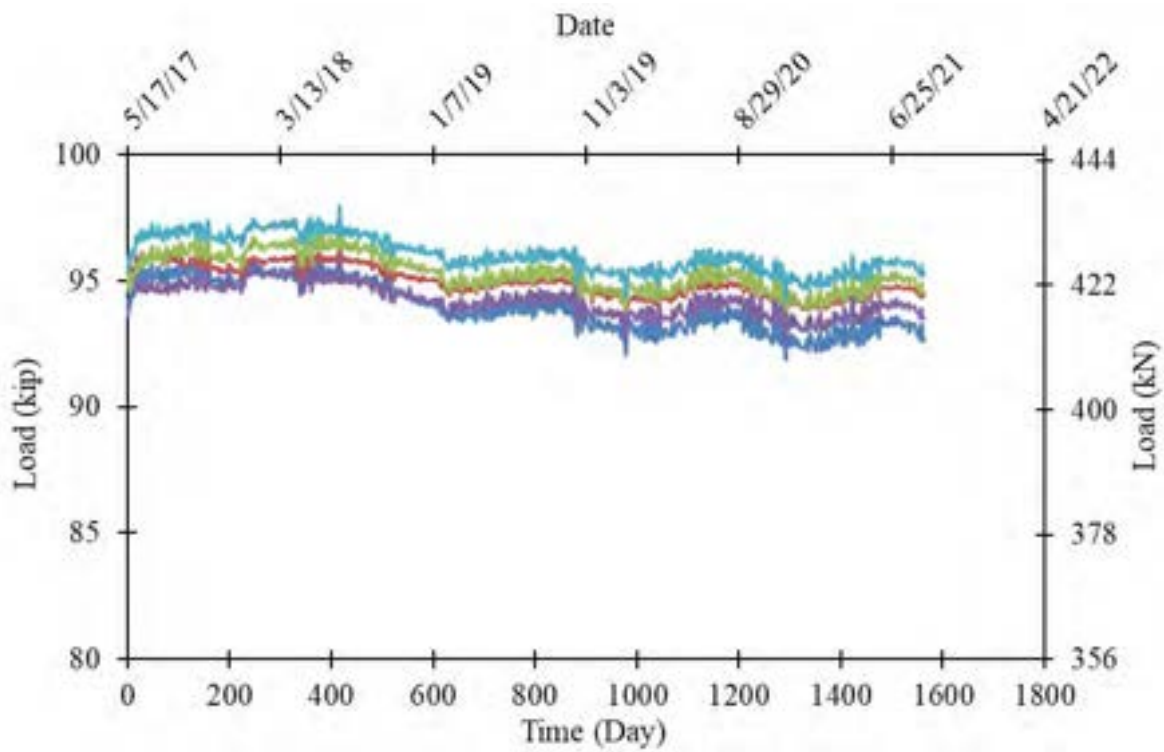
Figure 3.2-11 Force vs. time of 0.7″ CFCC specimens with 85 % load ratio
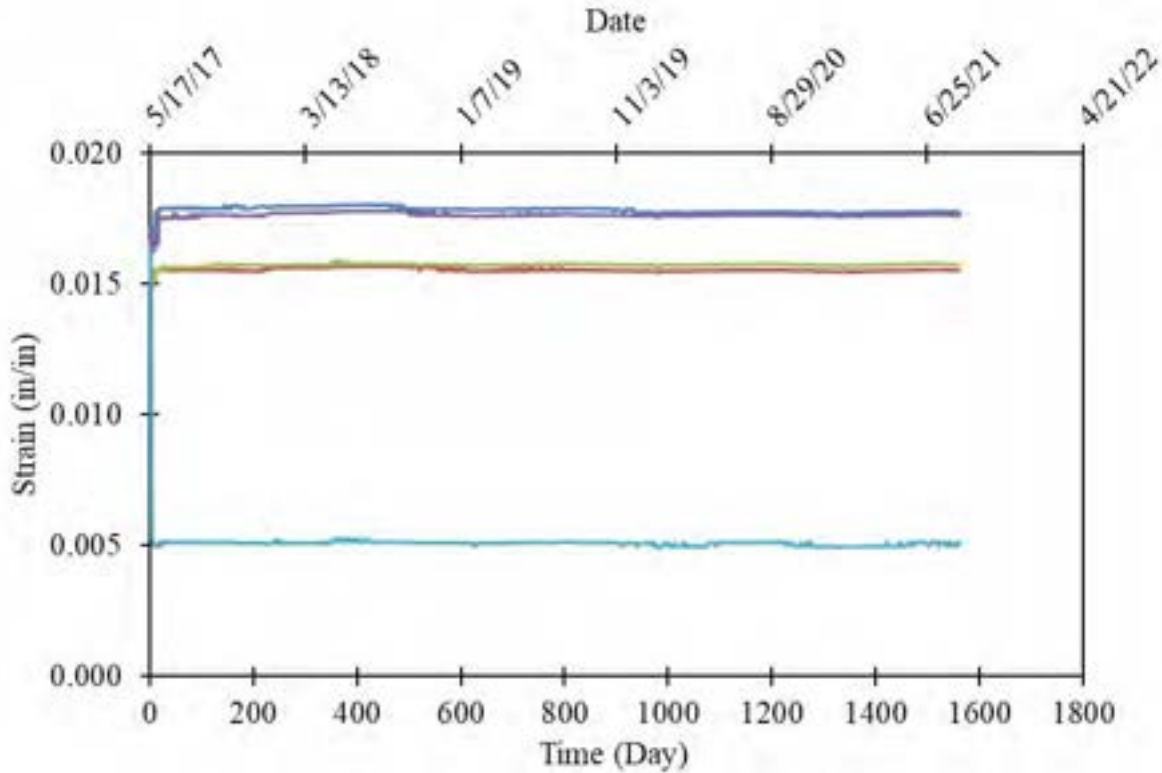
Figure 3.2-12 Strain vs. time of 0.7″ CFCC specimens with 85 % load ratio

Test results of the third test setup performed in the MTS four-post loading actuator are summarized in Table 3.2-1. As shown in the table, 13 out of 14 test specimens failed before achieving 1000 hr. One specimen sustained the applied load without failure and then, the test was discontinued. It should be noted that one load level resulted in several outcomes and the results did not seem to follow a trend. For instance, Specimen #10 with a load level of 110.5 kip (492 kN) sustained the load for approximately 0.1167 hours before rupture. Specimen #11, on the other hand, sustained the same load level for 1000 hours, after which it was released from the load. The difference in performance can be attributed to different factors such as preparation and handling of the specimens or curing of the HEM for the anchorage. But overall, it appears that the rupture was less likely due to a typical creep phenomenon but rather due to the load being very close to the tensile strength of the specimen. The load-time history and strain-time history for all creep specimens are shown on a logarithmic scale in Figure 3.2-13 and Figure 3.2-14, respectively. The strain of the loaded specimens displayed a similar pattern over time until the end of the test.

Table 3.2-1 Results of creep rupture test performed on 0.7″CFCC specimens

Test #	Average tensile strength, kip (kN)	Sustained load, kip (kN)	Load ratio, %	Time, hr	End of test
1		111.6 (497)	98.0	0.15	Failure
2		111.7 (497)	98.0	0.05	Failure
3		111.3 (495)	97.7	0.000167	Failure
4		111.0 (494)	97.5	1.166667	Failure
5		111.0 (494)	97.5	0.033333	Failure
6		111.0 (494)	97.5	26	Failure
7	113.9 (507)	111.0 (494)	97.5	0.416667	Failure
8		111.0 (494)	97.5	15	Failure
9		111.0 (494)	97.5	0.183333	Failure
10		110.5 (492)	97.0	0.116667	Failure
11		110.5 (492)	97.0	1000	Suspended
12		109.4 (486)	96.0	54	Failure
13		109.4 (486)	96.0	200	Failure
14		108.6 (483)	95.3	0.000167	Failure
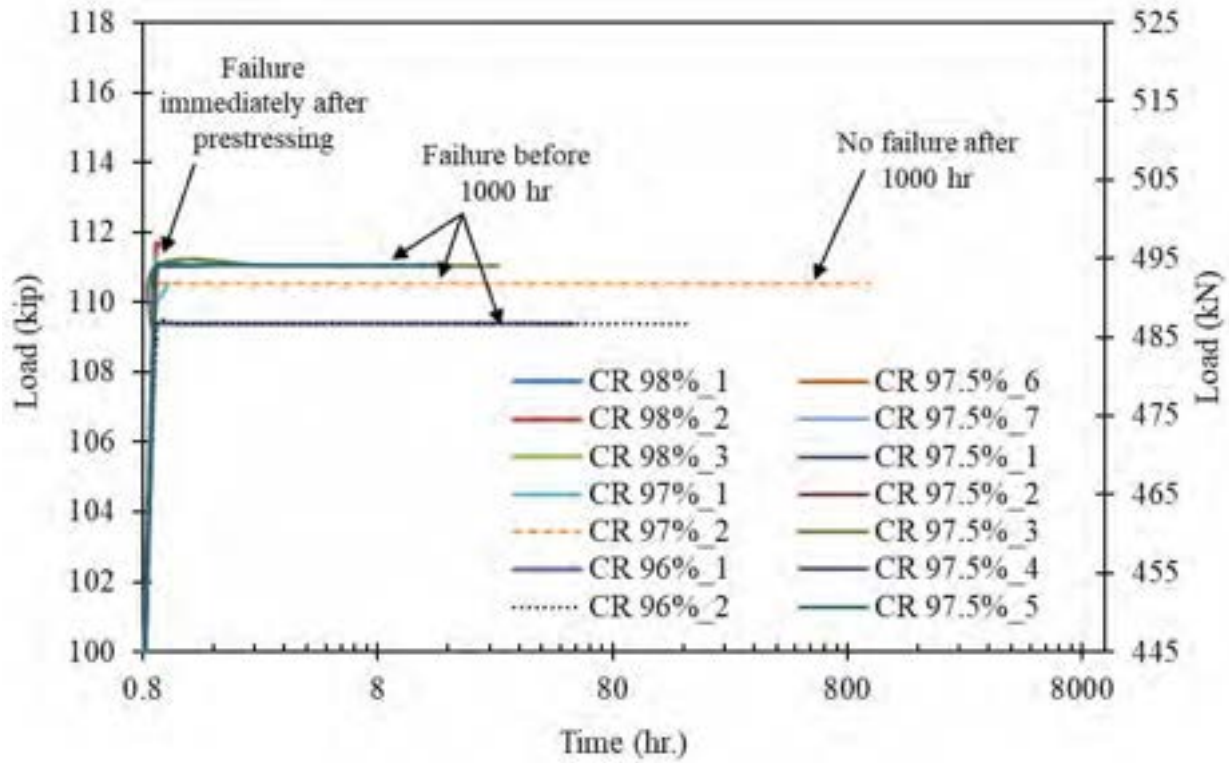
Figure 3.2-13 Load vs. logarithmic time for 0.7″ CFCC specimens
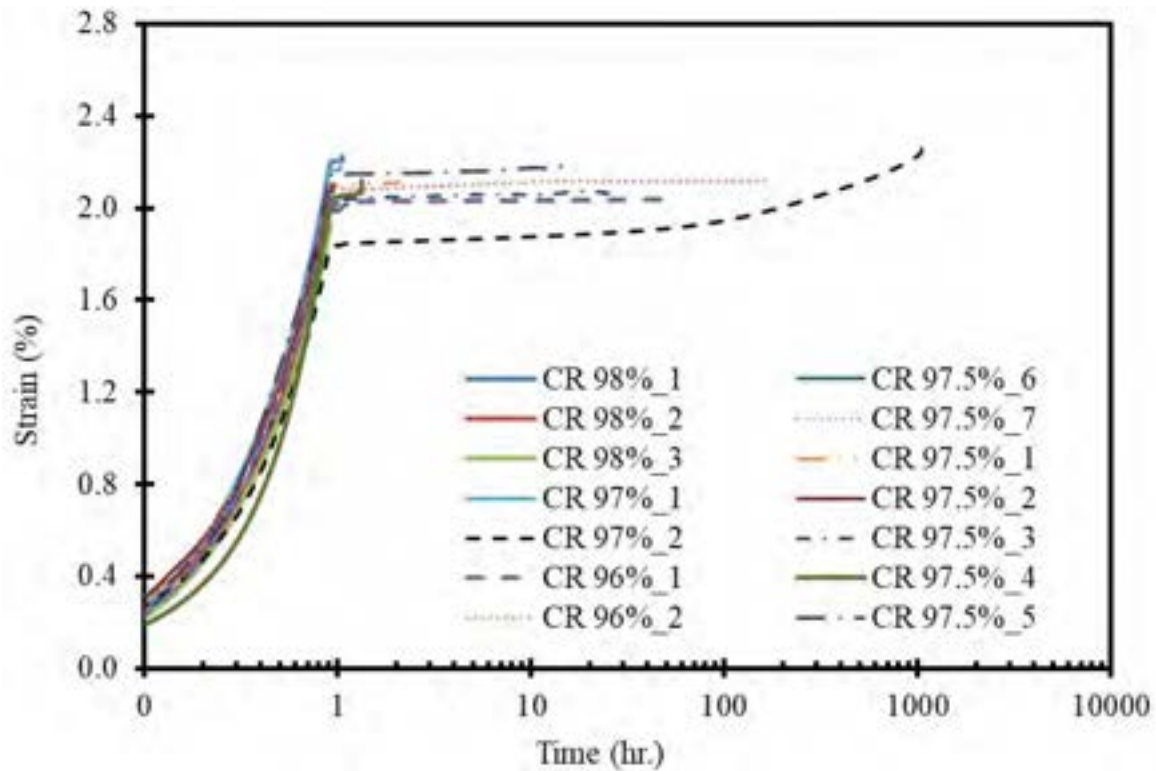
Figure 3.2-14 Strain vs. logarithmic time for 0.7″ CFCC specimens

42

3.2.3 Discussion of Test Results

At the time of writing this report, the 0.6″ CFCC and 0.7″ CFCC specimens loaded with the closed loop hydraulic system have been sustaining the applied load for 30,154 hours and 37,522 hours, respectively, while the 0.6″ CFCC specimens loaded with the steel spring setup have been sustaining the applied load for 66,586 hours. The test results from the three sets were assembled together with test results compiled from earlier research investigations (Grace et al., 2019) to establish and verify the one-million-hour creep rupture strength of the CFCC strands and confirm the recommendations for the limits of jacking and prestressing forces.

By plotting the test results for different diameters of CFCC strands as shown on Figure 3.2-15, a one million-hour creep-rupture strength was estimated by drawing a line separating the failed specimens from those still sustaining the applied load and under continuous monitoring or specimens that sustained the load for a period of time before they were released without failure. To establish the estimation, the failed specimens from different diameters should appear above the line, while non-failed specimens should appear either above or below the line. In other words, this line separates the unsafe stress zone from the safe stress zone. By extending the line to the end of the graph, an estimate for the one-million-hour creep-rupture strength was determined.

Based on available test results at the time of writing this report, the minimum one-million-hour creep-rupture strength for CFCC strands cannot be less than 86 % of the average tensile strength. For instance, for 0.7″ CFCC strands with average tensile strength of 113.9 kip (507 kN), the lower bound for one-million-hour creep rupture strength is approximately 98.6 kip (439 kN). In other words, 0.7″ CFCC strands can be safely loaded to its guaranteed strength of 78.7 kip (350 kN) for 114 years (one-million hour) without experiencing creep rupture. Using the value of 86 %, a creep rupture strength can be estimated for different diameters of CFCC, based on their established average tensile strength.
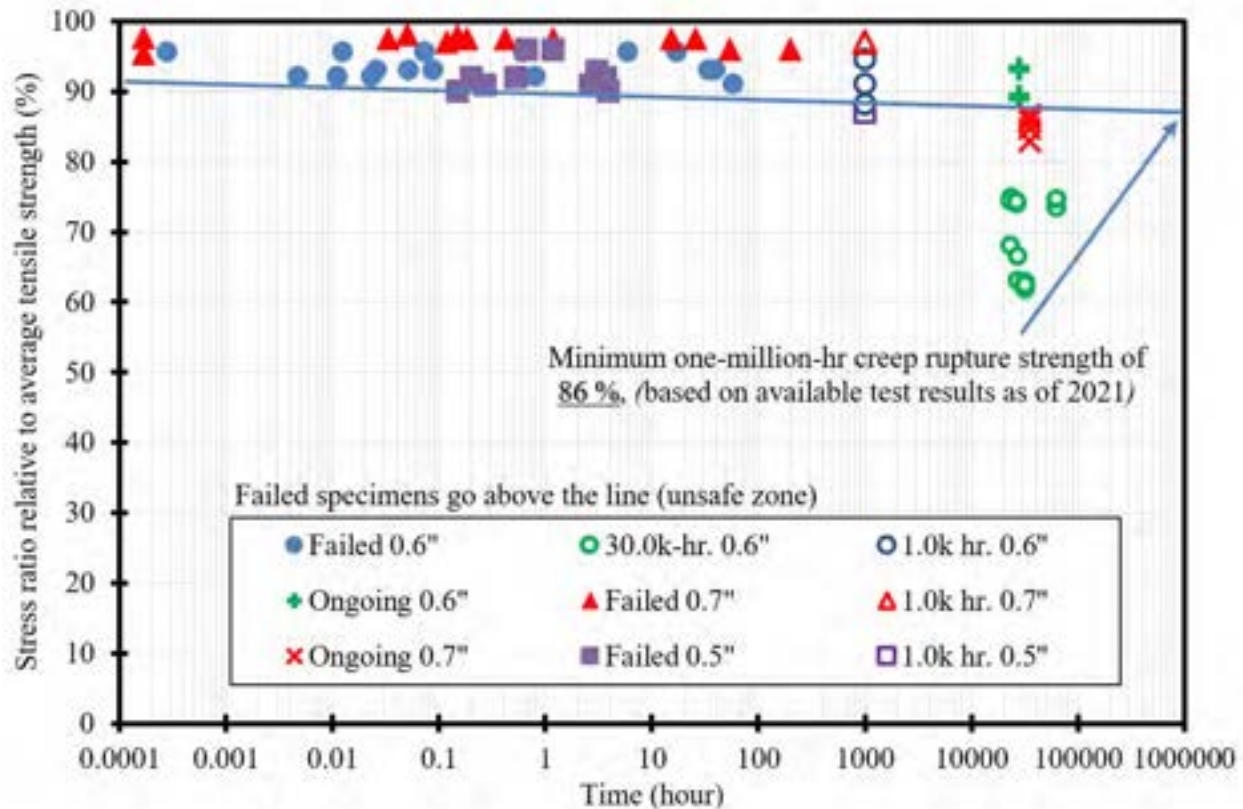
Figure 3.2-15 Lowest estimate for one-million-hour creep-rupture strength based on available test results to date

3.3 Relaxation of CFCC Strands

3.3.1 Test Setup

Similar to creep rupture specimens, five 0.7″ CFCC strand specimens were tensioned and are currently being monitored for force reduction in custom-made steel frames provided with a hydraulic jacking and pump system as shown in Figure 3.3-1. Test setup and testing conditions follow the specifications of JSCE 534-1995 (JSCE 1995), "Test Method for Long-Term Relaxation of Continuous Fiber Reinforcing Materials". The specimens were initially tensioned to a stress level of 94 kip (418 kN), which represented approximately 85 % of the average tensile strength of CFCC. The temperature of the test setup and specimens is maintained at 68 ± 4 °F (24 ± 2.2 °C). It should be noted that this load level was higher than the jacking strength recommended by ACI-440-4R-04, ACI 2004 (53 kip or 236 kN) and higher than the guaranteed strength as recommended by the manufacturer. The specimens have been monitored for relaxation loss for over 4.5 years since April 2017.

44

As shown in Figure 3.3-1, CFCC specimens were connected to a hydraulic pressure system with load cells at one end (dead end) and fastened at the other end (live end) by a high strength steel nut and washer. Prestressing force was applied at the live end through a hydraulic jack at a rate of 2 kip/min (8.9 kN/min). The relaxation of the CFCC strands is calculated by recording the loss in force monitored through the load cells and the pressure gage of the hydraulic system (Figure 3.3-2), while the change in the strain was recorded using Geokon vibrating wire strand meters attached to the strands (Figure 3.3-3). The load cells and the strand meters are connected to a data acquisition system that captures and stores the data continuously.

Figure 3.3-1 Test setup for evaluating relaxation of CFCC strands

Figure 3.3-2 In-line load cells and hydraulic pressure systems to monitor the force loss

Figure 3.3-3 Strand meters to evaluate the strain in CFCC relaxation specimens

3.3.2 Test Results

Figure 3.3-4 shows the load vs. time curve for the five CFCC relaxation specimens. All specimens displayed a bi-linear pattern of load loss with approximate force loss of 4.2 % in the first 8 months (244 days) and additional force loss of 3 % between 8 and 53 months. The average total loss at the time of writing this report is approximately 7.2 %. As shown in Figure 3.3-4, two of load cells attached to CFCC specimens experienced connection malfunction, while one specimen exhibited a pressure loss. The results from these specimens were discarded in the final evaluation of the one-million-hour relaxation rate of CFCC.

Observing the strain vs. time readings, shown in Figure 3.3-5, it appears that the loss of the prestressing force was accompanied by a reduction in the strain readings over time. In an ideal situation, where the loss in prestressing force occurs due to strand relaxation only, the strain readings should be increasing with time, not decreasing. That is because relaxation of the strand leads to strand elongation between the anchor points, which causes the prestress loss. Therefore, the recorded reduction in the strain readings indicated that the loss in the prestressing force was due to a combination of strand relaxation and anchorage relaxation.

The loss in prestressing force due to strand relaxation and due to anchor relaxation can be mathematically separated by analyzing the strain readings vs. the corresponding load cell reading. If strand relaxation loss is denoted (X) and anchor relaxation loss is denoted (Y), then the attached load cells in the setup measures total relaxation losses (X+Y) from the anchor and the strand. The strand-meter, on the strand, measures the net loss due to anchor relaxation and strand relaxation (Y-X). By converting the strain reading to equivalent loss in prestressing force and solving the two equations simultaneously, the loss due to strand relaxation (X) and due to anchorage relaxation (Y) can be determined.

As shown in Figure 3.3-6, the average loss of the prestressing force was approximately 5.1 kip (22.7 kN) in the three valid specimens. After separating the strand relaxation from the anchorage relaxation, the loss due to anchorage relaxation (Figure 3.3-7) was calculated as 3.6 kip (16 kN), while the loss due to strand relaxation (Figure 3.3-8) was approximately 1.5 kip (6.7 kN). This loss accounts for approximately 1.7 % of initial prestressing force as shown in Figure 3.3-9. When relaxation loss is plotted on a logarithmic scale, the estimated one-million-hour relaxation loss (relaxation rate) is approximately 2.2 % as shown in Figure 3.3-10.
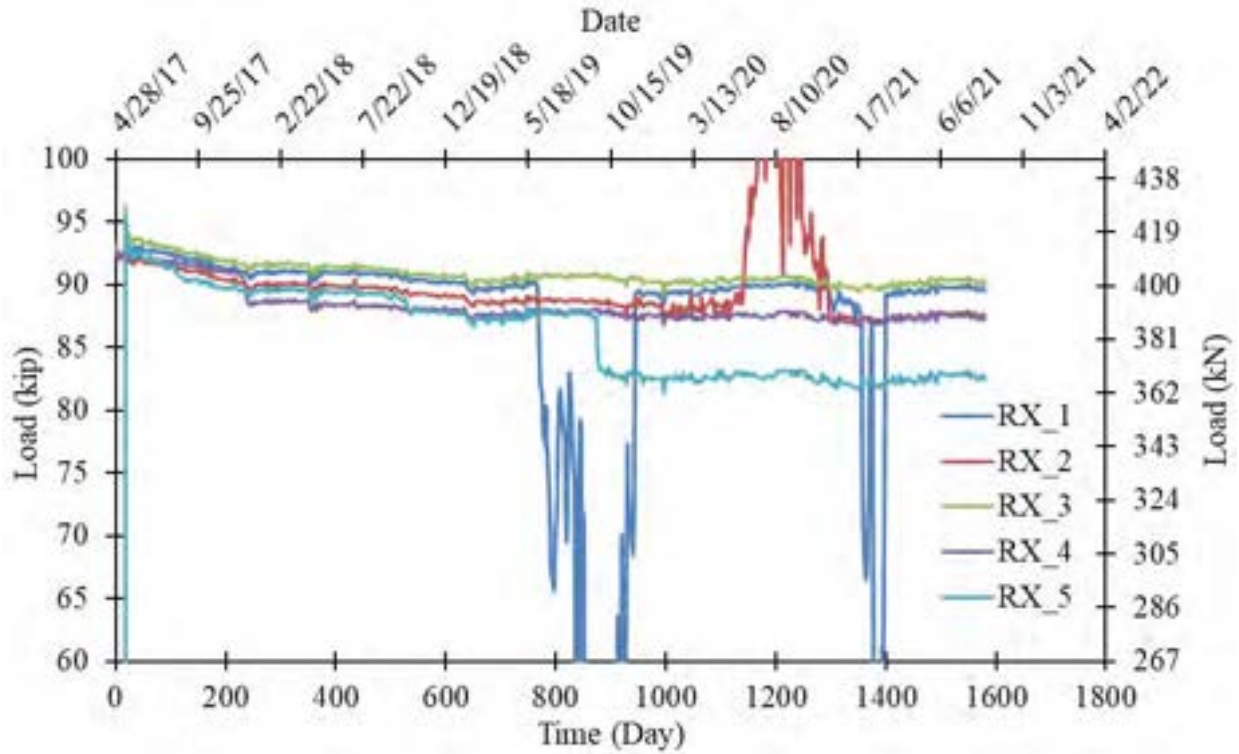
Figure 3.3-4 Force monitoring in relaxation CFCC specimens
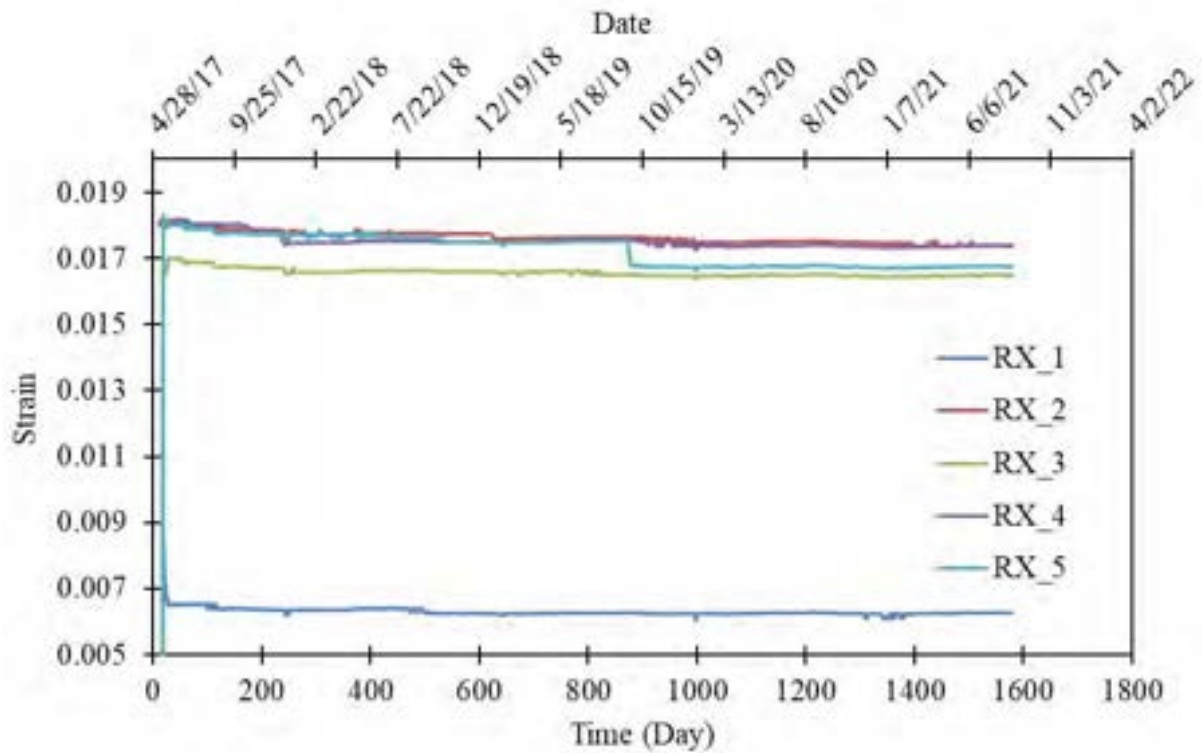
Figure 3.3-5 Strain monitoring of relaxation CFCC specimens

48
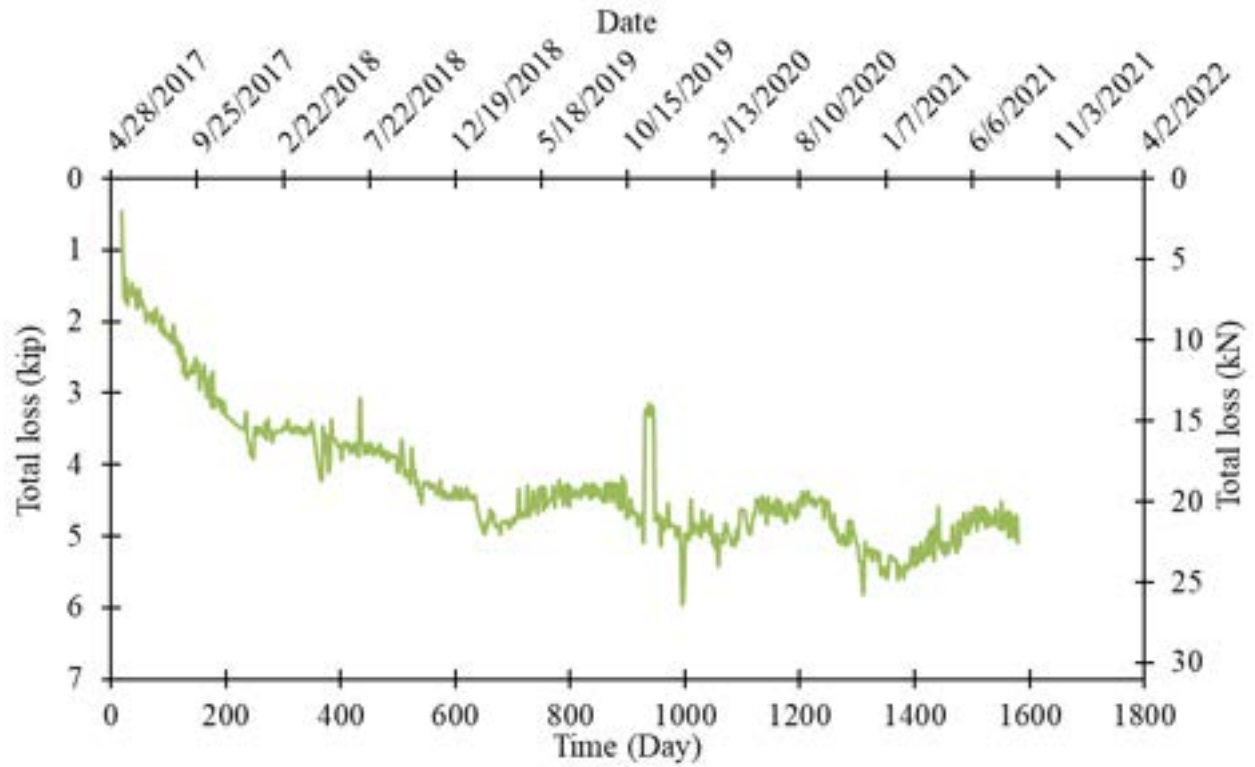
Figure 3.3-6 Total loss of the force in CFCC specimens due to anchorage and CFCC relaxation
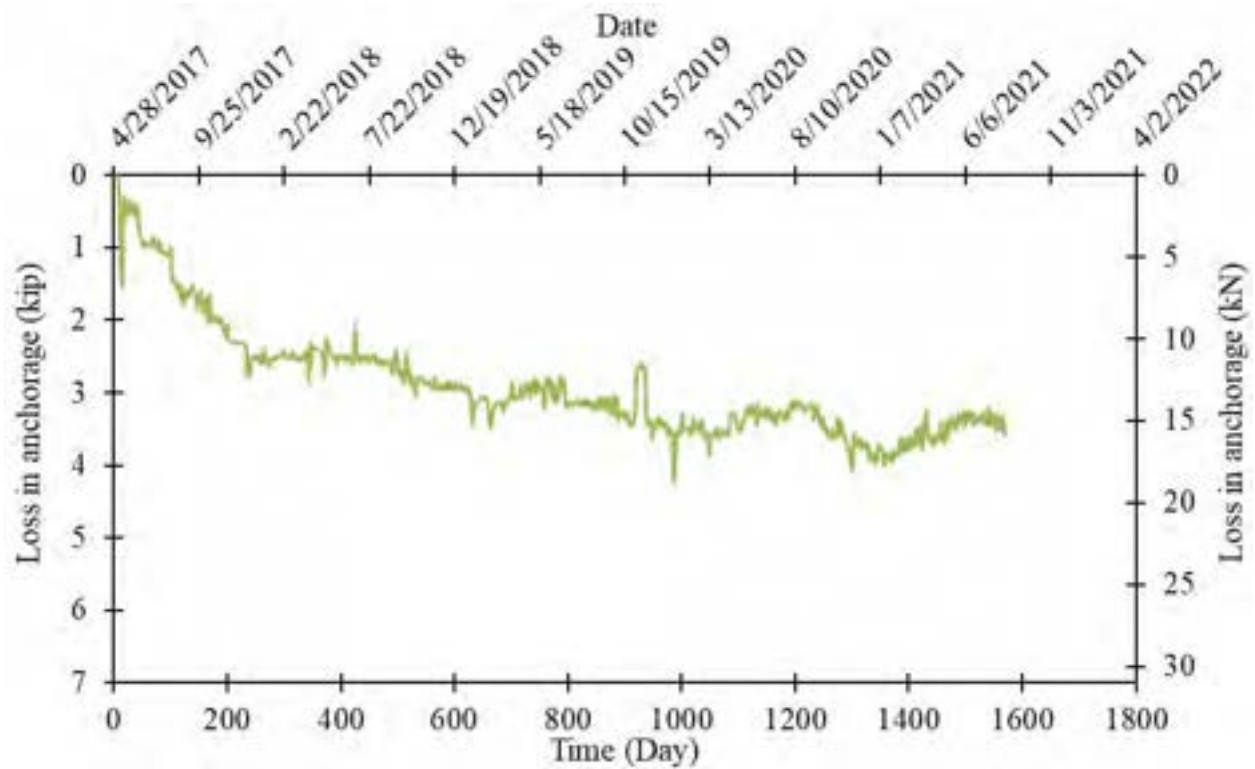
Figure 3.3-7 Loss of the force in CFCC specimens due to anchorage relaxation

49
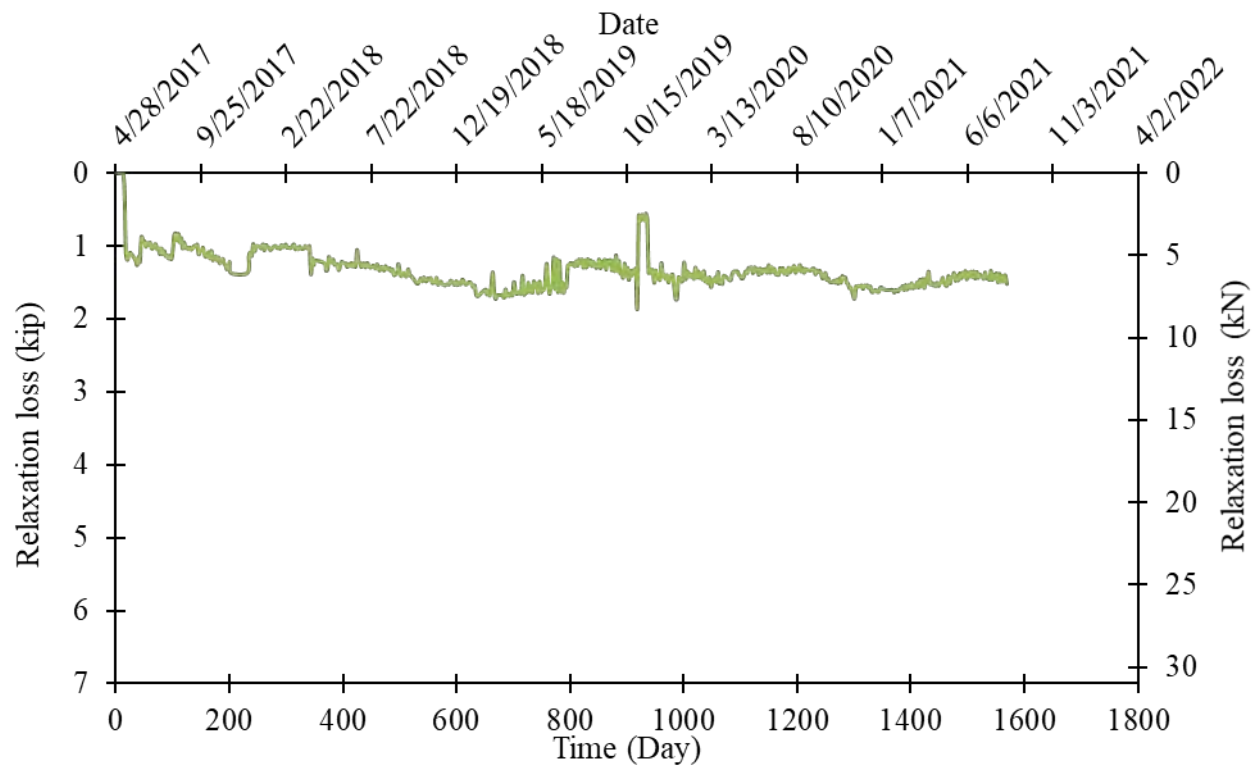
Figure 3.3-8 Loss of force in CFCC specimens due to CFCC relaxation
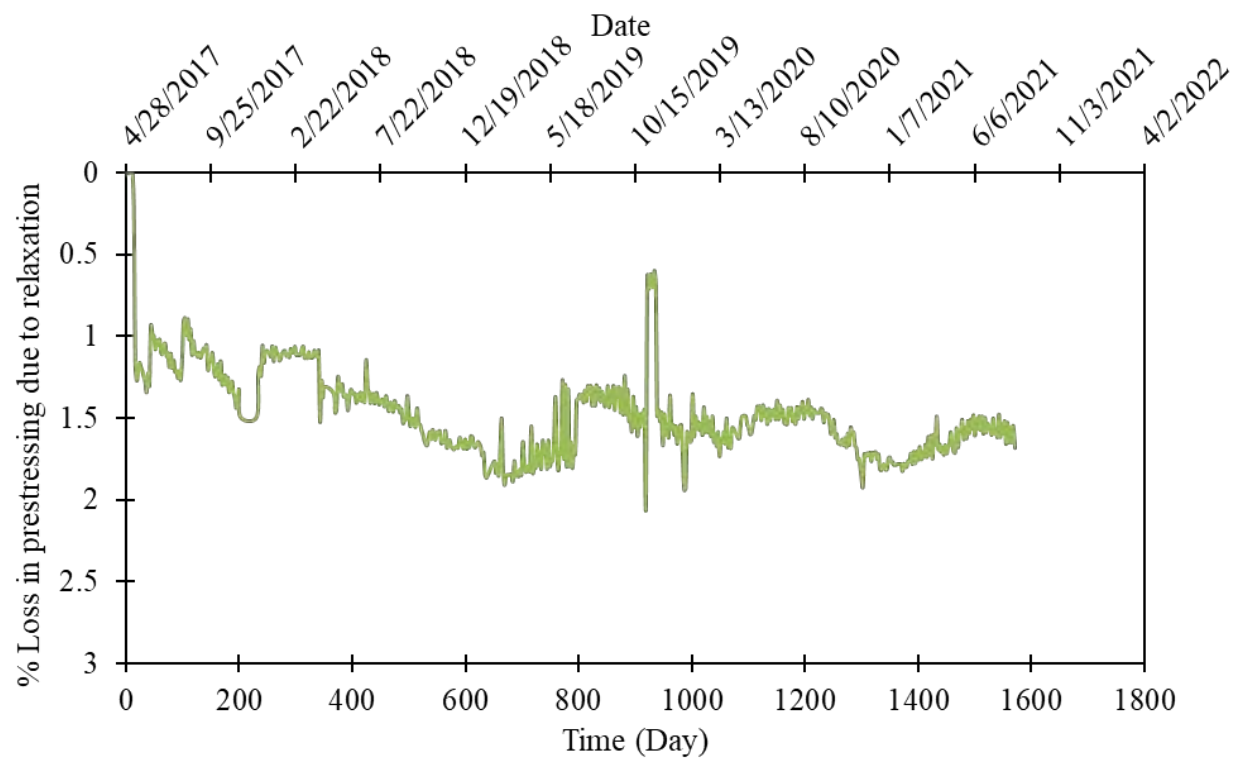
Figure 3.3-9 Percentage loss of force in CFCC specimens due to CFCC relaxation only

50
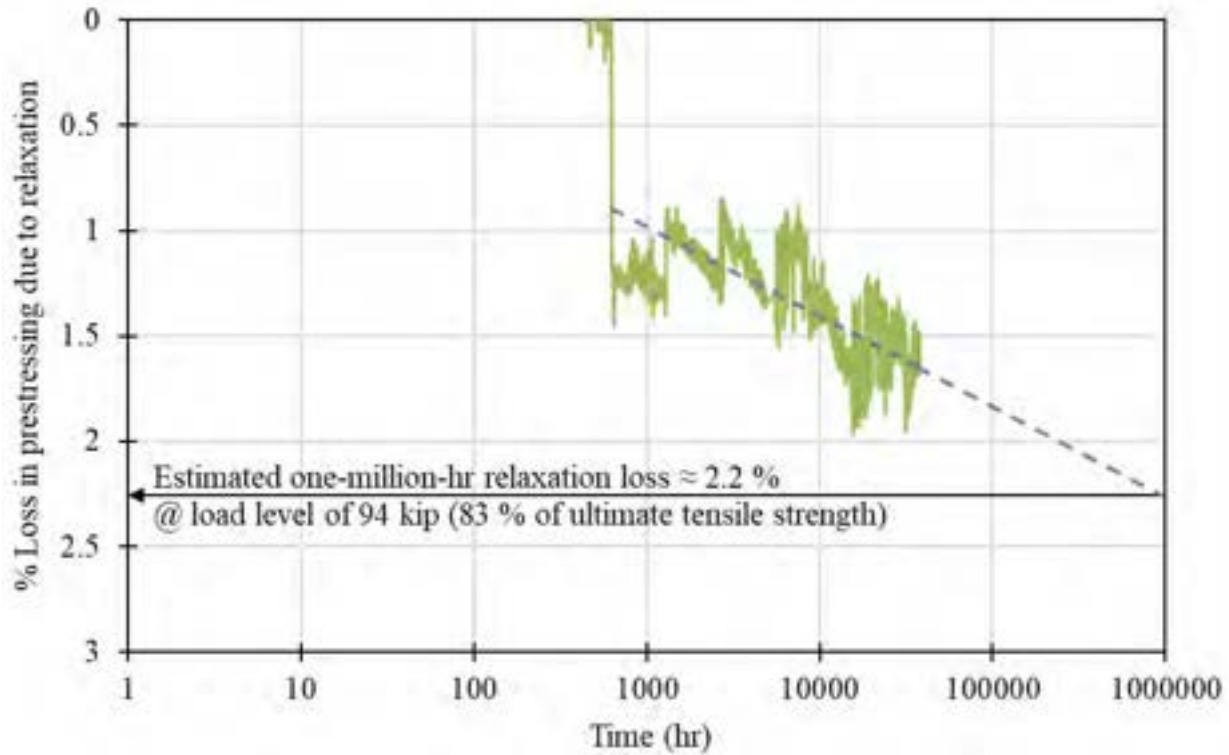
Figure 3.3-10 Estimated one-million-hour relaxation rate in CFCC specimens

3.4 Heat Relaxation of CFRP Strands

Heat relaxation of CFCC strands was observed when stressed 0.6″ strands were exposed to elevated temperatures (Grace et al. 2019). The test was repeated for 0.7″ strands to assess the level of heat relaxation with the increase in temperature and thereby evaluate the change in the prestressing force during construction as the concrete goes through temperature increase during hydration.

To achieve this objective, five 0.7″ CFCC test specimens, tensioned to a force level of 51 kip (227 kN), were monitored for load loss while being subjected to different elevated temperatures. The nomenclatures of the test specimens are: TH-S1, TH-S2, TH-S3, TH-S4, and TH-S5. The thermal test program was executed through three phases: I, II, and III. The temperature matrices and details of Phases I and II are discussed in subsequent sections, while Phase III included testing the specimens to failure through uniaxial tensile tests to evaluate the residual tensile capacity and elastic modulus of CFCC. The 64 in. (1626 mm) long thermal test specimens, shown in Figure

51

3.3-11 and Figure 3.3-12, consisted of CFCC strands provided with two sleeve anchors. Details on CFCC materials and anchorage preparation were presented in Chapter 2.
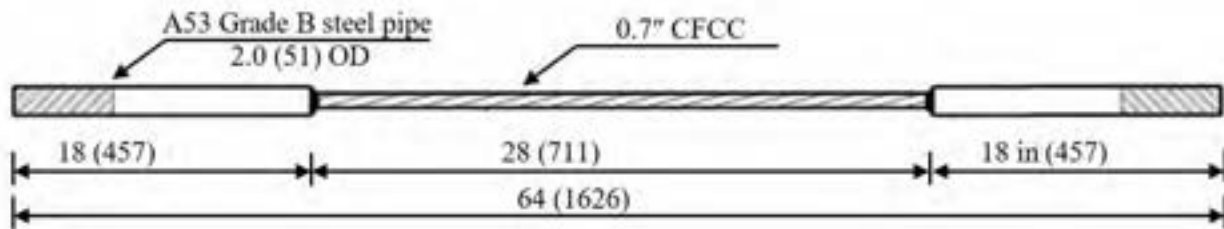
Figure 3.3-11 Details of test specimens

Figure 3.3-12 Five test specimens used to evaluate heat relaxation

The thermal test of CFCC specimens was performed in an MTS® electrically heated environmental chamber as shown in Figure 3.3-13. The external dimensions of the chamber are 36 in. × 28 in. × 21.5 in. (914 mm × 711 mm × 546 mm) with a wall thickness of approximately 3.0 in. (76 mm). The chamber is designed to reach a maximum temperature of 662 ºF (350 ºC) and is provided with a temperature controller that displays a set point and current temperature. Heating is achieved using electrical heating elements and a circulation fan that ensures uniform temperature

distribution throughout the chamber while also shielding the specimen from direct exposure to radiant heat. Cooling of the chamber is typically accomplished using liquid nitrogen. However, liquid nitrogen was not used in the current study. The chamber is designed to accommodate small scale specimens with two access holes at the top and bottom of the chamber for gripping purposes. Those holes were blocked with thermal blanks during the test to maintain uniform temperature and eliminate any temperature increase of the anchorage devices at the ends of the specimens.

The loading frame used to apply force to CFCC specimens was manufactured by MTS®. This four post 220-kip (978-kN) loading frame shown in Figure 3.3-13 includes a force transducer (load cell) to measure the axial force applied to the specimen and an LVDT to measure the displacement of the actuator. An MTS FlexTest™ GT Station Manager controls a hydraulic actuator that applies the load to the test specimens in the loading frame. For this test, the force was applied to CFCC specimens in a force-control mode with rate of 2 kip/min (9 kN/min) until the load reached 51 kip (227 kN). Then, the MTS software automatically switched the mode to displacement-control mode and locked the actuator heads in place.

Figure 3.3-13 Heat relaxation test setup

In Phase I thermal testing, the stressed CFCC test specimens were subjected to different elevated temperatures as shown in Figure 3.3-14, while the loss in the force due to the increased temperature was monitored at each temperature range. Specimen TH-S1 served as a control specimen and was loaded to the assigned force level, 51 kip (227 kN), at a room temperature of 76 °F (24 °C) for four hours and then the load was removed without activating the environmental chamber. The loss in the load due to strand and anchorage relaxation was monitored and captured.

The second test specimen (TH-S2) was loaded at room temperature and the load was monitored for two hours at room temperature. After the two-hour monitoring period, the environmental chamber was activated and the temperature of the heated length of the specimen (segment passing through the chamber) increased to 150 °F (65 °C). The temperature was maintained at 150 °F (65 °C) for two hours. Then, the heat chamber was turned off and the specimen was allowed to naturally cool down to room temperature. After one hour, the load was removed. The heating and cooling rates were approximately 20 °F (10 °C) per minute. The third test specimen (TH-S3) was loaded at room temperature and after two hours, the temperature of the heated length increased to 150 °F (65 °C). Two hours later, the temperature increased again to 235 °F (112 °C) and remained for two hours. After that, the environmental chamber was allowed to cool down to room temperature. An hour later, the load was removed. The fourth test specimen (TH-S4) was loaded at room temperature for two hours. Then, the temperature increased to 150 °F (65 °C) for two hours, to 235 °F (112 °C) for two hours, and to 316 °F (158 °C) for two hours. After that, the specimen was allowed to cool down and the load was removed an hour later. The fifth test specimen was loaded at room temperature for two hours. Then, the temperature increased to 150 °F (65 °C) for two hours, to 235 °F (112 °C) for two hours, to 316 °F (158 °C) for two hours, and to 400 °F (204 °C) for two hours. Finally, the specimen was allowed to cool down for an hour and the load was removed.

In Phase II, the specimens were heated through a single-step heating to their maximum reached temperature in Phase I as shown in Figure 3.3-15. For instance, the fifth test specimen (TH-S5) was loaded to 51 kip (227 kN) at room temperature and after two hours, the temperature was increased and maintained at 400 °F (204 °C) for two hours. Then the specimen was allowed to cool down to room temperature and the load was removed after two hours, with a total test duration of six hours.
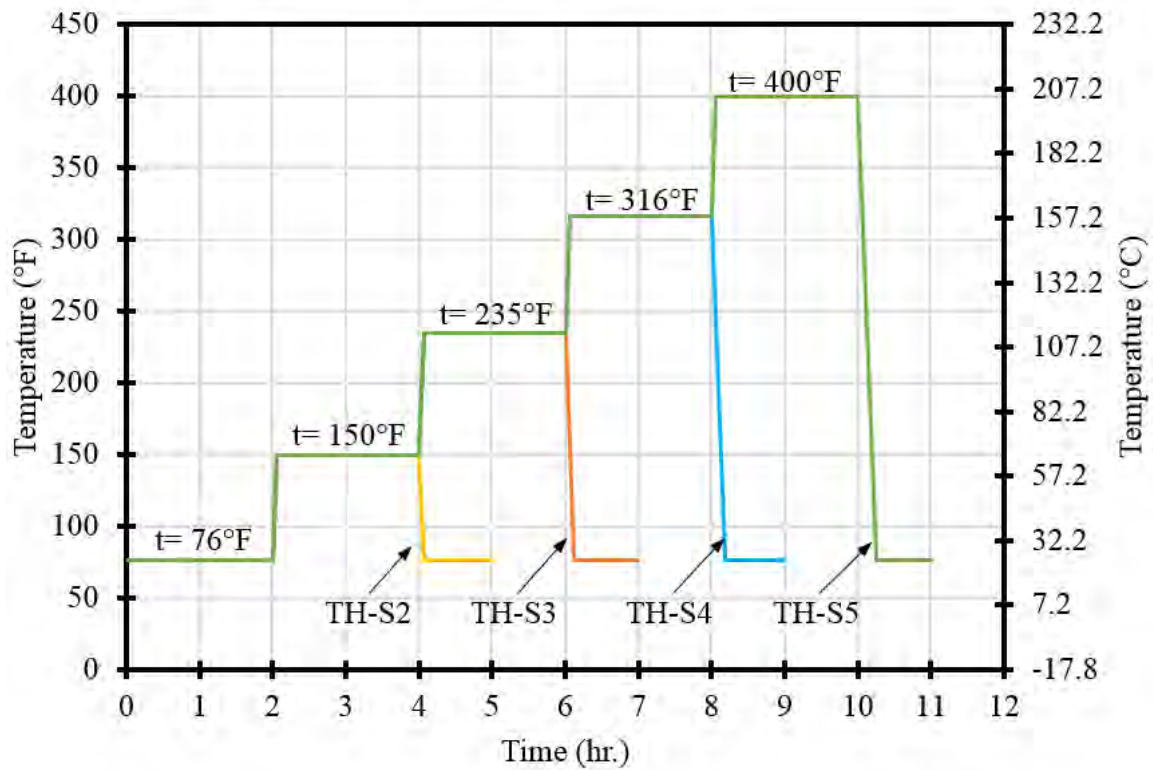
Figure 3.3-14 Idealized time-temperature curves for heat relaxation specimens in Phase I
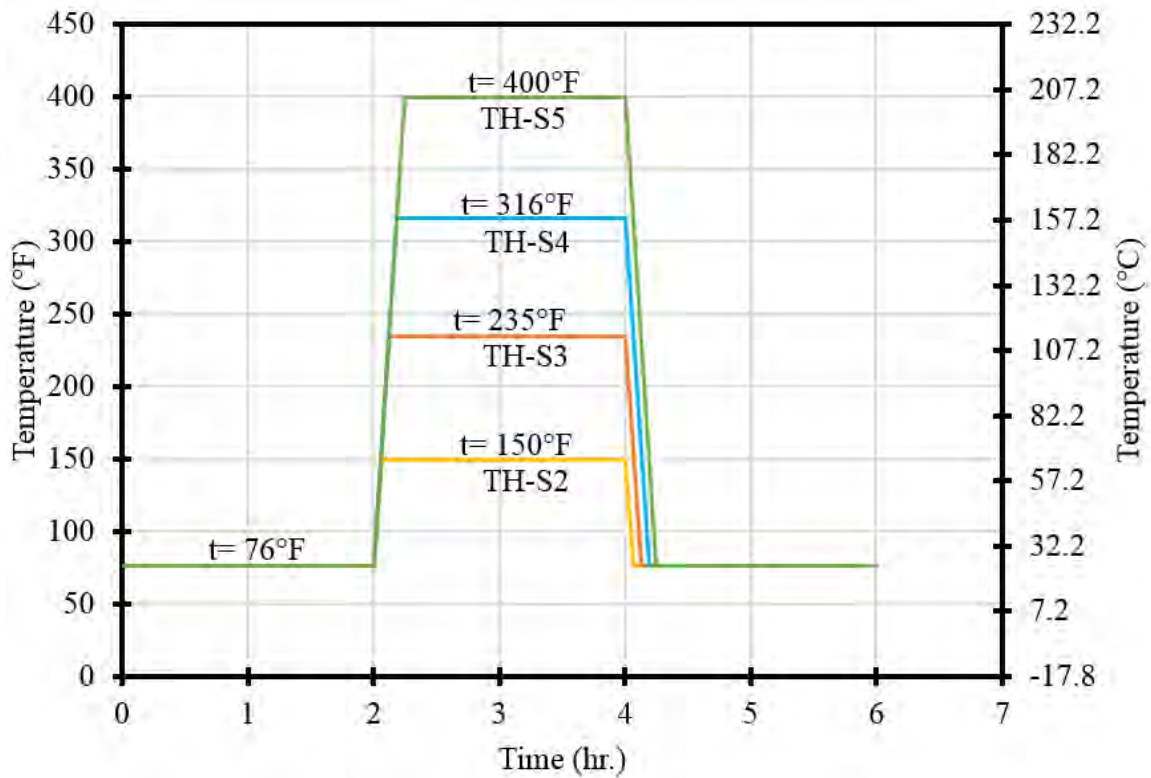
Figure 3.3-15 Temperature profiles for heat relaxation specimens in Phase II

55

In Phase III, CFCC specimens were placed in the MTS Frame for a uniaxial tensile test without the environmental chamber. Tensile force was applied in a force-control mode at a rate of 2 kip/min (9 kN/min) to failure. The tensile test was conducted in accordance with ASTM Standard D7205/7205M-06: "Standard Test Method for Tensile Properties of Fiber Reinforced Polymer Matrix Composite Bars".

3.4.1 Test Results

The load vs. time curves for all test specimens in Phase I are presented in Figure 3.3-16 through Figure 3.3-20 and a summary of the force loss at different stages is presented in Table 3.3-1.

Specimen TH-S1 experienced a typical relaxation loss that was discussed earlier in the report. The prestressing force decreased with time, with a loss of approximately 1.27 kip (5.6 kN) and 1.34 kip (6.0 kN) after 2 and 4 hrs, respectively, which corresponds to a total prestress loss of 2.6 %.

Specimen TH-S2 displayed the same pattern with a load loss of 1.2 kip (5.3 kN) in the first 2 hrs. (ambient temperature). When the temperature of the specimen was raised to 150 °F (66 °C), there was a step decrease in the load. In order to precisely estimate the load loss that occurred in the specimen due to the thermal change, the slope of the unheated segment was estimated and extended as a linear function between the load and the time. The thermal load loss was determined as the difference between the linear slope and the actual load-time curve. The load loss due to temperature increase was estimated as 0.75 kip (3.4 kN).

Specimen TH-S3 was exposed to two temperature increases. With each temperature increase, the specimen exhibited a loss in the load. That is in addition to the initial loss of the load during the first two hours of loading with no heating. A load loss of 1.23 kip (5.5 kN) was observed in the first 2 hrs with no heat. As shown in Table 3.3-1, a load loss of 0.83 kip (3.7 kN) was associated with the increase in temperature from ambient to 150 °F (66 °C), while a load loss of 1.52 kip (6.8 kN) was associated with the increase in temperature from 150 °F (66 °C) to 235 °F (112 °C).

In addition to the loss in load of 1.21 kip (5.4 kN) before heating, Specimen TH-S4 exhibited a 3-stage loss in load associated with three increases in temperature. The recorded losses were 0.8 kip (3.6 kN), 1.43 kip (6.4 kN), and 0.31 kip (1.4 kN) with the increase in temperatures from ambient to 150 °F (66 °C), to 235 °F (112 °C), and to 316 °F (158 °C), respectively.

Specimen TH-S5 displayed a similar load loss pattern with load losses of 1.26 kip (5.6 kN) before heating, and then losses of 0.79 kip (3.5 kN), 1.46 kip (6.5 kN), 0.34 kip (1.5 kN), and 0.32 kip (1.4 kN), corresponding to the temperature increase in the specimen from ambient to 150 °F (66 °C), to 235 °F (112 °C), to 316 °F (158 °C), and to 400 °F (204 °C), respectively.
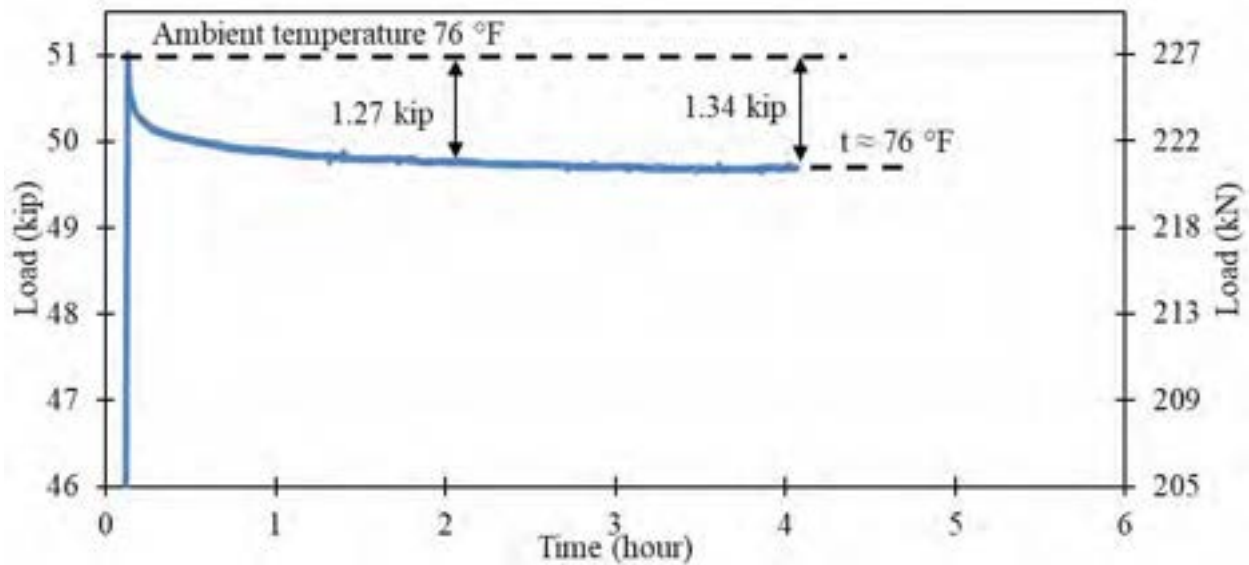
Figure 3.3-16 Load vs. time for TH-S1 in Phase I of thermal testing
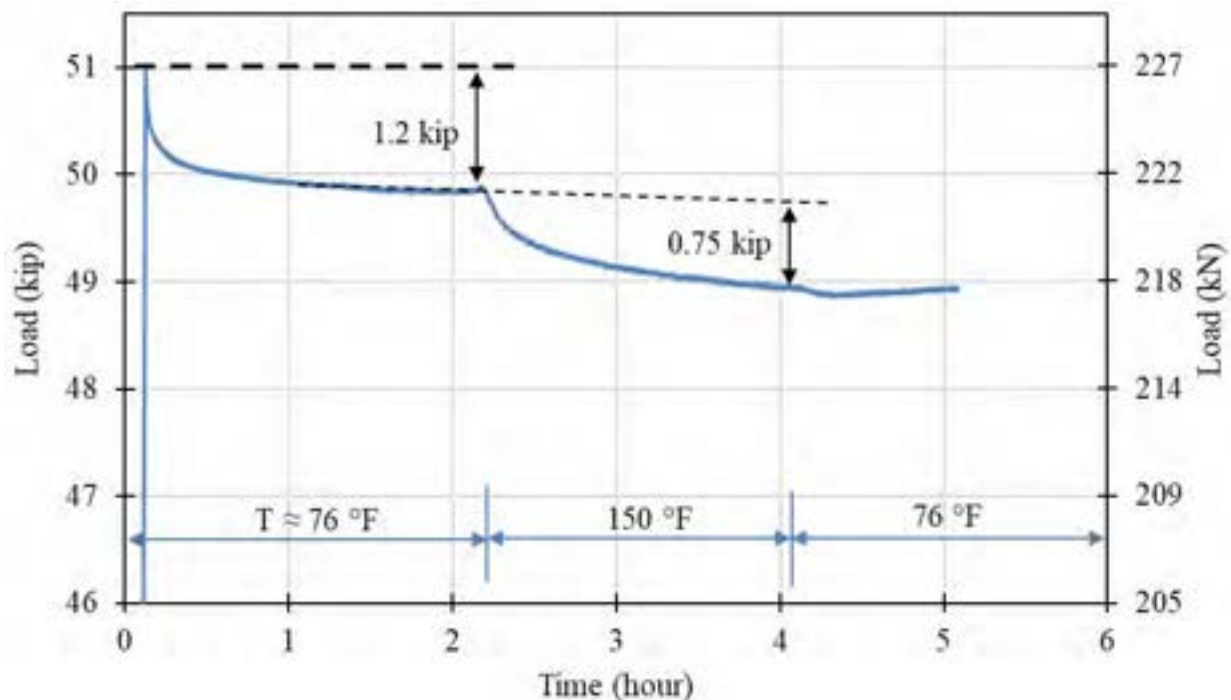
Figure 3.3-17 Load vs. time for TH-S2 in Phase I of thermal testing
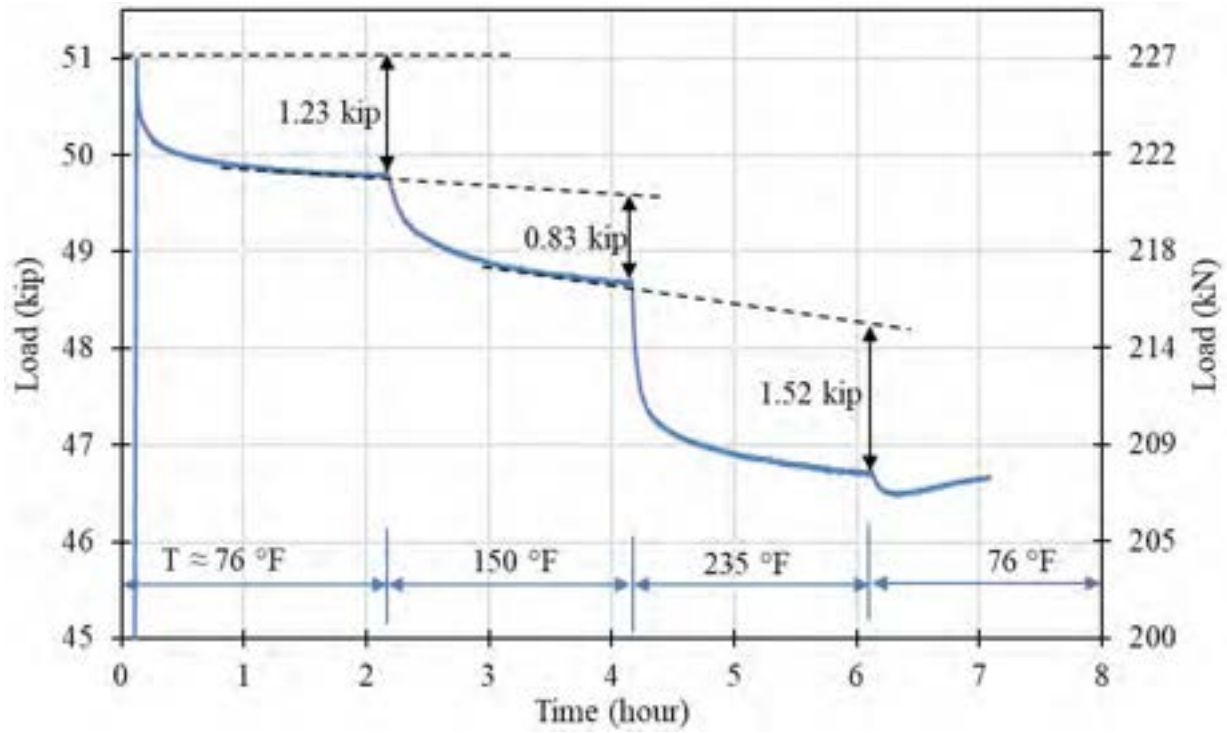
Figure 3.3-18 Load vs. time for TH-S3 in Phase I of thermal testing
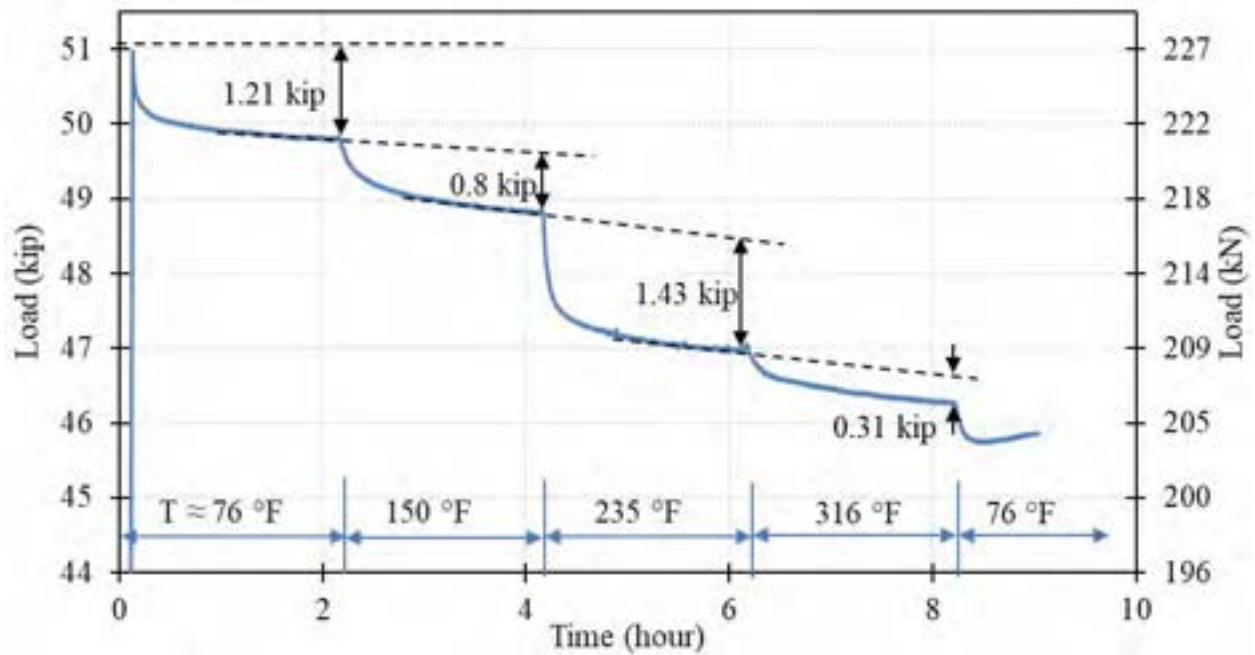
Figure 3.3-19 Load vs. time for TH-S4 in Phase I of thermal testing

58
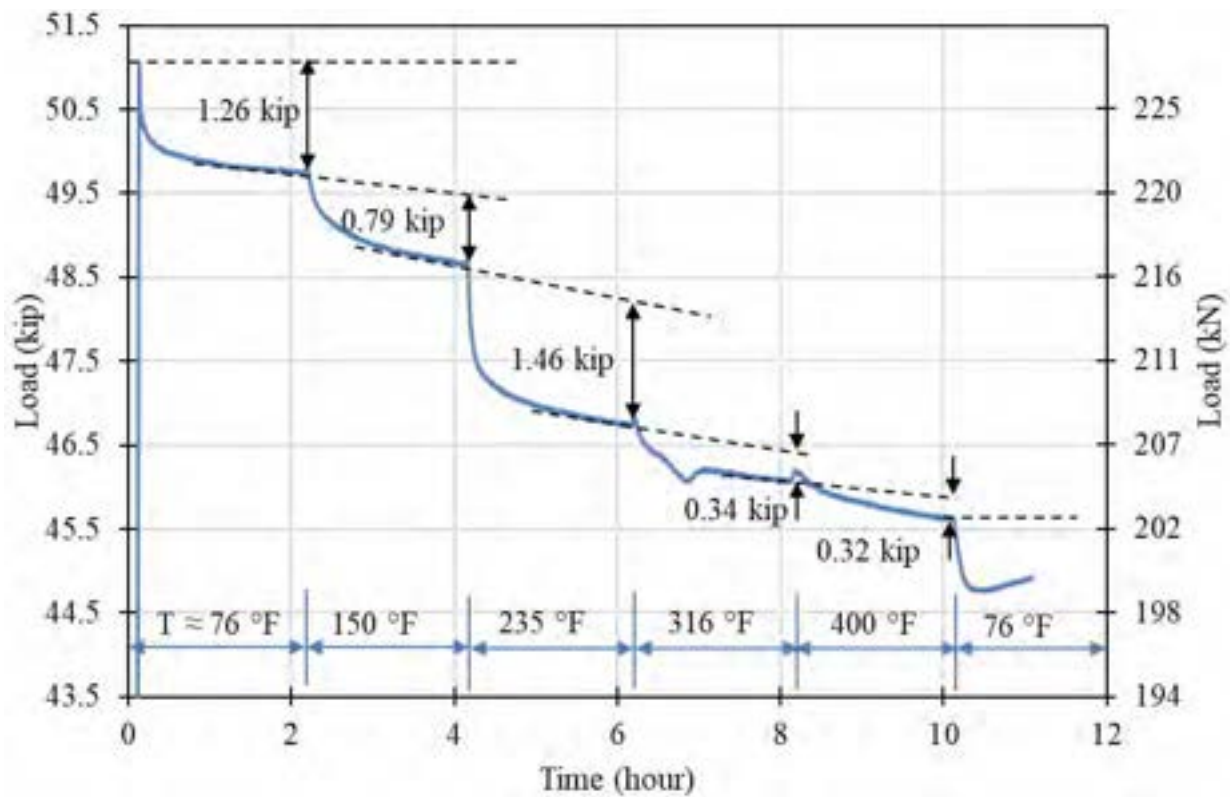
Figure 3.3-20 Load vs. time for TH-S5 in Phase I of thermal testing

Table 3.3-1 Summary of observed load loss due to increase in temperature in Phase I

Start Temp.	End Temp.	TH-S1	TH-S2	TH-S3	TH-S4	TH-S5
°F (°C)	°F (°C)	kip (kN)	kip (kN)	kip (kN)	kip (kN)	kip (kN)
76 (24)	76 (24)	1.27 (5.7)	1.2 (5.3)	1.23 (5.5)	1.43 (6.4)	1.26 (5.6)
76 (24)	150 (65)	-	0.75 (3.3)	0.83 (3.7)	0.8 (3.6)	0.79 (3.5)
150 (65)	235 (112)	-	-	1.52 (6.8)	1.43 (6.4)	1.46 (6.5)
235 (112)	316 (158)	-	-	-	0.31 (1.4)	0.34 (1.5)
316 (158)	400 (204)	-	-	-	-	0.32 (1.4)

Load loss in Phase II was significantly less than that observed in Phase I, even though the specimens were heated to the same maximum temperatures as in Phase I. The load vs. time curves for Specimens TH-S2 to TH-S5 during Phase II is presented in Figure 3.3-21 through Figure 3.3-24. In all the specimens, the increase in the temperature did not results in any significant loss of the load and the drop of the load was almost gradual and similar to a typical load loss that is observed at ambient temperatures in this research. It appears that initial heating of a CFCC specimen to a certain temperature level caused the epoxy matrix to relax and expand. Since the specimen was loaded during the heating period, this expansion/relaxation of the epoxy matrix was converted into a loss in the load. After the specimen was allowed to cool down, the epoxy matrix solidified in its standing shape, which explains the inability of the specimens to regain the lost load when they were allowed to cool down. When the CFCC specimens were heated for the second time in Phase II, the epoxy matrix did not experience any further relaxation since the temperature in the second heating cycle did not exceed that of the first cycle. It should be noted that when the specimens were allowed to cool down at the end of Phase I, the lost load was not recovered, which indicated that the loss in the load was not related to the thermal expansion of the specimens and that the heat relaxation was non-recoverable. This was also confirmed in Phase II since any loss of the load due to thermal expansion of the specimens would have been evident during the heating segment of Phase II.
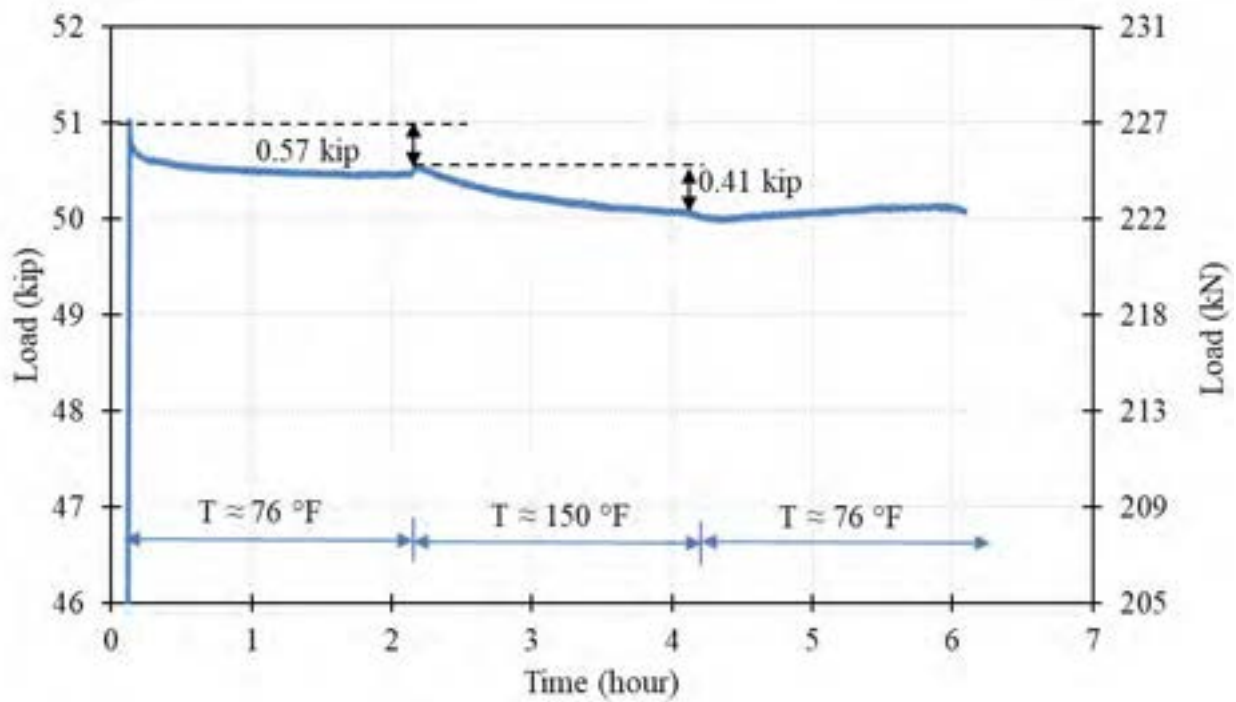
Figure 3.3-21 Load vs. time for TH-S2 in Phase II of thermal testing
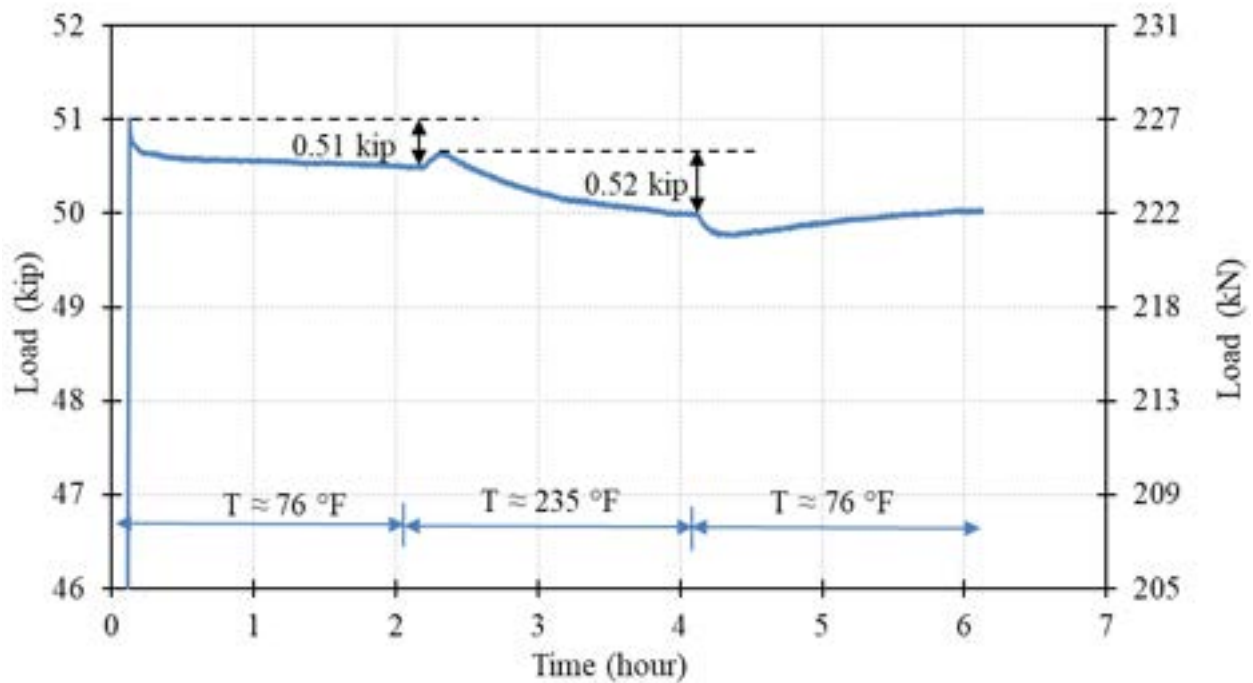
Figure 3.3-22 Load vs. time for TH-S3 in Phase II of thermal testing

61
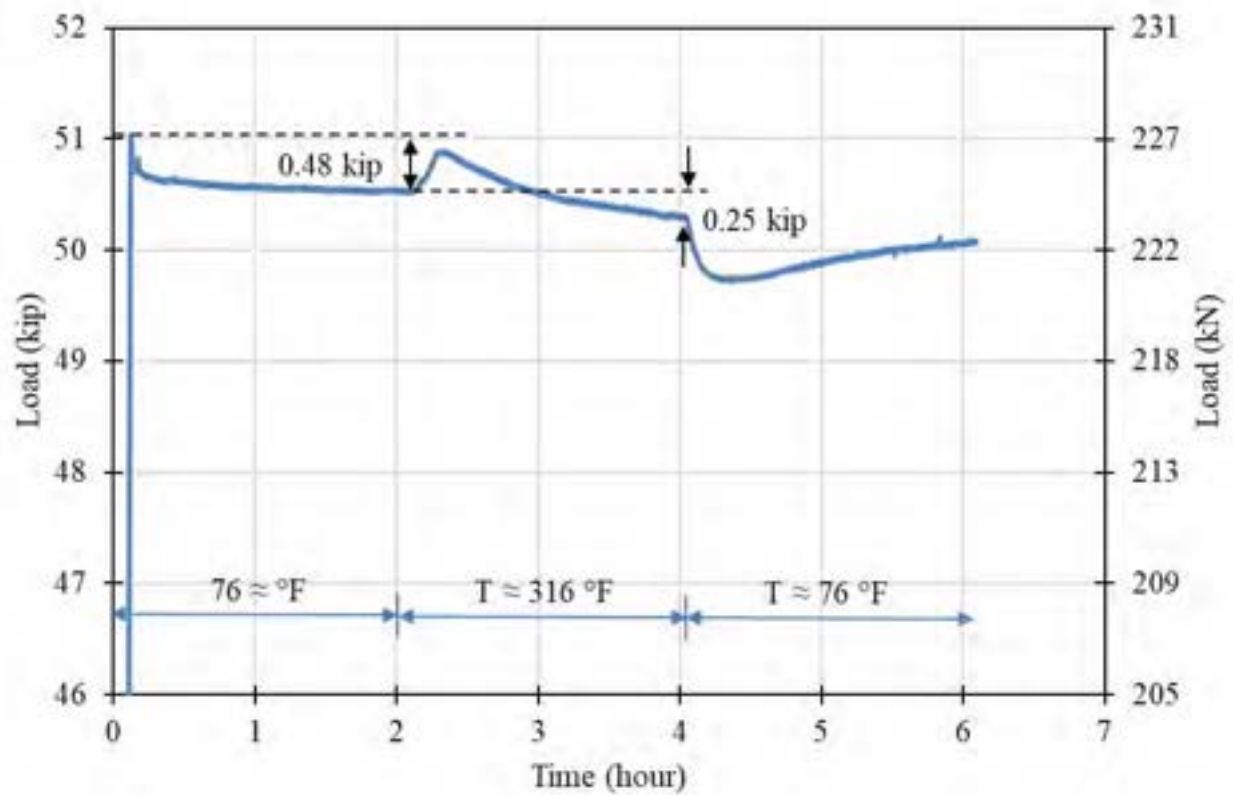
Figure 3.3-23 Load vs. time for TH-S4 in Phase II of thermal testing
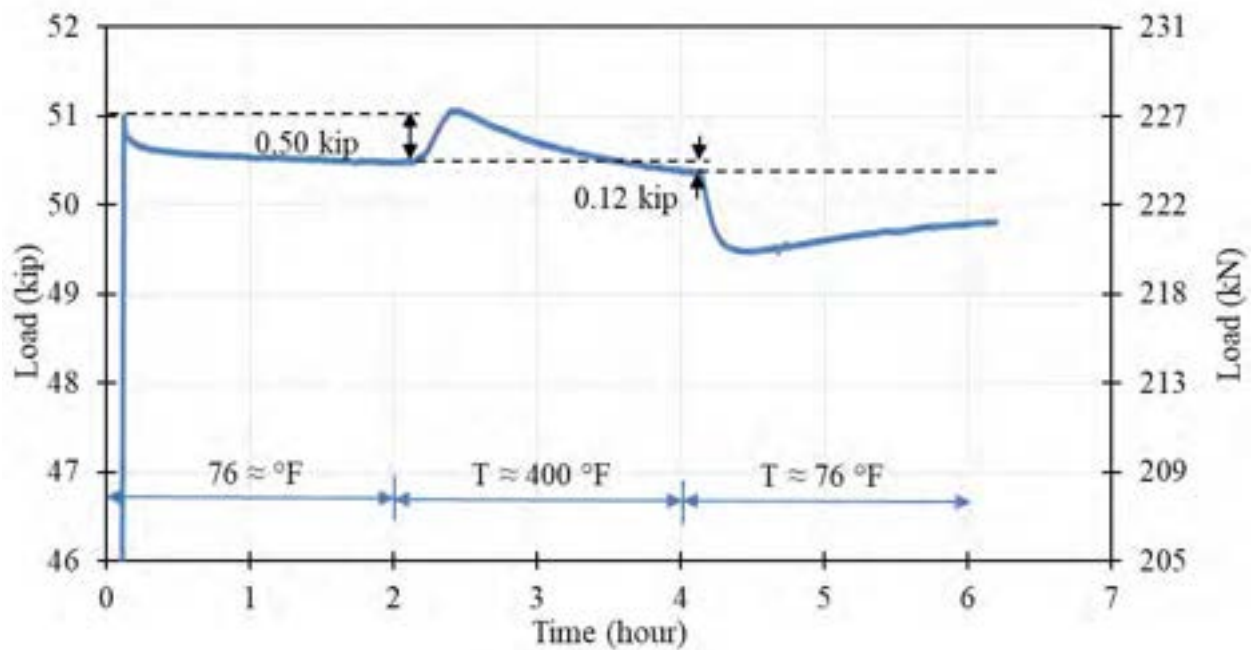
Figure 3.3-24 Load vs. time for TH-S5 in Phase II of thermal testing

The loss in the load due to the increase in temperature of the test specimens in Phase I was used to calculate the heat relaxation loss and estimate the loss in prestressing force during construction when the concrete is placed around the pretensioned CFRP strands and the heat is generated by concrete hydration. Several studies (Swenson and French 2015; Barr et al. 2005) place the maximum concrete temperature during hydration at 150 °F (65 °C), which corresponds to a relaxation loss in the heated segment of approximately 307 µε or a prestress loss of approximately 6.75 ksi (46.5 MPa). The calculations of the heat relaxation loss follow the basics of mechanics of materials. For instance, the heated segment of the CFCC specimen was 24 in. (610 mm) and since both heads of actuator were locked in position, the heat relaxation of the heated segment caused the loss in the load. When heating the specimens from ambient to 150 °F (66 °C), the average load loss among all specimens was 0.79 kip (3.5 kN). The loss of the load happened over the entire length of the specimen. In other words, between the two fixed heads of the actuator. The heat relaxation strain in the heated segment of the specimen is calculated based on load loss as follows:

$$\Delta\varepsilon = \frac{\Delta L}{L_h} \tag{1}$$

$$\Delta L = \frac{\Delta P L_T}{EA} \tag{2}$$

Where:

$\Delta\varepsilon$ = heat relaxation strain of the specimen (relative to the heated segment only)

ΔL = change in length of heat segment due to added heat relaxation, in. (mm)

L_T = length of the specimen between the fixed actuator heads

L_h = heated length of the specimen = 24 in. (610 mm)

A = cross sectional area of the specimen = 0.234 in.^{2} (151 mm^2)

E = elastic modulus of CFCC, ksi (GPa)

ΔP = change in the force due to increase in temperature, kip (kN)

The length of the specimen between the fixed actuator heads (L_T) is challenging to estimate. The total length of the specimen was 64 in. (1626 mm), which includes two 18 in. (457 mm) long anchorage devices. With a gripping length of 2.5 in. (64 mm) on each end, the specimen length

between the fixed heads, from grip to grip, was 59 in. (1499 mm). However, this length had a free strand length of 28 in. (711 mm) and an embedded length inside the anchorage devices of 31 in. (787 mm). Bond mechanism and force transfer in the embedded length complicates the calculations of the elongation in the embedded region.

To avoid estimating L_T, along with the need for estimating the elastic modulus of CFCC, Eqn. 2 can be rewritten using the load-elongation curve of the specimen (from zero loading to 51 kip (227 kN)). The displacement of the actuator was recorded during the loading of the specimen. Therefore, the relationship between the elastic modulus and the length of the specimen can be written as:

$$\frac{L_T}{EA} = \frac{\Delta L_L}{\Delta P_L} \tag{3}$$

Where:

ΔP_L = change in the load during the loading of the specimen

ΔL_L = corresponding elongation of the specimen estimated using actuator displacement

From the loading-elongation curves of the five specimens, the average (L_T/EA) was 0.00922 in./kip (0.053 mm/kN), calculated based on an observed change in displacement of 0.1383 in. (3.513 mm) over a change in the load from 36 to 51 kip (160 to 227 kN). Therefore, the heat relaxation strain in the CFCC specimen can be calculated as:

$$\Delta L = \Delta P \frac{L_T}{EA} = 0.79 \times 0.00922 = 0.00736 \; in. \tag{4}$$

$$\Delta \varepsilon = \frac{\Delta L}{L_h} = \frac{0.00736}{24} = 307 \times 10^{-6} = 307 \; \mu\varepsilon \tag{5}$$

It should be noted that these calculations are based on a conservative estimate for the heated length of 24 in. (610 mm), which represents the interior height of the heat chamber. The actual heated length of the CFCC strand specimens was slightly longer than 24 in. (610 mm) since the heat radiated beyond the interior cavity of the heat chamber through the top and bottom holes (holes were block with thermal blanket to minimize heat escape). Consequently, a more accurate heated length may be taken as 27 in. (686 mm) considering an additional 2.0 in. (51 mm) of heated

length through the top hole and 1.0 in. (25.4 mm) through the bottom hole, with a resulting additional strain of 272 $\mu\varepsilon$.

Figure 3.3-25 and Figure 3.3-26 show the testing and failure of the test specimens in Phase III. Test results are also presented in Table 3.3-2. The ambient uniaxial tensile test of the four previously-heated test specimens revealed an average breaking load of 113.4 kip (504 kN), which is slightly higher the breaking load of the non-heated test specimen. The average elastic modulus from the uniaxial tensile tests of the four previously heated test specimens was calculated as approximately 23,728 ksi (163 GPa), which is also slightly higher than the elastic modulus of the non-heated specimen. No noticeable physical difference was observed during the test for between the first specimen (non-heated) and the rest of the specimens. Table 3.3-2 also lists earlier test results of 0.6″ CFCC specimens (Grace et al. 2019) and test results showed a similar pattern.

Figure 3.3-25 Uniaxial testing of CFCC specimens in Phase III
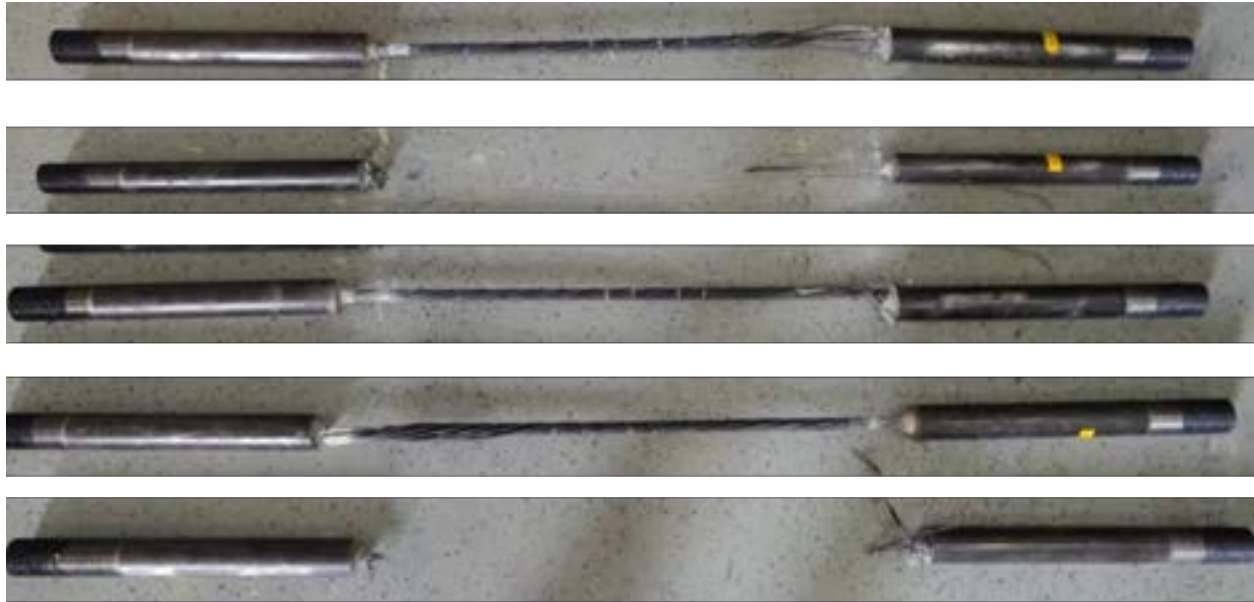
Figure 3.3-26 Failure of Test Specimens TH-S1 (top) to TH-S5 (bottom)

Table 3.3-2 Summary of the test results of Phase III (uniaxial tensile test) and previous results of testing 0.6" CFCC strands

Specimen	Max. Temperature, °F (°C)	Breaking Load, kip (kN)		Elastic Modulus, ksi (GPa)	
		0.6″ CFCC	0.7″ CFCC	0.6″ CFCC	0.7″ CFCC
1	76 (24)	71.0 (316)	112.7 (501)	22,245 (153)	23,557 (162)
2	150 (66)	71.2 (317)	114 (507)	22,947 (158)	23,543 (162)
3	235 (112)	66.0 (294)	113 (503)	22,967 (158)	23,877 (165)
4	316 (158)	70.6 (314)	114 (507)	23,051 (159)	23,753 (164)
5	400 (204)	74.1 (330)	112.5 (501)	23,440 (162)	23,740 (163)

3.5 Summary

Based on the test results obtained from loading and monitoring CFCC strands with different diameters and at different stress levels, the one-million-hour creep rupture strength of CFCC strands is not less than 86 % of the average CFCC tensile strength. For 0.7″ CFCC strands, the minimum one-million-hour creep rupture strength is approximately 98 kip (436 kN), which is higher than the guaranteed strength recommended by the manufacturer (78.7 kip or 350 kN). Similar to 0.6″ CFCC, under sustained load levels higher than 95 % of the average tensile strength of CFCC, test specimens either ruptured within the first 100 hours of loading or continued to sustain the load without signs of creep. Consequently, the jacking and prestress levels of CFCC

strands can be safely increased beyond the levels established in ACI 440-4R-04 without triggering creep-rupture failure during the lifespan of the structural element.

The one-million-hour relaxation rate, defined as the expected percentage loss in the force in a CFRP strand over one-million hours, of 0.7″ CFCC strands, is approximately 2.2 % based on available test results of strands initially tensioned to a force level of 94 kip (418 kN). In addition, high temperature seems to induce additional heat-related relaxation. For instance, at a temperature similar to the heat curing temperature of concrete (150 °F or 66 °C), it was observed that 0.7″ CFCC strands experienced additional relaxation of approximately 307 $\mu\varepsilon$, which in prestressing applications represents a prestress loss of 6 to 7 ksi, or 1.4 to 1.6 kip (6 to 7 kN) per strand. This additional heat relaxation matched that observed in 0.6″ CFCC strands and did not appear to significantly impact the ambient tensile capacity or the elastic modulus of the strands.

CHAPTER 4: BOND, TRANSFER LENGTH, AND DEVELOPMENT LENGTH

4.1 Introduction

Bond between CFRP strands and surrounding concrete is the key in establishing the integrity of the section and achieving the design flexural and shear capacities, especially in prestressing applications. The bond can be achieved through chemical adhesion, shear resistance, and interlock mechanisms between the FRP bars and the concrete (Kanakubo et al. 1993).

Test standards that evaluate the bond strength between CFRP and concrete were developed and included in different design guides, such as ACI 440-4R-04 (ACI 440, 2004). Pullout testing is considered the simplest and is commonly accepted. However, stress conditions during pullout experiments are rarely found in practice and bond strength values established under this test setup may vary considerably from those in practical circumstances (Achillides and Pilakoutas 2004). Other test standards are also available and different research teams developed multiple bond and bond-slip analytical models to estimate the bond strength between concrete and internal reinforcement. For instance, a bond slip model was developed by Alsiwat and Saatcioglu (1992) using the distribution and transfer of forces between steel rebars and concrete. Harajli (2009) examined the bond slip relationship for different concrete covers and confinement conditions. Tastani and Pantazopoula (2010) also conducted detailed experiments that showed that the force distribution in the rebar is not uniform along the embedment length.

While the bond between steel reinforcement and concrete has been a focus of decades of research studies (Akbas et al, 2016), bond between CFRP and concrete lacks the experimental work and the corresponding analytical models. Nevertheless, it is widely accepted that, similar to steel, the bond-slip relationship between CFRP and concrete depends on factors such as degree of confinement, bar size, bar composition, surface conditions, casting position, concrete cover, embedment length, and surface deformation (Achillides and Pilakoutas 2004; Malvar 1994). Current guidelines such as ACI 440.01-15 (ACI 2015) provides formulas to estimate the bond strength between CFRP and concrete. However, recent research suggests that these formulas are too conservative (Harajli and Abouniaj 2010; Hao et al 2008).

This chapter presents a detailed experimental investigation that was executed with the main objective of establishing the characteristics of the bond strength between CFCC and concrete. The

experimental investigation is composed of three test programs. The first test program included evaluating the bond strength between CFCC strands and uncracked concrete in a pullout test setup. The second test program evaluated the transfer length in concrete prisms, with or without confinement reinforcement. The third test program evaluated the development length of CFCC strands by pulling the strands to failure from concrete prisms at different lengths. Details of each test program and the main findings and conclusions are provided in the following sections.

4.2 Pullout Test of CFCC Strands

A total of 35 pullout test specimens were constructed according to ACI 440.3R-12-B.3 (ACI 2012): "Test Method for Bond Strength of FRP Bars by Pullout Testing". Four different types of strands were evaluated through the study. Out of the thirty-five specimens, twenty specimens were constructed using 0.7″ CFCC strands, five were constructed using 0.6″ CFCC strands, five were constructed using 0.6″ steel strands, and five were constructed using 0.7″ steel strands. In addition, out of the twenty specimens with 0.7″ CFCC strands, five specimens were tested to failure at ambient conditions, five specimens were subject to 150 cycles of heating and cooling, five specimens were subjected to 150 cycles of freezing and thawing in a water tank, and five specimens were subjected to 150 cycles of freezing and thawing in air.

Each specimen consisted of a single strand, with an anchorage device on one end, embedded at the center of a concrete cube and with a side length of 8 in. (203 mm). The bonded length of the strand was maintained at 3.5 in. (89 mm). The remaining embedded length was shielded against concrete bonding using a bond breaker Polyvinyl Chloride (PVC) pipe. Specimen configuration is shown in Figure 4.2-1. As shown on the figure, the strand extended 0.5 in. (12.7 mm) beyond the concrete cube to facilitate monitoring the slippage of the strand when the specimen was loaded.

Figure 4.2-2 through Figure 4.2-5 show the construction of the test specimens. A wooden formwork was prepared with a side length of 8 in. (203 mm) and the strand specimen was passed through the formwork and protruded 0.5 in. (12.7 mm) from the bottom side. PVC pipe was provided for debonding,
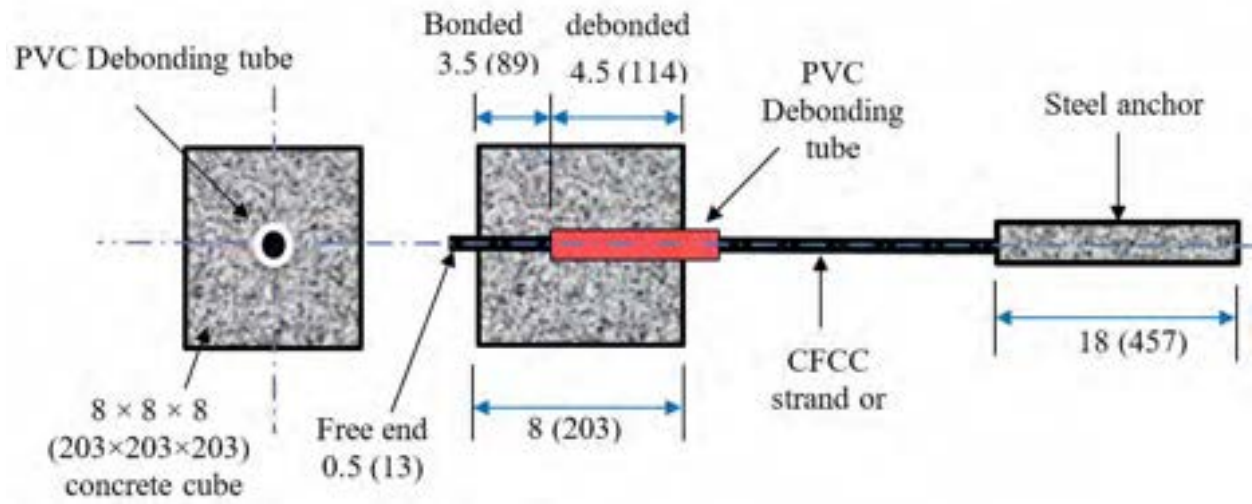
Figure 4.2-1 Schematic diagram of pullout specimens (dimensions in inches (mm))

Figure 4.2-2 Preparing the formwork for the test specimens

Figure 4.2-3 Inserting debonding PVC tubes to control the bond length

Figure 4.2-4 Pouring concrete

Figure 4.2-5 Pullout specimens ready for curing

The concrete cube specimens were cast using a concrete mix with a design strength of 7000 psi (48 MPa). After casting the concrete, the specimens were covered with wet burlap and plastic sheets and were allowed to cure for 72 hours. The specimens were removed from the formwork and testing commenced 28 days after casting. The compressive strength of the concrete at the time of the testing averaged 8.66 ksi (60 MPa).

Pullout tests were conducted by subjecting the test specimen to a static uniaxial tensile load while monitoring the slippage of the strand from the concrete cube. As shown in Figure 4.2-6 through Figure 4.2-8, the specimens were mounted in a two-post MTS uniaxial testing machine. The sleeve anchorage of the CFCC strand was threaded into the moving head of the testing machine. For steel strands, a standard wedge anchorage was attached to the free end of the strand and a special coupler was used to attach the specimen to the head of the actuator. On the other end, a special high-strength steel head was fabricated to accommodate and hold the concrete cube. In addition, an LVDT was attached at the free end of the strand under the concrete block to capture the slippage of the strand. The specimens were loaded monotonically at a load rate of 0.1 in/min (2.5 mm/min) to failure.

Figure 4.2-6 Attaching LVDT to monitor the slippage of strands
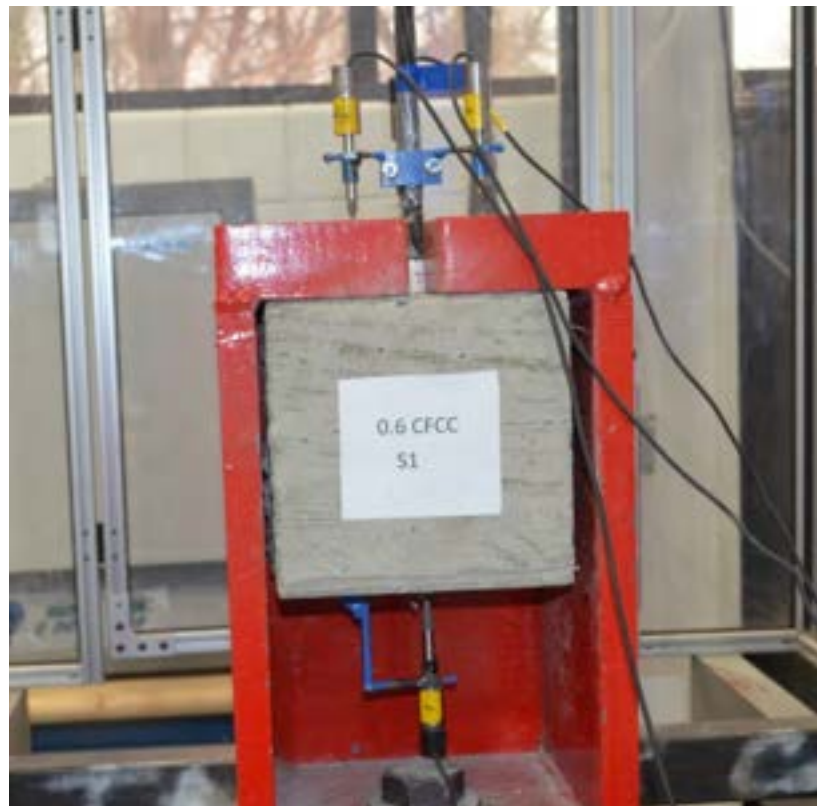
Figure 4.2-7 Test setup for pullout specimens

Figure 4.2-8 Test setup for pullout specimens

Figure 4.2-9 through Figure 4.2-12 show the load vs. slippage of the test specimens with CFCC and steel strands that were tested at ambient conditions with no prior environmental exposure. In addition, Table 4.2-1 through Table 4.2-4 present the load levels at key slippage values of 0.002, 0.004, and 0.01 in. (0.05, 0.10 and 0.25 mm). An LVDT malfunction was experienced in some of the test specimens and slippage readings were not collected. While both 0.6″ and 0.7″ CFCC showed similar load-slippage performance, steel strands of the two diameters exhibited a significantly different performance. CFCC strands exhibited negligible slippage before they reached their maximum load. After the maximum load, the slippage increased with a slight decrease in the load. Steel strands accumulated significant slippage at lower load levels than those of CFCC but the load continued to increase with the increase in the slippage until the strands fully pulled out of the concrete cubes. The maximum load level was achieved at maximum slippage. In

74

addition, while the test results of CFCC strands seemed consistent among the test specimens, the results of steel strands appeared more scattered. On average, the maximum load of 0.7″ CFCC strands before slippage was approximately 32 % higher than that of steel strands with the same diameter. The maximum load of 0.6″ CFCC strands before slippage was approximately 109 % higher than that of steel strands with the same diameter.

Post-testing evaluation of the test specimens showed that CFCC strands achieved their bond capacity mainly through adhesion to the concrete paste. Once the adhesion resistance was overcome, the strand gradually slipped from the concrete. On the other hand, the bond strength of steel strands to concrete was achieved through friction and interlock. As shown in Figure 4.2-13 through Figure 4.2-15, when exposing the bonded length of a CFCC strand after testing, the surface of the strand was smooth with no indication of interlock between the concrete and the strand. On the other hand, concrete keys were wedged between the twisted wires of the steel strands as shown in Figure 4.2-15. Therefore, the pullout strength was achieved through the mechanical resistance of the concrete keys wedged between the wires, rather than the adhesion of the concrete to the surface of the strands. This also explains the scattered performance of steel strands since the formation of concrete keys between the wires was not likely consistent among the test specimens considering the smaller bond length of 3.5 in. (89 mm). In addition, due to the change in bond mechanism between steel and CFCC strands, different bond lengths may result in different performance than that shown in the current test. For instance, if a longer bond length is allowed in the test specimens, the formation of key wedges of steel strands may result in a significantly larger pullout resistance. Similarly, longer bond length of CFCC strands will likely lead to increased overall pullout resistance, but at a different rate than that of steel strands.

Figure 4.2-16 through Figure 4.2-18 summarize the exposure of 0.7″ CFCC specimens to 150 cycles of heating with air temperature varying between 60 and 176 °F (15 to 80 °C) and core temperature of specimens varying approximately from 80 and 120 °F (27 to 49 °C). After concluding the heat cycles, the specimens were tested in pullout to failure at ambient conditions. Load-slippage curves of the test specimens are shown in Figure 4.2-19 and maximum pullout load is presented in Table 4.2-5. The test results did not show a significant change in bond capacity between CFCC and concrete after the heat cycles.

Exposure to 150 cycles of freezing and thawing inside a water tank resulted in disintegration of the concrete cubes as explained in detail in Chapter 7. On the other hand, exposure to 150 freeze-thaw cycles in the air, as shown in Figure 4.2-20 and Figure 4.2-21, resulted in a slight reduction in the bond strength between CFCC and concrete as indicated in Table 4.2-5. This confirms the hypothesis that freezing and thawing, with the presence of water, negatively impacts the concrete and consequently leads to a deterioration in the bond strength.
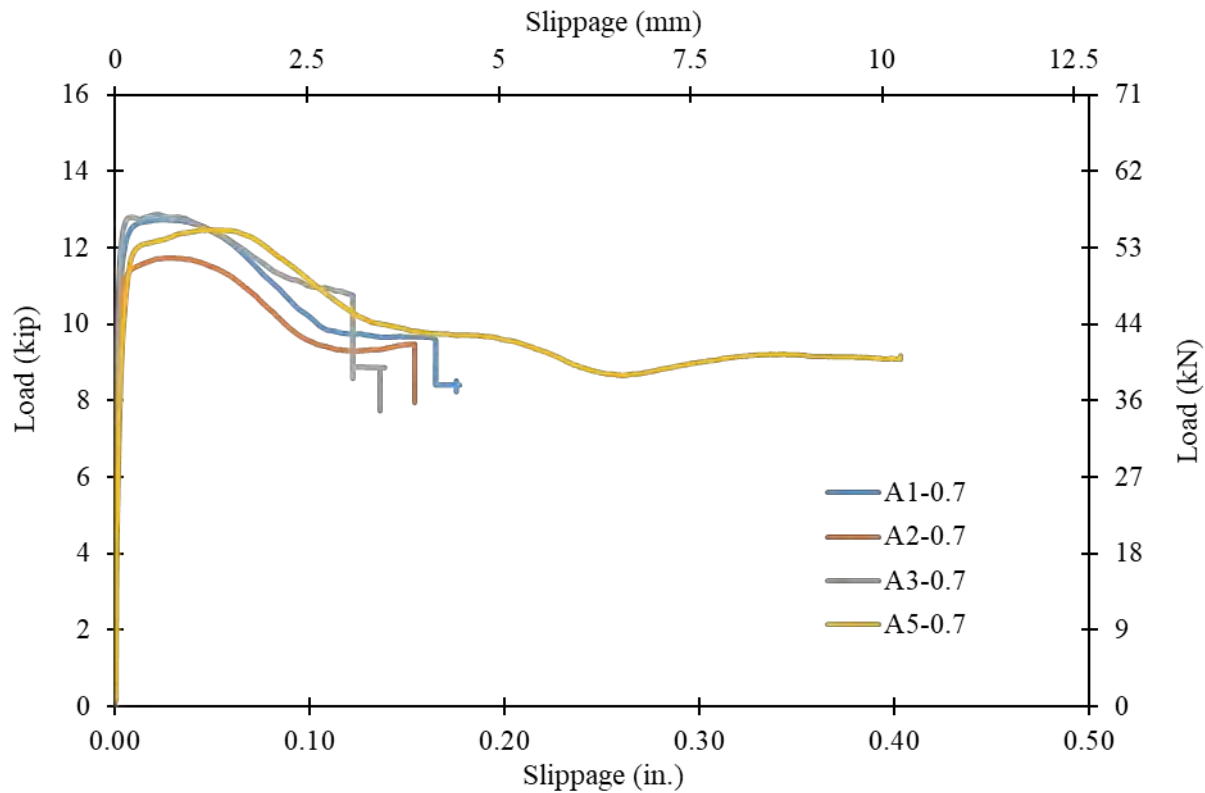
Figure 4.2-9 Load vs. slippage of pullout test specimens with 0.7″ CFCC strands
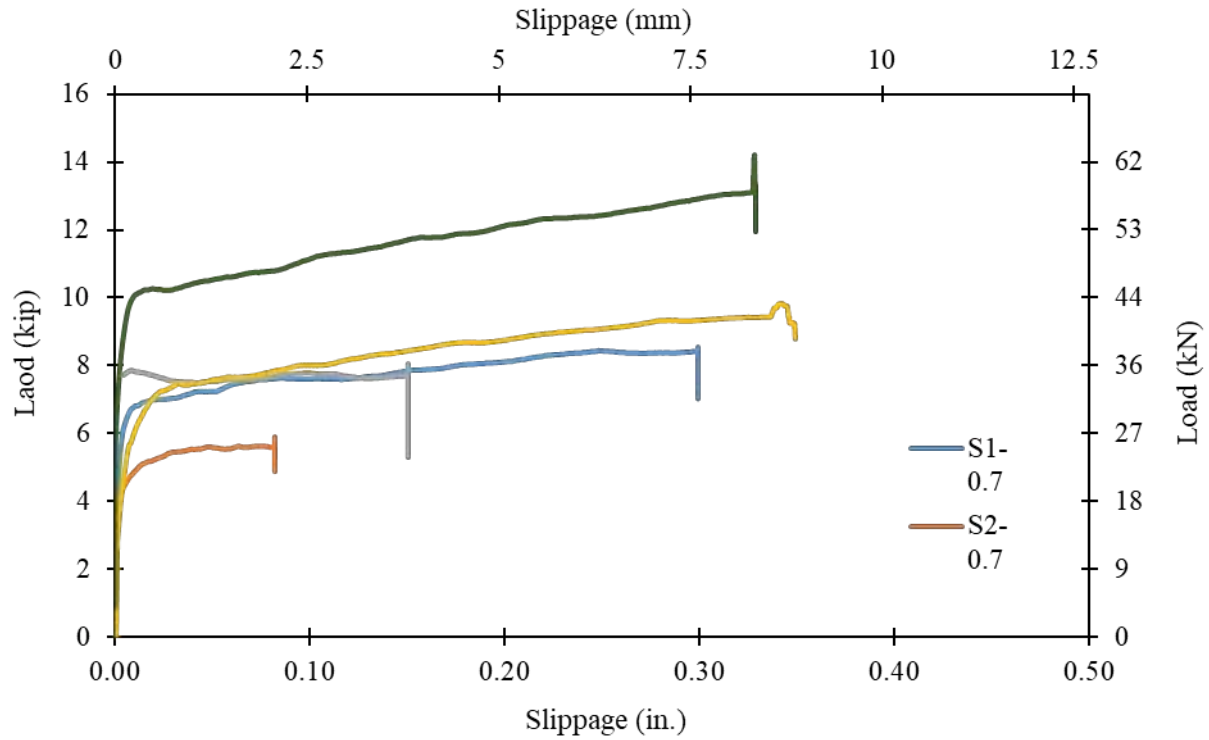
Figure 4.2-10 Load vs. slippage of pullout test specimens with 0.7″ steel strands
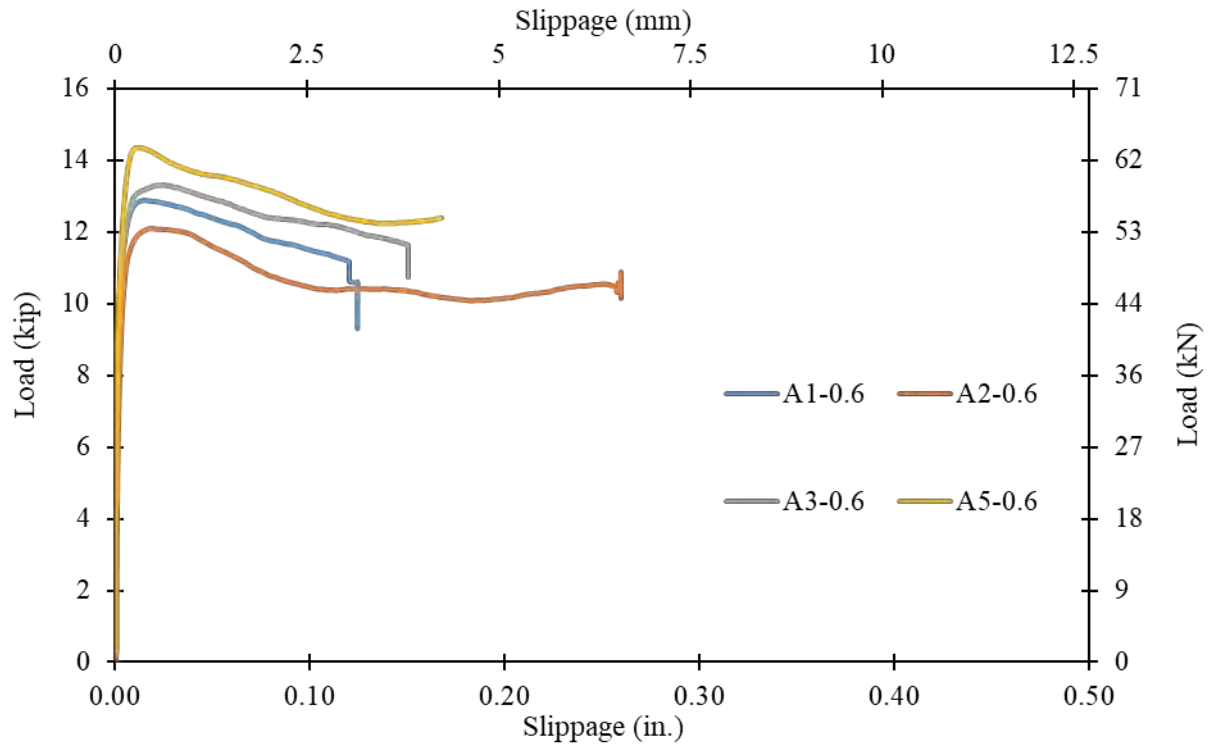
Figure 4.2-11 Load vs. slippage of pullout test specimens with 0.6″ CFCC strands

77
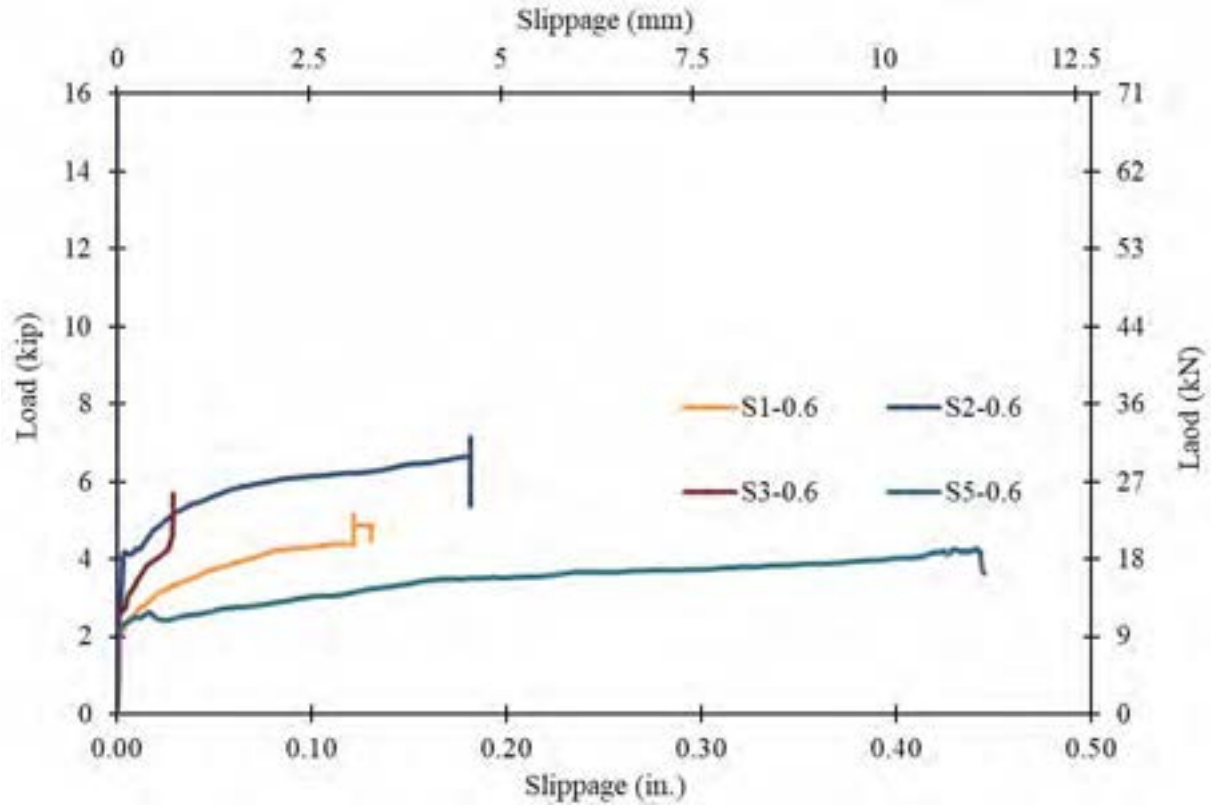
Figure 4.2-12 Load vs. slippage of pullout test specimens with 0.6″ steel strands

Table 4.2-1 Summary of slippage in pullout specimens with 0.7″ CFCC strands

CFCC (0.7″)	Bond pullout load, kip			Max load
	Slippage, in.			
	0.002	0.004	0.01	
1	9.878	11.638	12.595	12.738
2	8.998	10.791	11.462	11.715
3	10.934	12.441	12.771	12.859
4	-	-	-	11.640
5	7.788	10.065	11.935	12.452
Average	9.400	11.234	12.191	12.290

Table 4.2-2 Summary of slippage in pullout specimens with 0.6″ CFCC strands

| CFCC (0.6″) | Bond pullout load, kip | | | |
| | Slippage, in. | | | Max load |
	0.002	0.004	0.01	
1	9.867	11.275	12.771	12.881
2	7.920	10.263	11.858	12.089
3	9.614	11.286	13.002	13.299
4	-	-	-	13.090
5	9.955	12.254	14.355	14.355
Average	9.339	11.270	12.997	13.140

Table 4.2-3 Summary of slippage in pullout specimens with 0.7″ steel strands

| Steel (0.7″) | Bond pullout load, kip | | | |
| | Slippage, in. | | | Max load |
	0.002	0.004	0.01	
1	4.862	6.094	6.809	8.547
2	4.037	4.356	4.862	5.896
3	-	7.722	7.821	8.052
4	7.469	8.679	10.043	14.201
5	3.603	4.664	6.105	9.823
Average	4.993	6.303	7.128	9.304

Table 4.2-4 Summary of slippage in pullout specimens with 0.6″ steel strands

| Steel (0.6″) | Bond pullout load, kip | | | |
| | Slippage, in. | | | Max load |
	0.002	0.004	0.01	
1	2.068	2.266	2.662	5.159
2	2.761	4.202	4.290	7.161
3	2.684	2.728	3.443	5.709
4	-	-	-	9.03
5	2.233	2.332	2.508	4.257
Average	2.437	2.882	3.226	6.280

Figure 4.2-13 Exposing the bonded length of CFCC specimen in pullout specimen after testing

Figure 4.2-14 CFCC strand leaving impression of strand twist on concrete

Figure 4.2-15 Development of shear interlock between the concrete paste and steel strands

Figure 4.2-16 Heat chamber

Figure 4.2-17 CFCC specimens exposed to 150 cycles of heating and cooling
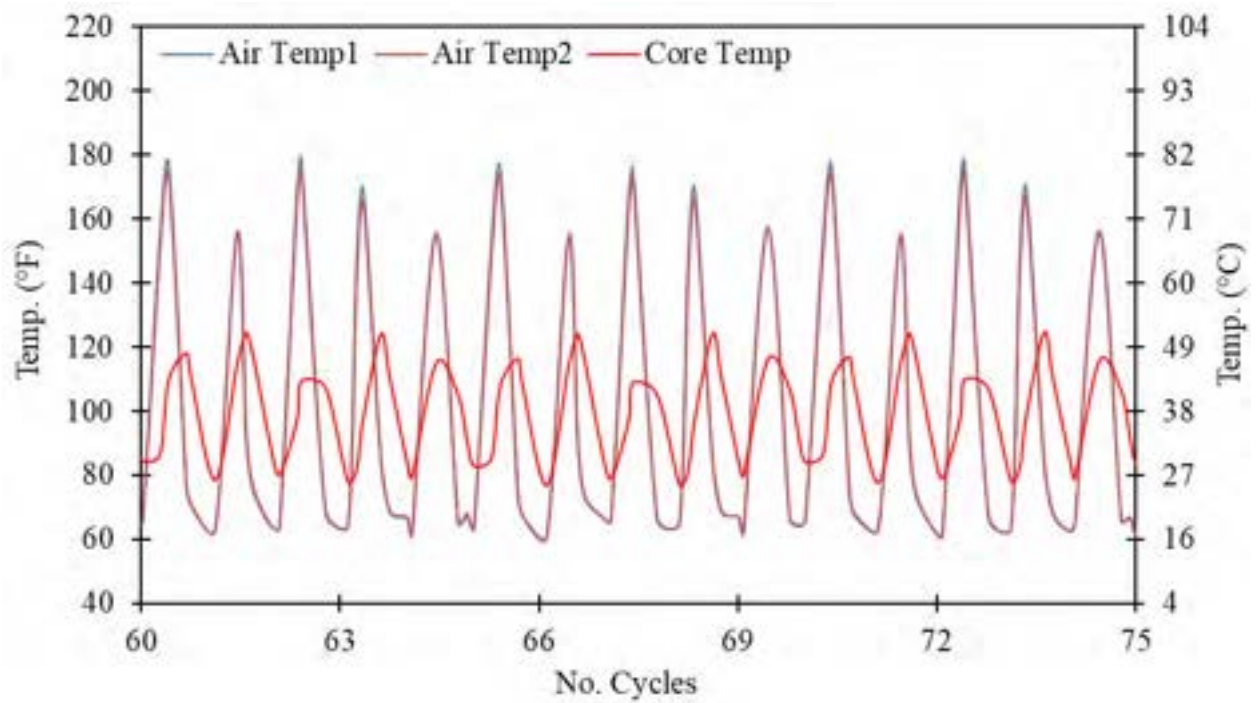
Figure 4.2-18 Example of change in temperature in pullout specimens under cyclic heating (Cycles 60-75 of 150 cycles)
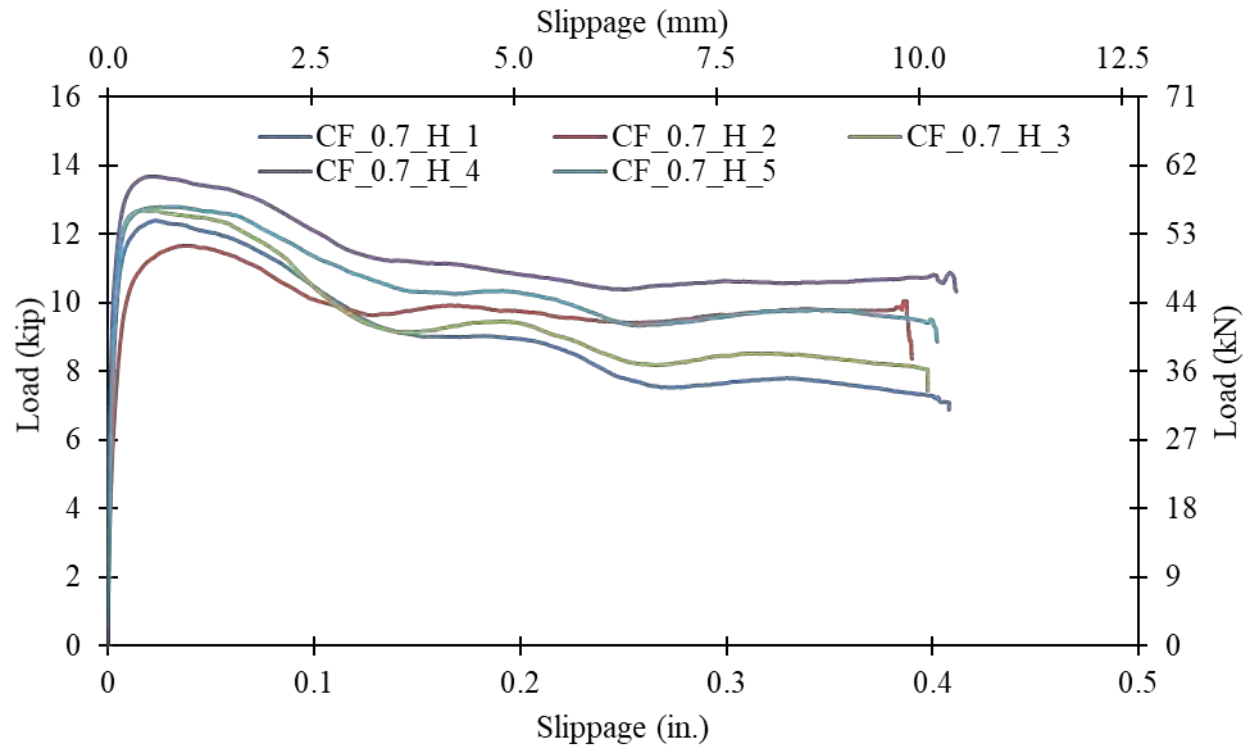
Figure 4.2-19 Load vs. slippage of pullout test specimens with 0.7″ CFCC strands after exposure to heat cycles

Figure 4.2-20 Pullout test specimens with 0.7″ CFCC strands under freeze-thaw cycles
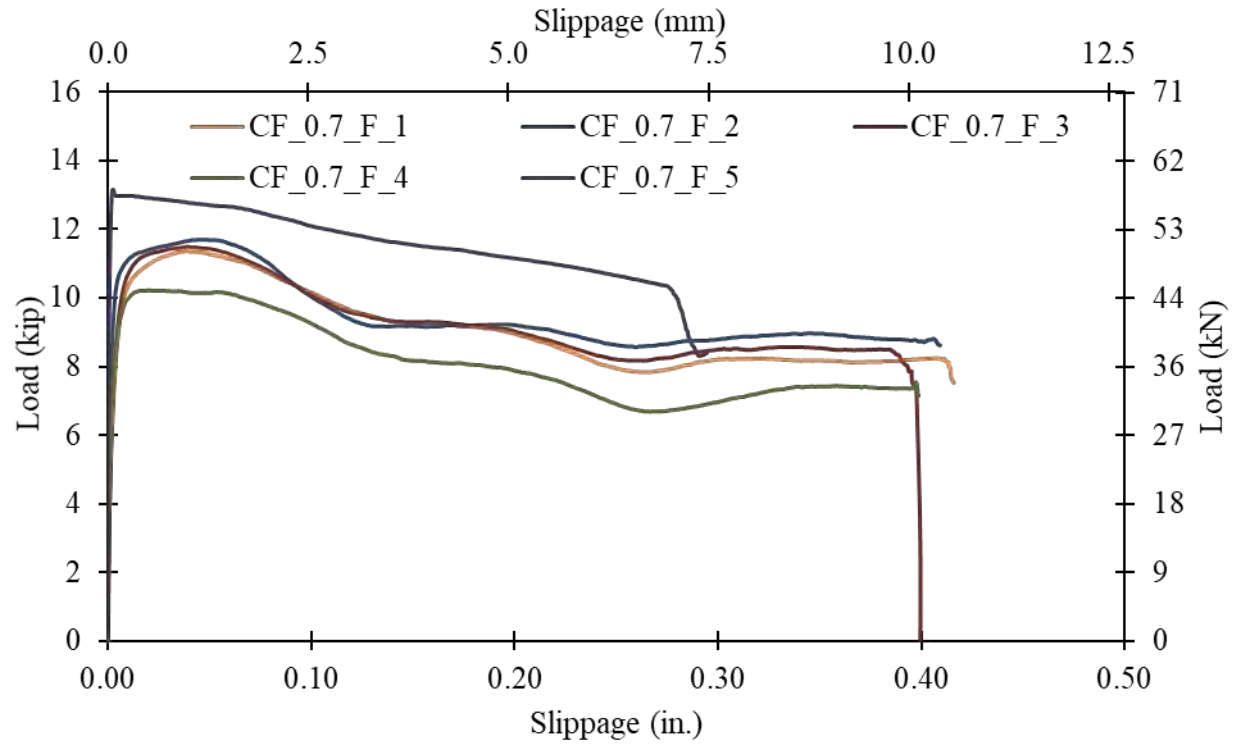
Figure 4.2-21 Load vs. slippage of pullout test specimens with 0.7″ CFCC strands after exposure to freezing cycles

Table 4.2-5 Summary of test results of pullout test specimens

| # | Failure load, kip | | | | | |
	0.7″ CFCC ambient	0.7″ CFCC heat	0.7″ CFCC freeze	0.7″ steel ambient	0.6″ CFCC ambient	0.6″ steel ambient
1	12.73	12.39	11.36	8.55	12.88	5.16
2	11.73	11.66	11.69	5.9	12.09	7.16
3	12.86	12.68	11.48	8.05	13.30	5.71
4	11.64	13.67	10.22	14.20	13.09	9.09
5	12.50	12.78	13.16	9.80	14.36	4.30
Average (kip)	12.29	12.64	11.58	9.30	13.14	6.28
Average bond strength (kip/in.)	3.51	3.61	3.31	2.66	3.75	1.79

4.3 Transfer Length of CFCC Strands

The transfer length test was the second test to evaluate the bond strength between concrete and 0.7″ CFCC strands. As shown in Figure 4.3-1 and Figure 4.3-2, the transfer length test specimens consisted of a pretensioned 0.7″ CFCC strand with an overall length of 89 in. (2260 mm). The strand was provided with two 18 in. (457 mm) long threaded sleeve anchor devices and was pretensioned inside a custom-made steel frame as shown in Figure 4.3-3. An in-line load cell was attached to the end of the strand to monitor the prestressing force (Figure 4.3-4). Right rectangular concrete prisms (cuboids) with square cross sections and varying lengths and with or without reinforcement were poured around the CFCC strands after it was tensioned to an initial force level of 53 kip (236 kN) per strand. After pouring, the concrete was properly cured and release of the prestressing force took place after the concrete achieved at least 80 % of its design 28-day compressive strength. Releasing of the strand was performed by slightly pulling the strand to a higher force and then releasing the locking nut on the anchor device. The change in the force level during and after releasing the strand was monitored through the load cell that was positioned on the other end of the test specimen.

Three sets of test specimens were constructed and tested. The first set of specimens (Figure 4.3-5 and Figure 4.3-7) was constructed with concrete prisms measuring 12 in. × 12 in. (305 mm × 305 mm) in cross section and with lengths of 18, 24, 30, 36, and 42 in. (457, 610, 762, and 1067 mm). In addition, the prisms were provided with a reinforcement cage made of No. 3 (M10) 10 in. × 10 in. (254 × 254 mm) square steel stirrups every 6 in., which were supported by four No. 3 (M10) bars at the corners.

The second set of specimens (Figure 4.3-8 and Figure 4.3-9) was constructed with concrete prisms measuring 8 in. × 8 in. (203 mm × 203 mm) in cross section and with lengths of 18, 24, 30, 36, and 42 in. (457, 610, 762, 914, and 1067 mm). Similar to the first set, the prisms were provided with a reinforcement cage made of No. 3 (M10) 6 in. × 6 in. (152 × 152 mm) square steel stirrups every 6 in., which were supported by four No. 3 (M10) bars at the corners.

The third set of specimens (Figure 4.3-10 and Figure 4.3-11) was constructed with concrete prisms measuring 6 in. × 6 in. (152 mm × 152 mm) in cross section and with lengths of 18, 24, 30, 36, and 42 in. (457, 610, 762, 914, and 1067 mm). This set of specimens was not provided with any additional steel reinforcement.

The 28-day compressive strength of the concrete averaged 9.13, 11.3, and 8.99 ksi (63, 78, and 62 MPa) for the three sets, respectively. After release of the specimens in the first set, the specimen with a concrete prism length of 18 in. (457 mm) showed a slight decrease of the load over time. This decrease in the load was not present in other test specimens (Figure 4.3-7) and indicated a finite slippage of the CFCC strand from the concrete prism. On the other hand, the test specimens in the second set, including the one with a concrete prism length of 18 in. (457 mm), did not experience any force loss after release as shown in Figure 4.3-9. The specimen with a concrete prism length of 18 in. (457 mm) in the third set did experience a prestress loss similar to that of the first set as shown in Figure 4.3-11.

The test results appear to indicate that a length of 18 in. (457 mm) may or may not be sufficient to transfer a prestressing force of 53 kip (236 KN), depending on the strength of the concrete. The following prism length of 24 in. (610 mm) seems adequate for transferring this level of prestressing force. This length is approximately 35 times the diameter of the strand. On the other hand, the size of the concrete prism and the presence of reinforcement did not seem to have an impact on the test results. This can be attributed to the large size of the prisms with regard to the prestressing force level. For instance, the third set of specimens with prism cross section of 6 in. $\times$ 6 in. (152 mm $\times$ 152 mm) sustained a compressive stress at release of approximately 1.4 ksi (10 MPa). This was approximately 20 % of the concrete compressive strength at the time of prestress release and generated a longitudinal compressive strain of approximately -300 $\mu\varepsilon$. Considering a Poisson's ratio of 0.2, the corresponding transverse tensile strain was approximately 61 $\mu\varepsilon$, which was well below the cracking strain of the concrete of approximately 130 $\mu\varepsilon$.
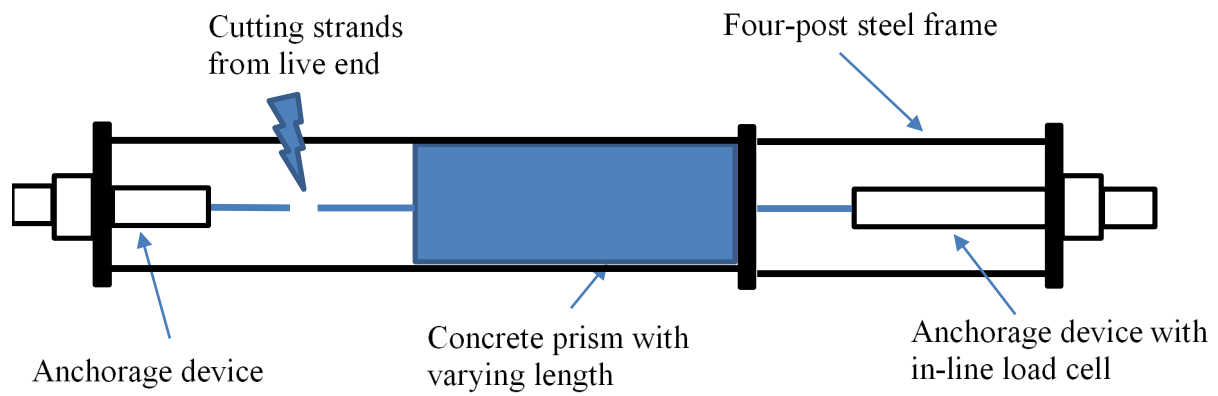
Figure 4.3-1 Establishing transfer length through testing concrete prisms with varying lengths

Figure 4.3-2 CFCC specimens prepared to evaluate the transfer length

Figure 4.3-3 Transfer length frame hosting five specimens at one time

Figure 4.3-4 In-line load cell attached to the end of the CFCC strands

Figure 4.3-5 First set of transfer length specimens prior to concrete pouring, measuring 12 in. ×
12 in. with lengths of 18, 24, 30, 36, and 42 in. (No. 3 steel stirrups every 6 in.)

Figure 4.3-6 Stressing CFCC specimens before pouring the concrete
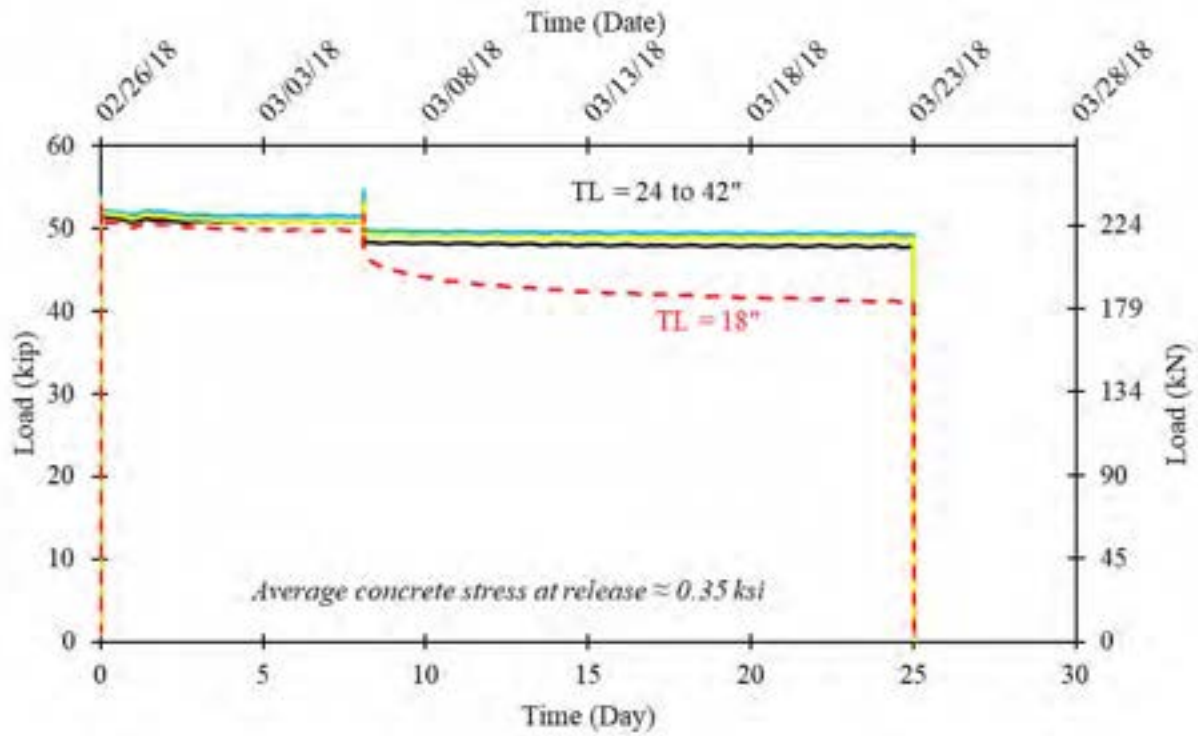
Figure 4.3-7 Monitoring force level in first transfer length set before & after stress release

Figure 4.3-8 Second set of transfer length specimens prior to concrete pouring, measuring 8 in. × 8 in. with lengths of 18, 24, 30, 36, and 42 in. (No. 3 steel stirrups every 6 in.)
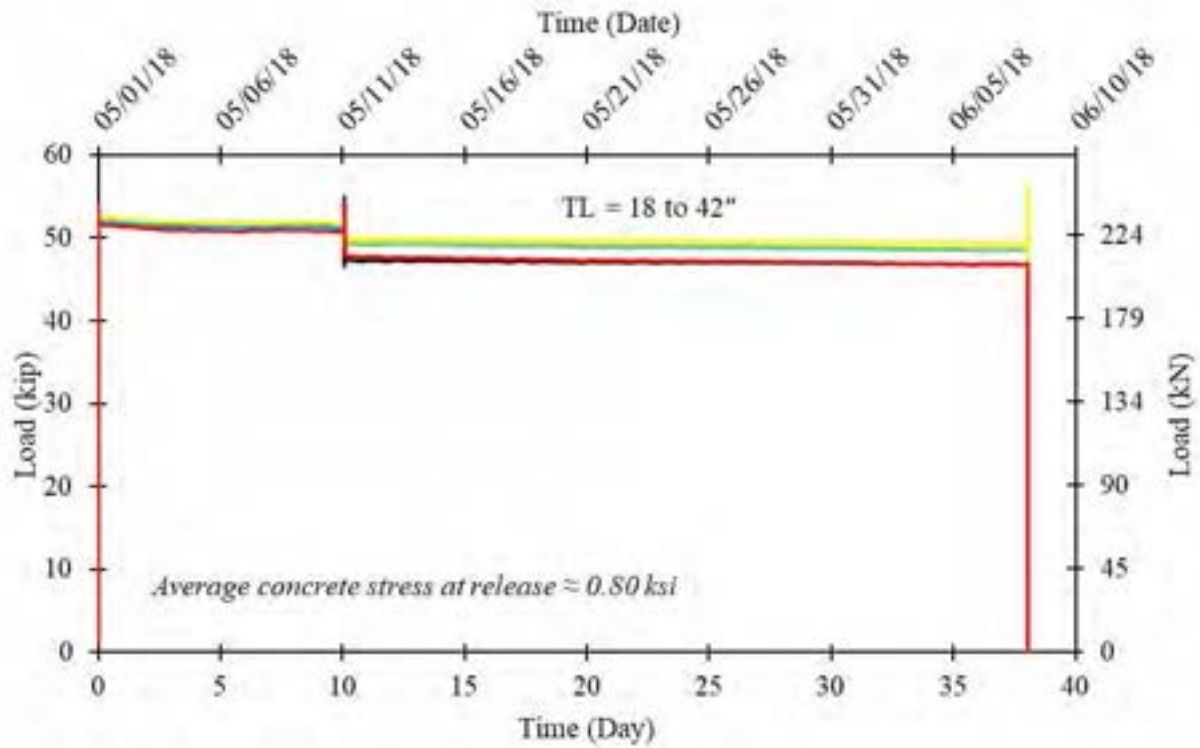
Figure 4.3-9 Monitoring force level in second transfer length set before & after stress release

Figure 4.3-10 Third set of transfer length specimens prior to concrete pouring, measuring 6 in. × 6 in. with lengths of 18, 24, 30, 36, and 42 in. (no steel stirrups)

91
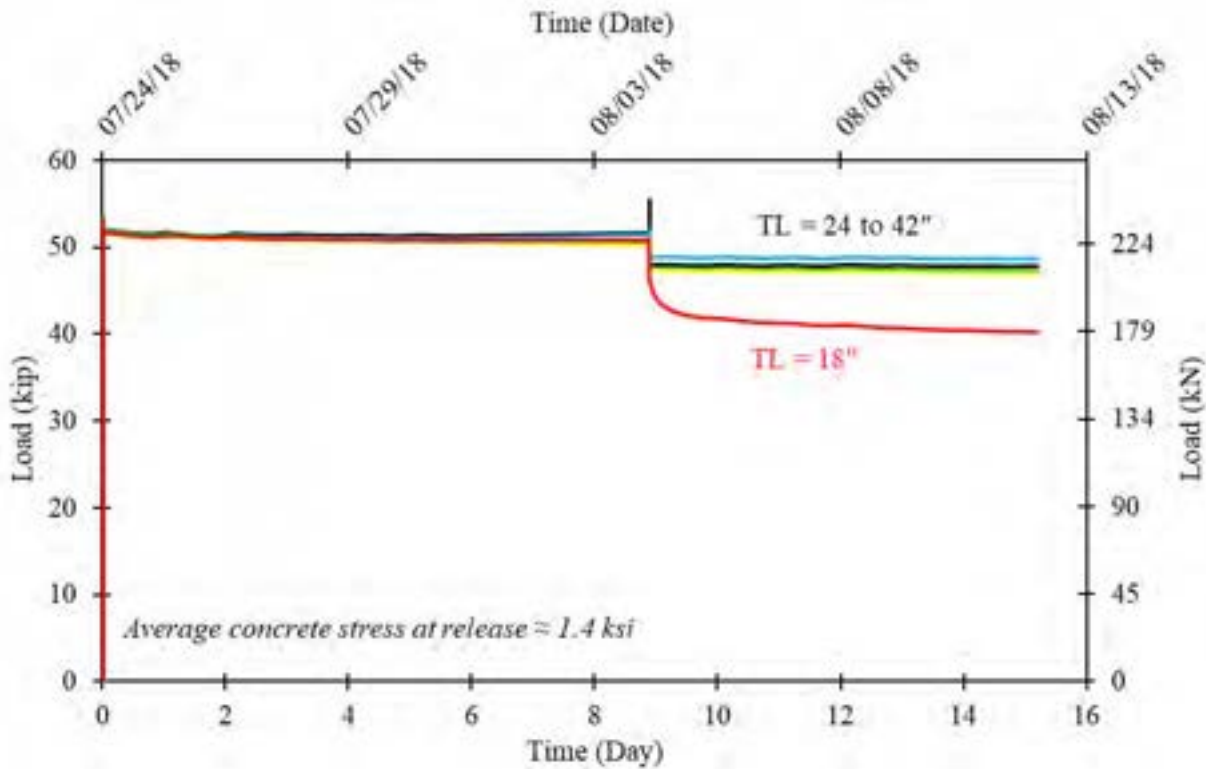
Figure 4.3-11 Monitoring force level in third transfer length set before & after stress release

4.4 Development Length of CFCC Strands

CFCC test specimens were prepared and tested to evaluate the development length of 0.7″ CFCC strands. The test setup for development length was similar to that used to evaluate transfer length with the exception that the CFCC test specimens had a length of approximately 134 in. (3403 mm) and longer concrete prisms were poured around the strands (Figure 4.4-1).

The test sequence started by pulling CFCC strands in custom-made steel frames to a force level of 53 kip (236 kN) and locking the force in the strands using high-strength steel nuts on both ends of the steel frames. After strand prestressing, concrete prisms with different lengths and reinforcement were poured around the strands. After proper curing and after verifying that the concrete strength has achieved 80 % of its 28-day compressive strength, the CFCC strands were released from one end and the force was transferred to the concrete. Then, after 28 days, the CFCC strands were pulled to failure from the other end. Failure took place either by slippage of the strand from the concrete prism or by rupture of the CFCC strand.

92

Construction of the custom-made steel frames and the test specimens is shown in Figure 4.4-2 through Figure 4.4-7. Similar to the transfer length specimens, three sets of test specimens were constructed and tested. The first set of specimens (Figure 4.4-5) was constructed with concrete prisms measuring 12 in. × 12 in. (305 mm × 305 mm) in cross section and with lengths of 18, 24, 36, 48, and 60 in. (457, 610, 914, 1219, and 1524 mm). In addition, the prisms were provided with a reinforcement cage made of No. 3 (M10) 10 in. × 10 in. (254 × 254 mm) square steel stirrups every 6 in., which were supported by four No. 3 (M10) bars at the corners.

The second set of specimens (Figure 4.4-6) was constructed with concrete prisms measuring 8 in. × 8 in. (203 mm × 203 mm) in cross section and with lengths of 24, 30, 36, 42, and 48 in. (610, 762, 914, 1067, and 1219 mm). Similar to the first set, the prisms were provided with a reinforcement cage made of No. 3 (M10) 6 in. × 6 in. (152 × 152 mm) square steel stirrups every 6 in., which were supported by four No. 3 (M10) bars at the corners.

The third set of specimens (Figure 4.4-7) was constructed with concrete prisms measuring 8 in. × 8 in. (203 mm × 203 mm) in cross section and with lengths of 24, 30, 36, 42, and 48 in. (610, 762, 914, 1067, and 1219 mm). This set of specimens was not provided with any reinforcement.

Test results for the development length of the three sets are presented in Table 4.4-1. In addition, Sets 2 and 3 of the transfer length specimens were also tested for development length and test results are presented in Table 4.4-2 and Table 4.4-3.

Some of the test specimens experienced slippage of the anchorage device due to failure of the high expansive grout (HEM). The rest of the specimens showed failure either by strand pullout from the concrete prism or by rupture of the strand before pullout. Due to the high strength of the second set of specimens, strand rupture was the mode of failure with a development length of 42 and 48 in. (1067 and 1219 mm). On the other hand, as concrete strength dropped in the third set of test specimens, the mode of failure of the 42 and 48 in. (1067 and 1219-mm) specimens changed from strand rupture to concrete pullout. Similar trends of pullout failure were observed in Sets 2 and 3 of the transfer length specimens. In addition, it appears that the relationship between the bond strength and the bond length is not linear. Based on the pullout loads, the bond strength per unit length seems to decrease with the increase in the bond length.

Based on the test results, a length of 48 in. (1219 mm) appears to be the minimum lower bound for development length. However, it should be stated that this test setup does not simulate the concrete state in bridge beams. For instance, the concrete in this test setup was subjected to compression, while the strand was subjected to tension. In real beam scenario, both the concrete and the strand would be subjected to tension and this is unfavorable for the bond between CFCC and concrete. Consequently, the test results of this test should be interpreted along with other test results presented in this report to evaluate the development length of 0.7″ CFCC strands.
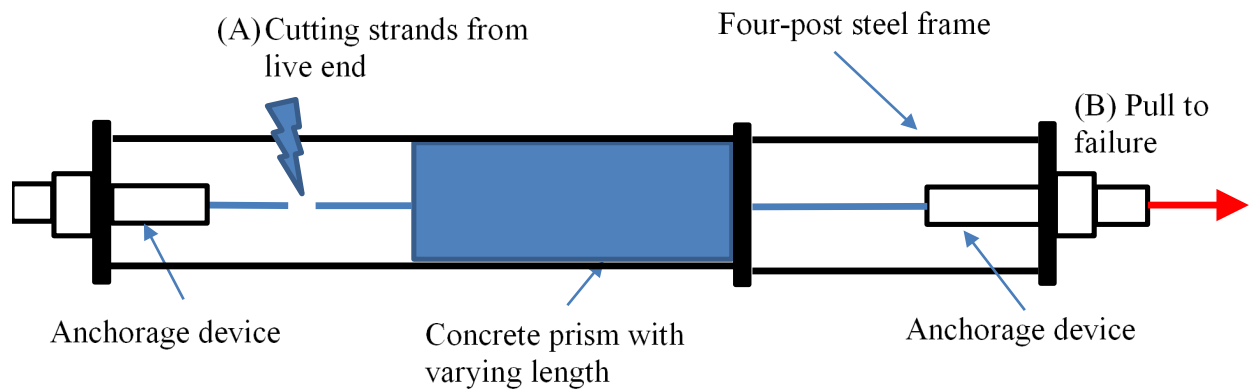
Figure 4.4-1 Development length test setup for concrete prisms with varying lengths

Figure 4.4-2 Constructing steel frames for transfer and development length evaluation

Figure 4.4-3 Development length frame for a single CFCC specimen

Figure 4.4-4 Development length frame showing access holes for the CFCC strand

Figure 4.4-5 First set of development length specimens, measuring 12 in. × 12 in. with lengths of 18, 24, 36, 48, and 60 in. (No. 3 steel stirrups every 6 in.), prior to pouring concrete

Figure 4.4-6 Second set of development length specimens, measuring 8 in. × 8 in. with lengths of 24, 30, 36, 42, and 48 in. (No. 3 steel stirrups every 6 in.), prior to pouring concrete

Figure 4.4-7 Third set of development length specimens, measuring 8 in. × 8 in. with lengths of 24, 30, 36, 42, and 48 in. (no steel stirrups and after pouring concrete)

Table 4.4-1 Summary of test results of three sets of development length specimens

Set	Cross sectional dimension (in²)	Length (in.)	28-day Conc. Comp. Strength (ksi)	Failure load (kip)	Type of failure	Average bond strength (kip/in.)
# 1	12 × 12 w/stirrups	18	9.13	58.35	Pullout	3.24
		24		75.04	HEM failure	--
		36		94.09	Pullout	2.61
		48		93.47	HEM failure	--
		60		98.49	HEM failure	--
# 2	8 × 8 w/stirrups	24	11.30	79.87	Pullout	3.32
		30		94.67	Pullout	3.16
		36		107.71	Pullout	2.99
		42		115.70	CFCC rupture	--
		48		113.80	CFCC rupture	--
# 3	8 × 8 No stirrups	24	8.99	64.81	Pullout	2.70
		30		77.36	Pullout	2.58
		36		87.37	Pullout	2.42
		42		100.59	Pullout	2.40
		48		107.59	Pullout	2.24

Table 4.4-2 Development length test results of transfer length specimens Set 2

Batch	Cross sectional dimension (in^2)	Length (in.)	28-day Conc. Comp. Strength (ksi)	Failure load (kip)	Type of failure	Average bond strength (kip/in.)
# 2	8 × 8 w/stirrups	18	11.3	61.85	Pullout	3.43
		24		76.63	Pullout	3.19
		30		96.25	Pullout	3.21
		36		103.54	Pullout	2.87
		42		96.80	HEM failure	--

Table 4.4-3 Development length test results of transfer length specimens Set 3

Batch	Cross sectional dimension (in^2)	Length (in.)	28-day Conc. Comp. Strength (ksi)	Failure load (kip)	Type of failure	Average bond strength (kip/in.)
# 3	6 × 6 No stirrups	18	8.99	48.65	Pullout	2.70
		24		70.85	Pullout	2.95
		30		82.95	Pullout	2.77
		36		92.78	Pullout	2.58
		42		100.76	Pullout	2.40

4.5 Summary

From pulling different strand specimens with a bond length of 3.5 in. (89 mm) from uncracked concrete with an average 28-day compressive strength of 8.66 ksi (60 MPa), the average pullout strength of 0.7″ CFCC strands was approximately 12.29 kip (55 kN), which was slightly less than the pullout strength of 0.6″ CFCC (13.14 kip or 58 kN). On the other hand, the pullout strengths of 0.6″ and 0.7″ steel strands averaged at 6.28 and 9.30 kip (28 and 41 kN), respectively. However, a difference in the bond mechanism was noted when comparing CFCC to steel specimens. The bond between CFCC strands and concrete is achieved mainly through adhesion between concrete and the surface of the strand. On the other hand, bond between steel strands and concrete seems to develop due to the locking interaction between the twisted strands and the surrounding concrete. This was evident from the significantly larger slippage in the case of steel strands. Due to the

difference in the bond mechanism, bond lengths longer than 3.5 in. (89 mm) could yield different bond strength ratios when comparing steel to CFCC strands.

The transfer length of 0.7″ CFCC strands with an initial prestressing force of 53 kip (236 kN) is nearly 24 in. (610 mm). This is approximately 35 times the diameter of the strand. In addition, the pullout of 0.7″ CFCC strands from concrete prisms with different bond lengths and concrete strengths showed a full development of 0.7″ CFCC strands at approximately 42 in. (1067 mm) of bond length. However, this length is influenced by different factors such as the compressive strength of the concrete and the state of stress in the concrete surrounding the prestressing strands. In addition, the size of the prism and the presence of lateral confinement appeared to enhance the development of the strands by shortening the required development length. It should be noted that typical flexural loading of prestressed beams results in tensile stress in the concrete at the level of the prestressing strands, while in the current test setup, the concrete was under compression. Therefore, results from pullout test shall be further evaluated in view of other test results to establish the proper development length.

CHAPTER 5: FULL-SCALE BEAM TESTING

5.1 Introduction

To evaluate the performance of 0.7″ CFCC strands in large-scale prestressed concrete bridge beams, three full-scale AASHTO I-beams were constructed, instrumented, and tested to failure under a flexural test setup. All beams had a span of 40 ft (12.2 m), a depth of 28 in. (711 mm), and were provided with a 9.0 in. (229 mm) thick steel reinforced composite deck slab with a width of 42 in. (107 cm). The three beams were prestressed with different prestressing materials; one with 0.6″ low-relaxation steel strands, one with 0.6″ CFCC strands, and one with 0.7″ CFRP strands. All three beams were designed according to AASHTO LRFD Bridge Design Specifications (AASHTO 2017) to resist the same level of service and factored loads. The load-deflection response, bond behavior, flexural performance, and energy absorption quantities of the three beams were evaluated and compared to each other. Furthermore, the reserve load capacity of the three beams, in comparison to their design load, was estimated and investigated in terms of overall safety factors. In addition to the three AASHTO I-beams, a full-scale 40 ft (12.2 m) long bulb T beam was designed, constructed and tested to failure. The results of the flexural tests provided guidance and construction specifications for 0.7″ CFRP strands and identified fabrication concerns with the larger diameter strands. The design procedure involving various design considerations, test methodology and results are presented in this chapter.

5.2 Beam Design

Each of the three beams was designed as a composite section composed of precast prestressed AASHTO Type I-beam with a cast-in-place reinforced concrete deck. This type of cross-section conforms to Type K, as described by AASHTO LRFD Table 4.6.2.2.1-1 (AASHTO 2017). Based on this criterion, a 40 ft (12.2 m) long simply supported I-beam with 28 in. (711 mm) height was selected (Figure 5.2-1).

To estimate the required number of prestressing strands in each beam, the beams were designed as part of an actual bridge superstructure subjected to loads and distribution factors according to AASTHO LRFD design specifications (AASHTO 2017). The bridge superstructure is composed of eight prestressed concrete I-beams supporting a 9 in. (230 mm) thick cast-in-place reinforced concrete deck slab. The total width of the bridge deck is 28 ft (8.5 m), with a clear roadway width

of 25 ft (7.6 m). The beams are equally spaced at 3.5 ft (1.1 m) and braced with a single steel intermediate diaphragm located at the midspan of each beam and cast-in-place diaphragms at the beam ends. The bridge accommodates two design traffic lanes with a single lane width of 12 ft (3.66 m). The effective width of the deck slab was determined per AASHTO LRFD specifications as 42 in. (1067 mm). This length is equal to the center-to-center spacing of the prestressed I-beams.
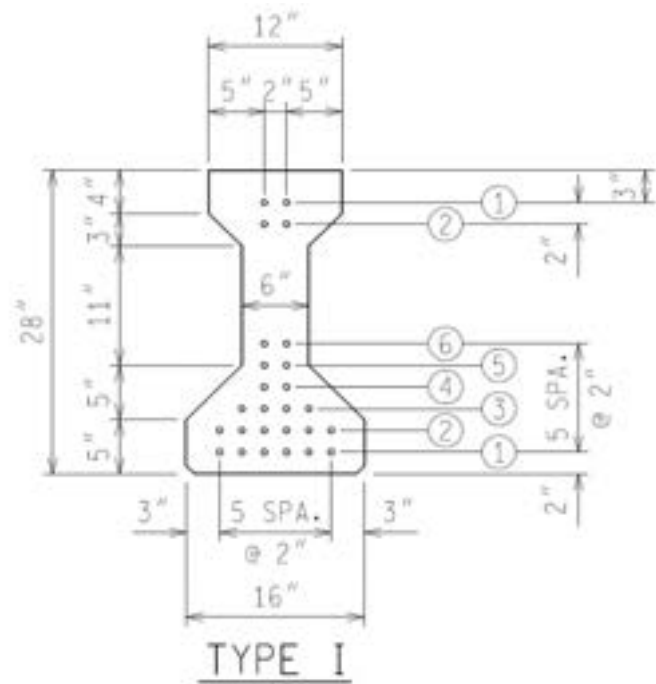
Figure 5.2-1 Cross-section details of AASHTO Type-I Beam

The design dead loads acting on the bridge beam included the self-weight of beam section, deck slab, and diaphragms. The superimposed dead load included wearing surface, sidewalk, stay-in-place forms and bridge barriers that were calculated according to MDOT Bridge Design Guidelines. The live loads were a combination of a standard HL-93 design truck per AASHTO LRFD or a design tandem of 60 kip (266.9 kN) point loads per MDOT Design Guidelines with a design lane load of 640 lb/ft (9.3 kN/m). In addition, a dynamic load allowance factor of 1.33 was applied to all vehicular live loads.

The Service Limit State was the governing state in establishing the number of strands based on the required level of prestressing force. The beams were designed to have no tension in the bottom flange under Service Limit State. Nominal moment capacity was estimated based on force

equilibrium and strain compatibility of the section. The beam section was analyzed as a T-section with the neutral axis located within the reinforced concrete deck slab.

The three beams were designed to fail in tension due to either rupture of CFCC strands or yielding of prestressing steel strands. To achieve the tension failure, the first beam, C0.7, was designed and constructed with five 0.7″ CFCC prestressing strands, all placed in the bottommost row. In addition, two 0.7″ non-prestressed CFCC strands were provided in the second row. All strands were arranged with 2 in. (51 mm) center-to-center spacing in all directions. Figure 5.2-2(a) shows the cross-section details of Beam C0.7.

Each of the five 0.7″ CFCC strands was prestressed with an initial jacking force of 53 kip (235.8 kN). This stress level corresponds to 75 % of the material guaranteed tensile strength (78.7 kip or 350 kN) after allowance is made for an environmental correction factor of 0.9 according to ACI 440.1R-15 (ACI 2015). To avoid excessive tensile stresses at the beam ends after prestress transfer, one of the CFCC strands in the bottom row was debonded for 10 ft (3 m) at the ends. In addition, the top flange of the beam section was reinforced with two 0.7″ non-prestressed CFCC strands to arrest any unforeseen tensile stresses and to serve as a stirrup hanger.

The second beam, Beam C0.6, was designed with seven 0.6″ CFCC prestressing strands where five CFCC strands were placed in the first (bottommost) row with 2 in. (51 mm) concrete cover. The remaining two CFCC strands were placed in the second row with a 4 in. (102 mm) distance from the bottom face of the beam. Furthermore, the second row has one additional non-prestressed CFCC strand of 0.6″ to satisfy the requirement for an under-reinforced section. All strands were located using a 2 in. (51 mm) spacing in all directions. The top flange was provided with two 0.6″ non-prestressed CFCC strands. Similar to Beam C0.7, two of the prestressed CFCC strands in the bottom row of Beam C0.6 were debonded for 10 ft (3 m) at the ends. Each of the seven 0.6″ CFCC prestressing strands was pulled to an initial jacking force of 41 kip (182.5 kN), which corresponds to 75% of the material guaranteed tensile strength (60.7 kip or 270 kN) multiplied by an environmental correction factor of 0.9. The cross-section details of Beam C0.6 is shown in Figure 5.2-2(b).

The third beam, Beam S0.6, was designed with six prestressing Grade 270 low relaxation steel strands of 0.6″ (15.2 mm) diameter. Five prestressed strands were placed in the first (bottommost) row, whereas the last prestressed strand was placed in the second row with two additional No. 5

(M16) Grade 60 steel rebars. The top flange of Beam S0.6 was reinforced with two No. 5 (M16) Grade 60 steel rebars. Figure 5.2-2(c) shows the cross-section details of Beam S0.6. The middle prestressing strand on the first row was debonded for 10 ft (3 m) at each end to avoid excessive tensile stresses. Similar to Beam C0.6 and C0.7, the center-to-center spacing in each direction for all the strands in Beam S0.6 was maintained at 2 in. (51 mm). Each of the six 0.6″ low relaxation steel prestressing strands was pulled to an initial jacking force of 44 kip (195.8 kN), which corresponds to 75% of the material ultimate tensile capacity (58.6 kip or 261 kN). This is the maximum force permitted by AASHTO LRFD design criteria in low relaxation strands immediately prior to transfer.

The transverse reinforcement for all three beams was assembled from No. 3 (M10) Grade 60 deformed steel bars with center-to-center spacing of 2.0 in. (51 mm) at the beam end diaphragms and 4.0 in. (102 mm) through the rest of the span. The deck reinforcement consisted of a bottom mesh, assembled from four No.5 (M16) longitudinal bars and No. 3 (M10) transverse bars, and a top mesh assembled from five No.5 (M16) bars and No. 3 (M10) transverse bars. The transverse deck reinforcement followed the spacing of the stirrups. Figure 5.2-3 shows a longitudinal section of the AASHTO I-beams with the shear and deck reinforcement configurations. The properties of the prestressing strands used in this experimental investigation are presented in Table 5.2-1, Table 5.2-2, and Table 5.2-3 for 0.7″ CFCC prestressing strands, 0.6″ CFCC prestressing strands and 0.6″ low relaxation prestressing steel strands, respectively.

The design factored load was analytically calculated by estimating the theoretical nominal capacity of each beam and multiplying this nominal capacity by the appropriate strength reduction factor to estimate the resistance moment capacity. A strength reduction factor of 0.85 (ACI 2004) was implemented in the design of CFRP-prestressed beams (C0.7 and C0.6) assuming tension failure, while Beam S0.6 was designed with a strength reduction factor of 1.0 (AASHTO 2017). The moment capacities were estimated as 1004, 1098 and 1114 kip.ft (1361, 1489 and 1510 kN.m) for Beams C0.7, C0.6 and S0.6, respectively, which corresponded to design factored loads of 99.4, 110 and 112 kip (442, 490 and 499 kN), respectively, after deducting the moment due to the self-weigh of the beams.
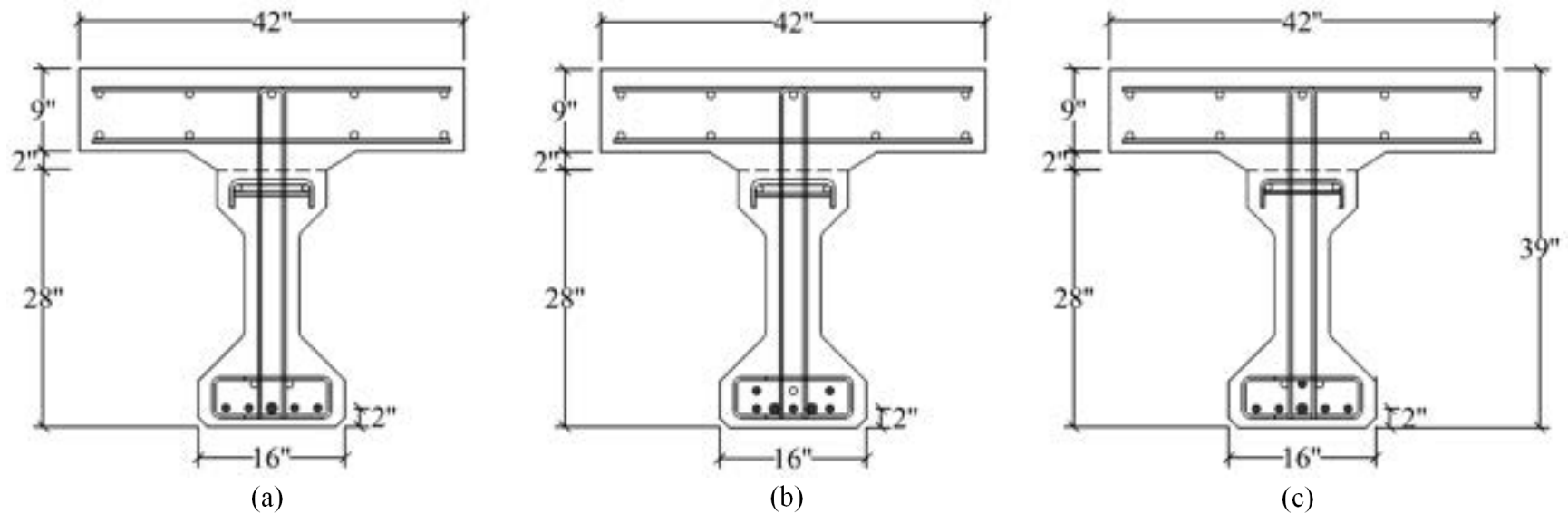
Figure 5.2-2 Cross-section details of AASHTO I-beams; (a) Beam C0.7, (b) Beam C0.6, (c) Beam S0.6 (1 in. = 25.4 mm)
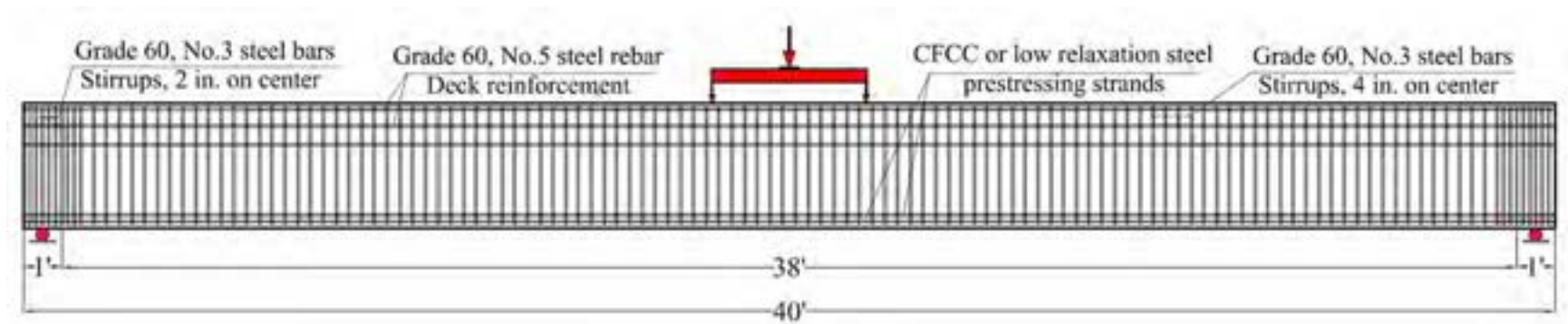
Figure 5.2-3 Elevational view shows the internal reinforcement configuration of AASHTO I-Beam (1 in. = 25.4 mm)

105

Table 5.2-1 Properties of 0.7″ CFCC Prestressing strand

Strand Configuration	1×7
Diameter, in. (mm)	0.7 (17.26)
Guaranteed breaking load, kip (kN)	78.7 (350)
Cross-sectional area, in.^{2} (mm^2)	0.234 (151.1)
Max. breaking load, kip (kN)	107.1 (476.3)
Min. breaking load, kip (kN)	104.1 (463.1)
Tensile strength, ksi (GPa)	451.1 (3.11)
Tensile modulus, ksi (GPa)	22626 (156)
Elongation, %	2.0

Table 5.2-2 Properties of 0.6″ CFCC Prestressing strand

Strand Configuration	1×7
Diameter, in. (mm)	0.6 (15.2)
Guaranteed breaking load, kip (kN)	60.7 (270)
CIMR Tensile Capacity, kip (kN)	113.9 (506.7)
Cross-sectional area, in.^{2} (mm^2)	(0.179) 115.6
Max. breaking load, kip (kN)	78.7 (350)
Min. breaking load, kip (kN)	72.8 (324)
Tensile strength, ksi (GPa)	425.0 (2.93)
Tensile modulus, ksi (GPa)	21611 (149)
Elongation, %	2.0

Table 5.2-3 Properties of 0.6″ low relaxation steel prestressing strand

Strand Configuration	1×7
Diameter, in. (mm)	0.6 (15.24)
Breaking Load, kip (kN)	58.6 (260.6 kN)
Nominal area, in.^{2} (mm^2)	0.217 (140)
Breaking load, kip (kN)	60.6 (269.7)
Tensile strength, ksi (GPa)	451.1 (3.11)
Modulus of elasticity, ksi (GPa)	28400 (195.8)
Ultimate elongation, %	5.43

5.3 Beam Construction

5.3.1 Construction of I-beam Sections

The construction of the I-beam sections started by setting up the formwork and assembling the reinforcement cages from the steel stirrups and the non-prestressed reinforcement. After reinforcement cages were completed, they were moved to the platform decking, where prestressing strands were passed through the cages, as shown in Figure 5.3-1. Steel prestressing strands were tensioned using conventional wedge-anchoring devices, while special coupler devices were used to connect prestressing CFCC strands with steel strands at both the live and dead ends (Figure 5.3-2). Consequently, prestressing of CFCC strands was executed by tensioning the steel strands at the live end of the prestressing bed. In-line load cells were attached to the dead end of the prestressing strands to monitor the prestressing force (Figure 5.3-2).

Placing of concrete took place one day after prestressing (Figure 5.3-3) using ready-mix concrete designed to achieve a 28-day compressive strength of 7 ksi (48 MPa). This concrete mix is a standard concrete mix used in highway bridge beams in Michigan in accordance with the Michigan Department of Transportation (MDOT). It should be noted that the same concrete mix design from the same supplier was used to build the three beams. However, due to space availability and schedule constraints, the beams were not built simultaneously. Instead, they were built using two concrete batches and concrete cylinders were prepared from each batch to evaluate the concrete uniaxial compressive strength following ASTM C39/C39M-20 (ASTM 2020). Results from uniaxial concrete compressive strength tests are shown in Figure 5.3-4 and Figure 5.3-5. The two concrete batches exceeded their design strength. Nevertheless, they achieved slightly different strengths. The design of the beams was verified using the actual concrete strength.

After concrete casting, the beams were covered with wet burlap and plastic sheets for curing (Figure 5.3-6(a)). Prestressing strands were released after the concrete achieved 80 % of its design compressive strength, which is equal to 5.6 ksi (38 MPa) and determined from the cylinder testing. Prestress release took place by torch cutting the steel strands on the live end (Figure 5.3-6(b)). Cutting of the strands was performed in a symmetrical order with respect to the beam centerline to limit inducing unforeseen stress in the beams. After prestress release, the entire beam surfaces were examined for any cracks that could jeopardize concrete integrity. No major cracks were

observed at the top or bottom flanges of the I-beams. However, minor local cracks were observed near the perimeter of the prestressing strands at the end faces of Beam C0.6 (Figure 5.3-7).
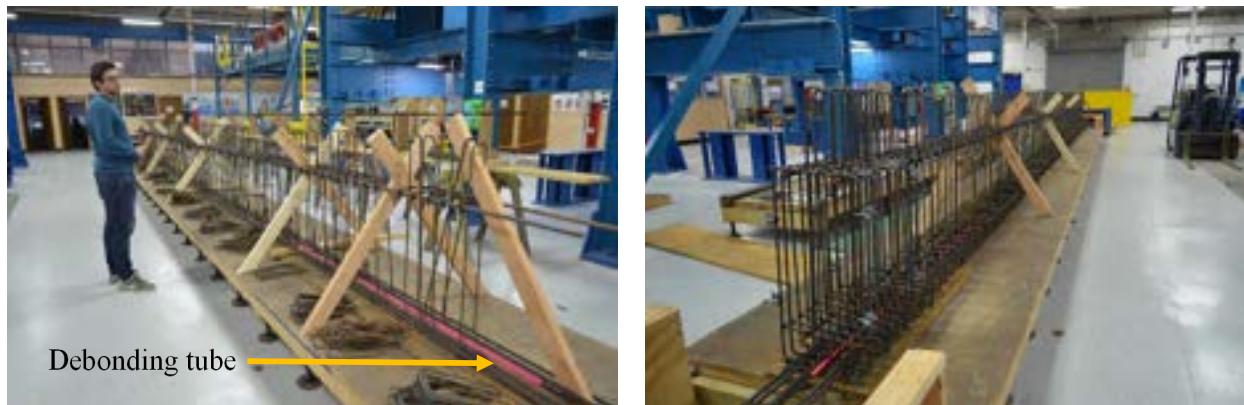
Figure 5.3-1 Assembling the reinforcement cage and passing CFCC through the cage

Figure 5.3-2 Live and dead-end anchorage set-up with load cells attached to the dead end

Figure 5.3-3 Concrete casting of AASHTO I beams
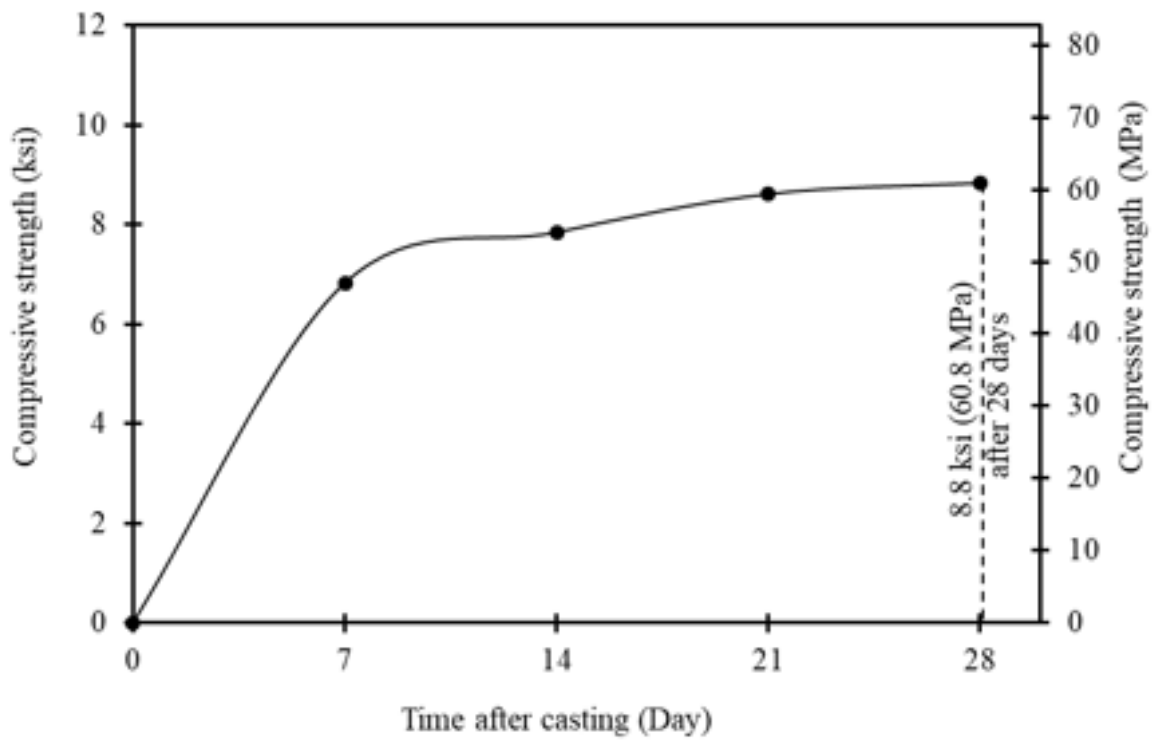
Figure 5.3-4 Concrete compressive strength test results for Beams C0.7 and C0.6
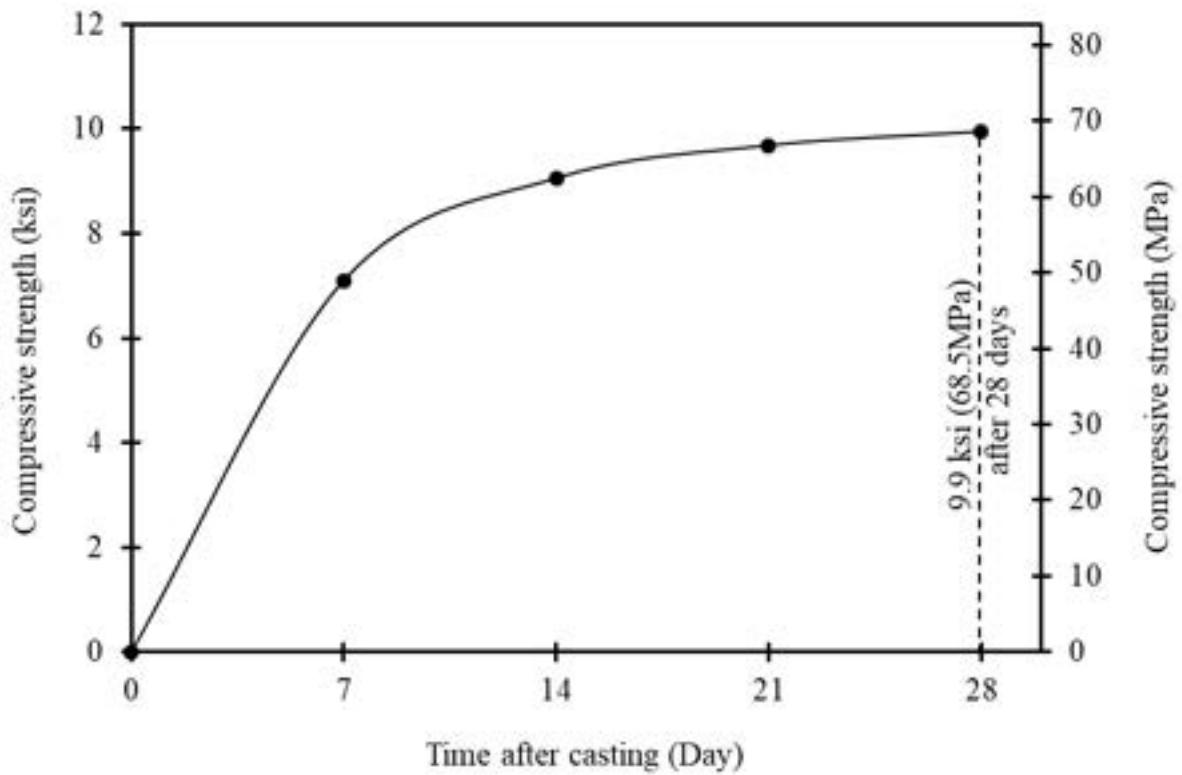
Figure 5.3-5 Concrete compressive strength test results for Beam S0.6

109
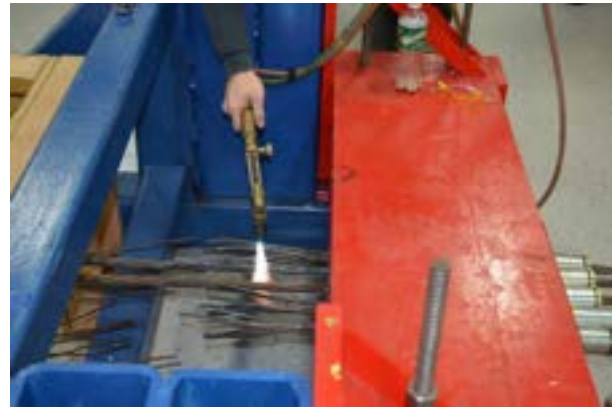
(a)   (b)

Figure 5.3-6 Curing and prestress release of the strands; (a) covering beam with wet burlap, (b) using acetylene torch for cutting CFCC strands

Figure 5.3-7 Completed Beam C0.6 after prestress transfer with minor cracks at the beam end

5.3.2 Construction of Deck Slab

After the construction of the three I-beams was complete, the beams were moved and placed side-by-side with 47 in. (1194 mm) center-to-center spacing between them to accommodate the formwork of the deck slab (Figure 5.3-8). The formwork was made of wooden walls surrounding the perimeter of each I-beam and mounted on wooden joists. The deck reinforcement was reinforced with steel rebar longitudinally and deformed steel bars with a 4 in. (102 mm) spacing transversely, as shown in Figure 5.3-9. Special steel chairs of 6.5 in. (165 mm) height were used to support the top mesh of reinforcement. The bottom mesh of reinforcement was supported on 1.25 in. (32 mm) plastic chairs.

The deck slabs of all three beams was cast on the same day using ready-mix concrete designed to achieve a 28-day compressive strength of 4 ksi (27.6 MPa). Before casting the deck sections, a slump test was performed and a slump of 7.0 in. (178 mm) was estimated for the concrete deck material. Concrete cylinders were cast to determine the strength of the concrete deck material over time. Casting, vibrating, screeding, and smoothening of the concrete is shown in Figure 5.3-10. The 28-day compressive strength of the deck section of all three beams was 3.67 ksi (25.3 MPa). This was slightly below the design 28-day concrete compressive strength of 4 ksi (27.6 MPa). After concrete casting, the deck sections were covered with wet burlaps and plastics for proper curing. Figure 5.3-11 shows the completed 0.6" CFCC beam after concrete deforming.

Figure 5.3-8 Building formwork for the deck slab of AASHTO I-beams

Figure 5.3-9 Building the reinforcement cage of the deck slab of AASHTO I-beams

Figure 5.3-10 Casting concrete and finishing concrete surface for deck slabs

Figure 5.3-11 AASHTO I-Beam C0.6 with a cast-in-place slab after construction

5.4 Instrumentation and Test Setup

As shown in Figure 5.4-1, each of the three AASHTO I-beams was tested in a four-point-load test setup and was simply supported over two 2 in. (51 mm) thick elastomeric bearing pads that were positioned on two steel supports. The effective span of the beam was 39 ft (11.9 m), while the distance between the two points of load was 4 ft (1.2 m). It should be mentioned that the load presented herein is the total load that was applied using a 224-kip (1000-kN) MTS hydraulic actuator. The actuator was programmed to apply loading/unloading cycles with a displacement control mode at a rate of 0.05 in./min (1.3 mm/min). Load cycles were performed at load increments of 10 kip (44.5 kN) until a load level of 100 kip (445 kip) was reached. After

completing the 100-kip (445-kN) load cycle, each beam was tested under monotonic loading to failure. The final loading step was force-controlled with a loading rate of 10 kip/min (44.5 kN/min). To support the beams laterally during testing, two steel bracing systems were constructed from HSS tubes and fastened to the loading frame to prevent the beams from tipping over during testing. Figure 5.4-2 shows the construction of the steel braces.

All beams were fully instrumented to measure the applied load, midspan deflection, and concrete strains at different section depths (Figure 5.4-3). The load was measured by a load cell that were built into the hydraulic actuator. Deflection at midspan was measured using two linear motion transducers (LMTs), which were attached to the deck surface. Four electrical strain gages (ESGs) were installed on the deck top surface near the loading points to monitor the concrete compressive strain. In addition, four LVDTs were placed alongside the strain gages on the deck surface to validate the strain gage readings. Furthermore, one strain gage was placed at 4.5 in. (114 mm) from the top deck surface at midspan to monitor the strain at mid-depth of the deck. To capture the strain of the prestressing strands during testing, one LVDT was placed on the concrete at an elevation corresponding to the bottommost layer of the strands. All sensors were calibrated and connected to a computerized data acquisition system that record the load, strains, and deflection data continuously during the test.

Figure 5.4-1 Test setup of full-scale AASHTO I-beams

Figure 5.4-2 Construction of lateral steel bracing system

Figure 5.4-3 Close up view showing the instrumentation for testing of AASHTO I-beams

5.5 Flexural Test Results

5.5.1 Beam C0.7

The service limit state testing of Beam C0.7 included loading the beam until the initiation of the first flexural crack. The first flexural crack was observed at a load level of 48.0 kip (213.5 kN). This was confirmed from the load-deflection curves and the load-strain curves that showed a significant change in the slope at nearly the same load level. At cracking, Beam C0.7 gained a residual deflection of 0.05 in. (1.2 mm). The decompression load was determined from the load-deflection curve at the 90-kip (267-kN) load cycle by estimating precisely the load at which the curve started to deviate from its linear uncracked (pre-compressed) segment. The decompression load was estimated at approximately 43.8 kip (195 kN).

After cracking, the load cycles continued and new cracks developed in the pure moment region and distributed uniformly under the loading spreader. These cracks were visible during the 70-kip (311-kN) load cycle. As the load increased, more vertical cracks developed at the soffit of the beams while inclined cracks were observed outside the loading points towards the supports due to the combined effect of shear and moment. Existing cracks increased in width and extended upwards towards the deck under higher load cycles. Figure 5.5-1 shows the crack pattern of Beam C0.7, which was characterized with a dense crack map before failure. The residual deflection at the end of the 100 kip (444.8 kN) loading cycle was 0.25 in. (6.4 mm).

The load cycle before failure reached 200 kip (890 kN) with a recorded deflection of 8.28 in. (210 mm). Upon unloading, the beam recovered a majority of the deflection with a residual deflection of 1.0 in. (25.4 mm). The failure of Beam C0.7 took place at a load level of 220.4 kip (981 kN) with a corresponding mid-span deflection of 9.9 in. (251.5 mm). The load-deflection curves of Beam C0.7 are shown in Figure 5.5-2. The failure of Beam C0.7 was characterized by rupture of CFCC prestressing strands, as shown in Figure 5.5-3 and Figure 5.5-4. The middle partially debonded prestressed strand slipped prior to the rupture of all the prestressing strands, as shown in Figure 5.5-5. The debonded length of this strand was 10 ft (3 m) with a bonded length of 8 ft (2.44 m), measured from the beginning of concrete bonding to the section of the maximum moment under the loading point.

At failure, no crushing of concrete was observed on the surface of the deck even though flexural cracks extended upward from the soffit into the deck (Figure 5.5-6). However, spalling of huge masses of concrete from the soffit of the beam occurred prior to rupturing of the CFCC prestressing strands. Based on the load-deflection curve from all load cycles including the ultimate load cycle, the total energy absorbed by Beam C0.7 was calculating by estimating the area under the load-deflection curve. According to Figure 5.5-7, the total energy absorbed by Beam C0.7 was approximately 1540 kip.in. (174 kN.m).

Figure 5.5-1 Development of flexural cracks during flexural loading of Beam C0.7
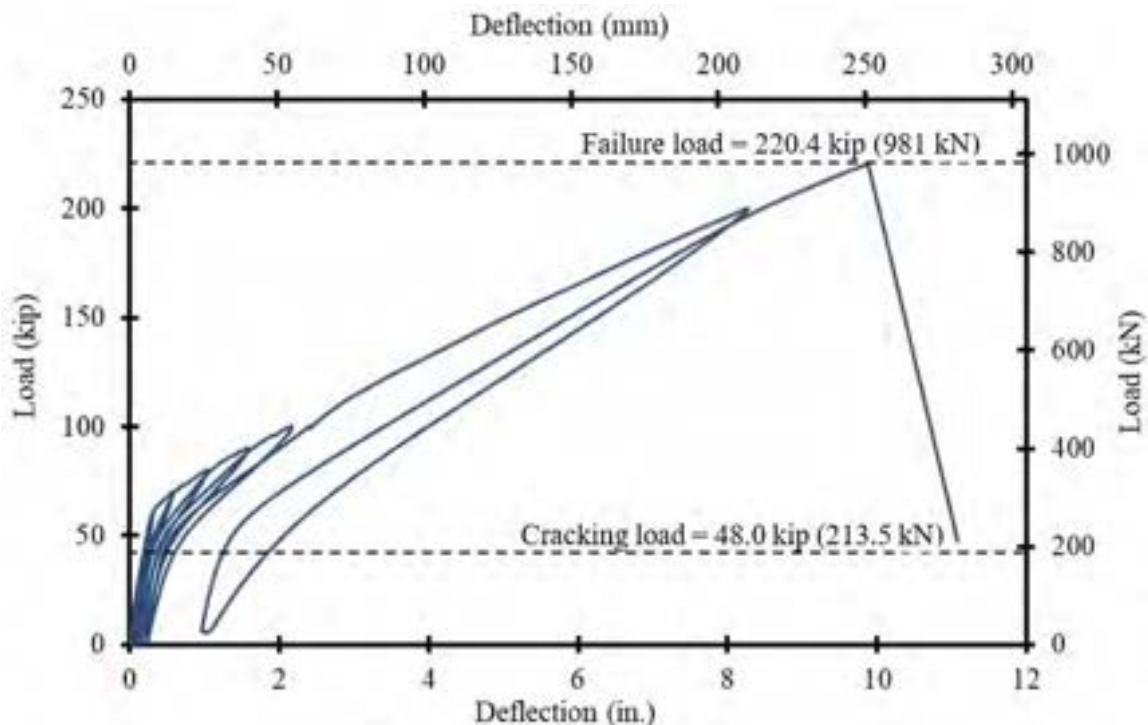
Figure 5.5-2 Load-deflection curves for Beam C0.7

Figure 5.5-3 Tension failure of Beam C0.7

Figure 5.5-4 Rupture of CFCC strands at failure of Beam C0.7

Figure 5.5-5 Slippage of partially debonded CFCC strands prior to failure of Beam C0.7

Figure 5.5-6 Deck surface of Beam C0.7 at failure with no concrete spalling
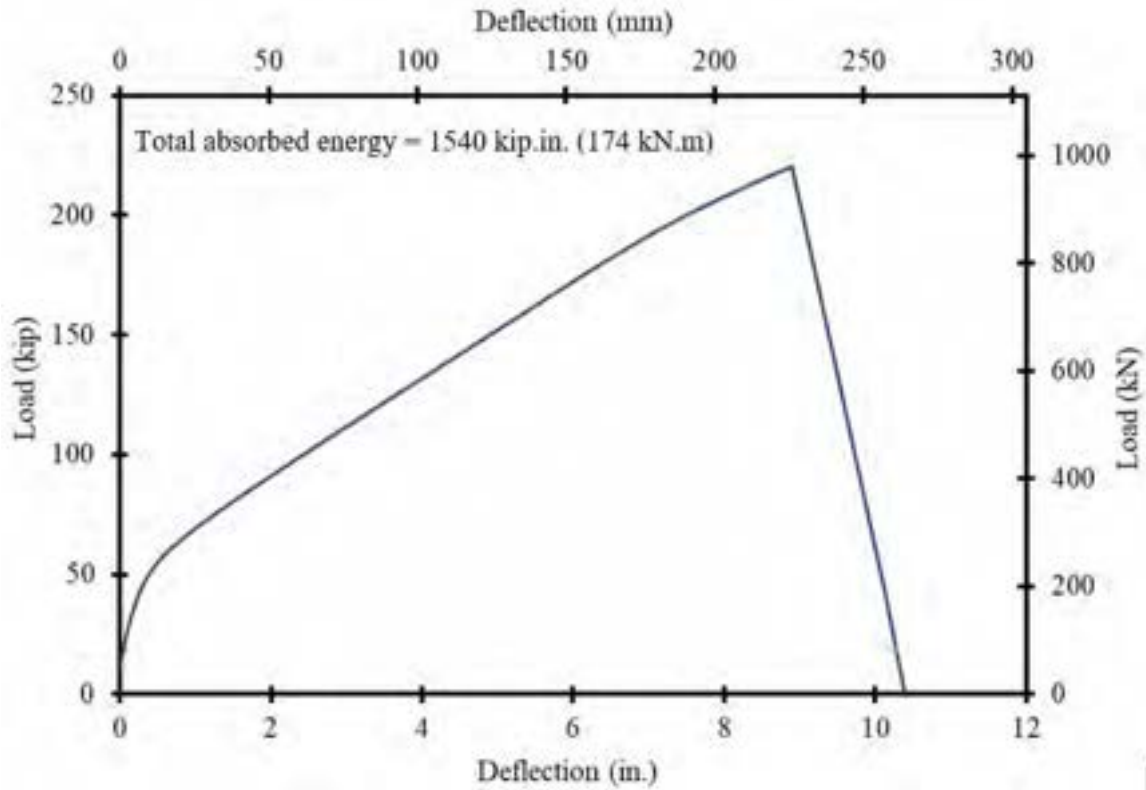
Figure 5.5-7 Energy absorption capacity of Beam C0.7

5.5.2 Beam C0.6

Figure 5.5-8 shows the load-deflection curves obtained from all load cycles carried out on Beam C0.6. Similar to Beam C0.7, mono-slope curves were obtained before cracking, while bilinear curves were obtained after cracking with the decompression load marking the change in the slope. The cracking load was estimated as 48 kip (213.5 kN), while the decompression load was determined as 43.8 kip (195 kN). The last load cycle before the failure cycle reached 100 kip (445 kN) with a corresponding deflection of 2.5 in. (66 mm). After unloading, the residual deflection from all load cycles was approximately 0.24 in. (6.1 mm).

Figure 5.5-9 shows the cracks that occurred in Beam C0.6 at the 100-kip (445-kN) load cycle. Extensive cracks were observed at the soffit of the beam. However, these cracks were not as wide as those formed in Beam C0.7. Flexural cracks developed vertically between the loading points and continued to increase in length and width. In addition, diagonal cracks were observed away from the midspan towards the supports.

119

As the load increased, flexural cracks continued to widen until a complete failure took place at a load level of 190.7 kip (848.6 kN) with a maximum midspan deflection of 8.9 in. (226.1 mm). The failure was characterized by rupture of CFCC prestressing strands accompanied by spalling of concrete at the top surface of the deck slab around the loading spreaders, as shown in Figure 5.5-10 to Figure 5.5-12. The strain gage readings at the deck surface indicated a concrete compressive strain of 2900 µε, which is less than the maximum theoretical compressive strain (3000 µε). This confirms that the failure of Beam C0.6 was designed as an under-reinforced section (tension-controlled). The two partially debonded prestressed strands in the lower row slipped prior to the rupture of the prestressing strands (Figure 5.5-13). These two strands had been debonded for 10 ft (3 m) during construction and at each end of the beams. The bonded length measured from the beginning of concrete bonding to the constant moment region in the beam was 8 ft (2.44 m).

Similar to Beam C0.7, the energy absorbed by Beam C0.6 was estimated by calculating the area under the load-deflection curve (Figure 5.5-14). The total energy absorbed by Beam C0.6 was estimated as 1250 kip.in. (141 kN.m), which is slightly lower than that for Beam C0.7 since Beam C0.7 failed at a higher load with higher deflection.
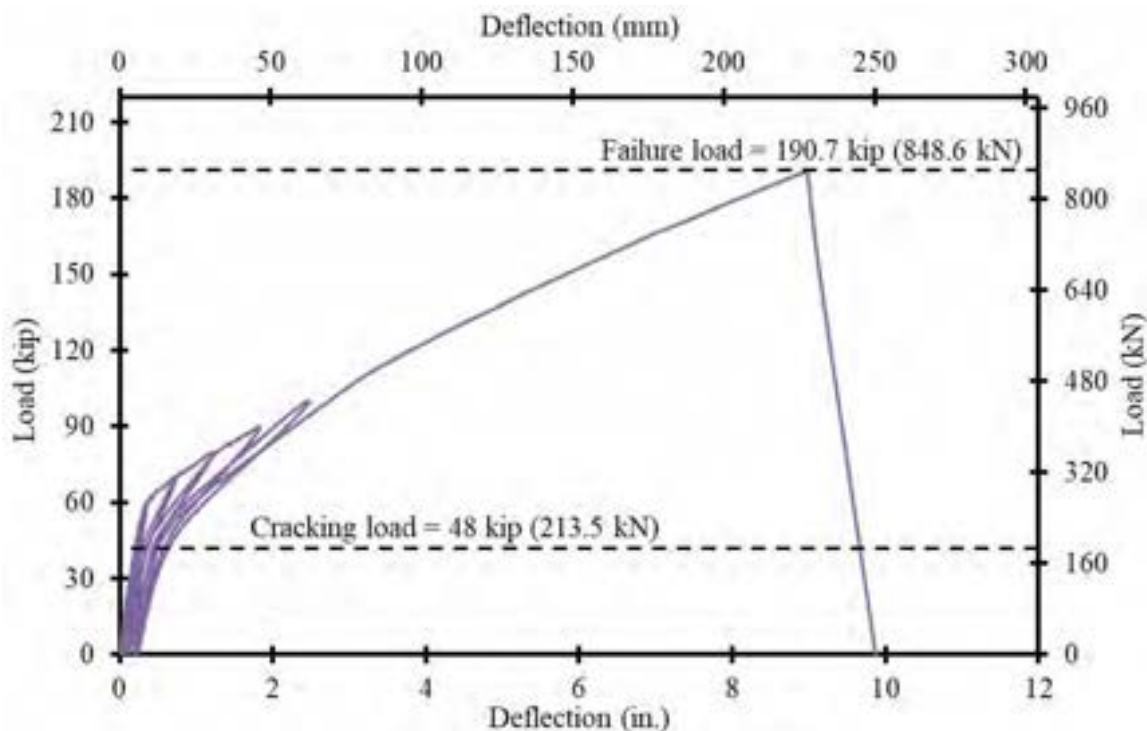
Figure 5.5-8 Load-deflection curves for Beam C0.6

Figure 5.5-9 Development of flexural cracks during flexural loading of Beam C0.6 before failure

Figure 5.5-10 Tension failure of Beam C0.6

Figure 5.5-11 Rupture of CFCC prestressing strands at failure of Beam C0.6

Figure 5.5-12 Spalling of concrete at the top surface of the deck slab at failure of Beam C0.6

Figure 5.5-13 Slippage of partially debonded stands prior to failure of Beam C0.6
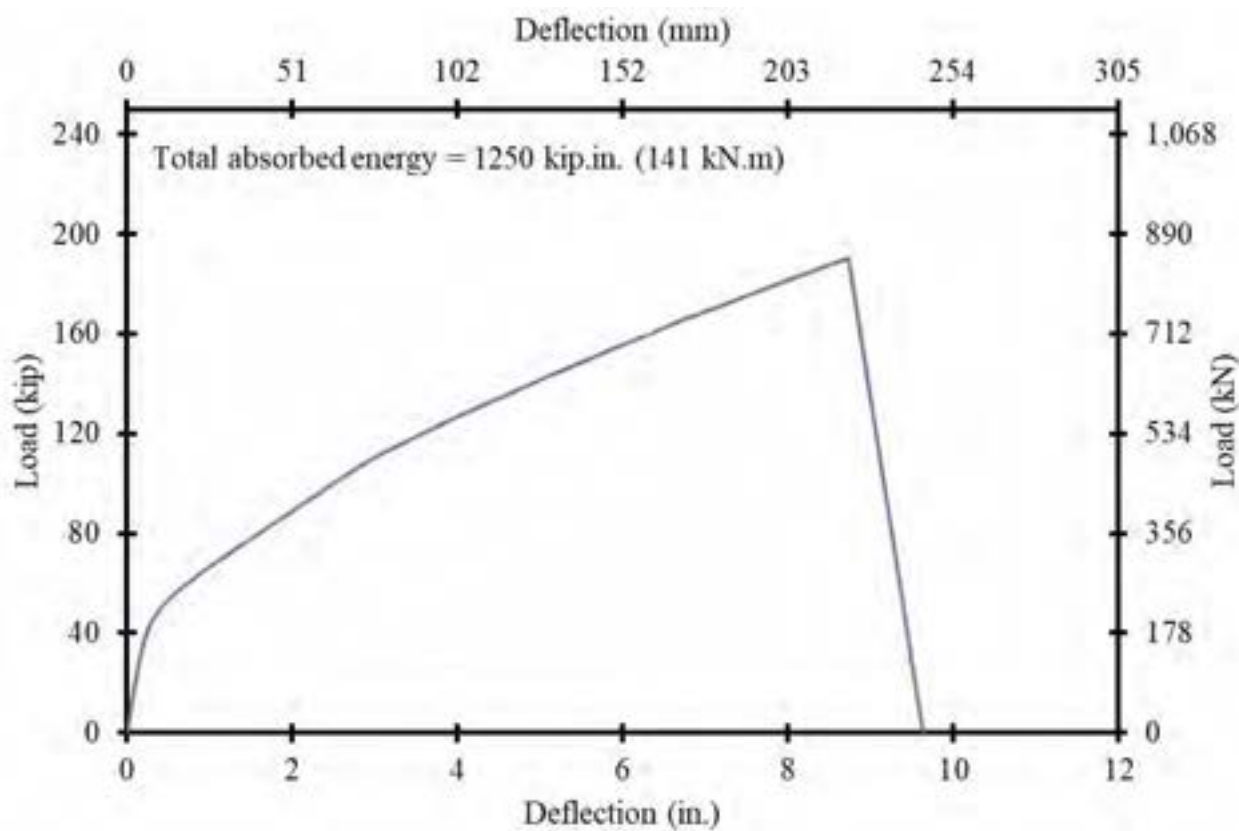
Figure 5.5-14 Energy absorption capacity of Beam C0.6

5.5.3 Beam S0.6

Similar to other beams, Beam S0.6 was tested under four-point loading applied through cycles of loading and unloading. The cracking load and the decompression load were approximately 48 kip and 43.5 kip (213.5 and 193.5 kN), respectively. The last load cycle before failure reached 100 kip (445 kN) with a corresponding deflection of 1.5 in. (38.1 mm). After unloading, the residual deflection was approximately 0.19 in. (4.8 mm). At the 100-kip (445-kN) load cycle, Beam S0.6 experienced extensive flexural cracks as shown in Figure 5.5-15.

During the last load cycle, Beam S0.6 exhibited yielding of steel prestressing strands at a load level of 106 kip (472 kN) with a corresponding deflection of 1.8 in. (45.7 mm), including the residual deflection. After yielding, the deflection of the beam progressed at a faster rate than the applied load. The load-deflection curve of Beam S0.6 is shown in Figure 5.5-16. The slope of the load-deflection curve continued to reduce with an increase in deflection until a maximum load was reached at 132 kip (587 kN) with a corresponding residual deflection of 7.2 in. (183 mm). After the maximum load was reached, the deflection continued to increase followed by successive rupture of all the prestressing strands until the final strand ruptured at a load level of 125 kip (556 kN) with a corresponding deflection of 11.5 in. (292 mm). As shown in Figure 5.5-16, approximately 5.4 in. (137 mm) of deflection occurred between steel yielding and when the maximum load was obtained with a corresponding load increase of approximately 26 kip (115.7 kN). An additional 4.3 in. (109 mm) of deflection occurred from the maximum load to complete failure of the beam.

The failure of Beam S0.6 was characterized by yielding and then rupture of the prestressing steel strands, as shown in Figure 5.5-17 and Figure 5.5-18. Prior to rupture of the strands, the concrete in the top surface of the deck slab crushed and the top reinforcement showed signs of buckling as shown in Figure 5.5-19. At failure, no strand slippage was observed, which is dissimilar from Beams C0.6 and C0.7.

Similar to other beams, the energy absorption capacity was determined from the load-deflection curves of all load cycles (Figure 5.5-20). The total energy absorbed before failure was estimated as 1375 kip.in. (155 kN.m).
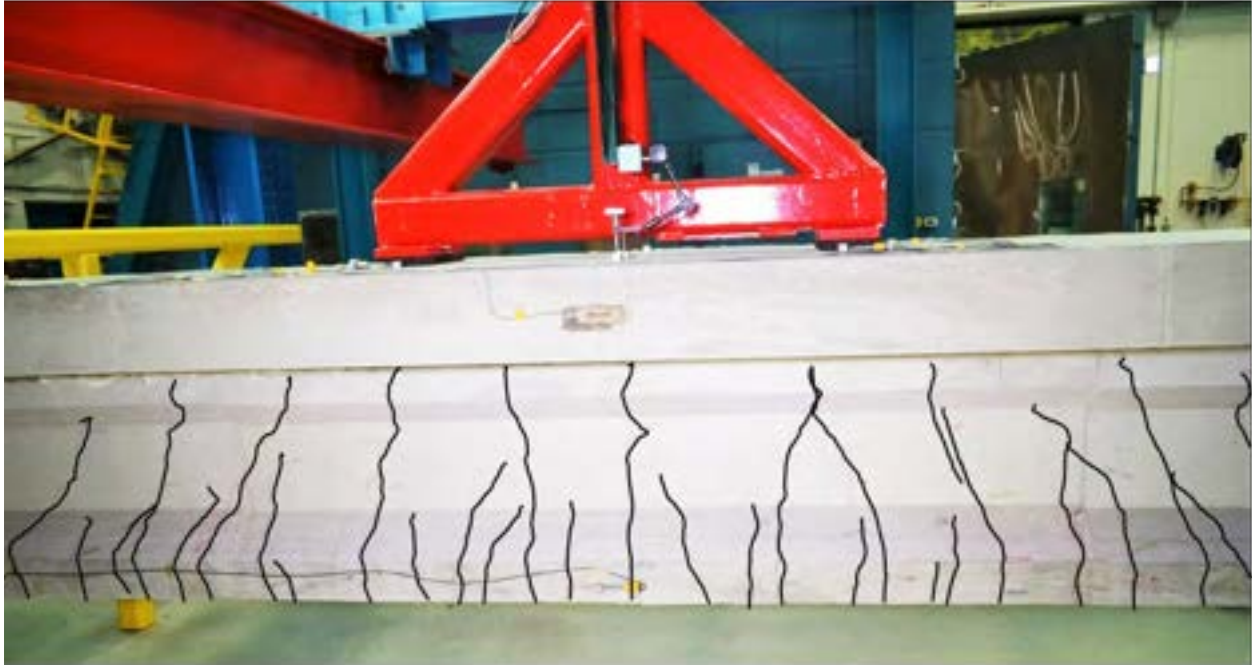
Figure 5.5-15 Development of flexural cracks during flexural loading of Beam S0.7
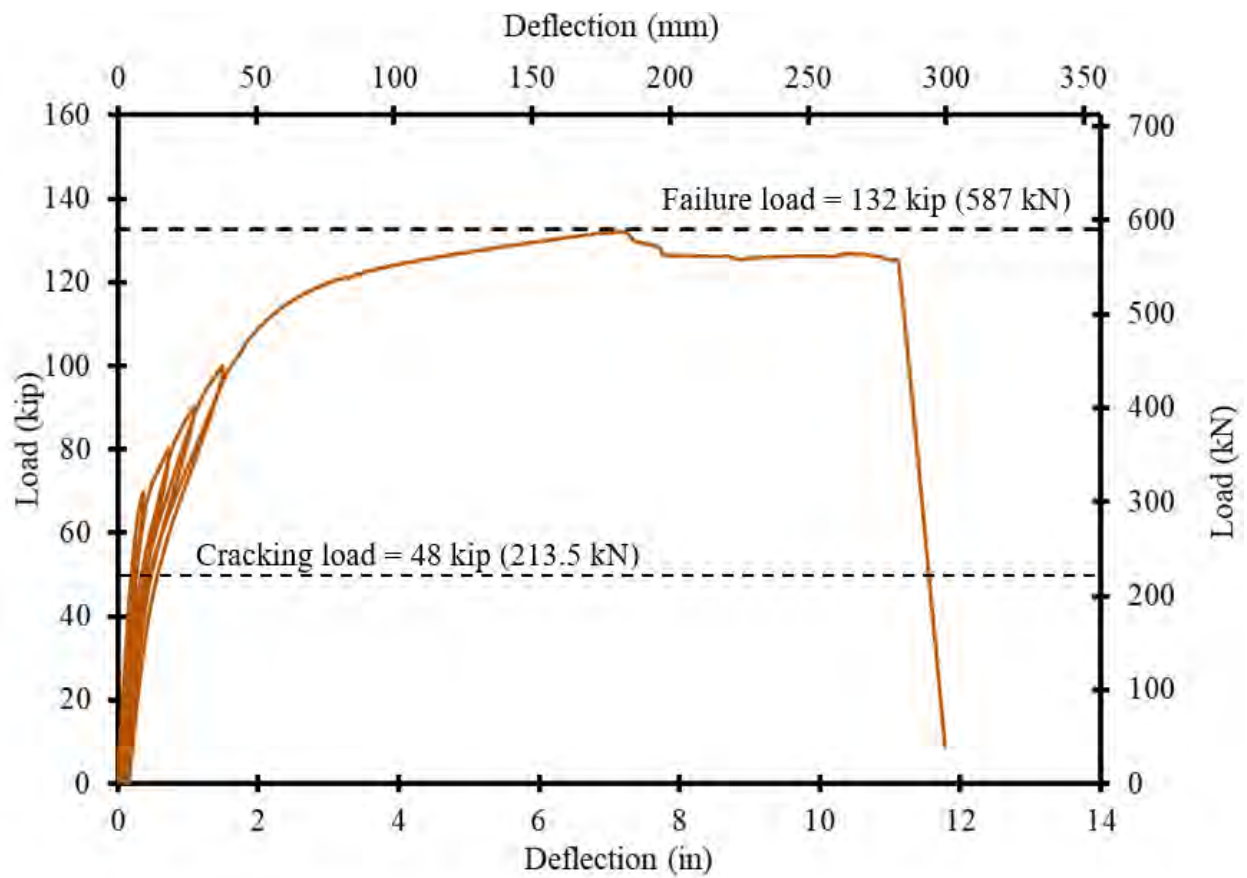
Figure 5.5-16 Load-deflection curves for Beam S0.6

Figure 5.5-17 Failure of Beam S0.6

Figure 5.5-18 Rupture of steel prestressing strands during failure of Beam S0.6

Figure 5.5-19 Buckling of top deck reinforcement at mid-span of Beam S0.6 at failure
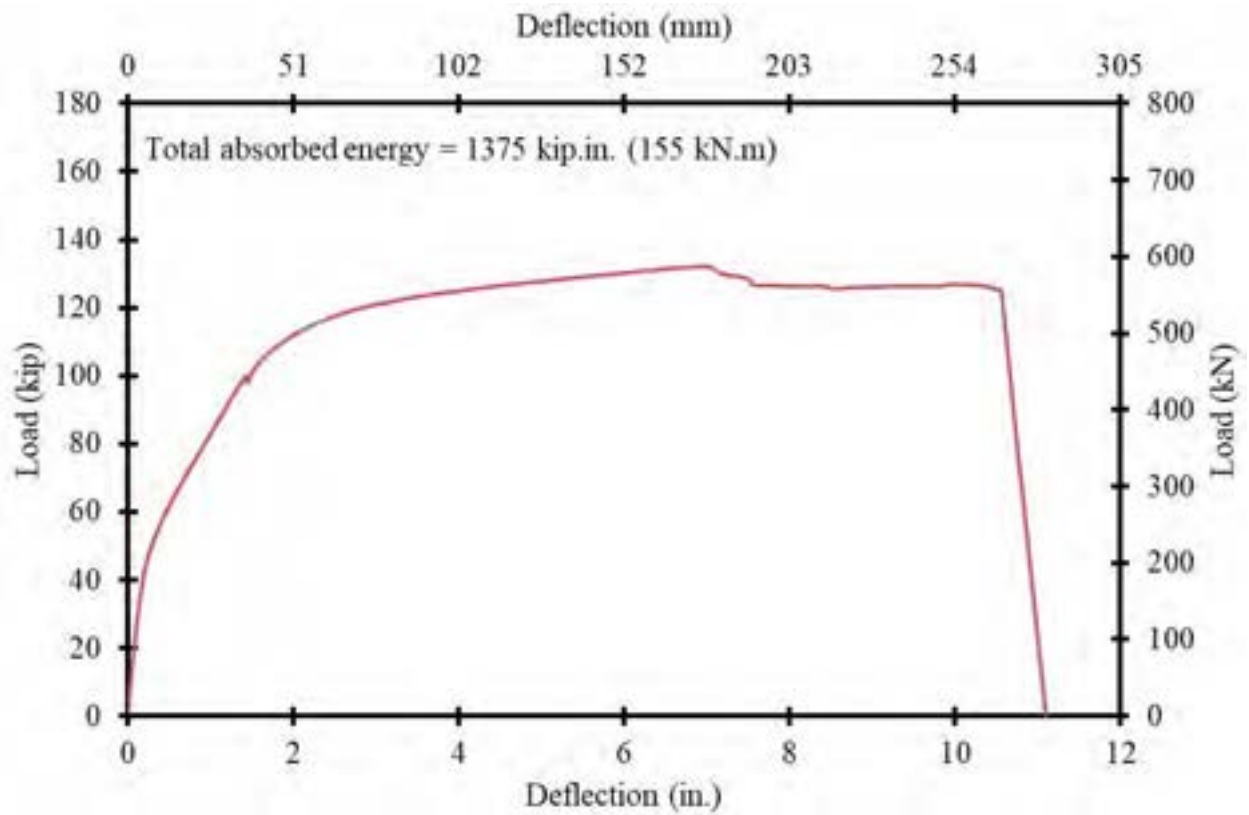
Figure 5.5-20 Energy absorption capacity of Beam S0.6

127

5.6 Discussion of Test Results

Table 5.6-1 summarizes the results from the flexural testing of the three beams. The load-midspan deflection curves during the ultimate load cycle for the three beams are plotted together in Figure 5.6-1, with elimination for the residual deflection from previous load cycles. The three beams demonstrated similar deflection response before reaching the decompression load. After the decompression load, Beam S0.6 achieved a maximum deflection of 11.5 in. (292.1 mm). Beams C0.7 and C0.6 failed at a maximum deflection of 9.9 in. and 8.9 in. (251.5 mm and 226.1 mm), respectively. The difference in bending stiffness between Beam C0.7 and C0.6 with CFCC reinforcement was attributed to the difference in reinforcement ratio and strand diameter. Whereas, the difference in stiffness between Beam S0.6 and other beams was attributed primarily to the difference in material properties between steel and CFCC.

By comparing the failure loads of the three beams, it was found that Beam C0.7 failed at a highest maximum load of 220.4 kip (980.8 kN), while, the design load capacity of the beam was estimated as 99.4 kip (442 kN). These are the remaining capacities after subtracting the effects of self-weight of the beam. The actual failure load in comparison to the expected failure load corresponds to a ratio of 2.21. Beam C0.6 failed at a maximum load of 190.7 kip (848.6 kN), while the expected resistance load capacity, not considering the self-weight of the beam, was 110 kip (489.3 kN). The actual failure load in comparison to the expected represents a ratio of 1.72. In other words, the ultimate failure loads of Beam C0.7 and C0.6 were 2.21 and 1.72 times the design capacity, respectively. High experimental-to-analytical ratios could be the result of the lower manufacturers guaranteed tensile strength compared to the actual ultimate tensile strength of CFCC. Also, it is important to note that both beams exhibited slippage of the partially debonded CFCC strands, which triggered failure and led to rupture of the remaining bonded strands.

Beam S0.6 achieved a maximum load of 132.0 kip (587.0 kN), while the remaining resistance capacity after subtracting the influence of the self-weight of the beam was estimated as 112 kip (498.2 kN). Consequently, the actual failure load was only 17 % higher than the design failure load, representing a ratio of 1.17.

The recorded concrete strains in the three beams at mid-span during the ultimate load cycle are shown in Figure 5.6-2. Strain readings in Beam S0.6 were significantly less than those in other

beams until yielding occurred. After yielding, the concrete strain in Beam S0.6 increased rapidly until reaching the maximum concrete compressive strain at failure.
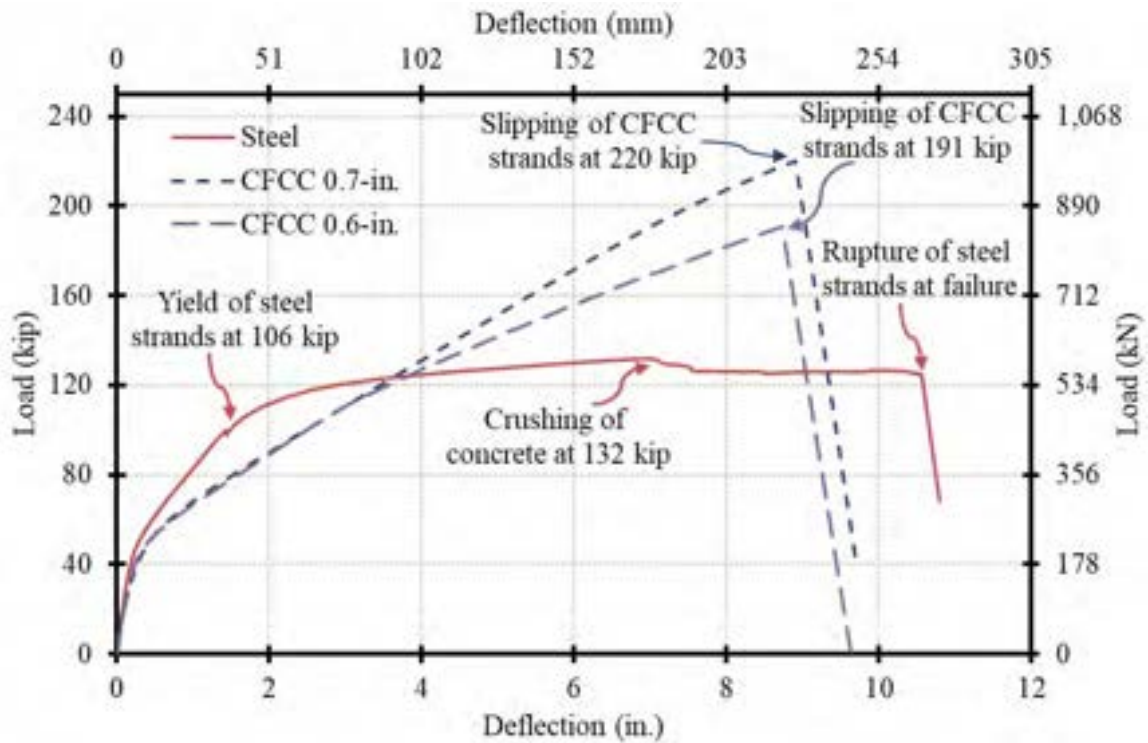
Figure 5.6-1 Load vs. mid-span deflection of the three tested AASHTO I-beams
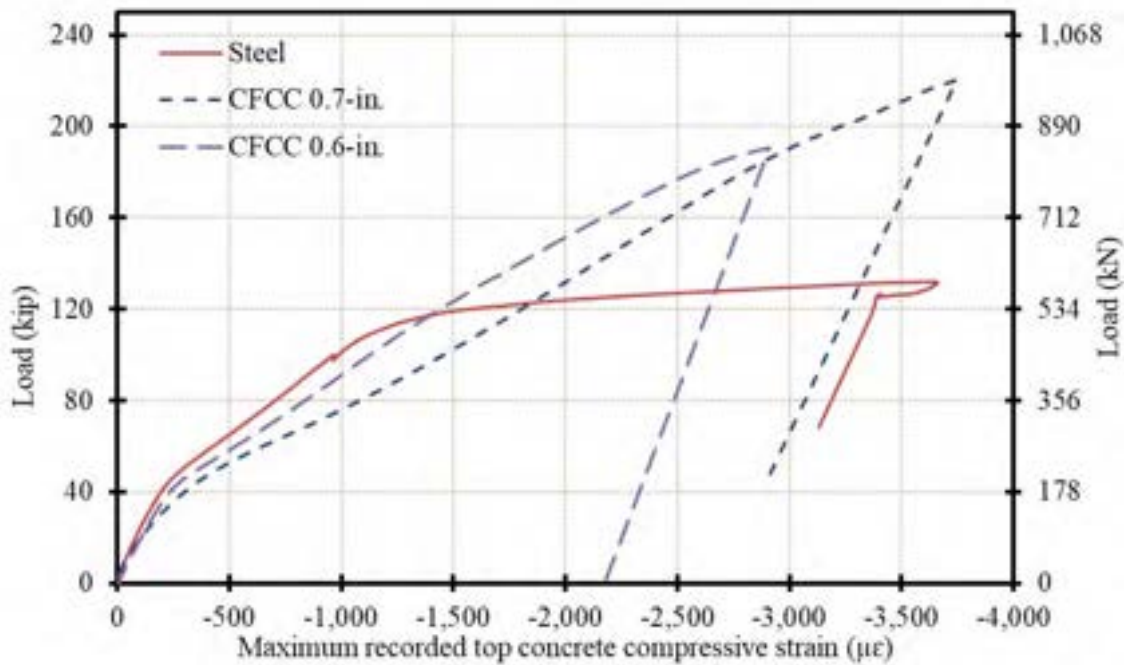
Figure 5.6-2 Load vs. concrete strain at the top deck surface of the three AASHTO I-beams

Table 5.6-1 Summary of flexural test results for Beams C0.6, C0.7, and S0.6

Parameter	Beam		
	C0.7	C0.6	S0.6
Nominal load capacity, kip (kN)	148 (657)	135 (600)	127 (566)
Resistance factor, Ø	0.85	0.85	1.0
Resistance load capacity per design, kip (kN)	115 (510)	125 (558)	127 (566)
Resistance load capacity per design*, kip (kN)	99.4 (442)	110 (489)	112 (498)
Cracking load, kip (kN)	48.0 (213.5)	48.0 (213.5)	48.0 (213.5)
Decompression load, kip (kN)	43.8 (194.8)	43.8 (194.8)	43.5 (193.5)
Experimental failure load, kip (kN)	220.4 (980.34)	190.7 (848.14)	132.0 (587.0)
Midspan deflection at failure, in. (mm)	9.9 (251.5)	8.9 (226.1)	11.5 (292.1)
Compressive strain at top deck surface at failure, $\mu\varepsilon$	3745	2908	3658
Total energy absorption kip.in. (kN.m)	1540 (174)	1250 (141)	1375 (155)
Experimental/Resistance (design)	2.21	1.72	1.17
Mode of failure	Rupture of prestressing strand	Rupture of prestressing strand	Yielding then rupture of prestressing strand

*After subtracting the influence of the self-weight of the beam

5.7 Testing of Full-scale Bulb T beam

To further investigate the flexural performance of concrete beams prestressed with large diameter CFCC strands, a full-scale bulb T beam was designed, constructed, and tested under four-point flexural test setup. The beam had a length of 40 ft (12.2 m), a depth of 36 in. (914 mm), and a top flange width of 49 in. (1245 mm). The beam cross section is shown in Figure 5.7-1. The beam was prestressed with five 0.7″ CFCC strands, with an initial prestressing force of 53 kip/strand (236 kN/strand). In addition, the beam was provided with six top non-prestressed CFCC strands in the top flange. In the transverse direction, the beams were reinforced with No. 3 (M10) Grade 60 steel stirrups spaced at 4 in. (101.6 mm) on center.

The construction of the bulb T beam went through the same construction phases of the three AASHTO I-beams, which included setting up the formwork, assembling the reinforcement cages, placing the cages inside the formwork, pulling the pretensioning strands, casting the concrete, and finally, transferring the prestress force to the cured concrete beams. Figure 5.7-2 shows the construction stages of the full-scale bulb T beam.

The theoretical analysis for the bulb T cross-section using force equilibrium and strain compatibility indicated a tension failure by rupture of CFCC prestressing strands. During the test, the beam was simply supported over two elastomeric bearing pads with an effective span of 39 ft (11.9 m). The bearing pads had a length of 12 in. (305 mm), a width of 6 in. (152 mm), and a thickness of 1.0 in. (25.4 mm). Load was applied to the beam using a steel spreader with two load points as shown in Figure 5.7-3. The distance between the loading points was 4 ft (1.2 m).

The testing scenario included loading the beam through loading/unloading cycles until the 100-kip (445-kN) load level. The load cycles were applied in increments of 5 kip (22.3 kN) until the first flexural crack was observed and in increments of 10 kip (44.5 kN) from cracking until 100 kip (445 kN). After the 100-kip (445-kN) load level was achieved, the beam was loaded monotonically until failure. Strain gages, load cells, linear variable differential transducers (LVDTs), and linear motion transducers (LMTs) were used to capture the strain, applied load, deformation and deflection of the beam, respectively.
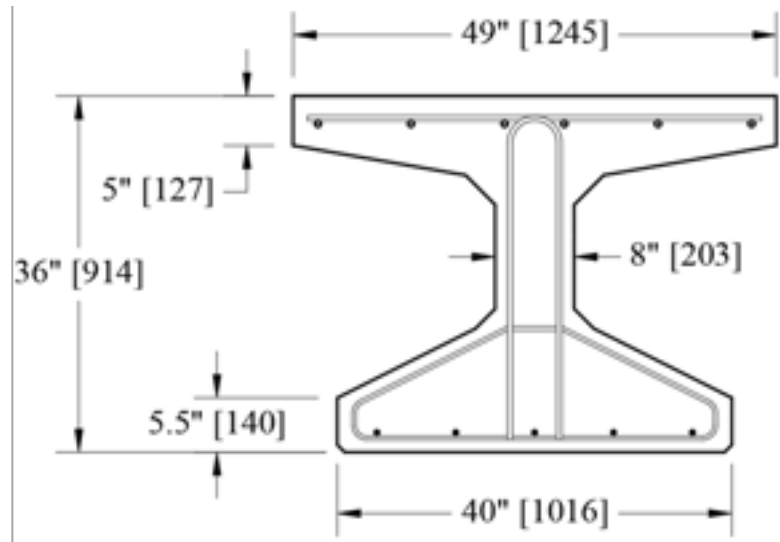
Figure 5.7-1 Cross-section of bulb T beam

(a) Assembling reinforcement cage

(b) Pulling 0.7 in. (17.3 mm) CFCC strands

(c) Placing concrete inside formwork

(d) Prestress release by cutting steel strands

Figure 5.7-2 Construction process of full-scale bulb T beam

Figure 5.7-3 Flexural testing of full-scale bulb T beam under four-point-loading setup

Figure 5.7-4 shows the load-deflection curves for the bulb T beam. Similar to AASHTO I-Beams, bilinear curves were obtained with the decompression load marking the change in the slope. The cracking load was determined as 85 kip (378 kN), while the decompression load was determined as 37.5 kip (167 kN) which represented an effective prestressing level of 238 kip (1059 kN) (prestress loss of 10%). The last load cycle before the failure load cycle reached 100 kip (445 kN) with a corresponding deflection of 1.5 in. (38 mm). After unloading, the residual deflection from all load cycles was approximately 0.1 in. (2.5 mm).

The bulb T beam failed at a maximum load of 162 kip (720 kN) with a corresponding deflection of 5.6 in. (142 mm). The failure was characterized by rupture of CFCC prestressing strands accompanied by spalling of concrete at the soffit of the beam as shown in Figure 5.7-5. The strain gage readings at the top flange surface indicated a concrete compressive strain of 1750 με, which is less than the maximum theoretical compressive strain (3000 με). This confirms that the beam was designed as an under-reinforced section. The estimated design load capacity was computed as 82 kip (365 kN). By comparing the actual failure load to the design failure load, it was found that

133

the actual failure load was 97 % greater than the design failure load, representing a an experimental-to-design ratio of 1.97.
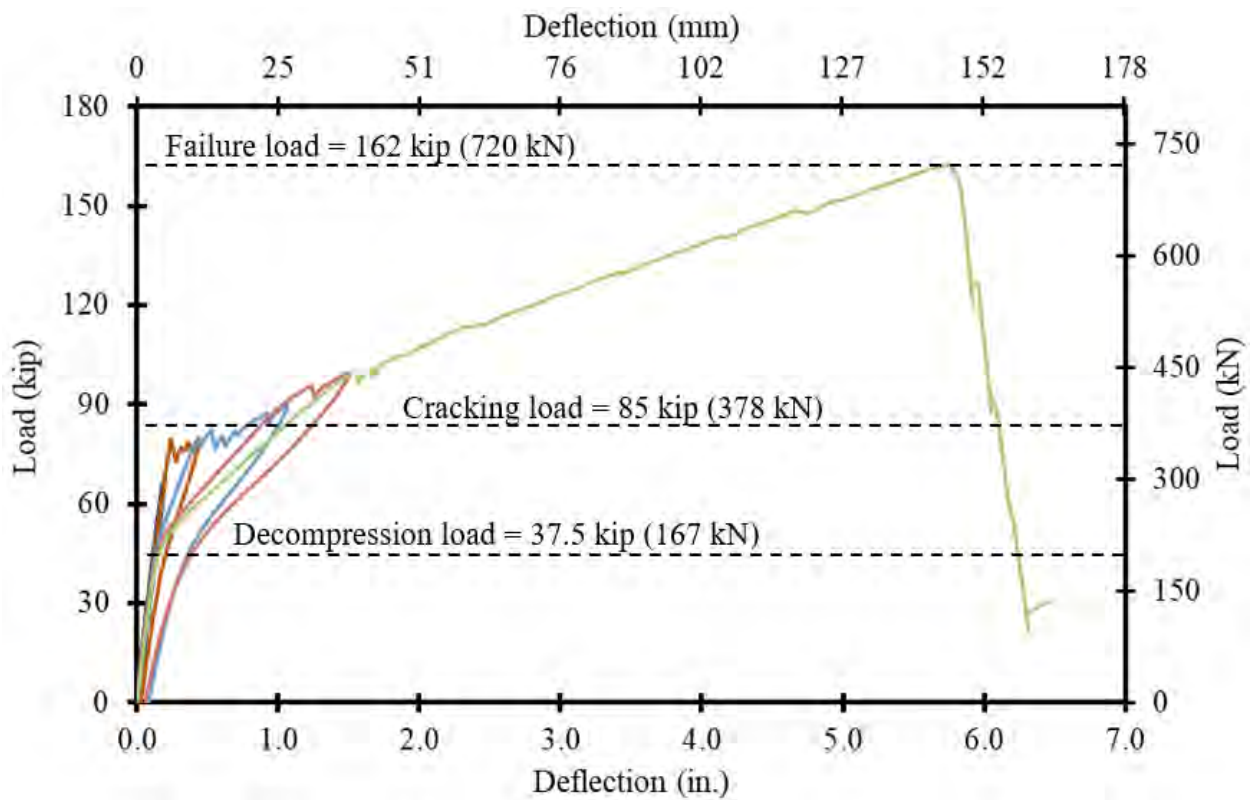
Figure 5.7-4 Load-deflection curves of bulb T beam including all load cycles to failure

Figure 5.7-5 Failure of bulb T beam due to rupture of CFCC prestressing strands

134

5.8 Summary

Based on the results of testing two full-scale AASHTO I beams prestressed with 0.6" and 0.7" CFCC strands and comparing the results with an identical beam prestressed with conventional 0.6" steel strands, it was observed that the deployment of 0.7″ CFCC strands is both feasible and efficient in beam construction. The use of 0.7″ CFCC strands reduced the number of anchorage devices and improved the beam design by meeting the load-carrying capacity requirements with higher prestressing force per strand and a lower number of strands as compared to when using 0.6″ CFCC strands.

All AASHTO I beams exhibited similar behavior before cracking and the effect of internal reinforcement was negligible. After cracking and prior to steel yielding of the steel strands, beams prestressed with CFCC strands showed larger deformation than that prestressed with steel strands at the same load level. This was attributed to the lower elastic modulus of CFCC compared to steel. After yielding of the steel strands, the steel prestressed beam exhibited a significant increase in deformation with a marginal increase in load. Conversely, CFCC prestressed beams continued their linear load-deflection relationship to failure.

Using a strength limit state design, a significant margin of safety was observed in beams prestressed with 0.6″ and 0.7″ CFCC strands. For instance, the AASHTO I Beam prestressed with 0.7″ CFCC strands achieved approximately 221 % of its theoretical design capacity. Likewise, the AASHTO I Beam prestressed with 0.6″ CFCC strands achieved approximately 172 % of its design capacity. On the other hand, the AASHTO I Beam prestressed with 0.6″ steel strands achieved approximately 117 % of its design capacity. The significant margin of safety of beams prestressed with CFCC strands is attributed to the environmental reduction factor (0.9), the strength reduction factor (0.85), and the ratio of the guaranteed strength to the average tensile strength (0.69 and 0.87 for 0.7 and 0.6 CFCC strands, respectively).

CHAPTER 6: FIRE AND HEAT RESISTANCE

6.1 Introduction

Regardless of the material under consideration, loss in strength under high temperature is inevitable (Rafi et al. 2007; Williams et al. 2008; and Grace and Bebawy 2014). For instance, concrete loses 50 % of its compressive strength at approximately 1292 ^{0}F (700 ^{0}C). Note that different concrete constituents exhibit different thermal decomposition trends that result in a wide range in the behavior of concrete at high temperatures (Kodur et al. 2005). Steel is also susceptible to fire and is expected to lose 50 % of its tensile capacity at 932 ^{0}F (500 ^{0}C). Likewise, CFRP is susceptible to fire and extreme high temperature events as the polymer matrix in CFRP softens and deteriorates with the increase in temperature. CFRP loses approximately 50 % of its ambient strength at 392 ^{0}F (200 ^{0}C) according to Robert and Benmokrane (2010).

Precise data regarding the fire endurance of beams prestressed with CFRP strands are not available. However, it is generally accepted that prestressed concrete structures are more susceptible to fire than reinforced concrete structures, since the prestressing strands (whether steel or CFRP) are already stressed to a significant level of their ambient capacity. For instance, Zhang et al. (2017) showed that under hydrocarbon fire, prestressed box beams with higher level of prestressing force have higher ductility and creep and lower fire endurance than those with a lower level of prestressing force. In addition, Maluk et al. (2010) studied the fire behavior of CFRP prestressed high strength concrete slabs and observed that when spalling of the concrete was avoided, the fire endurance of the prestressed slabs was influenced by the initial prestressing force as slabs with larger prestressing force achieved a shorter fire endurance.

It should be noted that fire endurance of a beam prestressed with CFRP strands may not necessarily be dependent on the heat resistance of CFRP, but rather on the ability of the prestressed beam to sustain a specific load at elevated temperatures (Abbasi and Hogg 2006). For instance, Maluk et al. (2010) suggested that the limiting factor for the fire endurance of CFRP reinforced or prestressed concrete is the deterioration in bond strength between CFRP and concrete at elevated temperatures rather than the flammability of the composite material or the deterioration of the epoxy matrix. This opinion is supported by earlier fire test results that showed 80 to 90 % reduction in the bond strength between concrete and CFRP as the temperature increased from 68 to 482 ^{0}F

(20 to 250 ^{0}C). This is compared to a 38 % reduction when conventional steel reinforcing bars were tested (Katz et al. 1999; Kodur et al. 2005).

Another aspect of the fire resistance of prestressed concrete structures is the concrete cover and the potential for concrete cover spalling at high temperatures. According to Kodur et al. (2005), the strength of concrete in fire is governed by its moisture content. Test results by Saafi (2002) showed that too much moisture in the concrete generates high pressure in the beam and causes spalling in the concrete cover, which results in the premature exposure of the internal reinforcement to high temperature and overall reduction in the strength of the structural element. In addition, the shape of the structural element plays an important role in the fire resistance. For instance, in comparing a rectangular section to an I-shape, it was found that the I-shape was more susceptible to spalling in comparison to the rectangular section (Ashton and Malhotra 1953). Furthermore, an increase in concrete cover should provide more fire protection of the internal reinforcement and prestressing strands and extend the fire endurance of structural elements (Kodur et al. 2005; Yu and Kodur 2013). For instance, Terrasi et al. (2010) investigated the performance of CFRP and steel prestressed beams at elevated temperatures. The failure mode was either concrete spalling or deterioration of the bond between the strands and the concrete accompanied by a loss of prestressing force. The results showed evidence of an increased fire endurance with the increase of concrete cover. It should be noted, however, that concrete cover thicker than 3.0 in. (7.5 mm) are deemed susceptible to spalling (Ashton and Malhotra 1953).

Through this part of the investigation, the performance of unprotected and protected 0.7″ CFCC strands at elevated temperatures was evaluated. CFCC specimens with a length of 6 ft (1626 mm) were subjected to elevated temperatures for at least 30 minutes before they were loaded to failure under uniaxial tensile load to evaluate the reduction in the strength with the increase in temperature. In addition, to evaluate the performance of CFCC strands embedded in concrete under a fire event, another research investigation was carried out on a series of 16-ft (4.876-m) long full-scale beams prestressed with CFCC strands. The beams were subjected to a fire event according to ASTM E119 (ASTM 2020) while sustaining a central load representing the traffic load in real bridge beams. Detailed discussion for both test setups, test results, and main conclusions are provided in the following sections.

6.2 Tensile Strength of CFCC at Elevated Temperatures

6.2.1 Test Setup

Twelve test specimens were tested at high temperature to evaluate the effect of temperature increase on the tensile strength of CFCC strands. Each specimen had a length of 64 in. (1626 mm) and was provided with two sleeve anchorages at the ends as described in Chapter 2.

The test setup included passing the test specimen through an Instron environmental chamber as shown in Figure 6.2-1 through Figure 6.2-4 and attaching its ends to the fixed and moving heads of the MTS four-post testing machine. After the specimen was fixed in place, the environmental chamber was activated to heat the middle portion of the specimen to a predefined temperature. To ensure a uniform temperature throughout the heated length of the specimen, the chamber was maintained at the predefined temperature for 30 minutes. After that, the MTS actuator was engaged and the specimen was loaded in a uniaxial tensile test setup to failure with a loading rate of 2.0 kip/min (8.9 kN/min), while the temperature of the environmental chamber remained at the same predefined level. The specimens were tested at temperatures ranging from 150 °F (65 °C) to 662 °F (350 °C).

Figure 6.2-1 Preparing anchors for test specimens

Figure 6.2-2 Completed test specimens with two anchor devices

Figure 6.2-3 CFCC strand passing through a central opening in the environmental chamber

Figure 6.2-4 Test specimens inside the environmental chamber before the heating phase

6.2.2 Test Results

With an increase in temperature, a reduction of strength of CFCC strands was observed in all test specimens. The common failure mode was rupture of the strands within the heated length as shown in Figure 6.2-5 through Figure 6.2-14. The tensile strength of CFCC at 150 °F (65 °C) was approximately 107.6 kip (479 kN), while its tensile strength at 662 °F (350 °C) was 39.26 kip (175 KN). Table 6.2-1 shows the test result of all 0.7″ CFCC specimens. As a reference, Table 6.2-2 shows the test results of 0.6″ CFCC (Grace et al. 2019) when heated to elevated temperatures. Table 6.2-3 compares the test results with earlier test results for smaller diameter strands as provided by the manufacturer. In addition, Figure 6.2-15 shows a comparison between the current test results and those obtained by the manufacturer for CFCC strands with different diameters with respect to the tensile strength. Figure 6.2-16 shows the reduction in strength with respect to the guaranteed strength of each strand diameter.
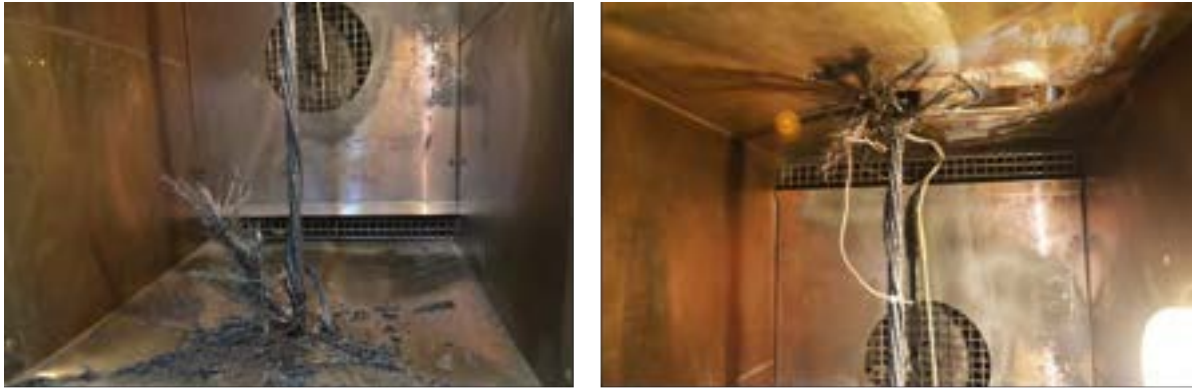
Figure 6.2-5 Typical failure of test specimen at elevated temperature

Figure 6.2-6 Failure of CFCC specimen at 302 °F (150 °C)

Figure 6.2-7 Failure of CFCC specimen at 347 °F (175 °C)

Figure 6.2-8 Failure of CFCC specimen at 392 °F (200 °C)

Figure 6.2-9 Failure of CFCC specimen at 437 °F (225 °C)

Figure 6.2-10 Failure of CFCC specimen at 482 °F (250 °C)

Figure 6.2-11 Failure of CFCC specimen at 527 °F (275 °C)

Figure 6.2-12 Failure of CFCC specimen at 572 °F (300 °C)

Figure 6.2-13 Failure of CFCC specimen at 617 °F (325 °C)

Figure 6.2-14 Failure of CFCC specimen at 662 °F (350 °C)

Table 6.2-1 Summary of test results for tensile strength of 0.7″ CFCC at elevated temperatures

Temperature, ⁰F (⁰C)	Failure Load, kip (kN)	Failure Stress, ksi (MPa)	Ratio to guaranteed (78.7 kip), %	Ratio to ultimate at ambient temp (113.93 kip), %
150 (65)	107.6 (479)	460 (3172)	137	94
302 (150)	87.39 (389)	373 (2572)	111	77
347 (175)	81.84 (364)	349 (2406)	104	72
392 (200)	78.67 (350)	336 (2317)	100	69
437 (225)	74.38 (331)	318 (2192)	95	65
482 (250)	63.93 (284)	273 (1882)	81	56
527 (275)	56.64 (252)	242 (1669)	72	50
572 (300)	46.63 (207)	199 (1372)	59	41
617 (325)	40.74 (181)	174 (1200)	52	36
662 (350)	39.26 (175)	168 (1158)	50	34

Table 6.2-2 Summary of test results for tensile strength of 0.6″ CFCC at elevated temperatures

Specimen ID	Temperature, °F (°C)	Failure Load, kip (kN)	Failure stress, ksi (MPa)	Ratio to guaranteed strength (60.7 kip or 270 kN) (%)
65-01	150 (65)	69 (306)	385 (2654)	113
150-01	302 (150)	54.79 (244)	306 (2110)	90
175-01	347 (175)	52.08 (232)	291 (2006)	86
200-01	392 (200)	52.37 (233)	293 (2020)	86
200-02	392 (200)	54.34 (242)	303 (2089)	89
225-01	437 (225)	52.14 (232)	291 (2006)	86
250-01	482 (250)	47.75 (212)	267 (1841)	79
275-01	527 (275)	45.82 (204)	256 (1765)	75
300-01	572 (300)	41.74 (186)	233 (1606)	69
325-01	617 (325)	36.16 (161)	202 (1393)	60
325-02	617 (325)	36.74 (163)	205 (1413)	60
350-01	662 (350)	34.12 (152)	191 (1317)	56
350-02	662 (350)	34.88 (155)	195 (1344)	57

Table 6.2-3 Summary of test results of CFCC at elevated temperatures

Temperature °F (°C)	Ratio to CFCC strength @ ambient (%)			
	0.7″ (17 .8 mm)*	0.6″ (15.2 mm)*	0.5″ (12.5 mm)**	0.3″ (7.5 mm)**
68 (20)	100	100	100	100
122 (50)		-	98	
212 (100)		-	88	-
302 (150)	77	79	72	-
392 (200)	69	76	61	-
482 (250)	56	69	58	55
572 (300)	41	61	48	-
662 (350)	34	49	-	-
752 (400)		-	-	40

* Based on ultimate strength of 70 kip (311 kN) for 0.6″ CFCC strands and ultimate strength of 113.93 kip (507 kN) for 0.7″ CFCC strands

** Tokyo Rope Mfg. Co., Ltd. based on tensile strengths of : 38.2 kip (145 kN) for 0.5″ (12.5 mm) CFCC, and 15 kip (67 kN) for 0.3″ (10 mm) CFCC strands.
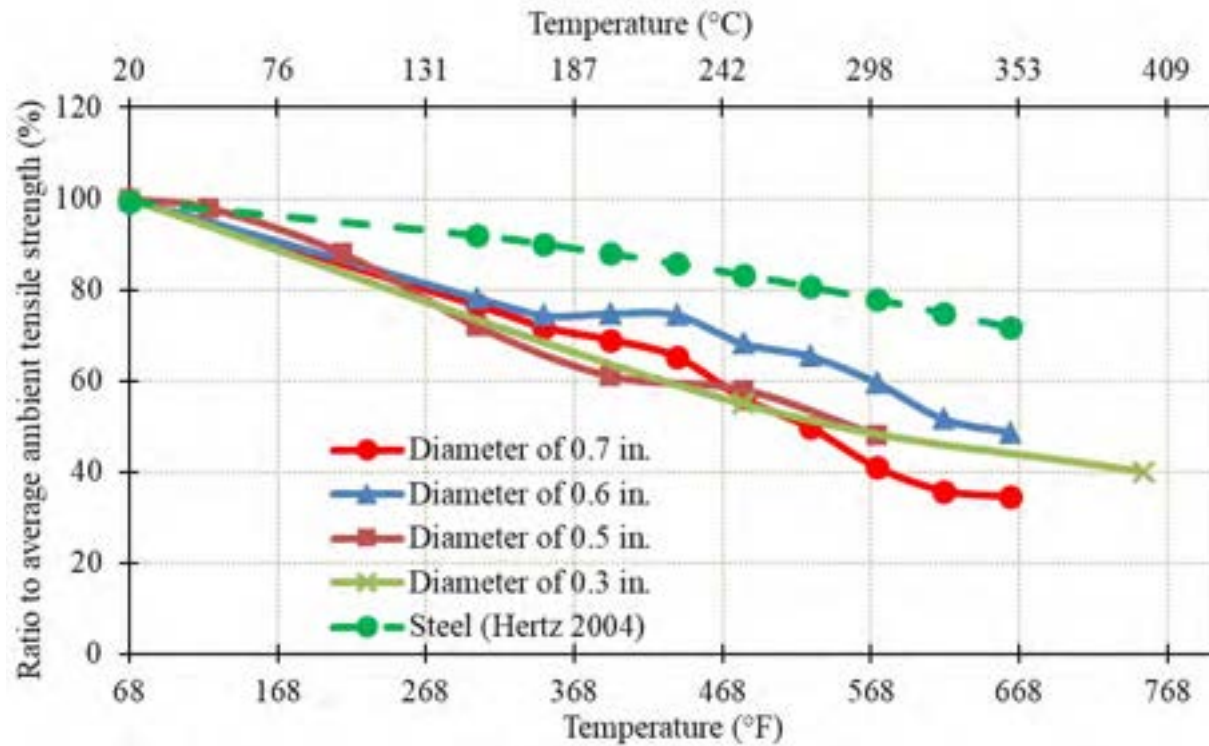
Figure 6.2-15 Decrease in tensile strength with increase in temperature for CFCC strands as a ratio to the ambient tensile strength
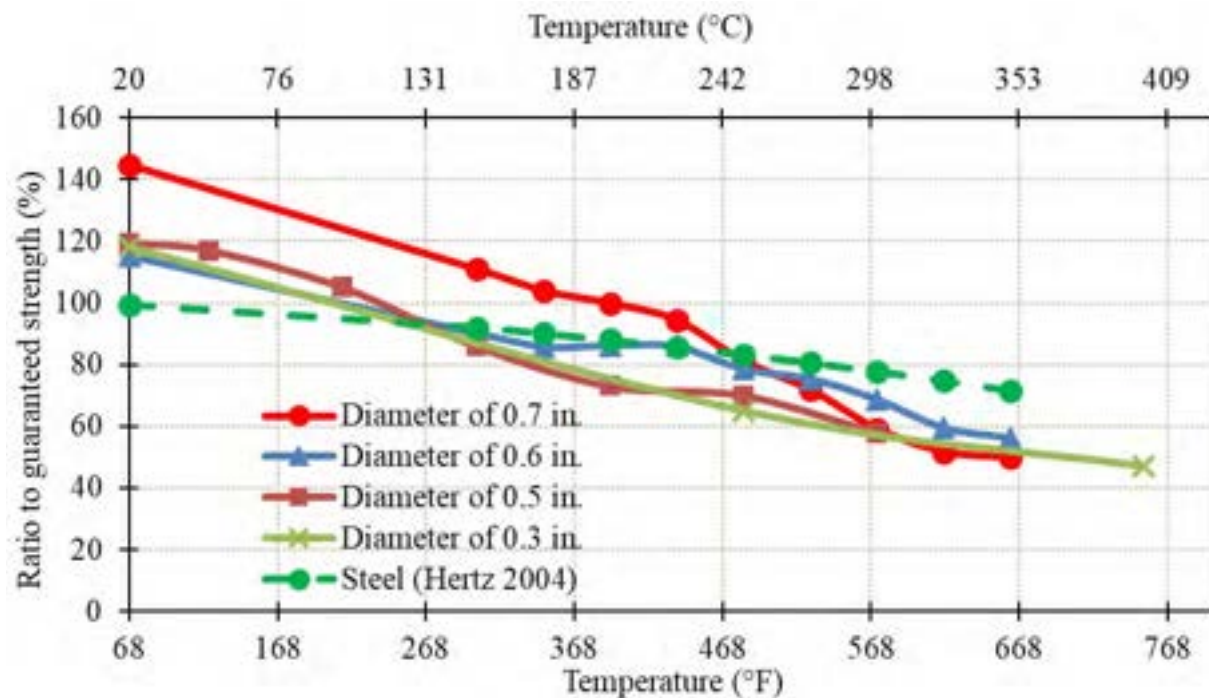
Figure 6.2-16 Decrease in tensile strength with increase in temperature for CFCC strands as a ratio to the guaranteed strength

145

6.3 Full-Scale Beams Under Fire/Loading

After establishing the relationship between the temperature and the strength of CFCC specimens, the test program extended to assess the performance of full-scale beams prestressed with CFCC strands. Through this part of the experimental program, a total of eight 16-ft (4877-mm) long full-scale prestressed beams were either salvaged from earlier tests or built for the purpose of fire testing. Different beam sections were investigated as follows:

1. Two box beams prestressed with 0.7″ CFCC strands (denoted herein as B-0.7C and RB-0.7C)

2. Two bulb T beams prestressed with 0.7″ CFCC strands (T-0.7C and RT-0.7C)

3. Two salvaged AASHTO I beams prestressed with 0.6″ CFCC strands (I-0.6C and RI-0.6C)

4. Two salvaged AASHTO I beams prestressed with 0.6″ Steel strands (I-0.6S and RI-0.6S)

In the notation of the beams, the acronym "T" refers to Bulb T beam, "B" refers to Box beam, "I" refers to AASHTO-I beam, "C" refers to carbon fiber strand, "S" refers to steel strand, and 0.6 or 0.7 refers to the diameter of the strand in inches. The letter R refers to residual capacity test or Phase II of testing as explained below.

The salvaged AASHTO beams were obtained from the full-scale beams after conducting the full-scale tests described in Chapter 5. Initially, it was also planned to use salvage segments from the AASHTO I beam with 0.7" CFCC strands. However, the flexural test resulted in a dense crack pattern that hindered the ability to salvage the beam.

The experimental program included two phases of testing. Each phase was conducted using four beams (one of each configuration). Phase I included loading the test beam in a three-point-load setup with a load of 50 kip (222 kN) at midspan and exposing the test beams to a fire event with a time-temperature curve following ASTM E119-20 (ASTM 2020): "Standard Test Methods for Fire Tests of Building Construction and Materials." The test continued until the beam failed to support the applied load of 50 kip (222 kN) and the duration of the test from the start of heating to failure was recorded along with the temperature profiles of the beam.

Phase II was similar to Phase I with regard to the loading and the exposure to an ASTM E119 fire event. However, the fire/load event was terminated after one hour and the beams were allowed

to gradually cool down to ambient temperature. The test beam was then moved to a loading facility, where it was loaded to failure in a three-point-load setup to establish the residual capacity after the one-hour fire/loading event.

6.3.1 Details of Test Specimens

The four AASHTO-I beams were segments from the full-scale 40-ft (12.2-m) long beams that were constructed originally for a flexural test, whereas the box and bulb T beams were newly fabricated beams. Figure 6.3-1 through Figure 6.3-4 show the dimensions and cross-sectional properties of all the beams. Properties of the sections are presented in Table 6.3-1, while the properties of three different prestressing materials used in the design and fabrication of the four beams are shown in Table 6.3-2. In all beams, the steel as well as CFCC strands were prestressed to 75 % of their design guaranteed tensile strength, which corresponded to 53 kip, 41 kip and 44 kip (235 kN, 182 kN, and 196 kN) for 0.7″ CFCC, 0.6″ CFCC and 0.6″ steel strands, respectively.

Construction of Beams B-0.7C and T-0.7C (along with RB-0.7C and RT-0.7C) included the typical construction sequence of building a formwork, assembling the reinforcement cages, prestressing, pouring the concrete, curing, and prestress release. The beams were constructed on a 50 ft (15.24 m) long prestressing bed with steel bulkheads anchored into a reinforced concrete floor. The side walls for the formwork were constructed from wood and Styrofoam. The hollow void in the box beam was formed using stacked Styrofoam that was strapped into position within the reinforcement cages to prevent floating during concrete pouring. Figure 6.3-5 through Figure 6.3-15 summarize various construction stages.

Beam T-0.7C was pretensioned with five 0.7″ CFCC strands. Each strand was tensioned with an initial force of 53 kip (236 kN). The center of CFCC strands was placed 2 in. (51 mm) from the soffit of the beam. The top flange of the beam was reinforced with five No. 6 (M19) Grade 60 (413 MPa) deformed steel bars. Beam B-0.7C was pretensioned with four 0.7″ CFCC strands. Each strand was tensioned to an initial force of 53 kip (236 kN). The strands were placed on a single row 2 in. (51 mm) above the soffit of the beam. The beam was also reinforced with five No. 6 (M19) Grade 60 (420) deformed steel bars as top reinforcement. Both beams were reinforced with No. 3 (M10) steel stirrups spaced 4 in. (102 mm) on center in the transverse direction.

The stirrups and the top reinforcement were assembled together on the prestressing bed before prestressing CFCC strands were passed inside the reinforcement cages. The dead and live ends of the CFCC strands were coupled with conventional 7-wire steel prestressing strands of the same diameter as shown in Figure 6.3-9. A set of in-line load cells were attached to the prestressing strands at the dead end. Prestressing of the strands to the target force was executed using a hydraulic pump and a jacking system. The force in each prestressing strand was verified through the readings from the load cells and the reading from the hydraulic pump. Type-K thermocouples with sensitivity of approximately 41 µV/ºC and a temperature range of -328 to 2462 ºF (-200 and 1350 ºC) were attached to each CFCC strand at the mid-section and quarter section.

Concrete for T-0.7C and B-0.7C were cast on different days. All the beams were cast using a ready-mix concrete. The concrete mix was designed to achieve a 28-day compressive strength of 7 ksi (48 MPa) with a maximum aggregate size of 0.75 in (19 mm). Before casting the beams, slump tests were performed in accordance to ASTM C143/C143M-05: "Standard Test Method for Slump of Hydraulic Cement Concrete." The slump values for Beams T-0.7C and B-0.7C were 9 in. (229 mm) and 8.5 in. (216 mm), respectively. In addition, twelve 6 in. $\times$ 12 in. (152 mm $\times$ 305 mm) concrete cylinders were cast for each batch of concrete to assess concrete strength over time. After concrete casting, the beams were covered with wet burlap and plastic sheets for proper curing. The cylinders were cured under the same conditions as the concrete beams and were tested under uniaxial compressive stress after 7, 14, 21 and 28 days. The compressive strength test was conducted in accordance to ASTM C39/C39M-14: "Standard Test Method for Compressive Test Method for Compressive Strength of Cylindrical Concrete Specimens." Figure 6.3-10 and Figure 6.3-11 show the process of casting of concrete.

The transfer of the prestressing force into the beams took place eight days after concrete casting. The force transfer was executed by cutting the prestressing steel strands using an acetylene cutting torch. This was done by slowly heating the steel strands until they broke. The compressive strength for T-0.7C and B-0.7C at transfer were 9 ksi (62 MPa) and 7 ksi (48 MPa), respectively. The transfer of prestressing force to the strands is shown in Figure 6.3-13.
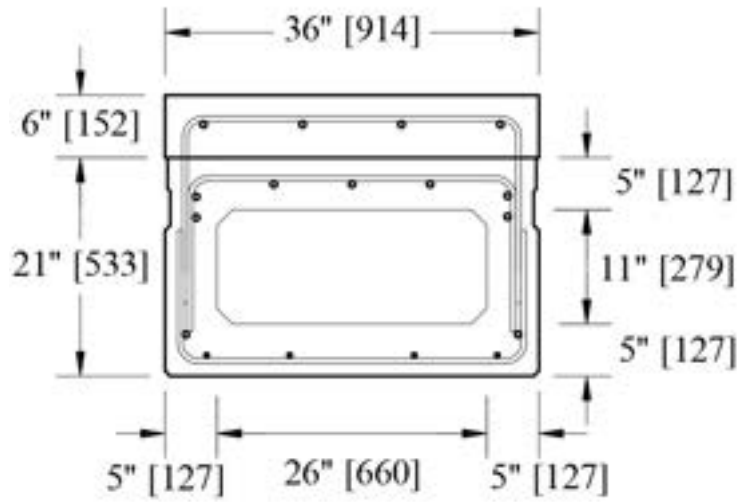
Figure 6.3-1 Cross-section of B-0.7C, all dimensions are in in. [mm]
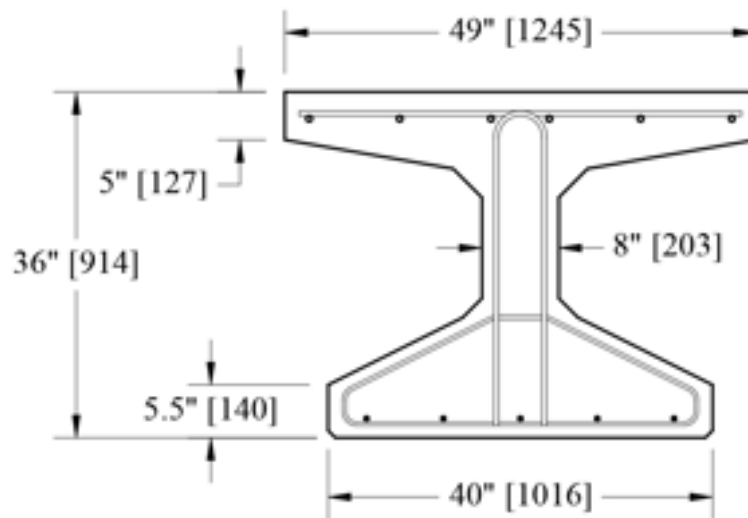
Figure 6.3-2 Cross-section of T-0.7C, all dimensions are in in. [mm]
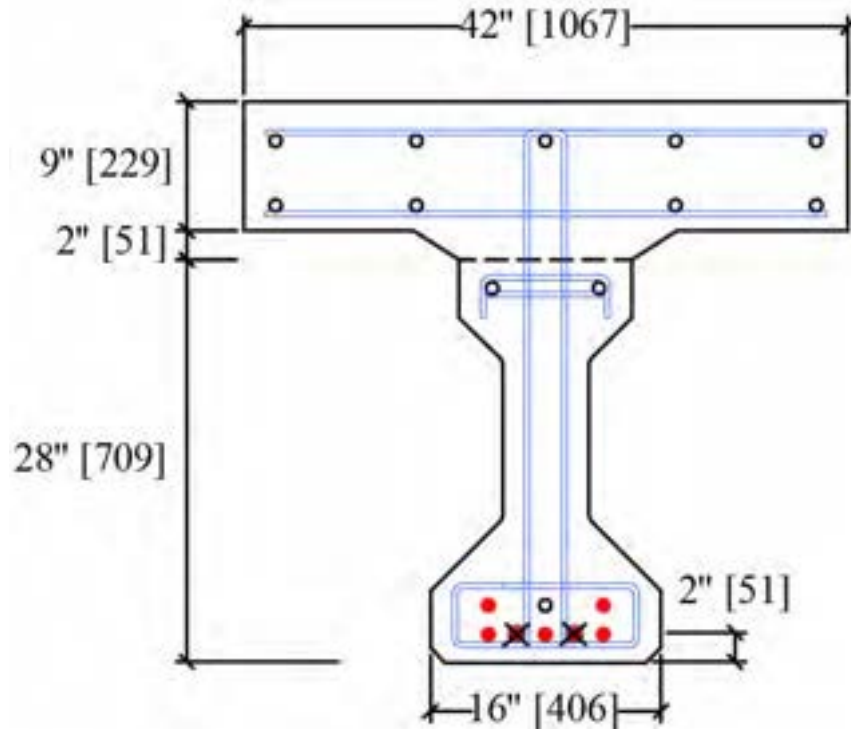
Figure 6.3-3 Cross-section of I-0.6C with two debonded strands marked with "x"
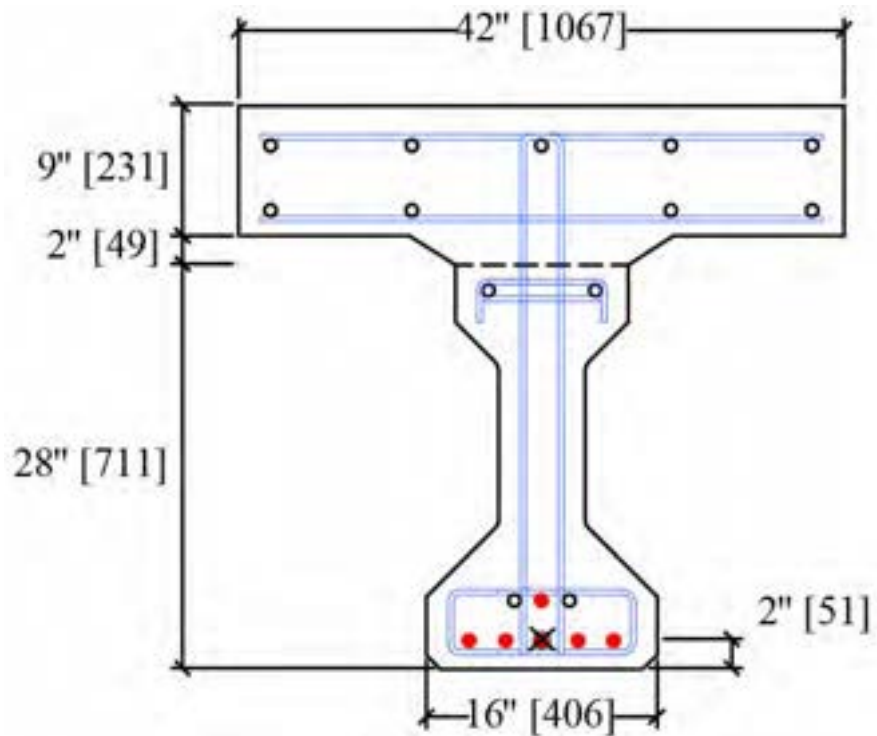
Figure 6.3-4 Cross-section of I-0.6S with the debonded strand marked with "x"

150

Table 6.3-1 Section properties of composite beam

	Box Beam	Bulb T Beam	AASHTO I-Beam
Area, in^2 ($\times 10^2$ mm^2)	683 (4406)	878.3 (5666)	682 (4400)
y$_{top}$, in (mm)	12.3 (312)	17.8 (452)	15.4 (391)
y$_{bottom}$, in (mm)	14.7 (373)	18.2 (462)	23.6 (600)
Top section modulus, in^3 ($\times 10^6$ mm^3)	4,279 (70)	8,179 (134)	5,942 (97.4)
Bottom section modulus, in^3 ($\times 10^6$ mm^3)	3,577 (58)	8,000 (131)	3,866 (63.4)
Inertia, in^4 ($\times 10^6$ mm^4)	52,604 (21,895)	14,5592 (60,599)	91,343 (38,020)
Weight, kip/ft (kN/m)	0.711(10.4)	0.915 (13.4)	0.711 (10.4)

Table 6.3-2 Properties of 0.7″ CFCC, 0.6″ CFCC and 0.6″ low relaxation steel strand

Property	0.7 CFCC	0.6 CFCC	0.6 Steel
Strand configuration	1 x 7	1 x 7	1 x 7
Diameter, in (mm)	0.7 (17.26)	0.6 (15.2)	0.6 (15.2)
Guaranteed breaking load, kip (kN)	78.7 (350)	60.7 (270)	58.6 (261)
Cross-sectional area, in.^{2} (mm^2)	0.234 (151)	0.179 (115.6)	0.217 (140)
Max. breaking load, kip (kN)	107 (476)	78.7 (350)	60.6 (269.7)
Min. breaking load, kip (kN)	104 (463)	72.78 (324)	-
Tensile strength, ksi (GPa)	451 (3.1)	425 (2.9)	451 (3.1)
Tensile modulus, ksi (GPa)	22625 (156)	21611 (149)	28400 (196)
Elongation, %	2.0	2.0	5.43

Figure 6.3-5 Gluing of Styrofoam layers together

Figure 6.3-6 Attachment of Styrofoam to side walls of the form

Figure 6.3-7 Assembling the reinforcement cage around the molded Styrofoam

Figure 6.3-8 Tying and placement of reinforcement cage on prestressing bed

Figure 6.3-9 Installation of prestressing anchorage and prestressing of strand

Figure 6.3-10 Concrete casting

Figure 6.3-11 Slump test and casting of concrete cylinders
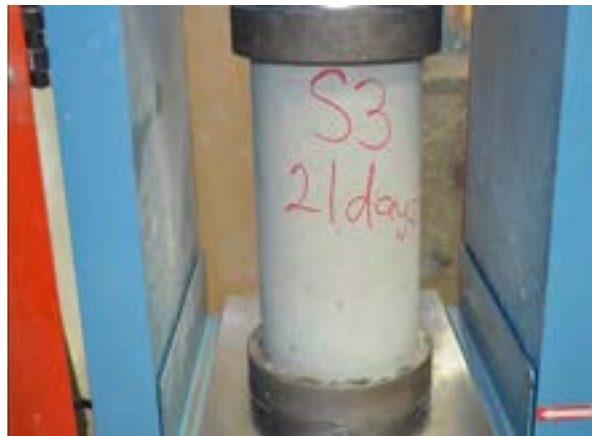
Figure 6.3-12 Uniaxial compressive strength test for concrete

Figure 6.3-13 Transfer of prestressing force into concrete

Figure 6.3-14 Removing the formwork of the beams

Figure 6.3-15 Prestressed CFCC bulb T beam (left) and box beam (right)

Beams I-0.6C and I-0.6S were salvaged from the 40 ft (12.2 m) beams that were tested in flexure, as described in Chapter 5. As the ends of the beams remained intact after flexural testing, two 16-ft (4.9-m) long segments were salvaged from each beam. Beam I-0.6C was originally pretensioned with seven 0.6″ CFCC strands. Five prestressing strands were placed in a single row 2 in. (51 mm) from the bottom of the beam. The remaining two prestressing strands were placed in a second row, 4 in. (102 mm) from the bottom face of the beam. Two of the strands in the bottom row were debonded in the original design for 10 ft (3 m) and these strands slipped during the prior flexural test. Therefore, the salvaged beam segment had only five effective prestressing strands for the fire tests. Each 0.6″ CFCC strand was prestressed with an initial force of 41 kip (182 kN). This corresponds to 75 % of the guaranteed design tensile strength and corresponds to a total prestressing force of 205 kip (912 kN) for all five strands. The top flange of the AASHTO I-beam was reinforced with two 0.6″ non-prestressed CFCC strands. A 9-in. (229-mm) thick deck

slab was cast on top of the beam. The 28-day compressive strength of the beam and the deck were 8820 psi (60.8 MPa) and 3670 psi (25.3 MPa), respectively. The salvaged beam segment was stored for 28 months (833 days) prior to testing.

Beam I-0.6S was pretensioned with six low-relaxation 0.6″ steel strands. Five of the prestressing strands were located on the first row, 2 in. (51 mm) from the bottom of the beam. The last prestressing strand and two additional No. 5 (M16) Grade 60 (414 MPa) deformed steel bars were placed 4 in. (102 mm) from the bottom of the beam. Beam I-0.6S had its middle strand in the first row debonded for a distance of 10 ft (3 m) from each end of the beam. Each steel prestressing strand was tensioned to an initial force of 44 kip (195.7 kN) resulting in a total prestressing force of 220 kip (978 kN) per beam segment after ignoring the debonded strand. This prestress level corresponded to 75 % of the material tensile capacity. The top flange of the beam was reinforced with No.5 (M16) Grade 60 deformed steel bars. The 28-day compressive strength of the beam and the deck were 9940 psi (68.5 MPa) and 3670 psi (25.3 MPa), respectively. The salvaged beam segment was stored for 24 months prior to testing.

The AASHTO I-beams were carefully drilled at mid, quarter and end sections to attach thermocouples. The holes were 3-in. (76-mm) deep from the face of the beam at the level of the first row of prestressing strands. Thermocouples were inserted and held in place with OMEGA CC high temperature cement capable of withstanding 1550 ºF (843 ºC). Figure 6.3-16 through Figure 6.3-18 show the various stages of salvaging the beam segments.

Figure 6.3-16 Salvaging 16 ft from 40 ft AASHTO I-beam

Figure 6.3-17 Cutting through the web with a circular concrete saw

Figure 6.3-18 Salvaged AASHTO I-beam segments

Special attention was given to evaluating moisture content of each beam before fire testing to avoid early concrete spalling. Moisture content is the ratio between weight of water/moisture contained in the beam to the total weight of the beam. All eight (8) beams were stored indoors under controlled conditions for different durations and moisture contents were recorded for all beams prior to the fire test. For comparison purposes, moisture content readings were also obtained from other beam specimens stored outdoors. A "Ligno-VersaTec Moisture Meter" was used to obtain the readings. The moisture meter consisted of an RH Probe, an RH BluePeg and the Ligno-VersaTec meter. The beam was first predrilled with a 5/8" (16 mm) drill bit, to a depth of 1.75 in. (45 mm), which is approximately the length of the RH BluePeg. The hole was cleaned and vacuumed to remove all dust particles. The BluePeg sleeve was inserted into the hole, flush with the face of the concrete. The RH Probe sensor was inserted 12 hours after drilling the hole. This

was to prevent the heat from drilling from affecting the readings. The BluePeg was sealed and the sensor was allowed to acclimatize inside the hole for about 72 hours. The cap was opened, and the meter was connected to obtain the humidity and the temperature readings. The moisture content was then obtained from a humidity-temperature chart. Moisture readings were taken from both the web and the top flanges of the beam. Table 6.3-3 shows the moisture content values obtained from the beams stored indoors and outdoors. Figure 6.3-19 through Figure 6.3-21 show the equipment and process for obtaining the moisture content readings. From Table 6.3-3, the moisture content for indoor beams averaged 12.4 % while that for the outdoor beams averaged 10.6 %. It was therefore concluded that the behavior of the beam segments used in the fire test replicated the behavior of bridge beams in the event of a fire reasonably well.

Table 6.3-3 Moisture Content value for indoor and outdoor beams

Locations	Indoor Beam		Outdoor Beam	
	Deck	Web	Deck	Web
Moisture Content (%)	12.2	-	10.3	10.6
	12.4	12.4	10.3	11.0
	-	-	-	10.4
	-	-	-	11.2
Avg. Moisture content (%)	12.4		10.6	

Figure 6.3-19 Ligno-VersaTec Moisture Meter

Figure 6.3-20 Installation of the sleeve and the RH Probe sensor

Figure 6.3-21 Obtaining humidity and temperature readings with the moisture meter

6.3.2 Beam Fire Test Phase I

The beams were tested in the fire chamber within CIMR. The furnace has an interior space of 9 ft × 22 ft × 10.5 ft (2.7 m × 6.7 m × 3.2 m) with nine burners on the backside and a hydraulic loading actuator with a capacity of 110 kip (489 kN) at the center of the furnace as shown in Figure 6.3-22. The furnace has an operation system box and a Yokogawa Data collection recorder for storing data during the test. Supports of the test specimens were built using 3 in × 9 in × 4.5 in (76 mm × 229 mm × 114 mm) heat resistant brick units. In addition, a 1.0-in. (25.4-mm) thick steel plate was placed on top of the brick units to provide a smooth bearing surface and distribute the reaction to the brick pyramid underneath. The beams were not axially restrained since they were designed for flexural loads based on simply supported end conditions. Section 7.4.4.1 of ASTM E119 requires that the test specimen sustains a superimposed load throughout the duration of the test. Therefore, a load of 50 kip (222 kN) was applied to the beam at midspan. This load level corresponded to

23.8 %, 13.6 %, 14.3 %, and 17 % of the theoretical load-carrying capacity of Beams B-0.7C, T-0.7C, I-0.6C and I-0.6S, respectively. It should be noted that in the case of fire on/under a bridge, the bridge is mostly shut down and the traffic is cleared. The 50-kip (222.4-kN) load was placed on the beam to simulate superimposed dead-weight on the bridge during the fire.
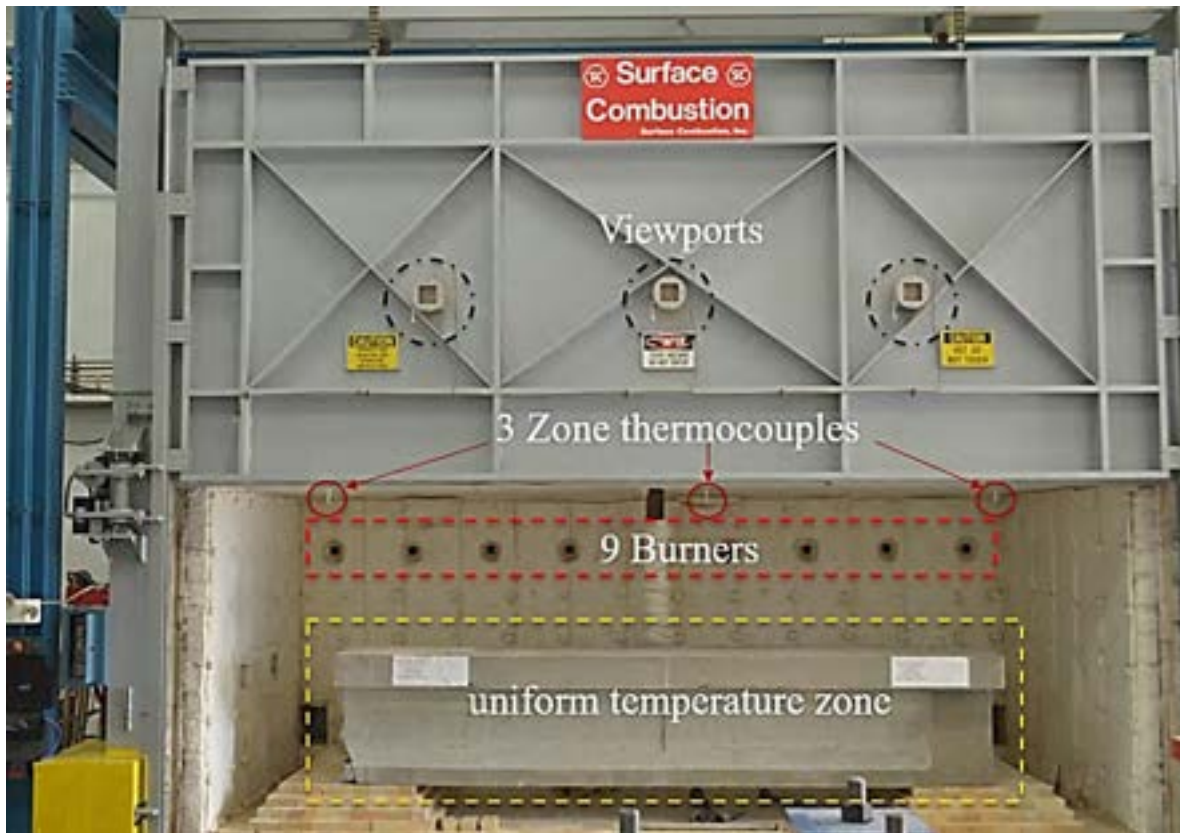
Figure 6.3-22 Furnace for fire testing

6.3.2.1 Test Setup & Instrumentation

The main objective of the tests was to determine the duration until failure of the beams under a fire/loading event. The test followed a three-step procedure that started with loading the specimens at ambient temperature in a three-point load test setup to a load level of 50 kip (222.4 kN) using a force-controlled module with a loading rate of 5 kip/minute (22.24 kN/minute). After reaching the load level of 50 kip (222.4 KN), the door of the heat chamber was closed and the fire test started and continued following the ASTM E119 time-temperature curve. The fire test was stopped when the beam specimen failed to support its own weight plus the applied load.

The linear transducer and the load cell of the hydraulic actuator were connected to a data acquisition system to monitor and record the deflection of the beam at midspan, as well as the applied load. Thermocouples embedded inside the beams recorded the temperature throughout the test as shown in Figure 6.3-23 and Figure 6.3-24. Additional thermocouples were placed around the beam to record air temperature within 10 in (254 mm) from the face of the beam. Figure 6.3-25 through Figure 6.3-28 shows schematic diagrams of all the beams showing the location of the thermocouples within the section of the beams. Figure 6.3-29 shows the setup of the fire test.

Figure 6.3-23 Installation of thermocouple into AASHTO I-beams

Figure 6.3-24 Measuring air temperature around the beam specimens
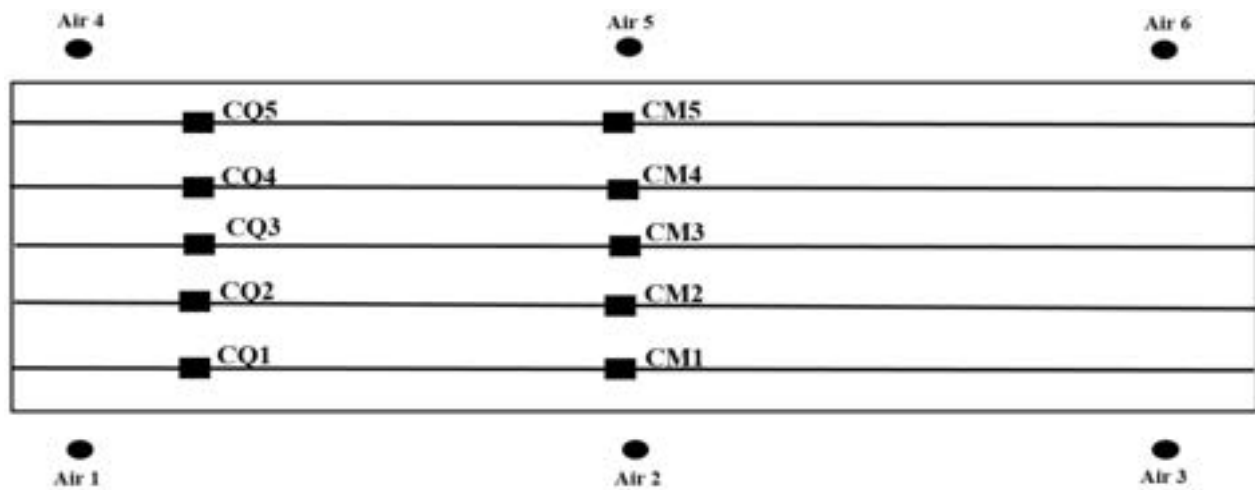
Figure 6.3-25 Location of thermocouples (on CFCC) in Beam T-0.7C
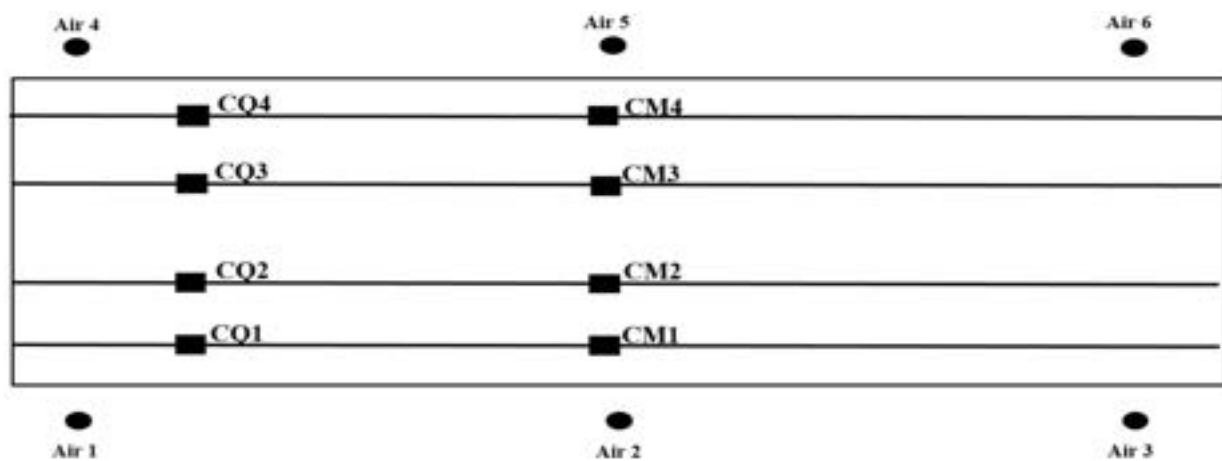
Figure 6.3-26 Location of thermocouples (on CFCC) in Beam B-0.7C
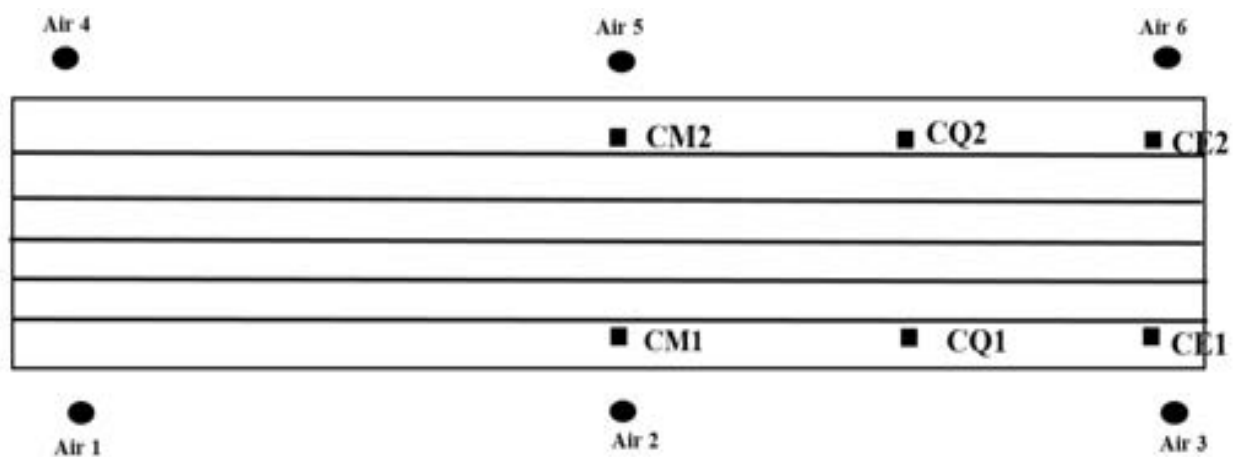
Figure 6.3-27 Location of thermocouples (on CFCC) in Beam I-0.6C

162
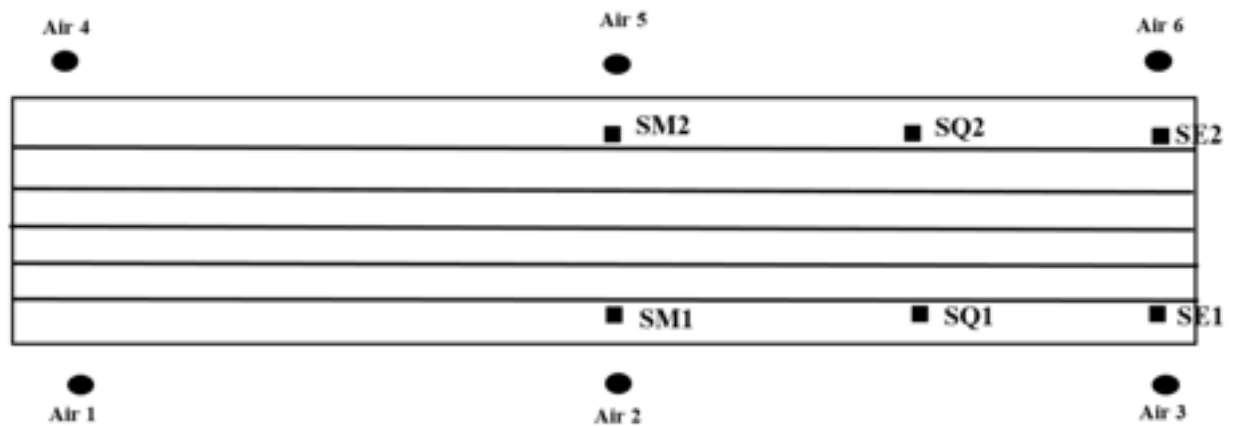
Figure 6.3-28 Location of thermocouples (on CFCC) in Beam I-0.6S

Figure 6.3-29 Beam I-0.6C before the fire test

6.3.2.2 Beam B-0.7C

Beam B-0.7C is a box beam pretensioned with four strands of 0.7″ CFCC. Figure 6.3-30 and Figure 6.3-31 show the time-temperature readings for all thermocouples on the CFCC at mid-section and quarter section of Beam B-0.7C, respectively. The average furnace temperature followed the ASTM E119 curve, with a maximum temperature of 1850 ºF (1010 ºC) after 136 minutes before failure of the beam.

163

The temperature of the CFCC strands gradually increased from 68 to 212 ºF (20 to 100 ºC) in 30 minutes followed by a phase of constant temperature plateau at 212 ºF (100 ºC), which lasted for 20 minutes. Lastly, the temperature of the CFCC strands at mid-section increased gradually to approximately 555 ºF (291 ºC) after an additional 86 minutes before failure of the beam. In summary, after 136 minutes of fire exposure, the maximum recorded temperature of the CFCC strands at mid-section was 555 ºF (291 ºC). All thermocouple readings at mid-section (CM1, CM2, CM3 and CM4) were uniform throughout the entire test, as shown in Figure 6.3-30. On the other hand, Figure 6.3-31 shows a little variation in the temperature of the strands at the quarter-section. Thermocouples CQ2 and CQ3 showed a similar temperature behavior as observed at mid-section, whereas thermocouples CQ1 and CQ4, corresponding to Strands 1 and 4, respectively, showed a higher variation in temperature. Higher temperature readings of 618 ºF (326 ºC) and 877 ºF (469 ºC) were recorded at Strands 1 and 4 in the quarter section at failure, respectively. This can be attributed to minor spalling of concrete around that section of the beam causing the outer strands to be exposed to more heat than the inner two strands. However, the research team found there was minimal spalling of the concrete along the length of the beam.

The mid-span deflection of Beam B-0.7C with respect to time and loading is shown in Figure 6.3-32 and Figure 6.3-33, respectively. The first 5 minutes show the loading phase of the beam at ambient temperature with a linear increase in deflection to 0.54 in (13.7 mm) as the 50-kip (222.4-kN) load was applied. The rest of the curve represented the deflection during the heating phase, while the beam was supporting the 50-kip (222-kN) load until failure. As shown in Figure 6.3-32, the beam maintained a constant stiffness (minor increase in deflection) during the first 75 minutes of heating. The minimum temperature of the CFCC strand at this stage was 276 ºF (136 ºC). Beyond this temperature, deflection gradually increased until it reached a maximum deflection of 4.9 in (124.5 mm). This increase was due to heat relaxation in the strands, which resulted in a loss of prestressing force. The increase in deflection continued until an abrupt failure was observed after 136 minutes of fire exposure and a maximum strand temperature of 877 ºF (469 ºC). From Figure 6.3-33, it was observed that the beam could not further sustain the 50-kip (222.4 kN) load, resulting in a sudden load drop until the beam split in half at midspan. Figure 6.3-34 through Figure 6.3-37 show the beam before and after testing. Figure 6.3-37 demonstrates that the strands debonded from the concrete at failure. Also, a close look at the strands through the opening at

164

midspan showed that all four strands were intact but the epoxy-matrix melted. It can be concluded that failure of the beam was triggered by a bond failure and not strand rupture. The average strand temperature at the time of failure was 752 ºF (400 ºC). At this temperature, the melting of epoxy matrix reduced the bond between the strands and the concrete, which caused the failure.
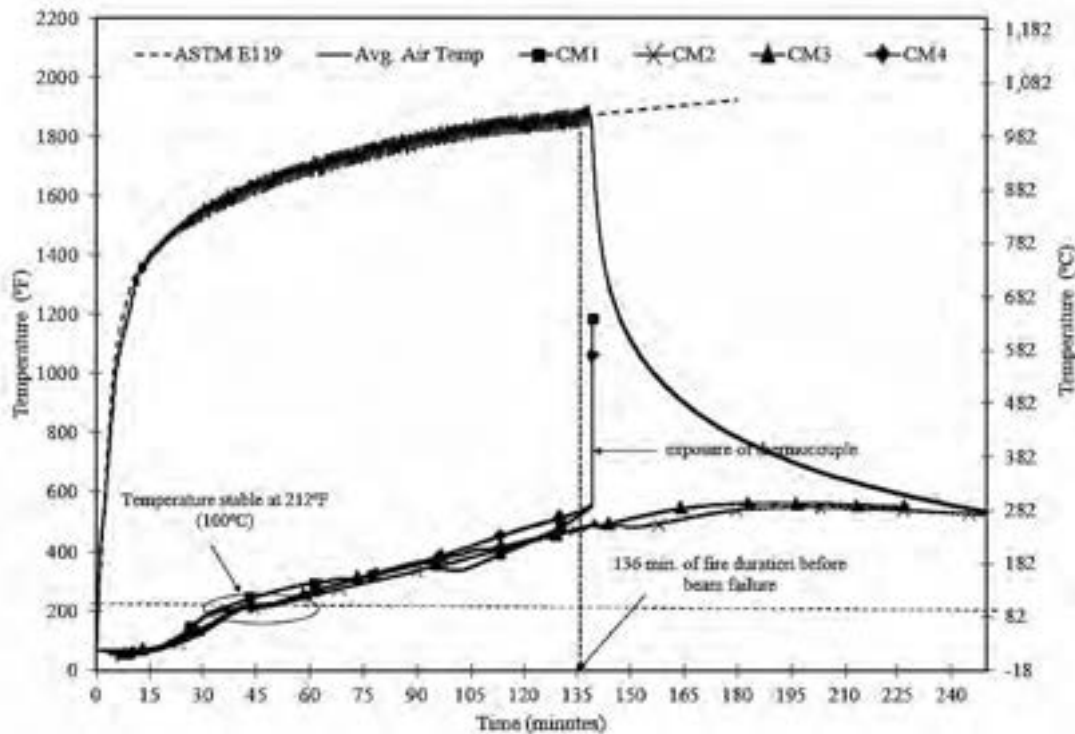
Figure 6.3-30 Time-temperature curve for B-0.7C (mid-section)
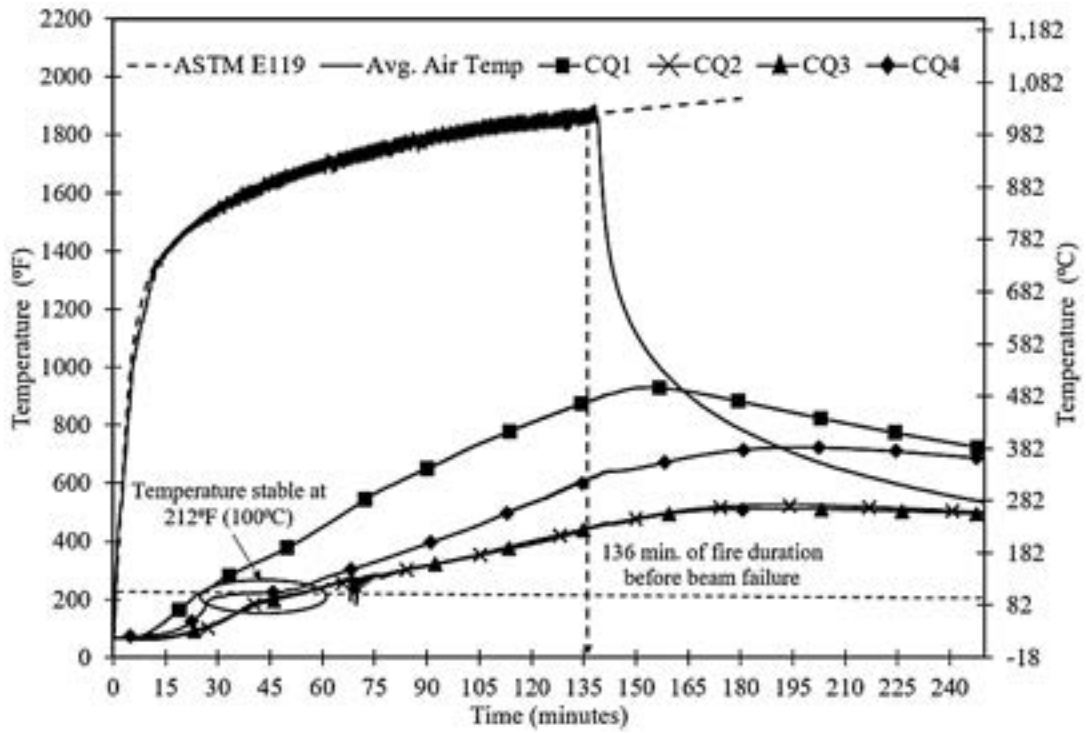
Figure 6.3-31 Time-temperature curve for B-0.7C (quarter-section)
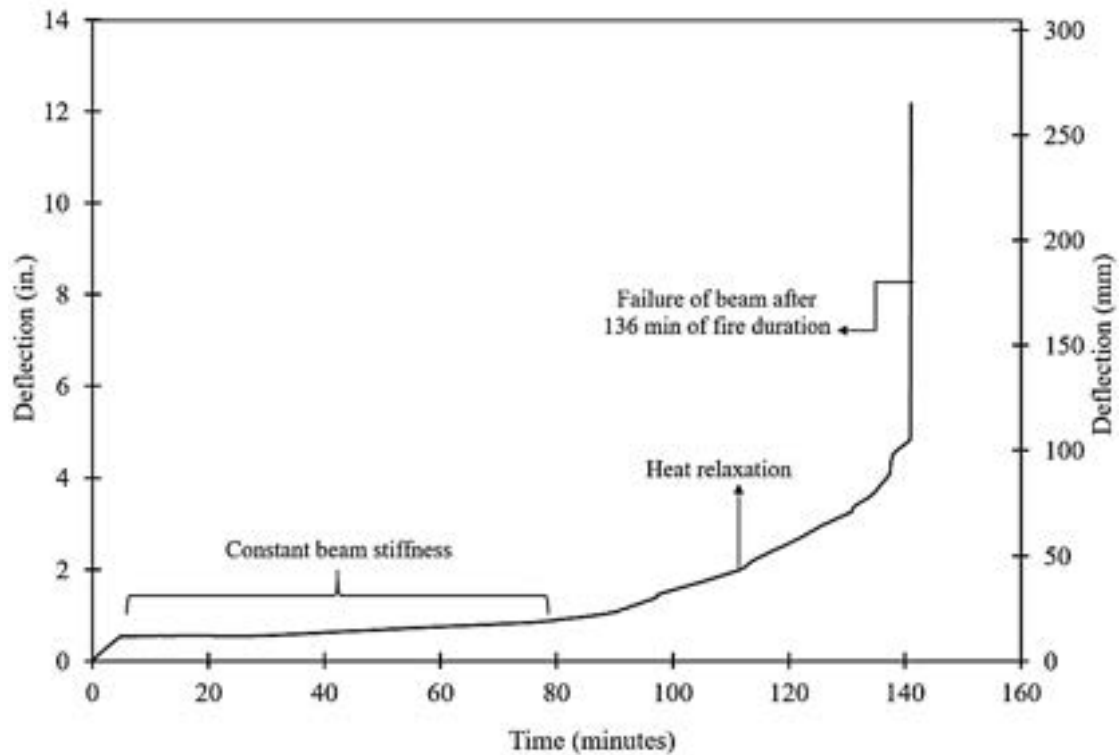
Figure 6.3-32 Time-midspan deflection curve for B-0.7C

166
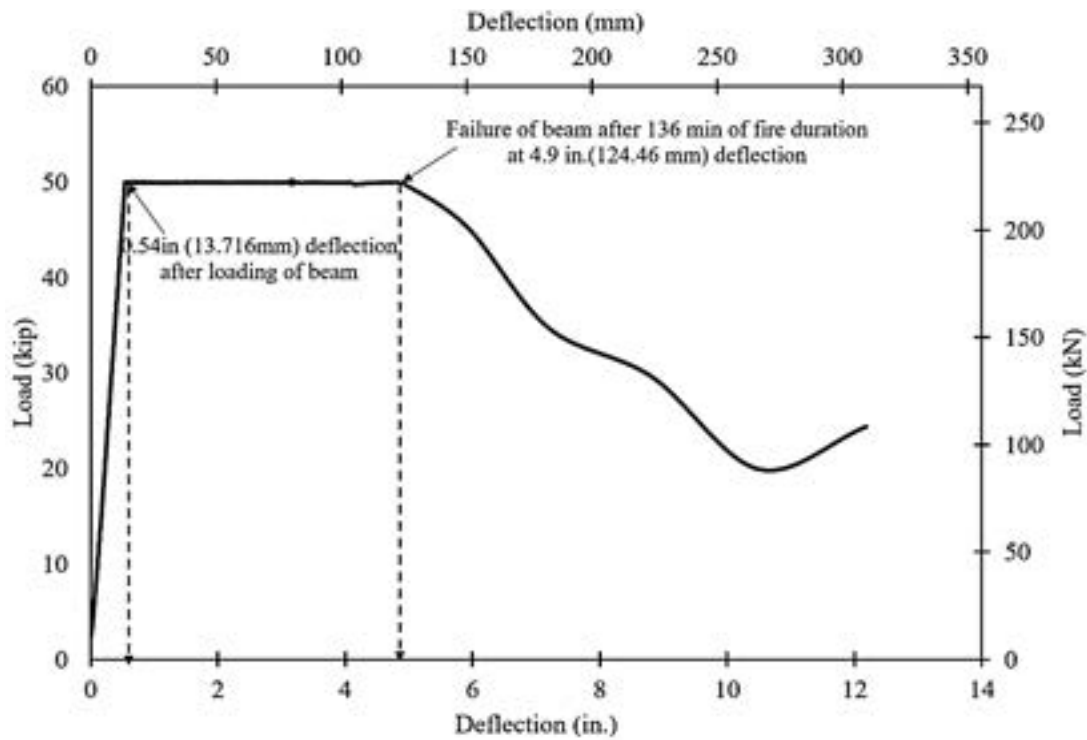
Figure 6.3-33 Load-midspan deflection curve for B-0.7C

Figure 6.3-34 Beam B-0.7C before fire test

Figure 6.3-35 Beam B-0.7C after fire test

Figure 6.3-36 CFCC strand exposed at midspan at failure

Figure 6.3-37 CFCC Strands debonded from concrete at failure

6.3.2.3 Beam T-0.7C

Beam T-0.7C, a bulb T beam pretensioned with five 0.7″ CFCC strands, was subjected to a load level of 50 kip (222 kN) during a fire event according to ASTM E119. The time-temperature readings of the CFCC strands at mid-section and quarter section of the beam are shown in Figure 6.3-38 and Figure 6.3-39, respectively. The average air temperature in the furnace closely followed the ASTM E119 time-temperature curve, with a maximum furnace temperature of 1775 ºF (968 ºC) after 93 minutes before failure of the beam.

As shown in Figure 6.3-38, there was a steady increase in the temperature of the CFCC strands at midspan from 68 to 212 ºF (20 to 100 ºC) in 20 minutes. After that, a temperature plateau of 212 ºF (100 ºC) lasted for 20 minutes. Spalling of concrete in the top flange of the beam was observed during this time and resulted in minimal temperature fluctuations. This could be attributed to the susceptibility of the cantilever flange of the bulb T section and the relatively young age (12 months) of the beam. After moisture escaped from the beam, the temperature increased continuously to a maximum of 511 ºF (266 ºC) and 625 ºF (329 ºC) at the mid-section and the quarter section, respectively, over a duration of 53 minutes. After which, the beam failed with a total fire endurance of 93 minutes. Despite the spalling of concrete in the top flange, as seen in Figure 6.3-47, the thermal profile showing the temperature increase in the strand for both mid-section and quarter-section were similar. In addition, CFCC strands closer to the edges of the bottom flange (CQ1, CM4, and CQ4) experienced higher temperatures than those of interior strands.
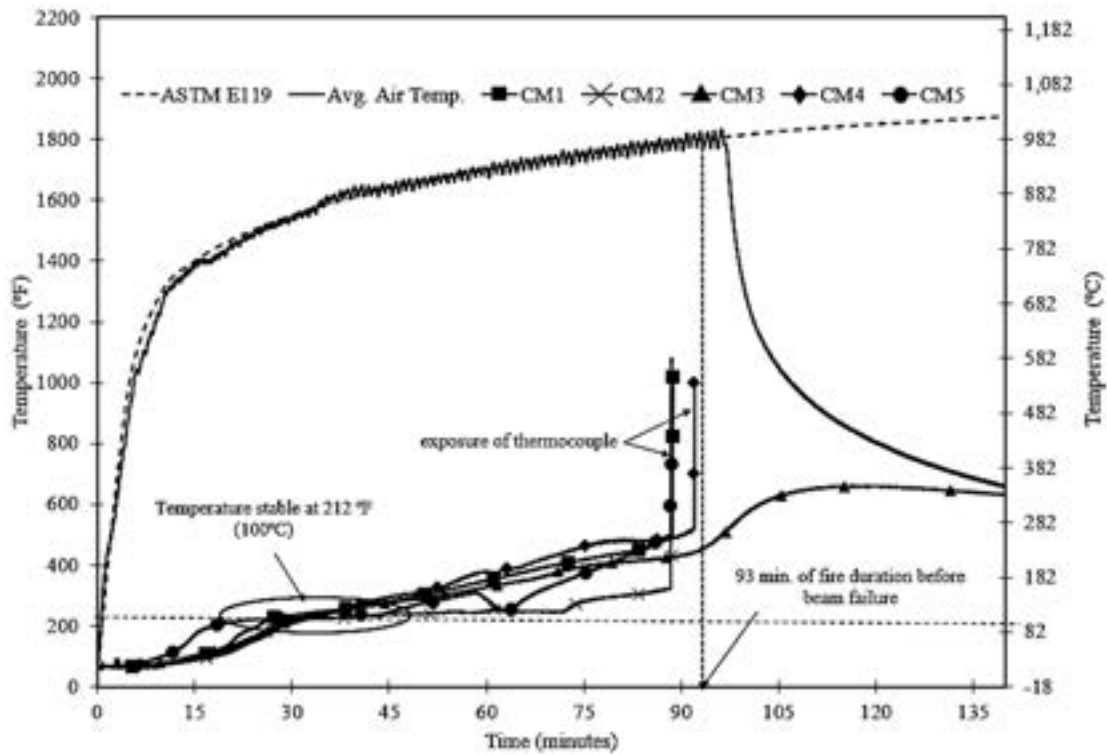
Figure 6.3-38 Time-temperature curve for T-0.7C (mid-section)
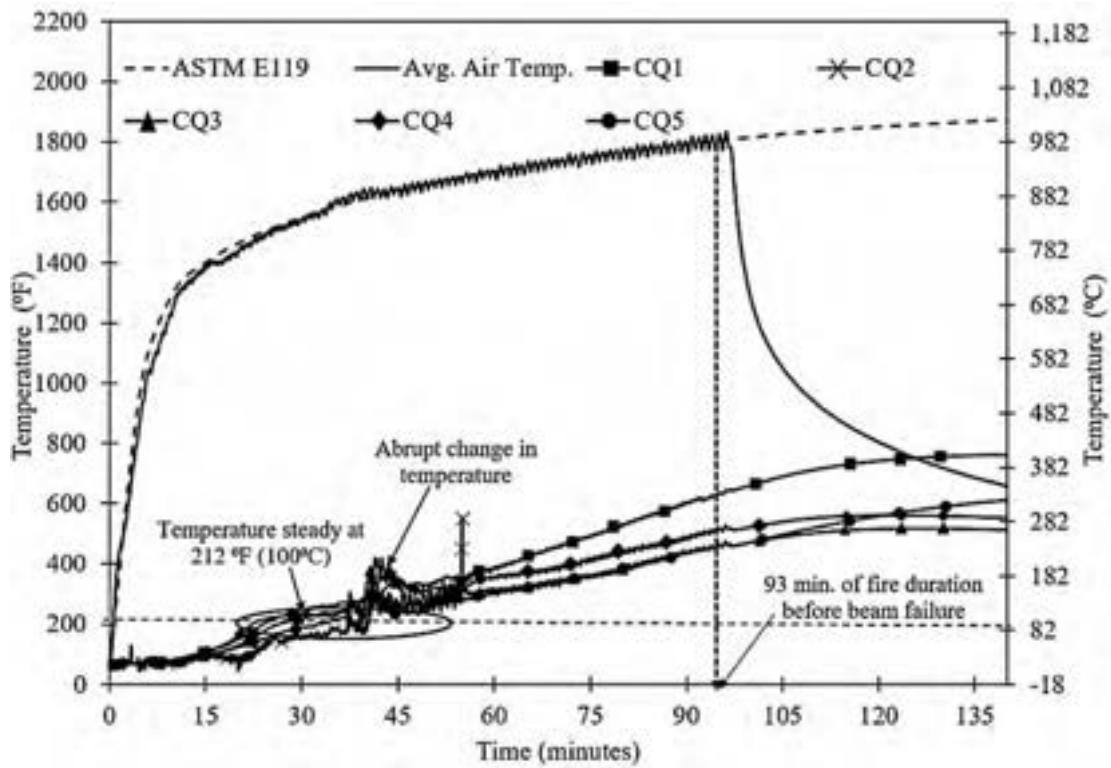
Figure 6.3-39 Time-temperature curve for T-0.7C (quarter section)

170

Figure 6.3-40 shows the time-deflection curve at mid-section. A steady increase in deflection during loading to 50 kip (222 kN) with a maximum deflection of 0.59 in (14.99 mm) was observed. The heating phase started after achieving the load level of 50 kip (222 kN). It was observed that the stiffness of the beam was fairly constant during the first 86 minutes of heating with negligible changes in deflection. The minimum strand temperature recorded by the thermocouples during the first 86 minutes of the test was 411 °F (210 °C). The deflection after this phase increased sharply until reaching a maximum deflection of 4.02 in (102.11 mm), when an abrupt failure was observed. The heating phase lasted for 93 minutes before failure of the beam. Figure 6.3-41 shows the load-deflection curve. A continuous decrease in the load level was observed at the time of failure. The conditions of the beam before, during, and after testing are shown in Figure 6.3-42 through Figure 6.3-47. Similar to Beam B-0.7C, all five CFCC strands debonded from the concrete at failure, as shown in Figure 6.3-46. Also, a close observation of the strands at mid-section and at failure indicated that the strands were still intact with significant damage to the epoxy matrix. Again, it can be concluded that the failure of the beam was triggered by the CFCC-concrete bond degradation due to the elevated temperature. Debonding of the strands from the concrete occurred at a CFCC temperature of approximately 625 °F (329 °C) as the epoxy matrix melted.
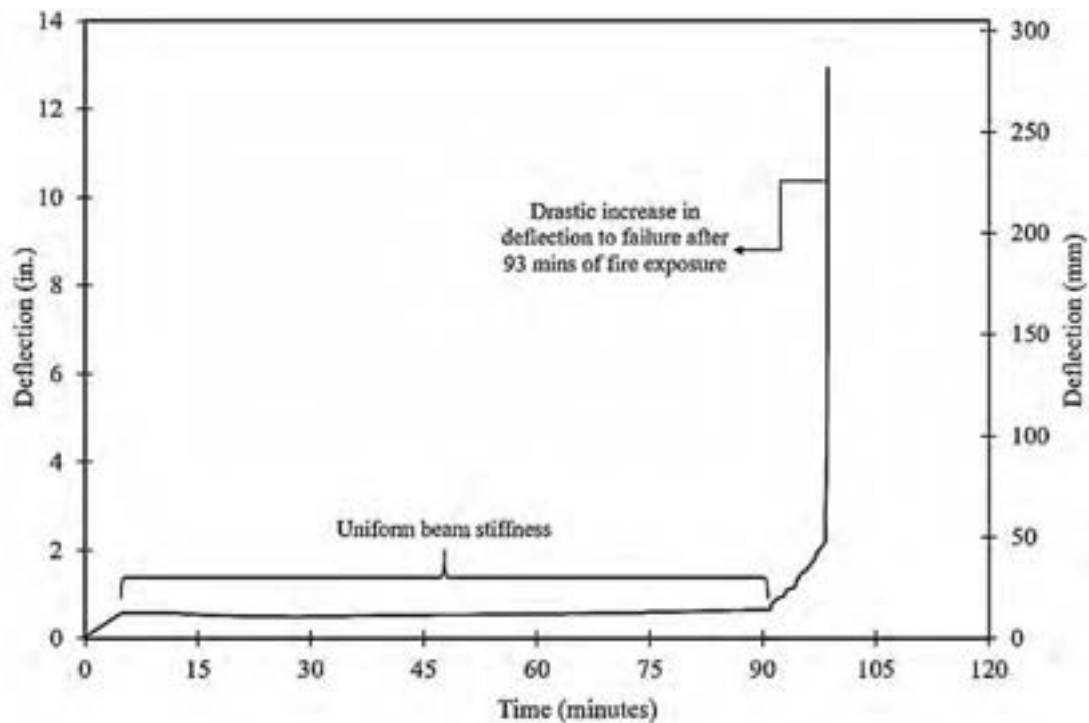
Figure 6.3-40 Time-midspan deflection curve for Beam T-0.7C
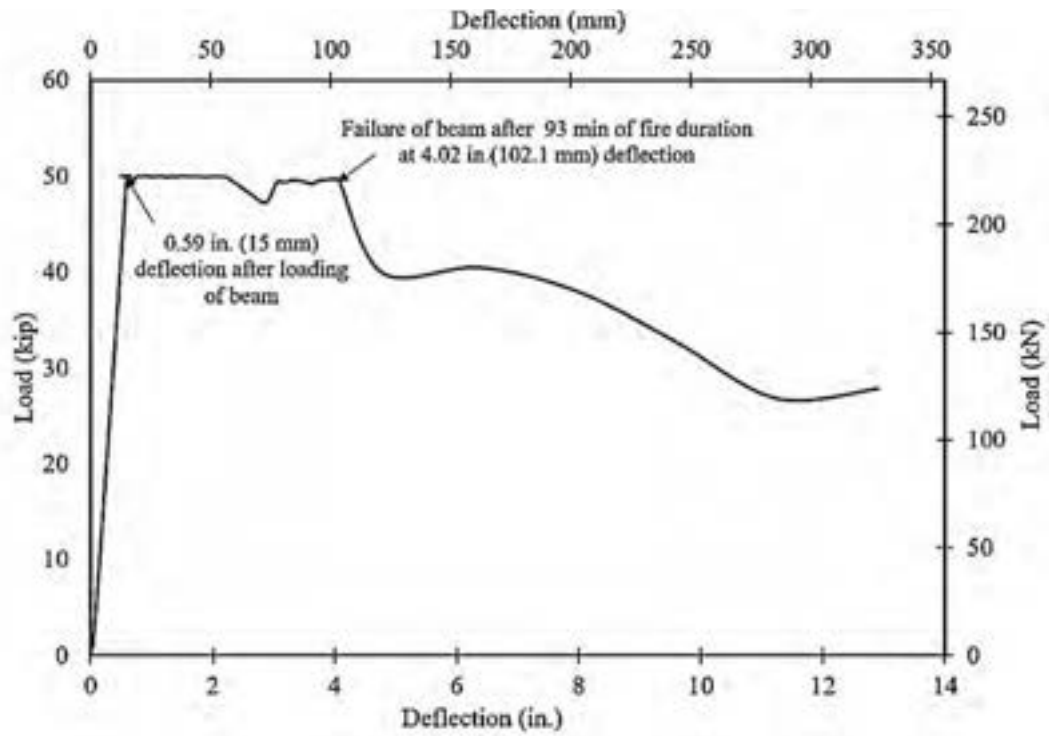
Figure 6.3-41 Load-midspan deflection curve for Beam T-0.7C

Figure 6.3-42 Beam T-0.7C before fire test

Figure 6.3-43 Beam T-0.7C during fire test

Figure 6.3-44 Beam T-0.7C after fire test

Figure 6.3-45 CFCC strands exposed at midspan at failure

Figure 6.3-46 Slipped CFCC strands from concrete at failure

Figure 6.3-47 Spalling of concrete at top flange of beam

6.3.2.4 Beam I-0.6C

Beam I-0.6C, a salvaged beam prestressed with five bonded 0.6″ CFCC strands, was subjected to a load/fire event similar to other beams. The furnace temperature reached 1840 ºF (1004 ºC) immediately before beam failure. A temperature plateau was also observed at 212 ºF (100 ºC), which lasted for 20 minutes. During this phase, moisture was visibly evaporating from the concrete. The temperature profile for Beam I-0.6C showed the temperature of the CFCC strands reaching a maximum of 885 ºF (474 ºC) after 136 minutes of fire exposure before failure. Figure 6.3-48 and Figure 6.3-49 show the time-temperature curves at mid, quarter and end-sections of the beam.

From Figure 6.3-50, it can be observed that Beam I-0.6C reached the target load-level of 50 kip (222.4 kN) with a corresponding midspan deflection of 0.73 in (29 mm) before the start of the fire test. During the fire test, the load level was sustained with a negligible change in deflection for the first 85 minutes. The maximum temperature for this constant stiffness (no increase in deflection) was 398 ºF (203 ºC). This temperature matches closely to that of Beam T-0.7C of 411 ºF (210 ºC). It should be noted that both beams, T-0.7C and I-0.6C, had the same area-to-volume ratio (0.28) and hence heat transfer through the concrete to the strands was similar. The deflection

175

increased gradually after the plateau stage. The gradual increase was due to the heat relaxation of the strands, which caused loss of prestressing force, crack development and subsequently more deflection in the beam.

Figure 6.3-51 through Figure 6.3-55 show Beam I-0.6C before and after the fire test. The maximum deflection before beam failure was 6.1 in (155 mm). Increase of deflection during the fire was observed at a CFCC temperature of 398 °F (203 °C), while melting of epoxy matrix occurred at approximately 885 °F (474 °C), causing bond failure and triggering the failure of the beam after 136 minutes of fire exposure. All CFCC strands debonded from the concrete as shown in Figure 6.3-54. As shown in the figures, a large midspan crack developed during the test and the CFCC strands were exposed at mid-section at failure. After 48 hours of cooling the beam, the concrete changed in color from gray to dark brown and disintegrated into very fine particle, as shown in Figure 6.3-55.
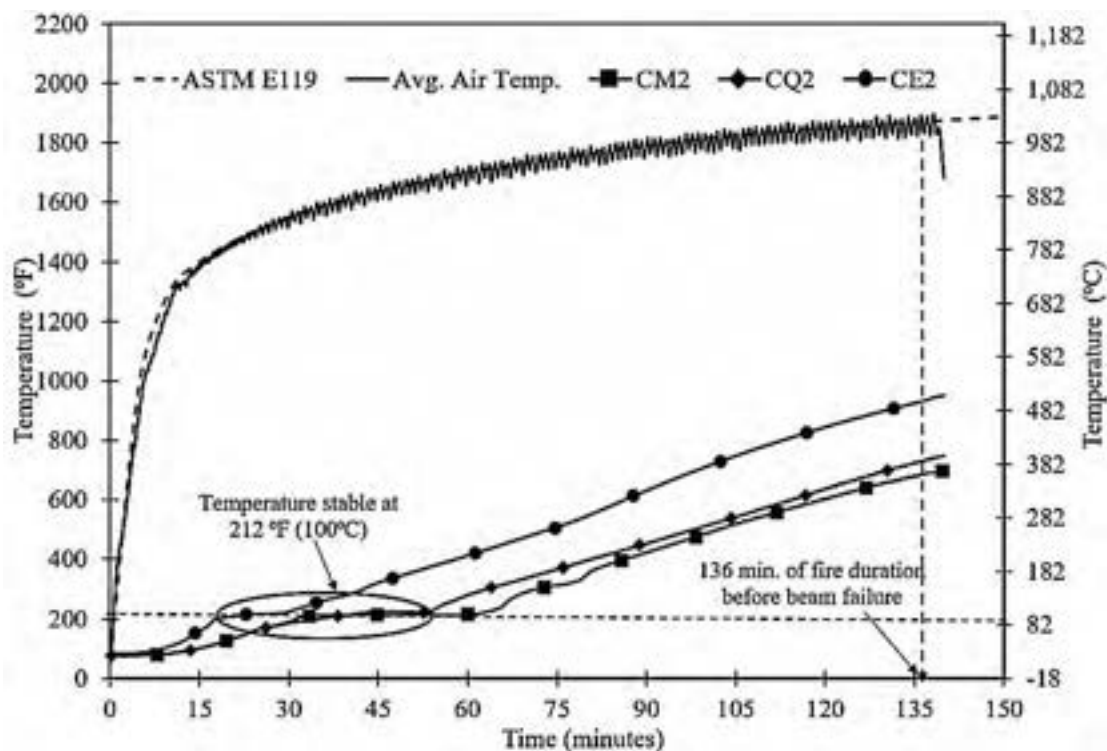
Figure 6.3-48 Time-temperature curves for Beam I-0.6C
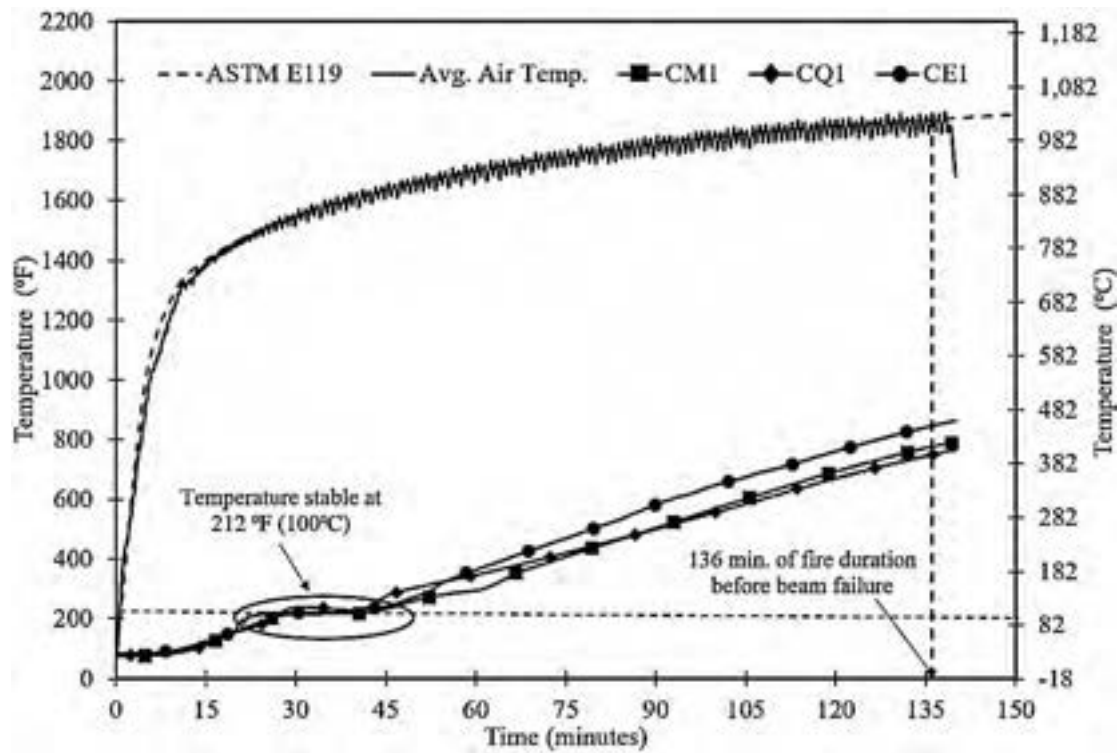
Figure 6.3-49 Time-temperature curves for Beam I-0.6C
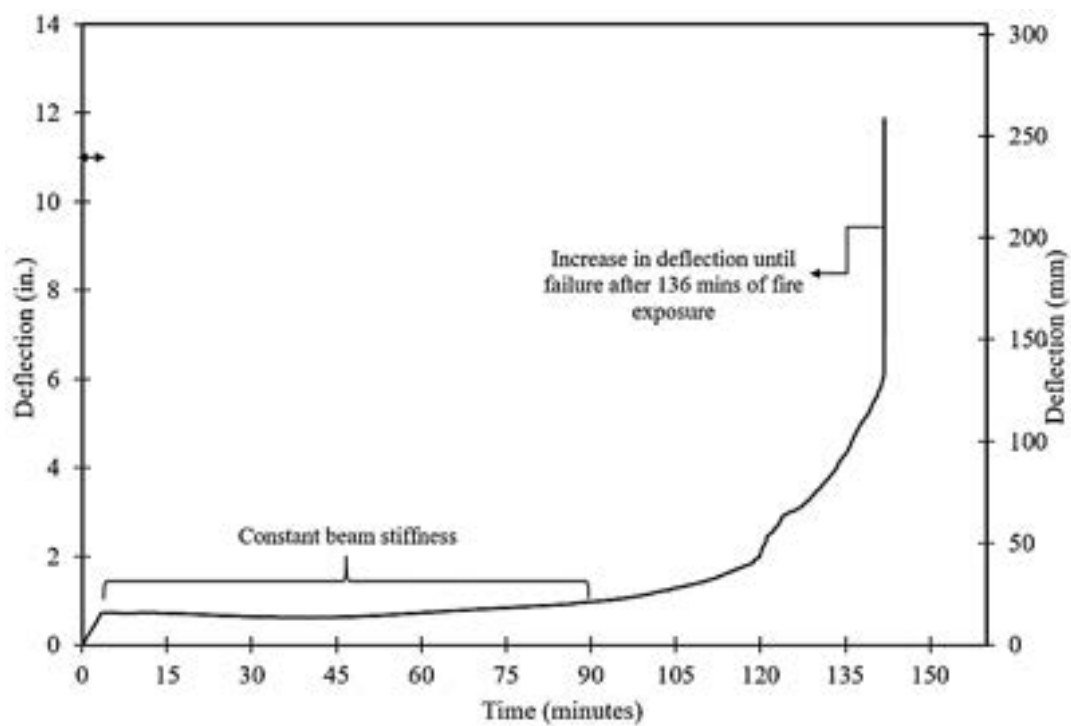
Figure 6.3-50 Load-time curve for Beam I-0.6C

Figure 6.3-51 Beam I-0.6C before fire test

Figure 6.3-52 Beam I-0.6C after fire test

Figure 6.3-53 CFCC strands exposed at midspan at failure

Figure 6.3-54 CFCC strands slippage from concrete at failure

Figure 6.3-55 Excessive spalling of concrete 48 hours after fire test

6.3.2.5 Beam I-0.6S

Beam I-0.6S, prestressed with five 0.6″ low-relaxation steel strands, was subjected to the same loading and fire events as described for other beams. The test lasted until beam failure after 330 minutes of fire exposure at an air temperature of 2130 ⁰F (1166 ⁰C). During the heating phase, the temperature of steel strands increased gradually until reaching a temperature plateau at 212 ⁰F (100 ⁰C). The temperature plateau continued for 18 minutes as shown in Figure 6.3-56 and Figure 6.3-57. After that, the strand temperature continued to increase with time. Out of six thermocouples at the level of the steel strands, five thermocouples disintegrated after 180 minutes of fire exposure with a average reading of 1280 ⁰F (693 ⁰C) at that time. The sixth thermocouple remained intact until the failure of the beam and indicated a temperature of 1391 ⁰F (755 ⁰C) at failure.

The failure temperature at the level of the steel strands in Beam I-0.6S was 1391 ⁰F (755 ⁰C) after 330 minutes. This was significantly higher than the failure temperature at the level of the CFCC strands of 885 ⁰F (474 ⁰C) in Beam I-0.6C after 136 minutes of fire exposure. The time-temperature profiles of the strands in both beams, where were identical in geometry, compared favorably well as shown in Figure 6.3-58.
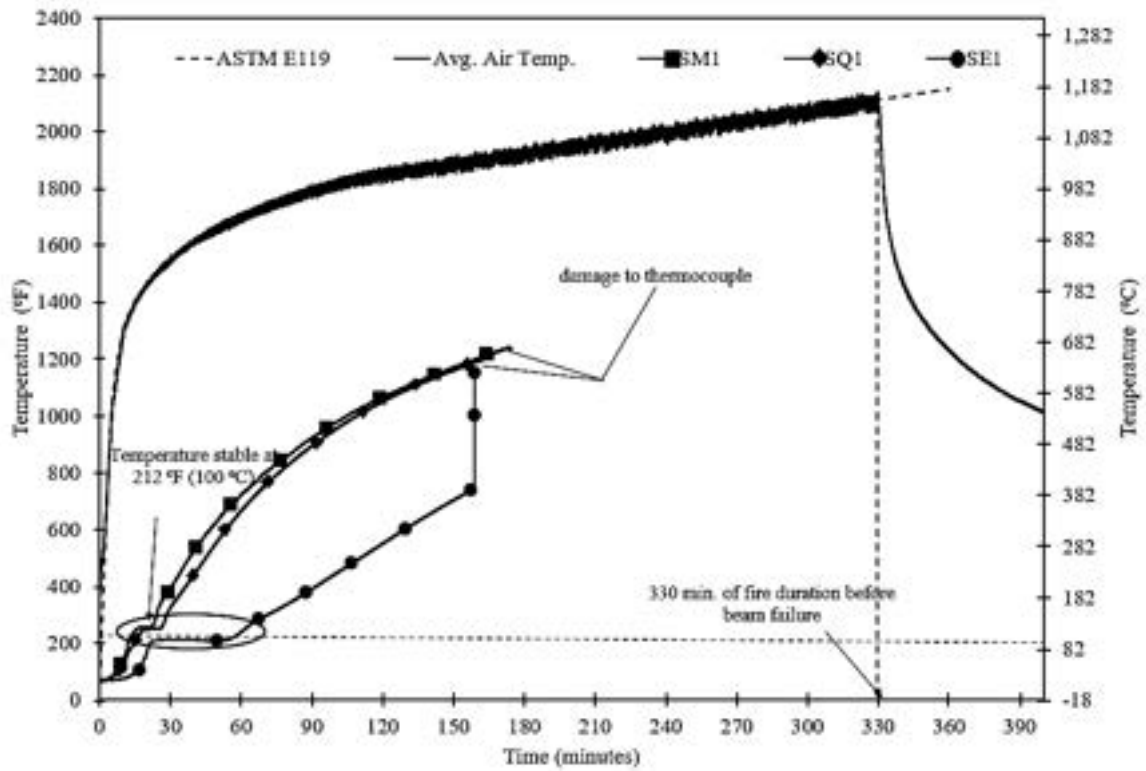
Figure 6.3-56 Time-temperature curves for Beam I-0.6S
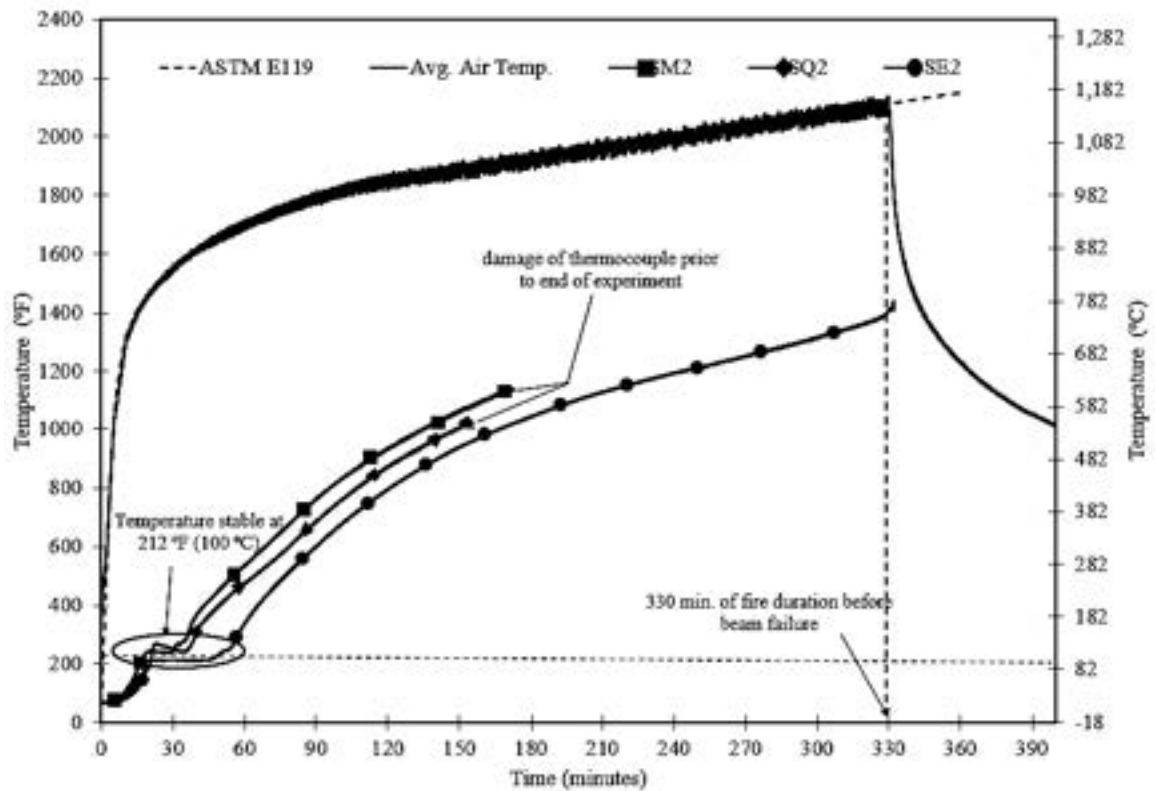
Figure 6.3-57 Time-temperature curves for Beam I-0.6S
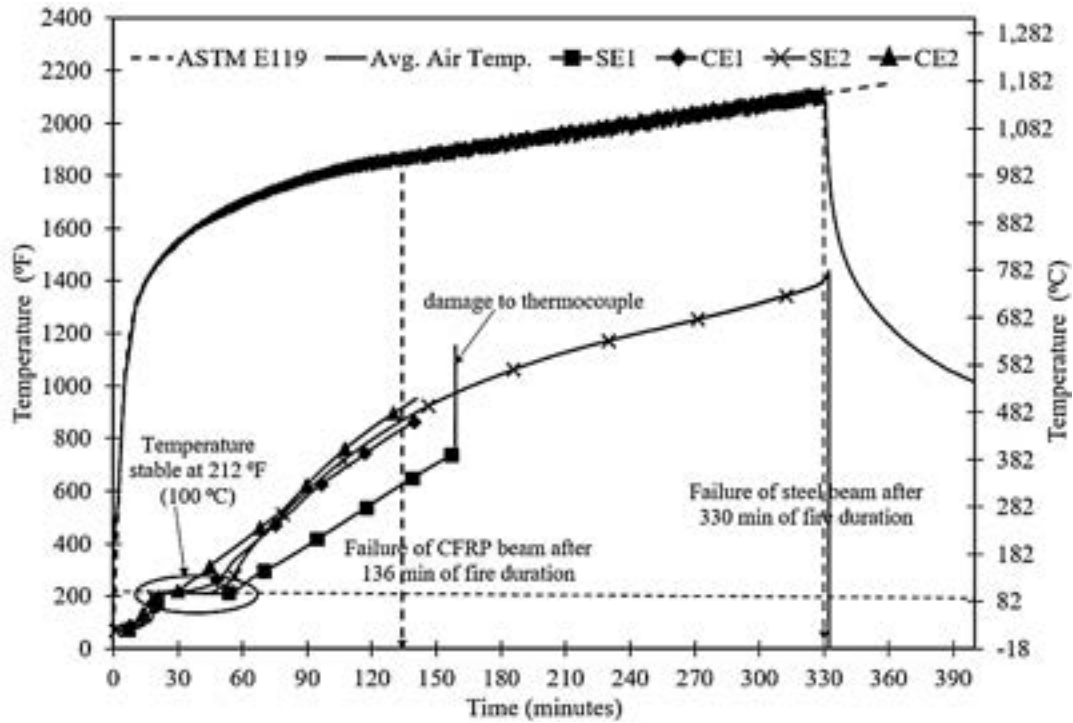
Figure 6.3-58 Time-temperature curves for Beams I-0.6C and I-0.6S (end-section)

Prior to the fire test, the deflection of Beam I-0.6S at midspan increased steadily under the 50-kip (222 kN) load to a deflection of 0.54 in (13.7 mm) in 5 minutes, as shown in Figure 6.3-59. The heating phase started immediately after loading. The deflection in the beam remained constant for the next three hours. The downward dip in the curve was due to the expansion of the steel loading ram. Afterwards, the deflection in the beam increased gradually to a maximum of 5 in (127 mm) at a temperature of 1390 ⁰F (754 ⁰C) immediately before failure. The gradual increase in deflection can be attributed to the loss in strength of the prestressing strands, which is estimated between a loss of 80 % (EN1991-1-2, CEN 2004) and 68 % (PCI 2004) at a steel temperature of 932 ⁰F (500 ⁰C). A comparison between the load-deflection curves of Beams I-0.6C and I-0.6S is presented in Figure 6.3-60.

Beam I-0.6S, before and after the test, is shown in Figure 6.3-61 through Figure 6.3-65. Figure 6.3-63 indicates that all strands ruptured with the exception of one strand that was originally debonded and slipped at prior flexural test. It can therefore be concluded that the failure of the beam was triggered by strand rupture as a result of loss of strength in the strands due to elevated temperatures.
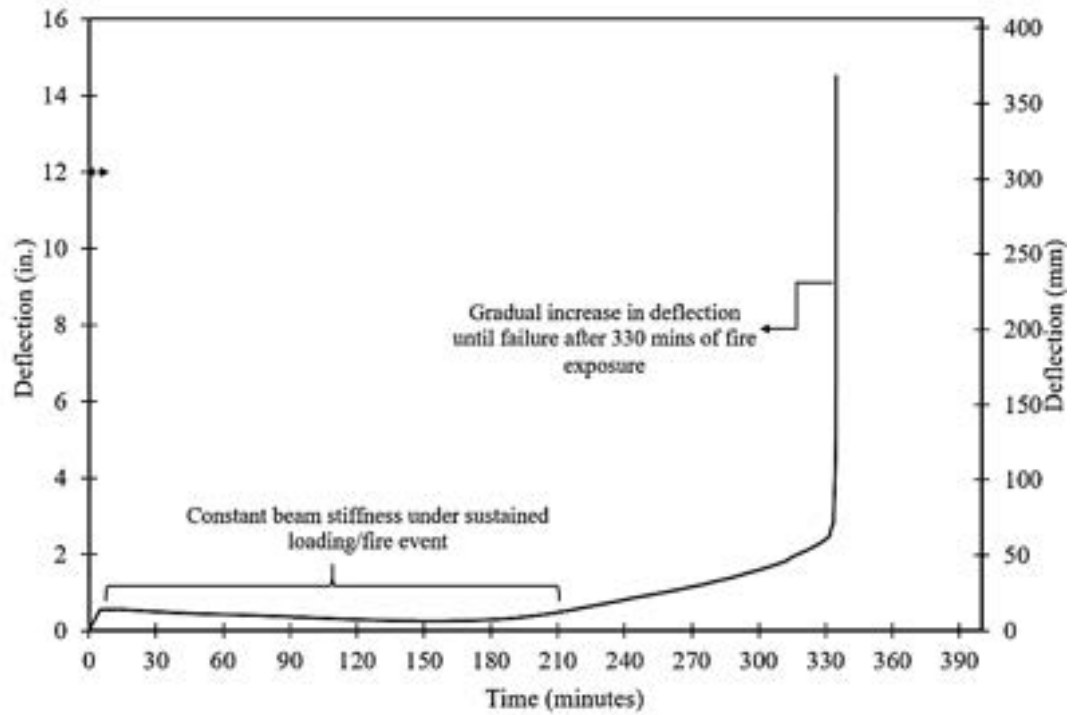
Figure 6.3-59 Time-deflection curve for Beam I-0.6S
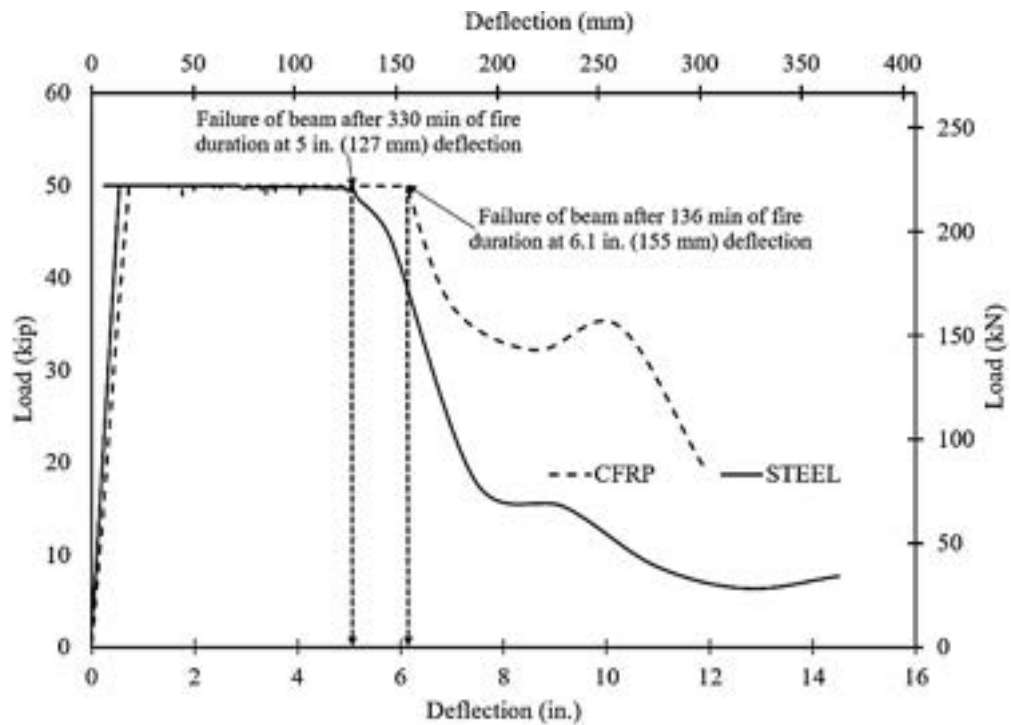
Figure 6.3-60 Load-deflection curves for Beams I-0.6C and I-0.6S

183

Figure 6.3-61 Beam I-0.6S before fire test

Figure 6.3-62 Beam I-0.6S after fire test

Figure 6.3-63 Rupture of steel strands at midspan

Figure 6.3-64 Steel strands remained bonded to concrete after testing of I-0.6S

Figure 6.3-65 Excessive spalling of concrete after 48 hours

6.3.3 Beam Fire Test Phase II

6.3.3.1 Details of Test Specimens

The objective at this test phase was to determine the residual flexural capacity and the mode of failure of the prestressed beams after exposure to the fire/loading event for one hour. The applied load and the time-temperature curve of the fire event were similar to those explained under Phase I with the exception that the tests lasted for only one hour. After that, the load was removed and the beam was allowed to cool down gradually to ambient temperature. The beams were then moved to a loading facility, where they were loaded at ambient conditions in a three-point-load test setup to failure. A displacement control module with a loading rate of 0.15 in/min (3.8 mm/min) was used for the flexural test. At a load level of 50 kip (222 kN), the test was paused and crack width at the mid-section of the beam was measured. Loading was then further applied until failure of the beam.

Similar to Phase I, all four beams at this stage of the test had thermocouples installed before the fire/loading stage of the test. Thermocouples were also used to obtain the air temperature around the beams during the fire test. The deflection of the beams was measured by recording the displacement of the loading actuator during the fire test.

In the flexural test, four String Pots (Figure 6.3-66 and Figure 6.3-67) were attached at midspan of the beam to capture the deflection during the test. Two of the String Pots were attached to the top of the beam and two were attached to the bottom of the beam. The load was applied using a 220-kip (980-kN) hydraulic actuator. All instruments were calibrated and connected to a data acquisition system (DAS) to record the load and deflection.

Figure 6.3-66 Installation of String Pot. at the soffit of the beam

Figure 6.3-67 Installation of String Pot. at the top of the beam

6.3.3.2 Beam RB-0.7C

The time-temperature curves of Beam RB-0.7C, Figure 6.3-68 and Figure 6.3-69, were similar to that observed for Beam B-0.7C in Phase I. The furnace reached a maximum air temperature of 1693 °F (923 °C) after the one-hour duration. When the heating phase ended after an hour, the temperature within the beam continued to increase during the cooling stage before eventually dropping. The maximum temperature recorded within the strands at both the midspan and quarter sections, after 3 hours of cooling, was 490 °F (254 °C). The rise in temperature within all four strands was relatively uniform. A temperature plateau was observed at 212 °F (100 °C), which lasted for 20 minutes before the temperature increased again.

The deflection (Figure 6.3-70) after loading the beam to 50 kip (222 kN) at ambient conditions was 0.6 in. (15 mm). This value remained constant for about 30 minutes through the heating cycle before it gradually increased to 0.9 in. (23 mm) by the end of the experiment. It should be noted that this recorded displacement is a combination of the beam deflection and the thermal expansion of the actuator ram. The maximum strand temperature was 400 °F (204 °C) after one hour of fire exposure.

A camber of 0.19 in. (5 mm) was measured at the soffit of the beam before the fire test. This value, however, decreased to 0.06 in. (1.6 mm) after the fire test. Also, an average end slippage of 1.57 in (40 mm) was recorded on each strand after one hour of fire duration. This shortening in length of the strand corresponds to 46 kip (206 kN) loss in prestressing force. Heat relaxation of the strand could also result in further loss of prestressing force after the fire test. After cooling the beam, visible cracks were seen on the beam. The maximum crack width observed at mid-section of the beam was 0.02 in. (0.5 mm). Figure 6.3-71 through Figure 6.3-73 shows the beam before, during and after the fire test.
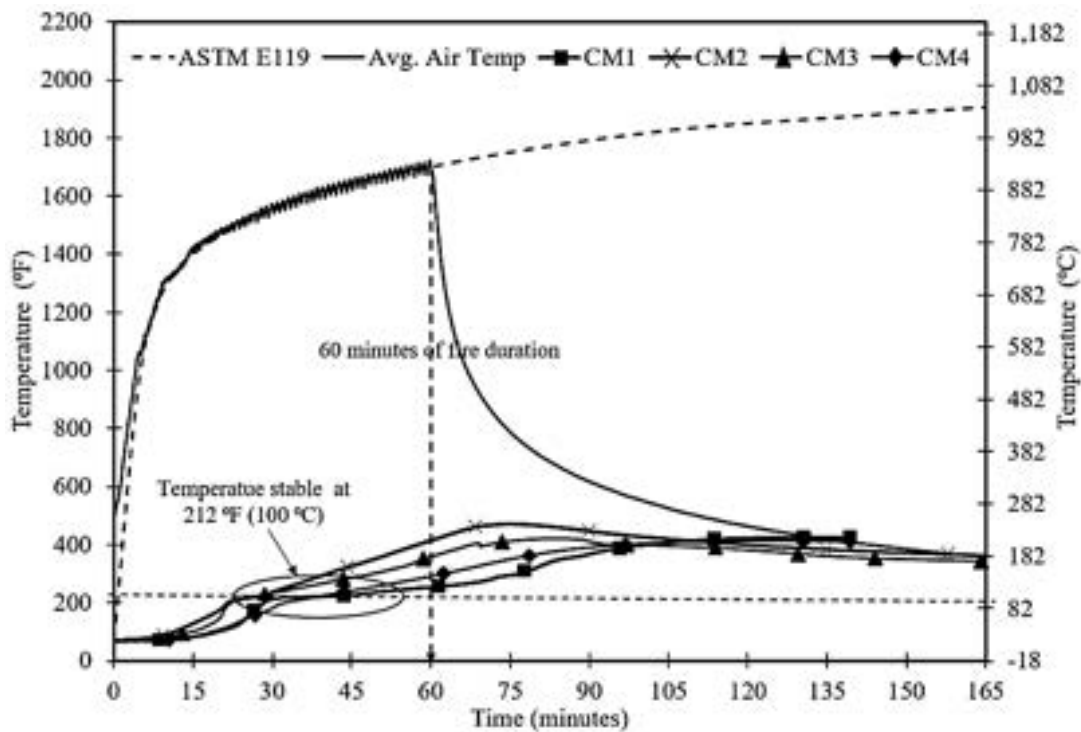
Figure 6.3-68 Time-temperature curves of Beam RB-0.7C (midspan)

189
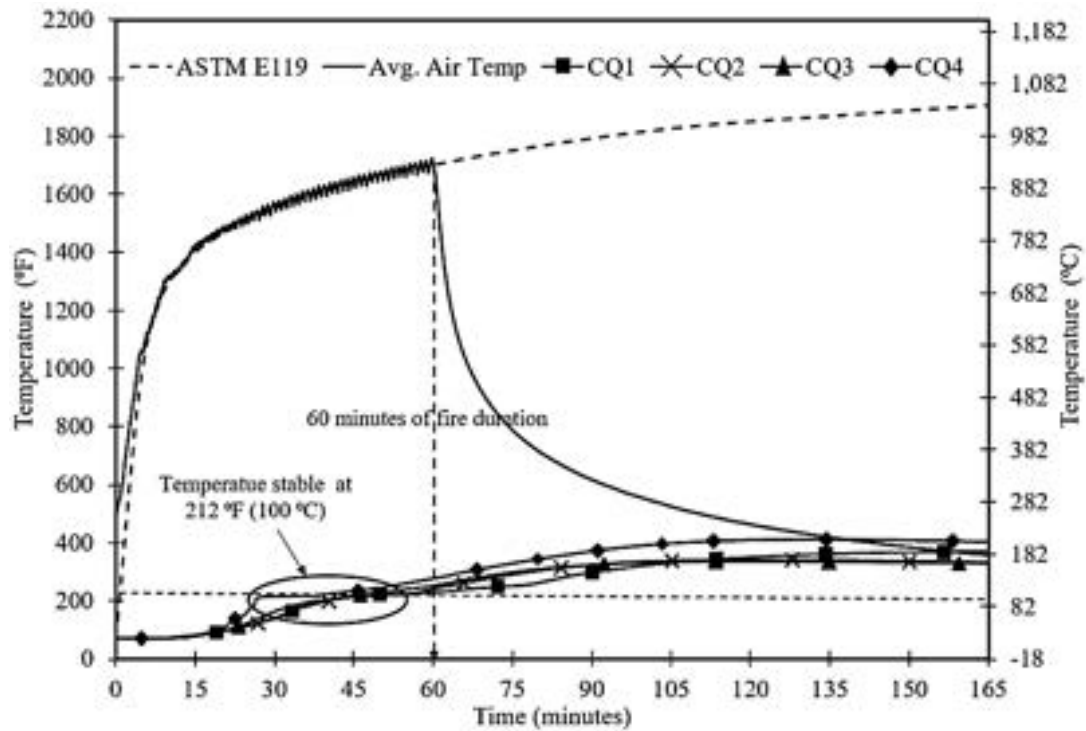
Figure 6.3-69 Time-temperature curves of Beam RB-0.7C (quarter section)
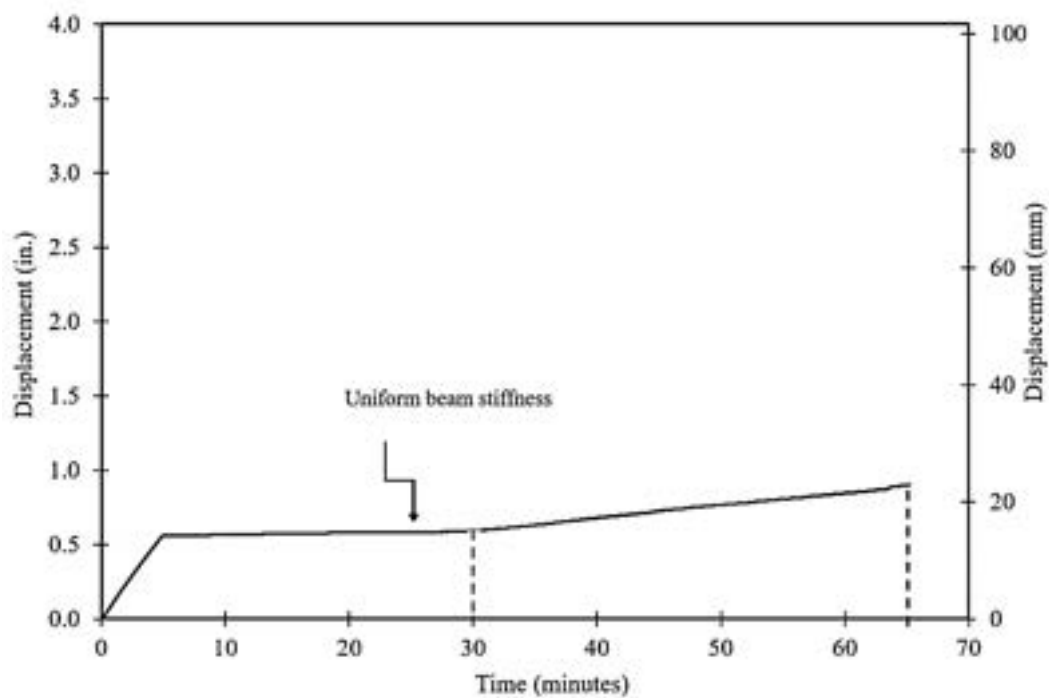
Figure 6.3-70 Time-deflection curve of Beam RB-0.7C (midspan) during fire

190

Figure 6.3-71 Beam RB-0.7C before fire test
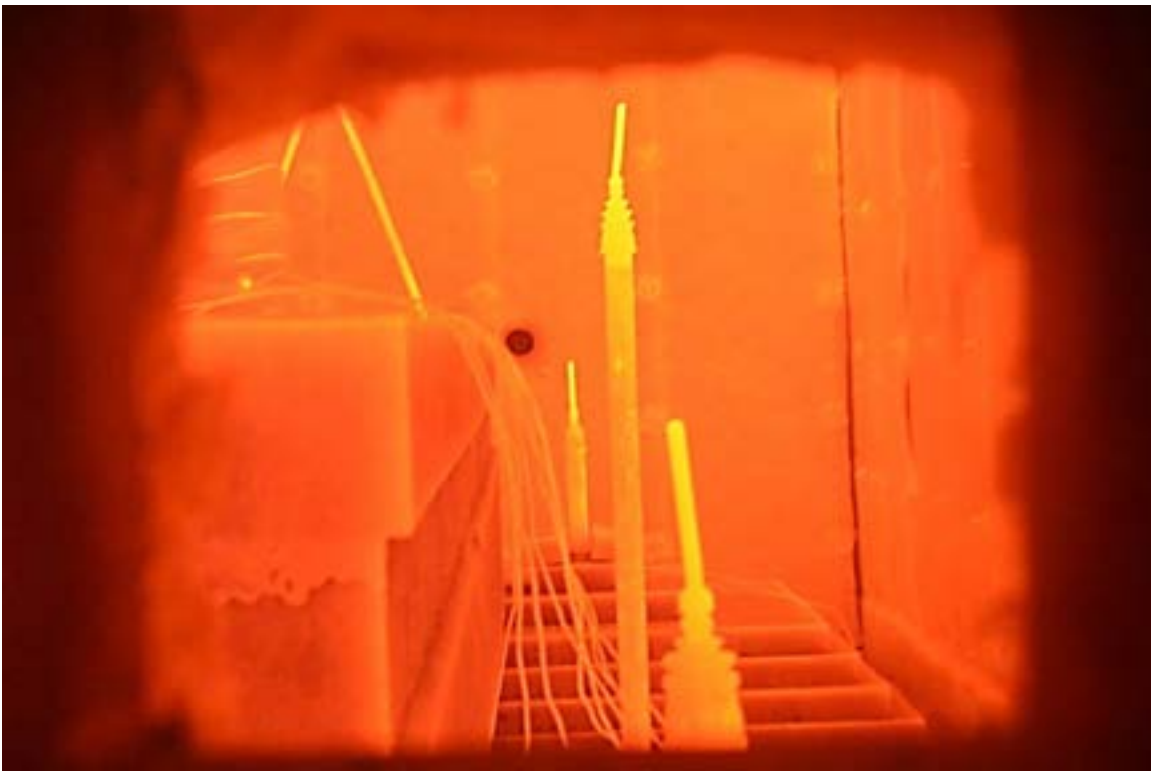
Figure 6.3-72 Beam RB-0.7C during fire test

Figure 6.3-73 Beam RB-0.7C after one-hour fire test

The theoretical capacity of Beam RB-0.7C was 210 kip (934 kN) without considering any previous fire loading. For the ultimate flexural test, the beam was loaded monotonically until failure. As shown in Figure 6.3-74, the load-deflection curve shows no decompression load. This behavior is similar to that expected for a reinforced concrete section that is not prestressed. The loss in the prestressing force occurred during the fire/loading phase of the experiment.

During loading, the deflection of the beam at 50 kip (222 kN) was 0.53 in. (14 mm). Cracks along the mid-section of the beam continued to widen and increased in length towards the deck. The linear segment in the load-deflection curve continued until the load reached 160 kip (712 kN). After that, the slope of the curve decreased with significant deflection occurring after a small change in load. This could be attributed to a gradual slipping of the strands. The deflection continued to increase until the failure of the beam at a maximum load of 179 kip (796 kN) and a corresponding deflection of 4.1 in. (104 mm). The failure was accompanied with a sudden drop in the load to 42 kip (187 kN). The load increased again to 92 kip (409 kN) but dropped instantly afterwards due to the continuous slippage of the strands. The residual capacity of the beam was

recorded as 179 kip (796 kN), which represented 85 % of the theoretical beam capacity of 210 kip (912 kN). A summary of the test results is presented in Table 6.3-4.

The failure of the beam was characterized by debonding of all four strands from the concrete. The change in the slope for the load-deflection curve after 160 kip (712 kN) denotes the start of strand slippage. The heating of the beam weakened the bond strength between the CFCC strand and the concrete. The average slippage measured at the end of the beam after the flexural test for each strand was 3 in. (76.2 mm). Figure 6.3-76 through Figure 6.3-79 show the failure of RB-0.7C.
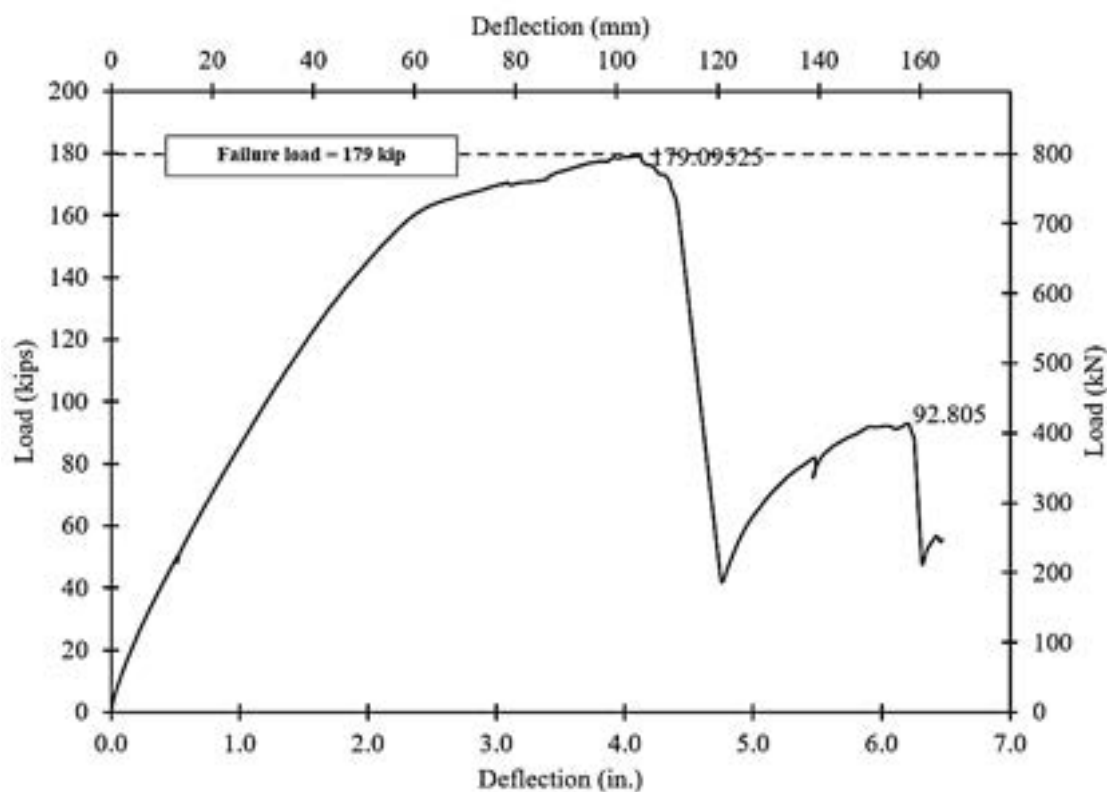
Figure 6.3-74 Load-deflection curve of RB-0.7C for the flexural test

Table 6.3-4 Summary of test results of Beam RB-0.7C

Deflection, in. (mm)	Additional during heating	0.32 (8)
	Under flexural testing prior to faliure	4.1 (104)
Maximum crack width, in. (mm)	After fire test	0.02 (0.5)
	At 50 kip (222 kN) loading	0.53 (14)
Temperature, ºF (ºC)	Maximum strand temperature	490 (254)
Strength, kip (kN)	Anticipated experimental strength (assuming non-slippage), calculated analytically	210 (934)
	Theoretical design strength (including applicable strength reduction factors $(f^*_{gu}{}_{/f^*_{pu}} = 0.758, C_E = 0.9, \emptyset = 0.85)$	122 (542)
	Residual strength (experimental)	179 (796)
Strength ratio (%)	Residual strength to anticipated experimental strength	85
	Residual strength to design strength	146 (No loss)

Figure 6.3-75 Test setup of Beam RB-0.7C after fire/loading event

Figure 6.3-76 Failure of Beam RB-0.7C

Figure 6.3-77 Close-up picture of CFCC strand after failure

Figure 6.3-78 Close-up view showing CFCC strand debonded from concrete

Figure 6.3-79 Measuring depth of slippage from the end of the beam

6.3.3.3 Beam RT-0.7C

The time-temperature curves for all ten thermocouples installed on the prestressed CFCC strands at midspan and quarter sections are shown in Figure 6.3-80 and Figure 6.3-81, respectively. When loading the beam under ambient temperatures to 50 kip (222 kN), a deflection of 0.56 in (14 mm) was recorded at midspan. Upon starting the heating phase, a temperature plateau was observed after 30 minutes of fire duration, with a temperature of 212 ⁰F (100 ⁰C) recorded in the strands. A maximum air temperature of 1700 ⁰F (927 ⁰C) was recorded after 62 minutes with an average strand temperature of 333 ⁰F (167 ⁰C).

No additional deflection was observed in the first 30 minutes of fire duration as shown in Figure 6.3-82. The last 30 minutes of heating was characterized with a gradual increase in the deflection to 0.9 in. (22.6 mm) with a maximum strand temperature of 333 ⁰F (167 ⁰C). The strand temperature continued to increase during the cooling phase of the test until a maximum strand temperature of 527 ⁰F (275 ⁰C) was reached within 3 hours of cooling.

An inspection of the CFCC strands at the end of the fire test revealed an average slippage of 1.55 in. (39 mm) from the end of the beam. The shortening in the strand length corresponded to a 45.6 kip (202 kN) loss in effective prestressing in the beam. In addition, the camber at midspan of the beam reduced from 0.19 in. (5 mm) from before the loading phase to 0.06 in. (1.6 mm) after the end of the fire test. This reduction in the beam camber validated the loss in the prestressing force at the end of the fire test. Several hairline cracks developed through the entire length of the beam. The maximum crack width observed at midspan of the beam was 0.015 in. (0.38 mm). Figure 6.3-83 through Figure 6.3-85 show the state of the beam before, during, and after the fire test, while Figure 6.3-86 shows the slippage of the strands at the end of the beam.
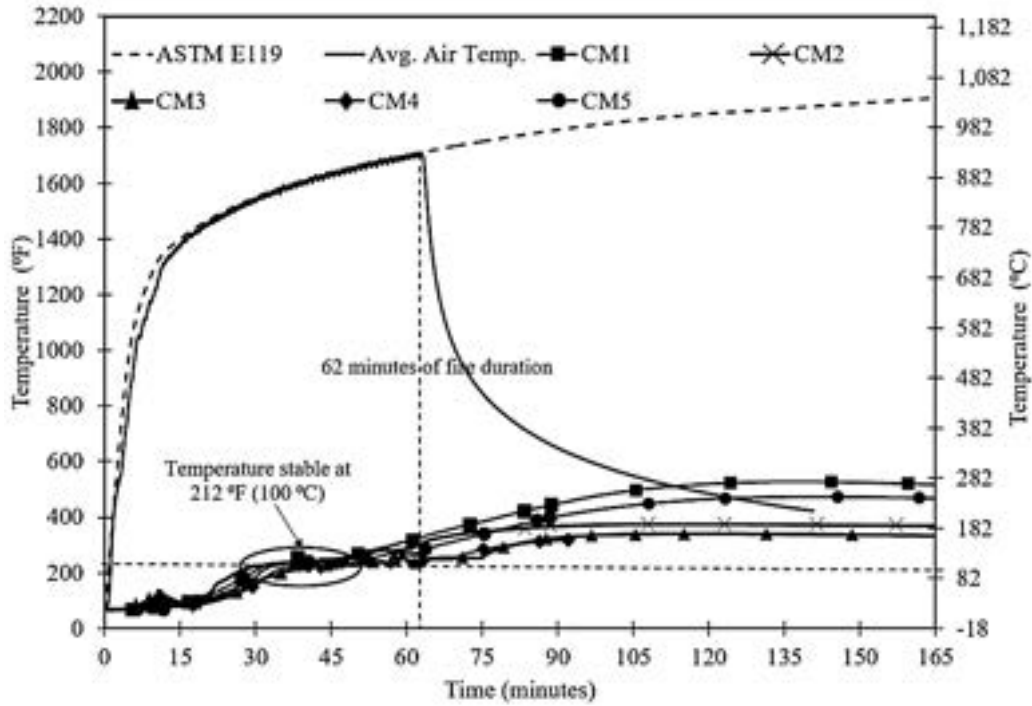
Figure 6.3-80 Time-temperature curves of Beam RT-0.7C (midspan section)
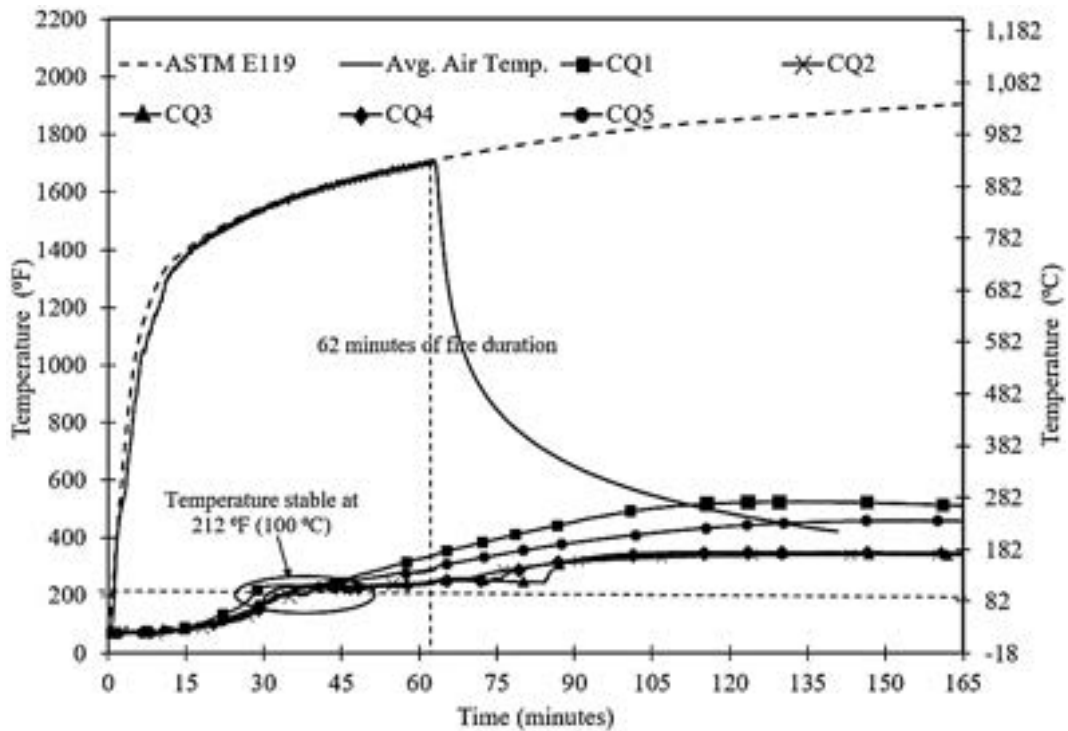
Figure 6.3-81 Time-temperature curves of Beam RT-0.7C (quarter section)

197
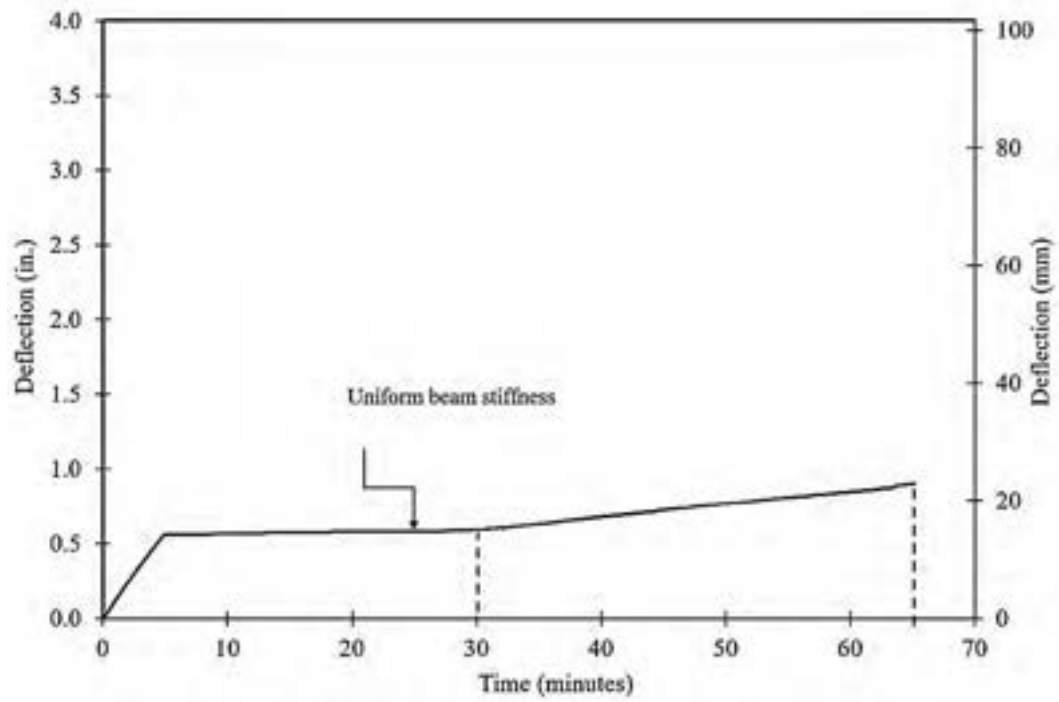
Figure 6.3-82 Time-deflection curve of Beam RT-0.7C (midspan) for one-hour of fire/loading

Figure 6.3-83 Beam RT-0.7C before one-hour fire test

Figure 6.3-84 Beam RT-0.7C during fire test

Figure 6.3-85 Beam RT-0.7C after one-hour fire test

Figure 6.3-86 Close-up view at end of beam after fire test showing slippage of the strands

The load-deflection curve for RT-0.7C during the flexural test performed under ambient conditions is shown in Figure 6.3-87. As shown in the figure, initially, a linear response is observed and remains during a period when most of the load is applied, which is similar to that observed for RB-0.7C. There was no decompression load observed in the load-deflection curve and the increase in the load was accompanied by an increase in deflection along with an increase in crack width and length. The maximum crack width recorded at an applied load of 50 kip (222 kN) was 0.03 in. (0.76 mm) at midspan of the beam. The initial slope of the curve, however, reduced after the 185 kip (823-kN) load point. The curve became flatter, with further increases in deflection at a relatively constant load of 211 kip (939 kN). This was due to the gradual slipping of the CFCC strand. Failure of the beam took place at a load level of 215 kip (956 kN). This failure load represented 58 % of the theoretical load capacity of the beam of 368 kip (1637 kN) and nearly the theoretical design capacity of the beam after including all strength reduction factors (213 kip or 949 kN). The failure of the beam was characterized by both strand slippage and strand rupture, as shown in Figure 6.3-88 through Figure 6.3-92. The average measured end slip for each strand at failure was 3.67 in. (93 mm). A summary of the test results is presented in Table 6.3-5.

200
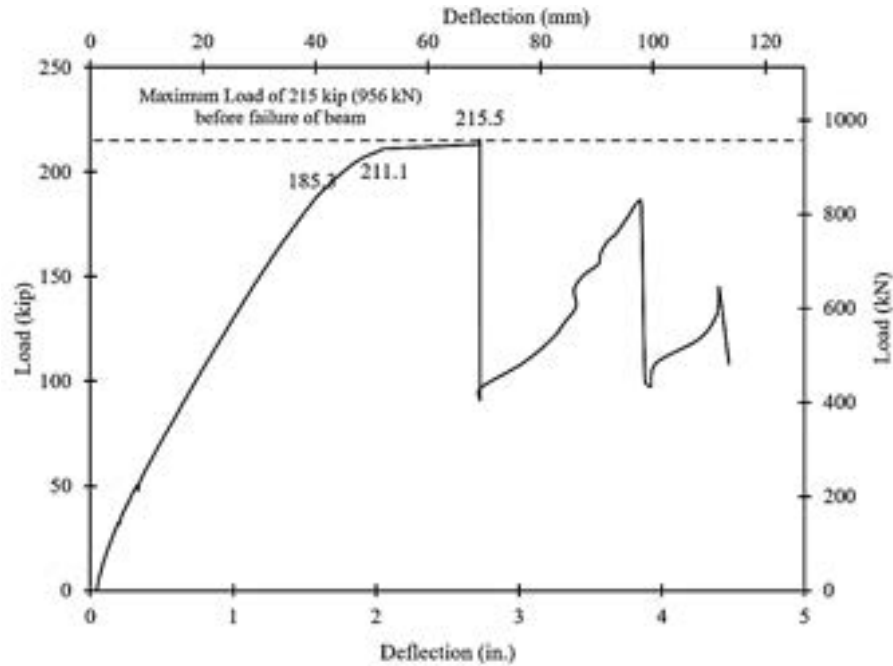
Figure 6.3-87 Load-deflection curve of Beam RT-0.7C for the flexural test

Table 6.3-5 Summary of test results of Beam RT-0.7C

Deflection, in. (mm)	Additional during heating	0.36 (9)
	Under flexural testing prior to faliure	2.72 (69)
Maximum crack width, in. (mm)	After fire test	0.015 (0.38)
	At 50 kip (222 kN) loading	0.035 (0.76)
Temperature, °F (°C)	Maximum strand temperature	527 (275)
Strength, kip (kN)	Anticipated experimental strength (assuming non-slippage), calculated analytically	368 (1637)
	Theoretical design strength (including applicable strength reduction factors ($f_{gu/f_{pu}^*}^* = 0.758$, $C_E = 0.9$, $\emptyset = 0.85$)	213 (949)
	Residual strength (experimental)	215 (956)
Strength ratio (%)	Residual strength to anticipated experimental strength	58
	Residual strength to design strength	101 (No loss)

Figure 6.3-88 Test setup for Beam RT-0.7C after fire test

Figure 6.3-89 Failure of Beam RT-0.7C after flexural test

Figure 6.3-90 Rupture of CFCC strand at failure

Figure 6.3-91 Measuring strand slip at the end of the beam

Figure 6.3-92 Strand pattern in concrete

6.3.3.4 Beam RI-0.6C

Figure 6.3-93 and Figure 6.3-94 show the time-temperature curves for CFCC strands at the midspan, quarter, and end sections. The curve demonstrates a 20 minutes plateau phase at a temperature of 212 ºF (100 ºC). The strand temperatures continued to increase to an average temperature of 393 ºF (200 ºC) after an hour. During the cooling stage, the strand temperature increased to a maximum of 528 ºF (276 ºC) within 3 hours of chamber cooling. As shown in Figure 6.3-95, the beam had an initial deflection of 0.58 in. (14.7 mm) after the initial load of 50 kip (222 kN) was applied. This deflection was nearly constant through the entire one-hour fire test. The average slippage on the strand was measured as 0.37 in. (9 mm) after the test. No camber was measured in the beam both before and after the test. As a salvaged beam, this beam was already cracked before the fire test due to the initial flexural test. Figure 6.3-96 through Figure 6.3-98 show the condition of the beam before and after the fire test.
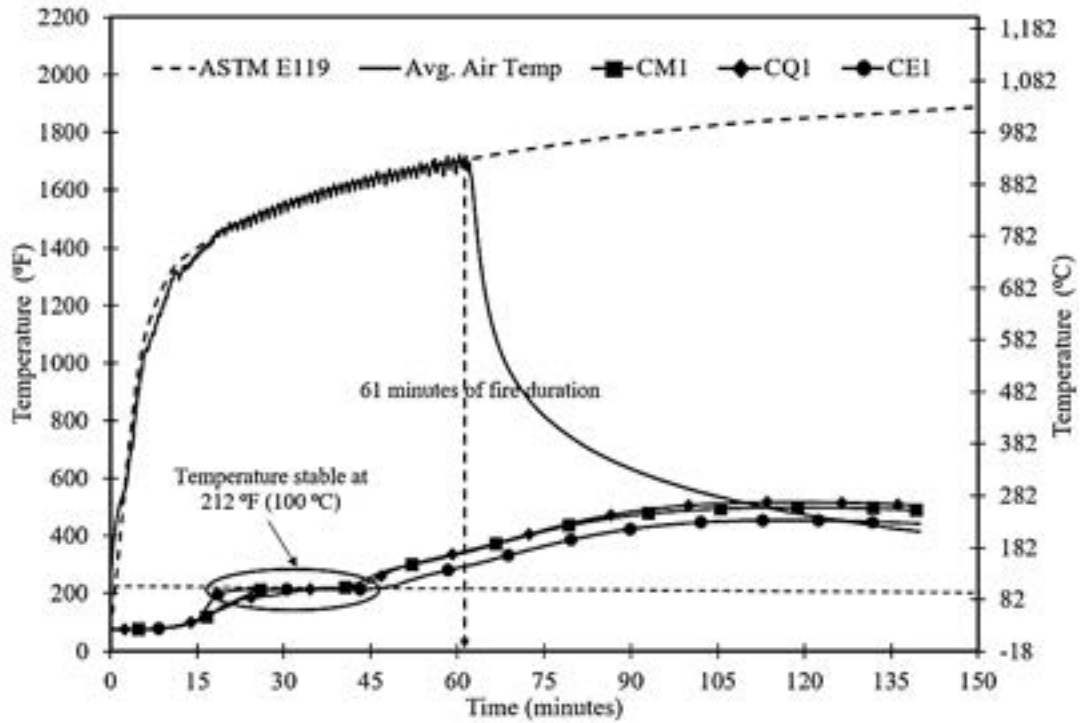
Figure 6.3-93 Time-temperature curve of Beam RI-0.6C (Section-1) for one-hour fire test
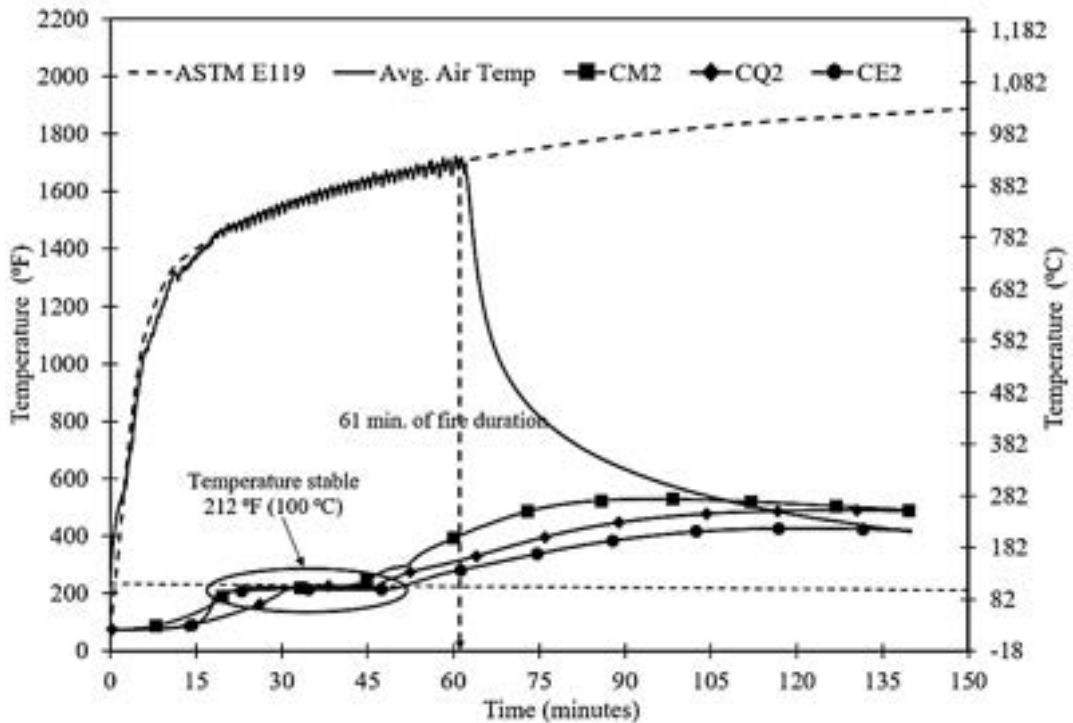
Figure 6.3-94 Time-temperature curve of Beam RI-0.6C (Section-2) for one-hour fire test

205
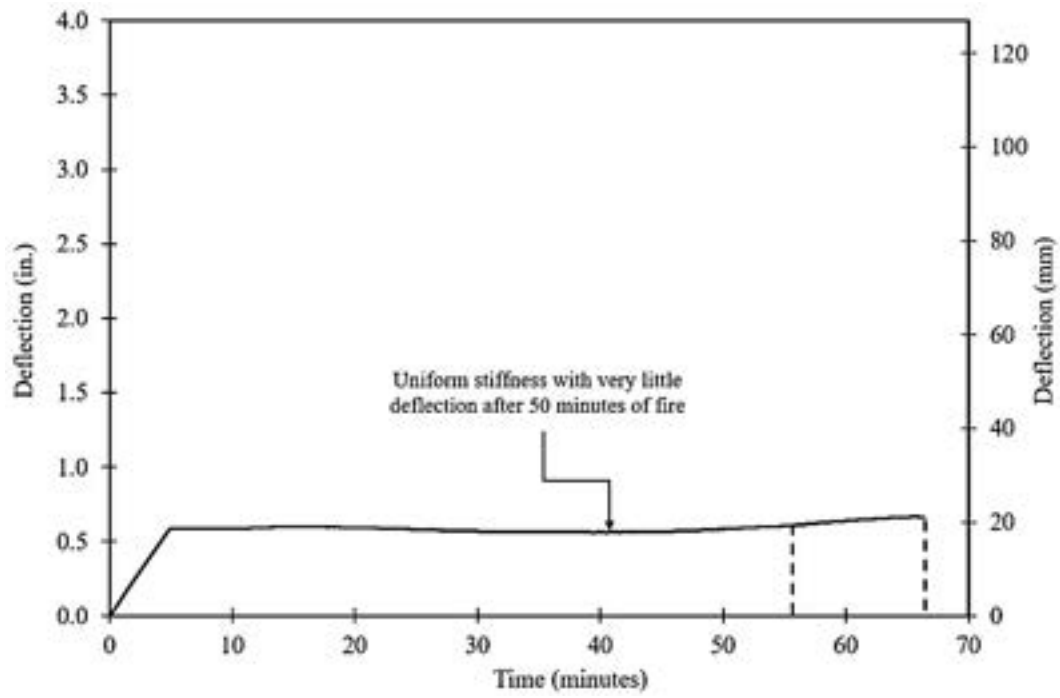
Figure 6.3-95 Time-midspan deflection curve of Beam RI-0.6C for one-hour fire test

Figure 6.3-96 Beam RI-0.6C before fire test

206

Figure 6.3-97 Beam RI-0.6C after one-hour fire test

Figure 6.3-98 Close-up look at the end of the beam after fire test

Figure 6.3-99 shows the load-deflection curve for Beam RI-0.6C during the flexural test. The curve showed a no decompression load. The slope for the load-deflection curve was nearly linear until failure of the beam at 180 kip (800 kN), as seen in Figure 6.3-99. Based on the flexural test of the full-scale 40-ft (12.19-m) long beam, the anticipated experimental capacity of the beam was 336 kip (1494 kN).

The failure was triggered by strand slippage. The failure load represented 54 % of the anticipated capacity of the beam but nearly 94 % of the theoretical design capacity of the beam after considering strength reduction factors as shown in Table 6.3-6. Figure 6.3-100 through Figure 6.3-103 show the condition of the beam before and after the flexural test.
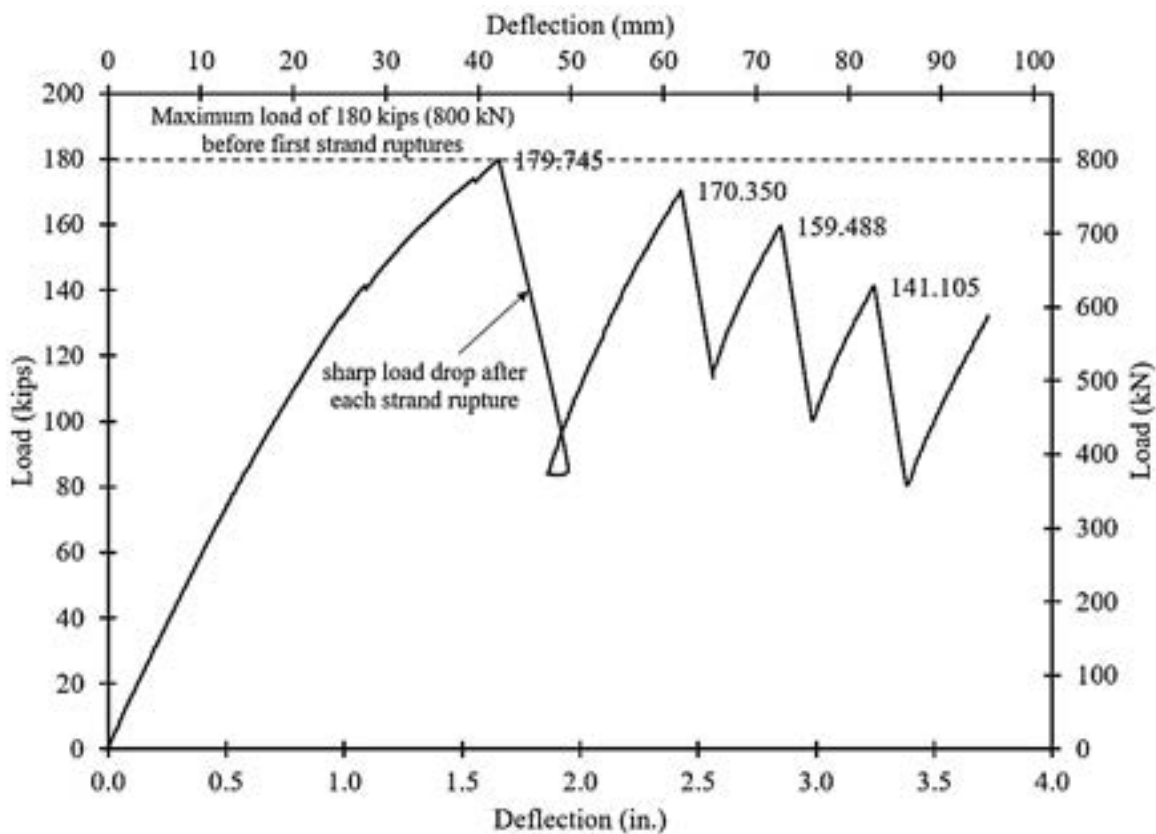
Figure 6.3-99 Load-deflection curve for Beam RI-0.6C

Table 6.3-6 Summary of test results of Beam RI-0.6C

Deflection, in. (mm)	Additional during heating	≈ 0.075 (2)
	Under flexural testing prior to faliure	1.63 (42)
Temperature, ⁰F (⁰C)	Maximum strand temperature	528 (276)
Strength, kip (kN)	Anticipated experimental strength (assuming non-slippage) *based on flexural test results of a 40-ft beam*	≈ 336 (1494)
	Theoretical design strength (including applicable strength reduction factors ($f_{gu}^*/_{f_{pu}^*} = 0.87$, $C_E = 0.9$, $\emptyset = 0.85$)	186.7 (830)
	Residual strength (experimental)	180 (800)
Strength ratio (%)	Residual strength to anticipated experimental strength	54
	Residual strength to design strength	96

Figure 6.3-100 Flexural test setup for Beam RI-0.6C after fire test

Figure 6.3-101 Failure of Beam RI-0.6C after flexural test

Figure 6.3-102 Rupture and slippage of CFCC strand at failure

Figure 6.3-103 Rupture and slippage of CFCC strand at failure

6.3.3.5 Beam RI-0.6S

As shown in Figure 6.3-104 and Figure 6.3-105, the time-temperature curves for the strands of RI-0.6S had a thermal profile similar to Beam RI-0.6C. A 20 minute temperature plateau was also observed at 212 ⁰F (100 ⁰C). A maximum strand temperature of 451 ⁰F (232 ⁰C) was recorded at mid-section after one hour of fire exposure. The strand temperature continued to increase during the cooling period before it eventually started to decrease. A maximum temperature of 580 ⁰F (304 ⁰C) was recorded within 3 hours of cooling.

Figure 6.3-106 shows the midspan deflection of Beam RI-0.6S during the one-hour fire test. The initial deflection of 0.53 in. (13.5 mm) was recorded after loading the beam at ambient conditions. The deflection remained constant throughout the duration of the fire test. The beam had a camber of 0.06 in. (4.7 mm) prior to loading and the fire test. This value reduced to zero after the fire test. All the strands remained bonded after the fire test. Figure 6.3-107 through Figure 6.3-110 shows the beam before, during and after the fire test.

211
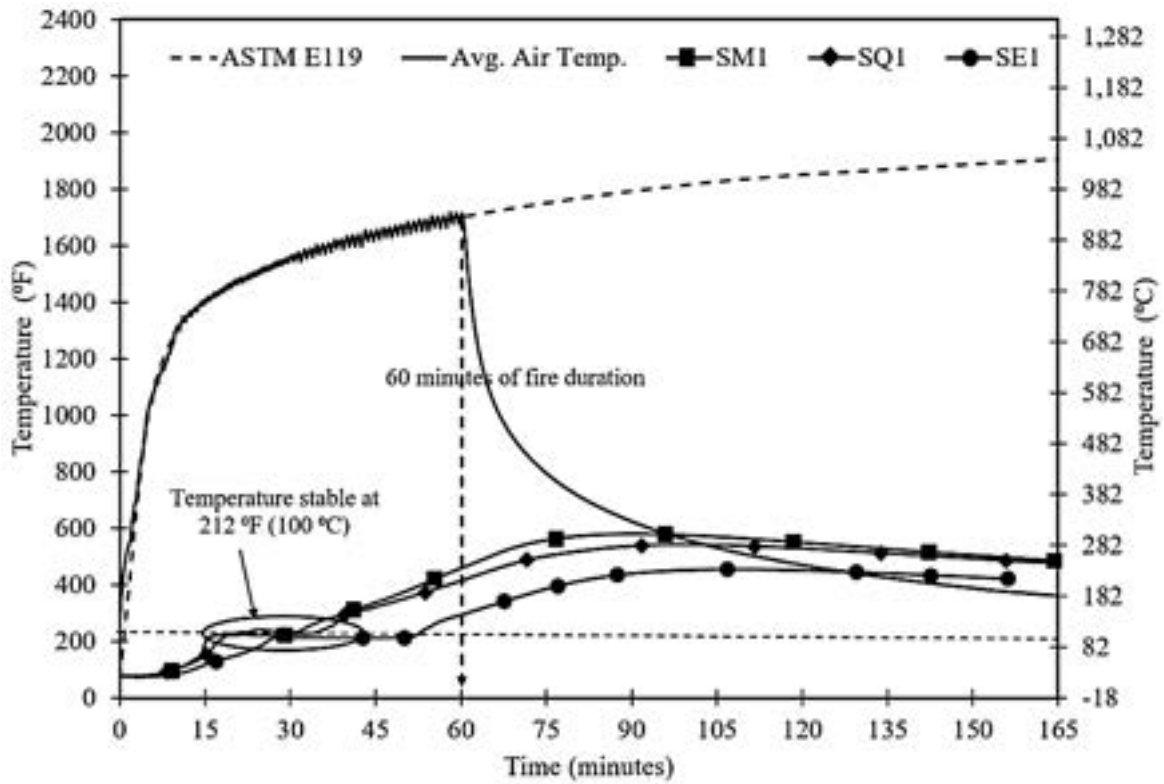
Figure 6.3-104 Time-temperature curve of Beam RI-0.6S (Section-1)
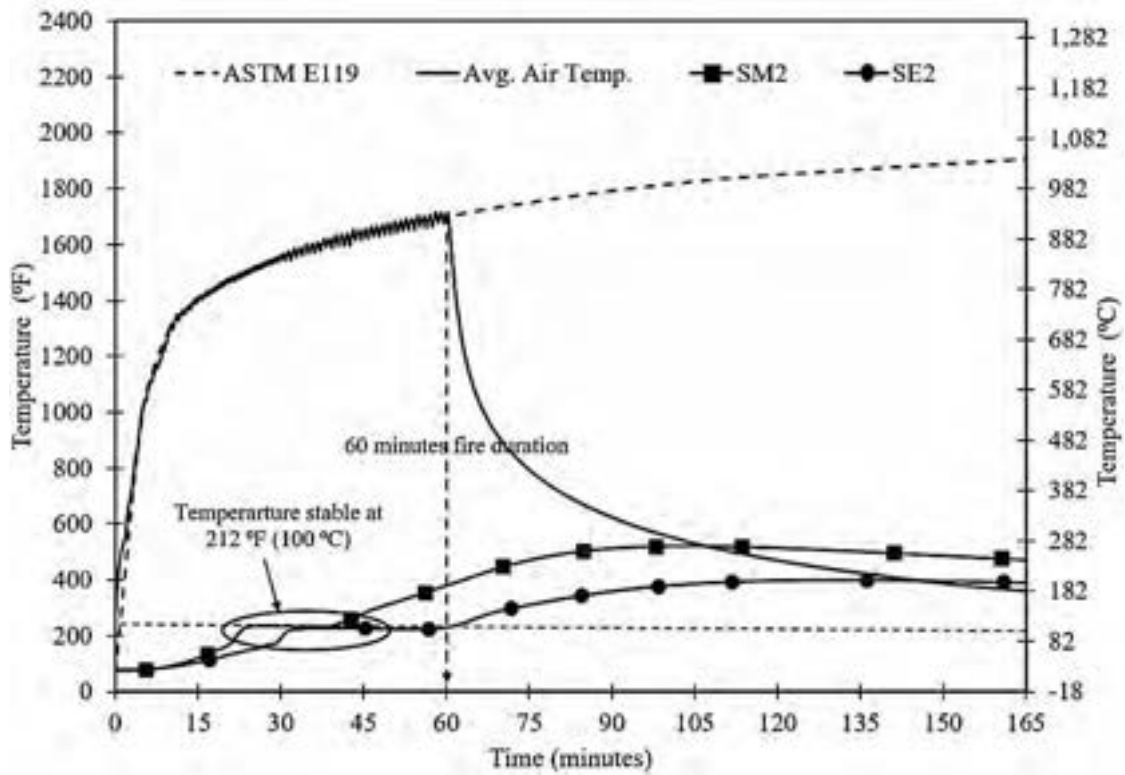
Figure 6.3-105 Time-temperature curve of Beam RI-0.6S (Section-2)

212
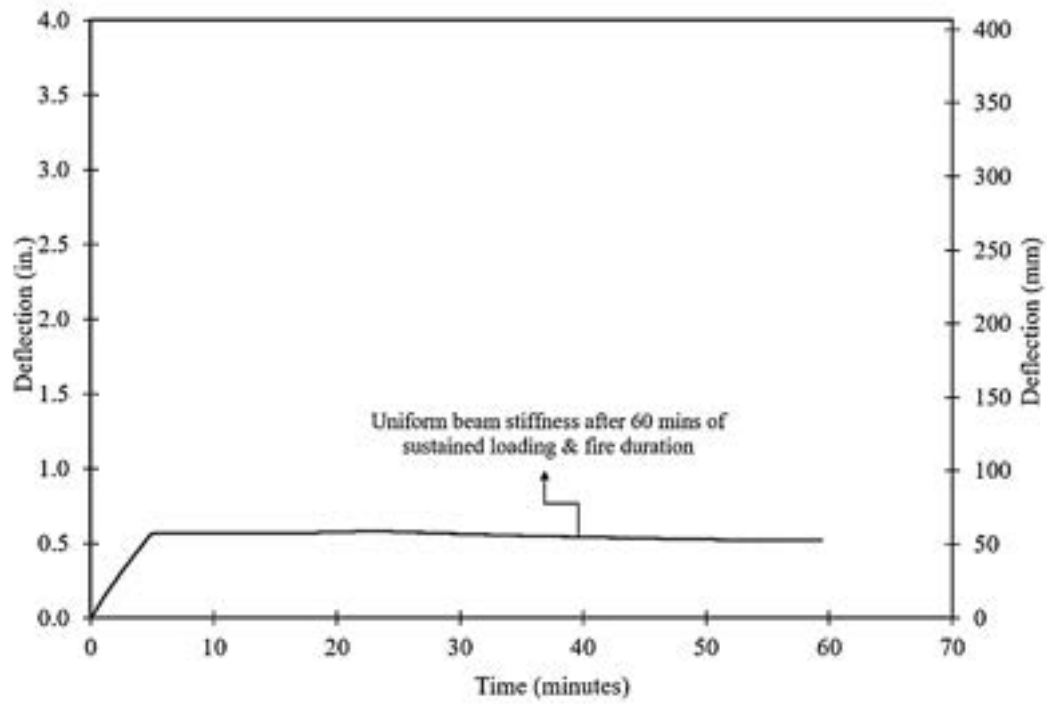
Figure 6.3-106 Time-deflection curve of Beam RI-0.6S during the fire test

Figure 6.3-107 Beam RI-0.6S before fire test

Figure 6.3-108 Beam RI-0.6S during fire test

Figure 6.3-109 Beam RI-0.6S after one-hour fire test

Figure 6.3-110 Prestressing strands remained bonded after fire test

Using the results of the full-scale flexural tests discussed in Chapter 5, the anticipated capacity of Beam RI-0.6S was 285 kip (1267 kN). During loading, the beam reached the maximum capacity of the actuator 220 kip (979 kN) without failure. The load-deflection curve is shown in Figure 6.3-111 and indicates that the beam had a linear response from start of loading until reaching the capacity of the actuator. Similar to other beams, the curve showed no decompression load suggesting a loss of the effective prestressing force in the beam. A summary of the test results is presented in Table 6.3-7.
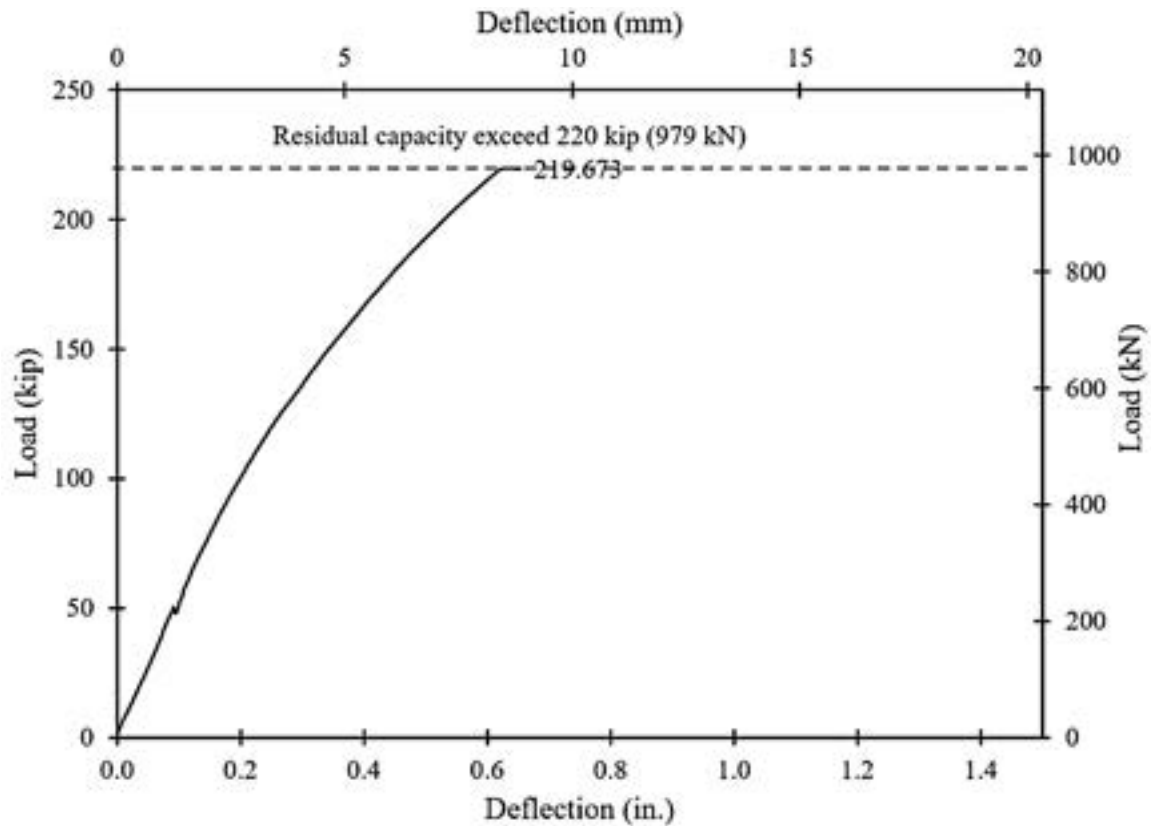
Figure 6.3-111 Load-deflection curve of Beam RI-0.6S under flexural test

Table 6.3-7 Summary of test results of Beam RI-0.6S

Deflection, in. (mm)	Additional during heating	-0.04 (1.0)
	At the end of flexural testing	0.87 (22)
Temperature, ⁰F (℃)	Maximum strand temperature	580 (304)
Strength, kip (kN) (five strands + two No. 5 bars)	Anticipated experimental strength (assuming non-slippage) *based on flexural test results of a 40-ft beam*	285 (1267)
	Theoretical design strength including applicable strength reduction factors ($\emptyset = 1.0$)	248 (1105)
	Residual strength	> 220 (978)
Strength ratio (%)	Residual strength to anticipated experimental strength	> 77
	Residual strength to design strength	> 89

216

6.4 Summary

Similar to other strand diameters, the tensile strength of 0.7" CFCC strands decreased almost linearly with the increase in temperature with tensile strength degrading to approximately 34 % of the ambient tensile strength (or 50 % of the guaranteed strength) when the strand was heated to 662 °F (350 °C). In prestressing applications and assuming an initial prestress of 75 % of the design guaranteed strength, it is expected that the effective prestressing stress in CFCC strands will hover around 50 to 55 % of the guaranteed strength. Therefore, it suffices to say that beams prestressed with CFCC strands lose their structural load carrying capacity when all CFCC strands reach a temperature of 662 °F (350 °C). The time to failure however will depend on many factors such as the shape of the beam, concrete cover, number of rows of prestressing strands, and type of fire.

Fire testing in Phase I gave a rough estimate for the time to failure of CFCC prestressed beams. As shown in Table 6.4-1, most CFCC prestressed beams supported the applied load for over two hours. The exception was Beam T-0.7C, which exhibited early failure due to significant concrete spalling. It should be noted that the prestressing strands were placed in a single row that only had a concrete cover of 2.0 in. (51 mm). Multiple rows of strands are expected to enhance the time to failure in the case of fire since strands in higher rows will take longer to reach their failure temperature. In addition, the maximum recorded temperature at the time of failure, as shown in Table 6.4-1, seems slightly higher than 662 °F (350 °C). However, this can be attributed to the development of cracks near some thermocouple locations that could have altered some of the temperature readings. Furthermore, the failure of the beams was triggered by debonding failure due to the short span of the beams and the fact that the entire beam segment was engulfed in the fire. It is also anticipated that the loss of bond strength is strongly associated with the loss in tensile strength of CFCC strands. Finally, beams prestressed with CFCC strands exhibited a gradual increase in deflection during the fire test and this could be attributed to either heat relaxation of CFCC strands and/or gradual deterioration of the bond between concrete and CFCC.

During Phase II, beams were exposed to fire/loading event for one hour. After which, the beams were cooled to ambient temperatures and then subjected to a flexural test to assess their residual capacity. During the fire test, beams prestressed with CFCC experienced strand slippage with an average slippage of 1.5 in (38 mm). This resulted in a loss in the prestressing force in the

217

strands. Beam prestressed with steel strands also experienced loss in the prestressing force during the heating phase but it was not due to strand slippage.

In the flexural test and under three-point loading setup, the beams reinforced with CFCC failed at a lower capacity in comparison to the anticipated capacity. The failure of CFCC prestressed beams was characterized by strand slippage. However, the failure load was nearly equal to the design load of each beam after accounting for different strength reductions factors that are included in design.

Table 6.4-1 Summary for test results of Phase I in fire/loading test

Specimen	Prestressing Force kip, (kN)	Load applied, kip (kN)	Failure Time, (min)	Failure mode	Max. deflection, in. (mm)	Avg. strand Temp. at failure, ⁰F (⁰C)
B-0.7C	212 (943)	50 (222.4)	136	Bond	4.9 (124.5)	752 (400)
T-0.7C	265 (1178)	50 (222.4)	93	Bond	4.02 (102.1)	625 (329)
I-0.6C	205 (912)	50 (222.4)	136	Bond	6.1 (154.9)	775 (412)
I-0.6S	264 (1174)	50 (222.4)	330	Strand rupture	5 (127)	1391 (755)

CHAPTER 7: EFFECT OF FREEZE/THAW CYCLES

7.1 Introduction

Exposure to fluctuation in temperature is inevitable when CFCC strands are used in highway bridge construction. Starting at the time of construction, CFCC strands are exposed to changes in temperature after they are prestressed and before pouring the concrete. While CFCC strands have a negligible coefficient of thermal expansion, the steel strands coupled to them, the concrete, and the steel formwork do not. Therefore, the difference in the coefficient of thermal expansion between CFCC and surrounding materials leads to a change in the prestressing force that must be calculated and included while establishing the jacking force. In addition, after pouring the concrete and during curing, the temperature of the concrete increases significantly. This increase in temperature could affect the level of the prestressing force in the CFCC strands by producing an additional heat-related relaxation as discussed in Chapter 3. Furthermore, the daily and seasonal change in temperature, while a CFCC prestressed beam is in service, also affects the level of the prestressing force in the CFCC strands due to the difference in the coefficient of thermal expansion between the CFCC and the surrounding concrete. It should be noted that the Laboratory Test Report No. R-5.10_TOK-JP_FDOT933.4, developed by the University of Miami Structures and Materials Laboratory, shows that the average glass transition temperature of CFCC samples is 245 °F (118 °C). Tests were conducted according to ASTM E1640-18 (ASTM 2018): "Standard Test Method for Assignment of the Glass Transition Temperature by Dynamic Mechanical Analysis".

Limited experimental data on relaxation of CFRP cables at elevated temperatures is available. However, the existing data is insufficient to suggest a specific relaxation loss at different temperatures. Saadatmanest and Tannous (1999) performed a preliminary study on the relaxation of Leadline tendons and CFCC cables at room and elevated temperatures. Twelve CFCC tendons of 16 in. (400 mm) length were tested for relaxation losses in air at temperatures of -30, 25 and 60 °C for a period of 3000 hrs, at stress ratios of 0.4 and 0.6. The authors concluded that the percentage loss in the tensile force increased with an increase of the initial stress level and the temperature of the environment. The extrapolated relaxation loss of CFCC was limited to 10 % over a 50-year period.

Enomoto et al. (2009) showed that relaxation and logarithm of passing time can be represented by a linear relationship at room temperature similar to steel tendons. They reported a one-million-hour relaxation rate of approximately 2 % for CFCC cables stressed to 70 % of the guaranteed standard load (average failure load minus three times the standard deviation) at room temperature. In their effort to the study the effect of steam curing of precast members, they carried out relaxation tests of CFCC cables according to JSCE-E 534 (JSCE 1995) at temperatures of 60, 80 and 100 °C. They concluded that the relaxation values at 20 to 80 °C were within the range of 2 %. Whereas, above 80 °C, the estimated relaxation increased sharply due to the softening of the epoxy resin. They also stated the necessity of conducting relaxation tests with temperature as a variable parameter.

Sasaki et al. (2012), in effort to address the lack of demonstrative data (actual long-term field exposure as opposed to the standard 1000-hour laboratory relaxation test), retrieved and evaluated several properties including relaxation of 17-year-old FRP specimens exposed to direct sunlight radiation and salt splash. The authors concluded that CFRP exhibited a negative response to direct sunlight for relaxation losses unlike AFRP, which showed no susceptibility and confirmed the use of the semi-logarithmic plot in a laboratory 1000-hour relaxation test. Apparent relaxation after one-million hours increased from 10 % for CFRP specimens (prestressed to 70 % of ultimate tensile capacity) not exposed to direct sunlight to between 16 to 19 % for specimens exposed to direct sunlight. The increased relaxation rate was attributed significantly to thermal fatigue resulting from stress induced by sunlight. Possibility of the stress increase resulting from matrix degradation to UV exposure was also not discounted, even though earlier tests indicated otherwise.

Limited research has focused on FRP behavior in prestressed members at different temperature conditions. Bryan and Green (1996) studied the short-term behavior of concrete beams prestressed with 8 mm diameter Leadline CFRP tendons at low temperatures. Based on the results, the flexural behavior of the beams was unaffected by short-term exposure to low temperatures. In addition, the ultimate stresses and strains in CFRP tendons exceeded those reported by the manufacturer. Sayed-Ahmed and Shrive (1998) investigated the thermal variation effect on post-tensioned CFRP prestressing tendons. In their experimental study, thermal and flexural tests were carried out on masonry diaphragm walls prestressed concentrically with CFRP Leadline tendons. It was reported that the level of prestressing force in the Leadline tendons increased with the increase in

temperature and decreased with the decrease in temperature. El-Hacha et al. (2004) studied the behavior of precracked concrete beams strengthened with prestressed CFRP sheets at low temperature. It was concluded that the decrease in temperature did not adversely affect the flexural behavior of beams strengthened with prestressed CFRP sheets. Saiedi et al. (2013) studied the behavior of concrete beams prestressed with CFRP Leadline rods under sustained load and low temperature environments. Results showed that the bond between CFRP rods and concrete was negatively affected by such exposure causing reduction in the strength of prestressed beams.

Exposure to cycles of freezing and thawing is another aspect of environmental conditions that can have a detrimental impact on prestressed beams, regardless of the prestressing material. Recent data (NIST 2014) indicated that approximately 102 freezing and thawing cycles occur annually in Michigan. Although freeze-thaw cycles have their documented detrimental effect on roads and bridges, little is known about the effect of freeze-thaw cycles on highway bridge beams prestressed with CFRP strands. Earlier research studies showed conflicting results. For instance, a study on FRP material showed that extreme low temperatures can cause micro cracking in the fiber matrix and high residual stress due to discrepancies in coefficients of thermal expansion of the constituent elements (Dutta 1988). However, Karbhari and Pope (1994) showed that FRP strength increases due to hardening at low temperature. Cusson and Xi (2002) reported 10 % reduction in the tensile strength of CFRP bars after exposure to 250 freeze-thaw cycles for 750 hrs.

The performance of CFRP-concrete bond at low temperatures has been the subject of several experimental studies (Green et al. 1997 & 2000; Elbadry et al. 2000; Subramaniam et al. 2008; Kim et al. 2011). Some researchers reported increased bond strength between CFRP and concrete under certain conditions. Whereas, others highlighted the detrimental effect of freeze-thaw cycles on CFRP-concrete bond strength. Part of the dilemma is that concrete itself loses strength with the exposure to extreme temperatures (Shoukry et al. 2011).

Many existing design codes and guidelines in USA, Canada and Japan were developed to account for potential deterioration of CFRP material caused by environmental and long-term effects (Ceroni et al. 2006). This is achieved by multiplying the guaranteed strength of the CFRP material by an environmental reduction factor less than 1.0. However, it should be noted that an unjustified reduction of material strength often leads to multiple design issues and results in congested sections with potential for further construction and service concerns.

Parallel to the study conducted on 0.6″ CFCC strands (Grace et al. 2019), this chapter addresses the performance and strength of 0.7″ CFCC prestressed beams and unbonded stressed 0.7″ CFCC strands during and after exposure to temperature fluctuation and freeze-thaw cycles.

For the unbonded stressed CFCC strands, two sets of CFCC specimens were prepared and subjected to successive 150 and 300 cycles of freezing and thawing induced in a large-scale environmental chamber in accordance with ASTM C666/C 666M-15 (ASTM 2015): "Standard Test Method for Resistance of Concrete to Rapid Freezing and Thawing". Each set contained five 0.7″ CFCC test specimens with dimensions and anchorage devices as discussed earlier. Each specimen was loaded with an initial force level of 57 kip (254 kN). The force was monitored during the exposure to freeze-thaw cycles and after concluding the specific number of cycles through attached in-line load cells. After the specimens were released from the loading frames, they were examined for deterioration and were tested in a uniaxial tensile test setup to evaluate the impact of successive freeze-thaw cycles on the residual strength of the CFCC strands.

Six decked bulb T beams prestressed with 0.7″ CFCC strands were designed, constructed, and tested under a simulated seasonal temperature fluctuation as well as freeze-thaw cycles. Out of the six beams, two beams served as control beams and were kept in a controlled laboratory environment. Two of the remaining beams were loaded in a freezing temperature (-40 °F or -40 °C), while the other two beams were loaded in a hot environment (176 °F or 80 °C). The load was applied in the form of loading-unloading cycles with the maximum loading cycle reaching approximately 75 % of the nominal load carrying capacity of the beam. The load cycles were later repeated at ambient conditions to assess the effect of temperature change on the prestress level as well as the overall performance of the beam. After completing this part of the test, the four beams were subjected to 300 cycles of freezing and thawing following ASTM C666/C666M-15 (ASTM 2015). Finally, all beams, including the control beams, were loaded to failure under a three-point-load test setup to establish their residual flexural strength and the impact of severe environmental conditions on the overall performance of the beams.

The following sections describe the specimen preparation, instrumentation, testing program and main findings along with the results of freeze-thaw tests, flexural tests of decked bulb T beams, and uniaxial tension tests of CFCC strands.

7.2 Freeze-Thaw Cycles of CFCC Specimens

7.2.1 Test Setup

Two sets of CFCC strands were prepared and subjected to 150 and 300 freeze-thaw cycles. Each set contained five CFCC 64-in. (1626-mm) long specimens with dimensions and anchorage devices as discussed in Chapter 2. The test specimens were loaded inside custom-made high-strength steel frames and were connected to in-line load cells and threaded rods at one end (dead end) and fastened at the other end (live end) with a high-strength steel nut and a washer. The load cells were connected to a data acquisition system to monitor the prestressing force continuously. After installing the specimens inside the steel frames, prestressing force was applied at the live end through a hydraulic jacking system and monitored through the installed load cells.

The steel frames of the first test set were placed in the environmental chamber and the specimens were subjected to 150 freeze-thaw cycles. After, the second test set was prepared and placed in the environmental chamber and subjected to 300 freeze-thaw cycles along with four decked bulb T beams. In both sets, the load cells were covered with insulation layers to minimize the damage during the freeze-thaw cycles. In addition, readings from the load cells were corrected according to the corresponding temperature.

After completion of the freeze-thaw cycles, the CFCC test specimens were released from the steel frame and were transported to the MTS four-post testing facility, where they were loaded in a uniaxial test setup to failure to estimate the residual CFCC strength after exposure to freeze-thaw cycles. Figure 7.2-1 through Figure 7.2-6 document the preparation and testing of the first set of the CFCC freeze-thaw test specimens, while Figure 7.2-7 through Figure 7.2-13 document the preparation and testing of the second set.

7.2.2 Test Results

As shown in Figure 7.2-4, the air temperature and temperature of CFCC strands ranged from +50 °F to -50 °F (10 °C to -46 °C). Along with the change in temperature, there was a corresponding change in the force level in the strands as shown in Figure 7.2-5. The change in the force level is attributed to the expansion and contraction of the steel frames with the change in temperature. By the end of the freeze-thaw cycles, the remaining force in the CFCC strands aligned with the

anticipated force level after deducting force loss due to relaxation of CFCC strands and anchorage relaxation (Table 7.2-1 and Table 7.2-2).

The failure load of the five test specimens averaged 106.5 kip (473 kN) and 102.1 kip (481 kN) after 150 and 300 freeze-thaw cycles, respectively. Both values are higher than the average ambient tensile capacity of this CFCC batch (104 kip (463 kN)). In addition, a marginal increase in the elastic modulus of CFCC specimens was observed in both cases. All specimens ruptured at failure, with no slippage within the anchors.

Figure 7.2-1 Environmental Chamber in CIMR
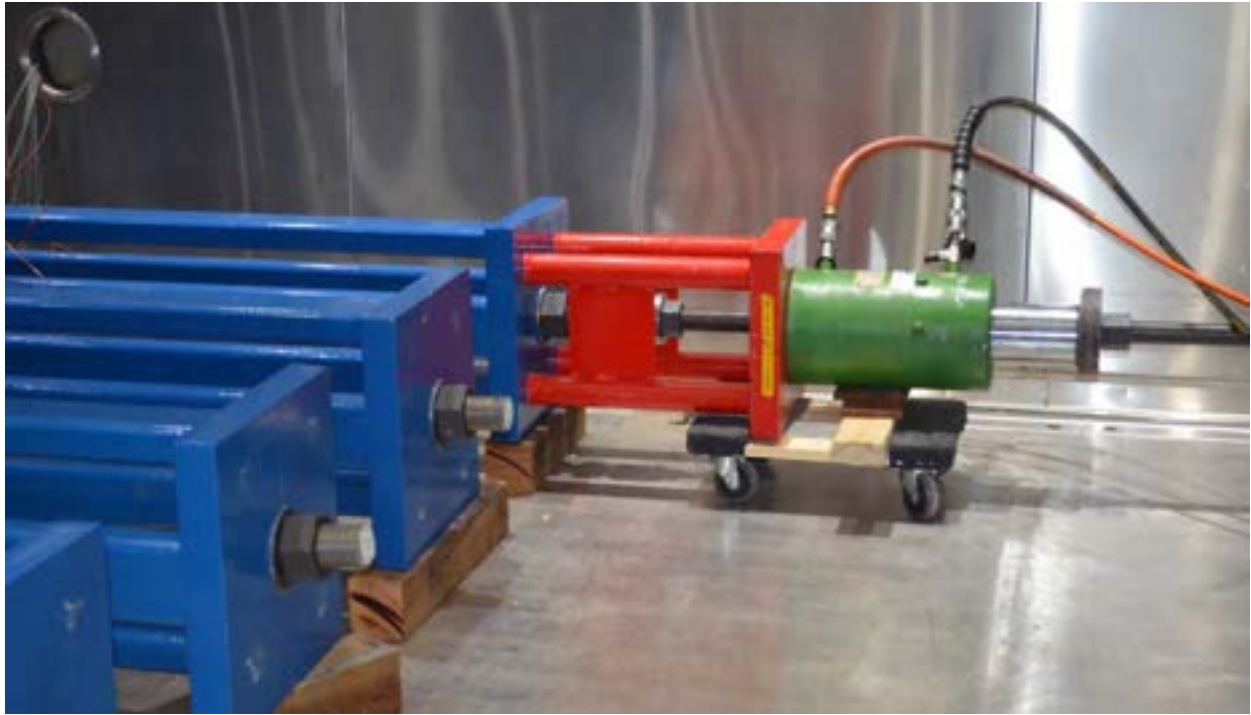
Figure 7.2-2 Stressing CFCC strands before exposure to freeze-thaw cycles

Figure 7.2-3 Stressed CFCC strands exposed to 150 freeze-thaw cycles
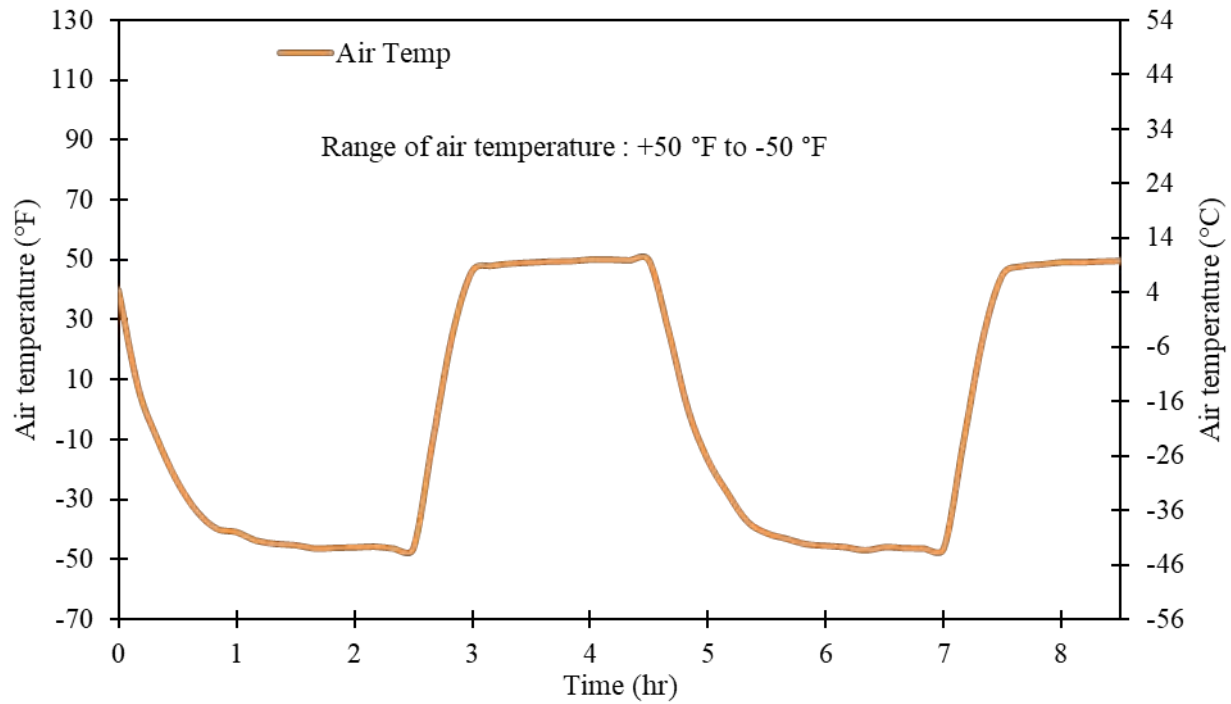
Figure 7.2-4 Air temperature during freeze-thaw cycles (approx. 2 cycles shown for clarity)
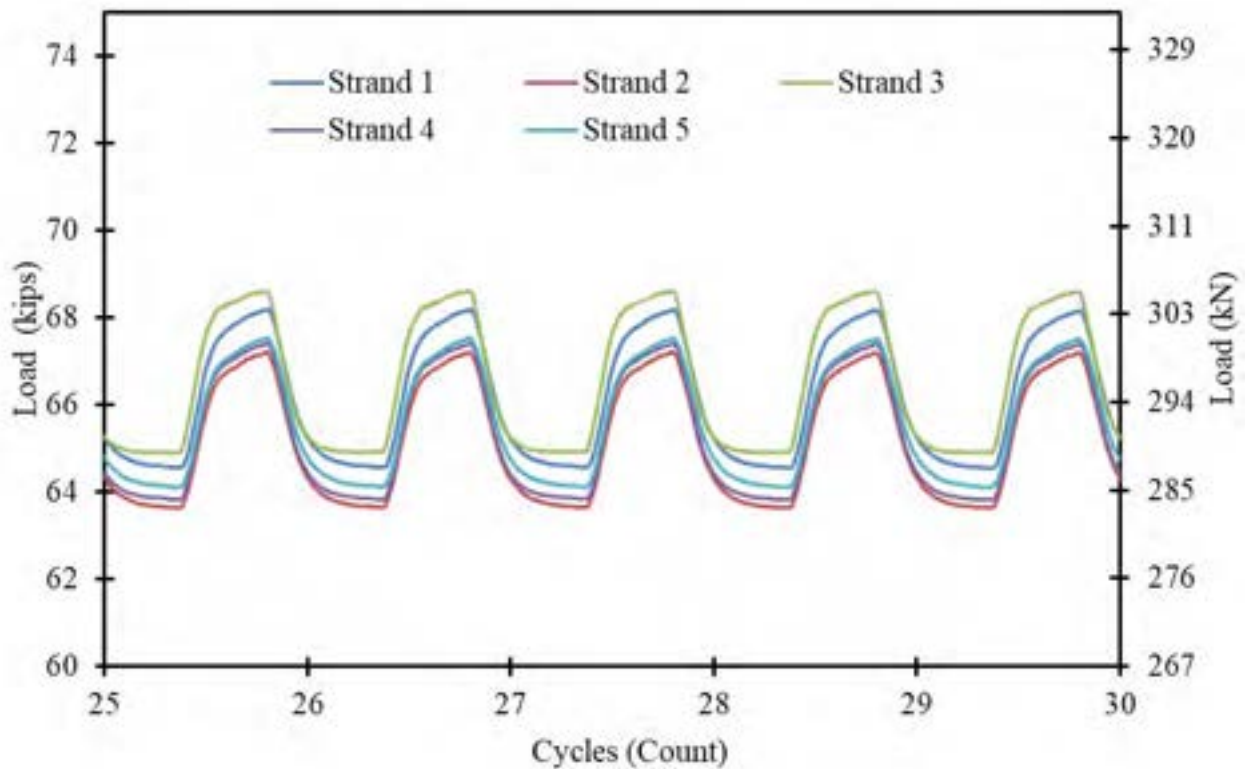
Figure 7.2-5 Change in the force in the strands due to the change in air temperature

226
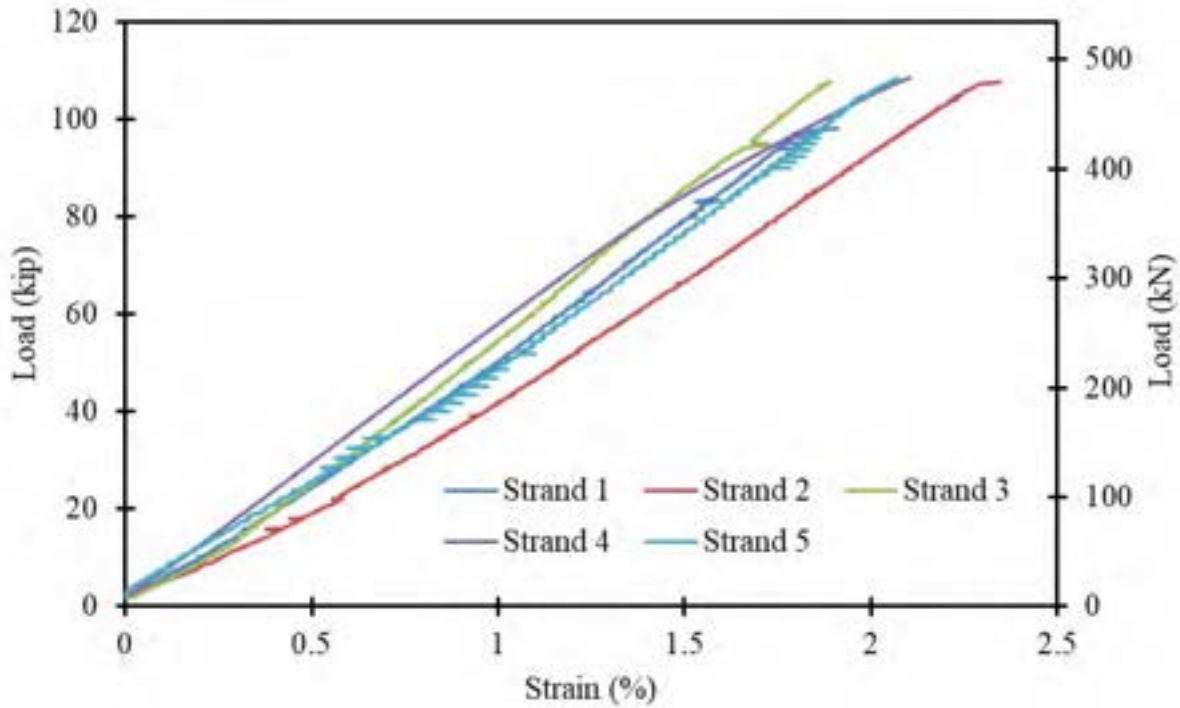
Figure 7.2-6 Load-strain curves of CFCC strands after exposure to 150 freeze-thaw cycles

Table 7.2-1 Summary of test results for CFCC strands exposed to 150 freeze-thaw cycles

| Specimen | Prestressing force @ freeze-thaw | | | Uniaxial tensile test | | |
| | Prestressing force, kip (kN) | | Loss in prestressing force (%) | Breaking load, kip (KN) | | Elastic modulus, ksi (GPa) |
	Before freeze/thaw cycles	After freeze/thaw cycles		Before freeze/thaw cycles	After freeze/thaw cycles	
S1	70.63 (314)	68.17 (303)	3.48		98.20 (437)	24,626 (170)
S2	69.02 (307)	67.23 (299)	2.60		107.76 (479)	22,532 (155)
S3	70.85 (315)	68.72 (306)	3.00	104.04 (463)	109.36 (486)	23,460 (162)
S4	70.23 (312)	67.48 (300)	3.92		108.62 (483)	22,961 (158)
S5	69.29 (308)	67.51 (300)	2.57		108.53 (483)	23,870 (164)

227

Figure 7.2-7 Stressing CFCC strands for 300 freeze-thaw cycles

Figure 7.2-8 Placing the stressed CFCC strands in the environmental chamber

Figure 7.2-9 Unbonded CFCC specimens after exposure to 300 freeze-thaw cycles

Figure 7.2-10 CFCC specimens after release from the stressing frames
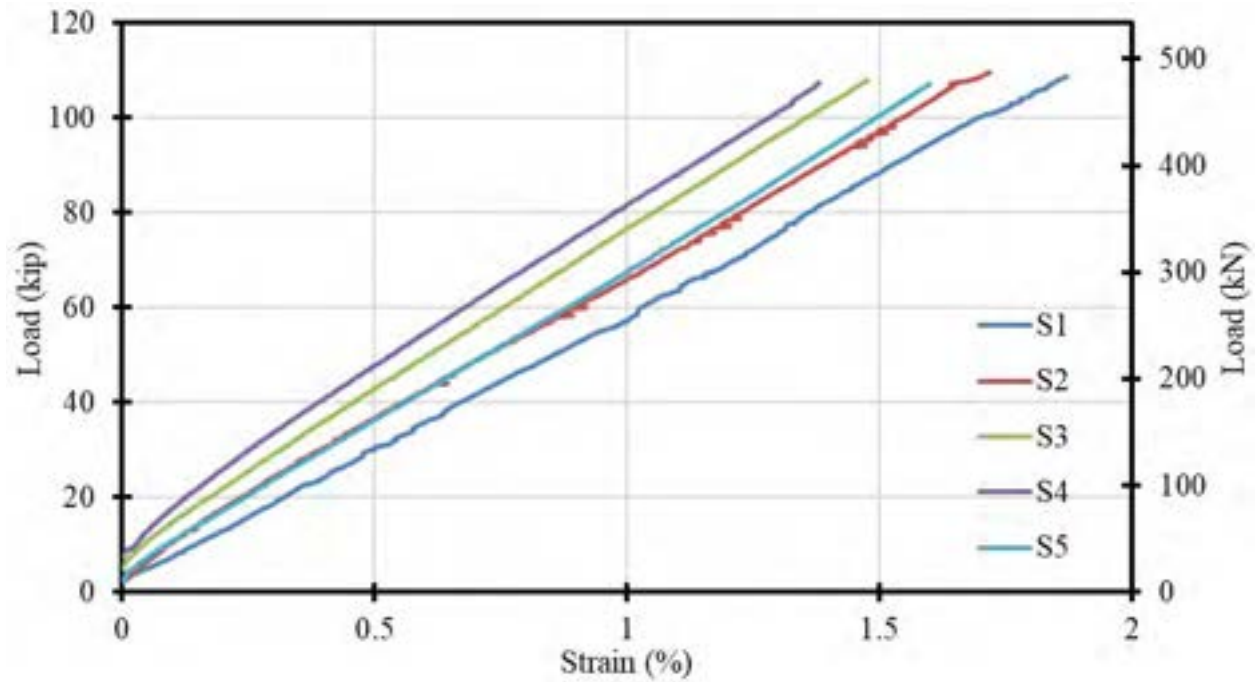
Figure 7.2-11 Load-strain curves of CFCC strands after exposure to freeze-thaw cycles
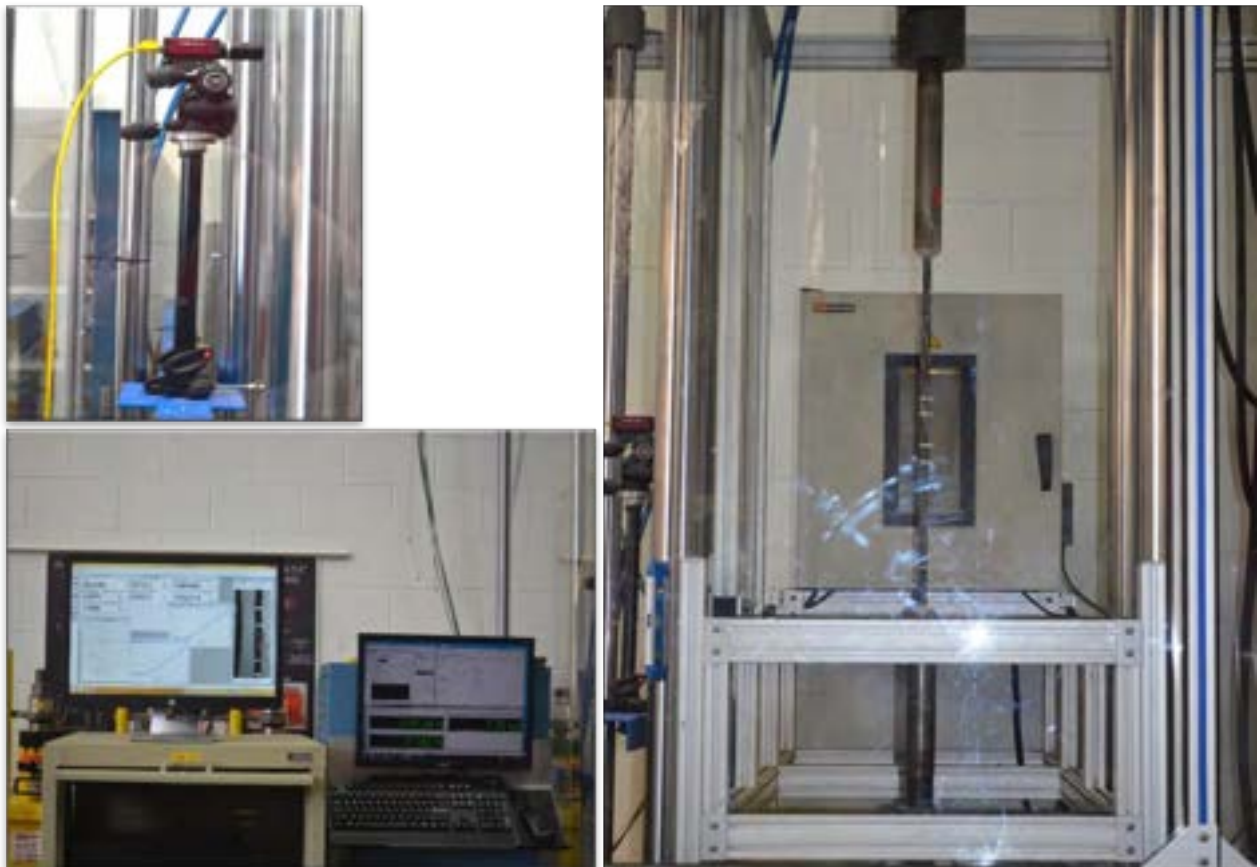
Figure 7.2-12 Uniaxial tensile test of CFCC strands after exposure to freeze-thaw cycles

Figure 7.2-13 Failure of CFCC strands under uniaxial tension test

Table 7.2-2 Tensile test results of CFCC strands after exposure to 300 freeze-thaw cycles

Specimen	Prestressing force, kip (kN)		Average losses of prestressing force (%)	Average failure load, kip, (kN)	
	Initial	After freeze/thaw cycles		Before freeze/thaw cycles	After freeze/thaw cycles
S1	72.70 (323)	70.60 (314)	2.88		108.90 (484)
S3	73.42 (327)	71.72 (319)	2.32		109.40 (487)
S4	73.97 (329)	71.48 (318)	3.37	104.05 (463)	106.90 (475)
S2	72.85 (324)	70.14 (312)	3.72		108.10 (481)
S5	72.54 (323)	69.98 (311)	3.53		107.30 (477)

7.3 Decked Bulb T Beams

7.3.1 Test Specimens

Six identical precast prestressed decked bulb T beams were constructed and tested under flexural loading at different temperatures. The cross-section and internal reinforcement details of these

beams are shown in Figure 7.3-1. The beams had a length of 16 ft (4.87 m), a top flange width of 18 in. (457 mm), and a depth of 16 in. (406 mm). Each beam was prestressed with two 0.7″ CFCC strands. In addition, an additional CFCC strand was passed through the beams but was fully unbonded. This strand was included during construction to assess the loss of prestressing force due to concrete hydration and verify the results from the heat relaxation testing. The reinforcement cages of the beams were assembled from five top No. 5 (M16) steel bars and No. 3 (M10) stirrups spaced 4 in. (102 mm) on center in the transverse direction. Both top reinforcement and stirrups were Grade 60 steel.

The decked bulb T beams were constructed at CIMR in a prestressing bed that can accommodate beams with a length of 50 ft (15.24 m) and a width of 48 in. (1.22 m). Therefore, there was enough space to accommodate the simultaneous construction of the six beams. The formwork for the beams included a wood platform decking and sides. The decking platform was constructed of plywood and dimension lumber. The sides of the formwork were constructed from layers of plywood and polystyrene (Styrofoam) to form the required bulb T shape and accommodate the end blocks (Figure 7.3-2 and Figure 7.3-3). The layers of polystyrene were pre-cut to shape using a table saw and attached to the plywood using adhesive and wood screws.

The steel stirrups were made of two pieces welded together with tack welds. End blocks were provided with rectangular stirrups every 2.0 in. (51 mm) to resist the bursting force at prestress release. After reinforcement cages were constructed, they were moved to the platform decking, where prestressing CFCC strands were passed through the cages.

To facilitate the prestressing and avoid damaging the CFCC strands, a special coupler system was used to connect the prestressing CFCC strands with conventional 7-wire 0.7″ (18 mm) low relaxation steel strands (Figure 7.3-4 through Figure 7.3-7). The couplers were provided on both the live and dead ends. Therefore, conventional steel anchorage was used at both bulkheads and the prestressing was executed by tensioning the steel strands. After completing the installation of the coupler system, the steel strands were tensioned from the live end while a set of in-line load cells was attached to the prestressing strands at the dead end. The prestressing was executed using a hydraulic pump and a jacking system. The strands were prestressed in a predetermined sequence to avoid generating a significant eccentricity in the bulkhead. The target initial prestressing force was 53 kip (236 kN) per strand. The force in each prestressing strand was verified through the

readings from the load cells, the readings from hydraulic pump and the measured elongation of the strands. A seating loss was expected and was accounted for when calculating the required jacking force. Therefore, the indicated prestress level represented the prestressing force after engaging the steel anchors at the live end. Type K thermocouples were attached to all CFCC strands at mid-span of each beam to evaluate the change in temperature during construction and to validate the temperature of the strands at different stages of testing.

All the beams were cast (Figure 7.3-8 and Figure 7.3-9) using a ready-mix concrete. Properties of the concrete mix are shown in Table 7.3-1. The concrete mix was designed to achieve a 28-day compressive strength of 7 ksi (48 MPa). The maximum aggregate size was limited to 0.75 in. (19 mm) and a slump of 10 in. (254 mm) was verified before pouring the concrete beams. This concrete mix is a typical concrete mix used in highway bridge beams. After concrete casting, the beams were covered with wet burlap and plastic sheets to prevent moisture escape and allow for proper curing. In addition, concrete cylinders with a diameter of 6 in. (152 mm) and a length of 12 in. (305 mm) were also cast from the same batch of concrete. The cylinders were allowed to cure under the same conditions as the concrete beams and were tested under uniaxial compressive stress according to ASTM C39/C39M-12a (2012): "Standard Test Method for Compressive Strength of Cylindrical Concrete Specimens", to determine the compressive strength of the concrete after 28 days.

Transfer of prestressing forces into concrete beams took place 7 days after casting of concrete and after verifying that the concrete had achieved at least 80 % of its 28-day compressive strength. With the exception of the middle unbonded strand, the prestress release was executed by slowly heating the steel strands using an acetylene/oxygen torch (Figure 7.3-10 through Figure 7.3-12). The camber of the beams was measured at the mid-span of the beam at prestress release. After prestress release, the beams were removed from the formwork and sent to the testing facility. The release of the unbonded strands was executed by jacking the strand to a higher force and removing the anchor system.

The results of the uniaxial compressive tests are shown in Figure 7.3-13. The concrete achieved a 28-day compressive strength of 8.86 ksi (61 MPa) as shown in Figure 7.3-13.
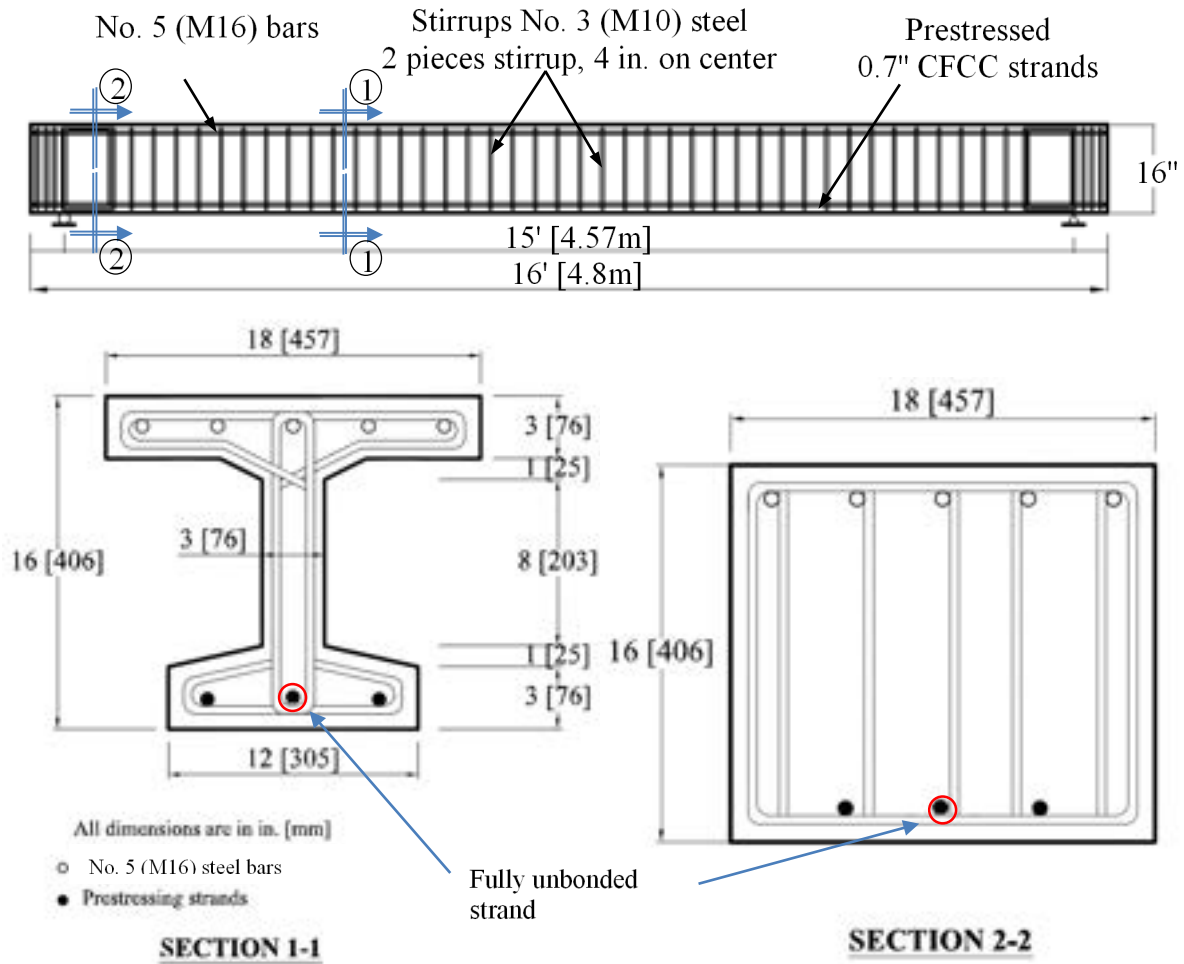
Figure 7.3-1 Cross-section and internal reinforcement details of decked bulb T-beams

Figure 7.3-2 Preparing and cutting the formwork for the beams

Figure 7.3-3 Building the sides of the formwork

Figure 7.3-4 Assembling reinforcement cages from steel stirrups and top steel reinforcement

Figure 7.3-5 Coupler system for strand prestressing

Figure 7.3-6 Prestressing the strands using a hydraulic pump and a jacking system

Figure 7.3-7 Completing the formwork

Figure 7.3-8 Pouring and compacting concrete

Figure 7.3-9 Preparing concrete cylinders
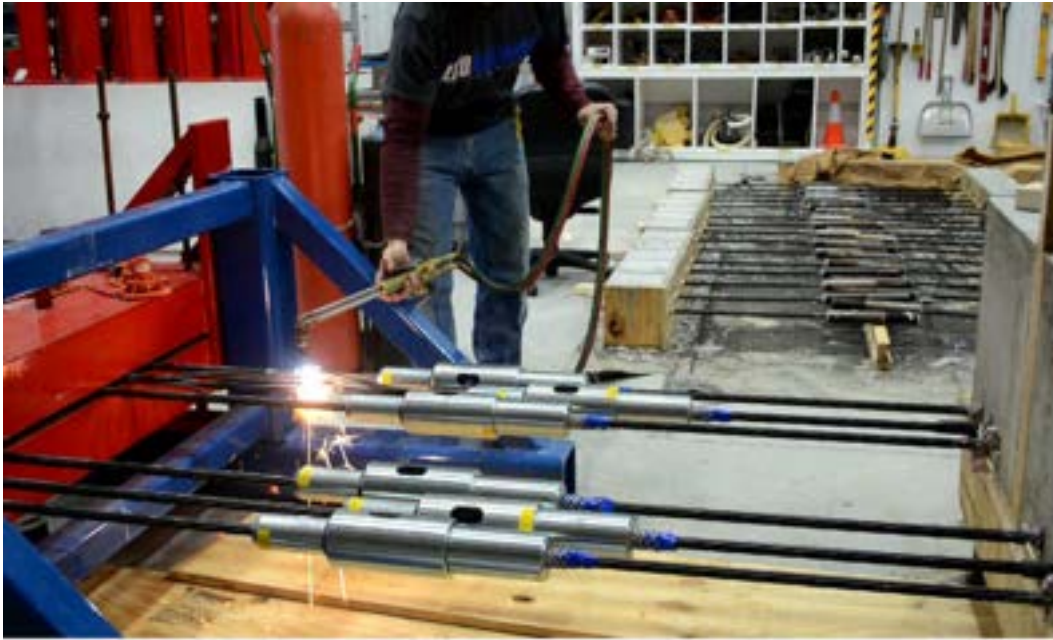
Figure 7.3-10 Cutting strands after proper curing

Figure 7.3-11 Beams after prestress release with the middle strand in each beam fully debonded

Figure 7.3-12 Prestressed decked bulb T beams after construction

Table 7.3-1 Concrete mix per cubic yard

Material	Units	Design Quantity per yd^3 (m^3)
Limestone Coarse Aggregate (LIA-OTT)	lb (kg)	1762 (1047)
Fine Aggregate (2NS-AAR)	lb (kg)	1265 (752)
Type 1 Cement (CMT1-LAA)	lb (kg)	534 (318)
Slag Cement (CMGS-LA)	lb (kg)	288 (171)
Water (WAT1)	gal (m^3)	31.8 (0.16)
Water/Cement ratio		0.37
Retarding Admixture (0STAB-PR)	oz (kg)	25 (0.92)
High Range Water Reducer (0HRWR-PR)	oz (kg)	53 (1.96)
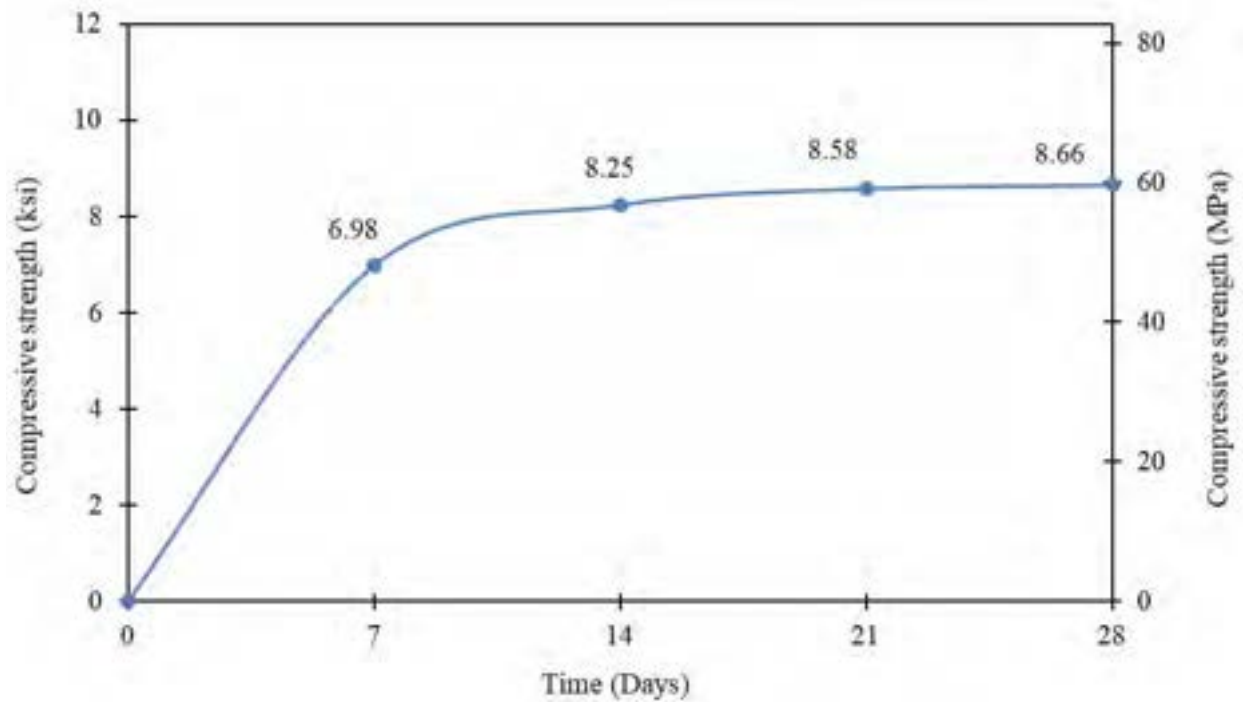
Figure 7.3-13 Concrete strength of decked bulb T beams after various days of curing

7.3.2 Heat Relaxation of CFCC Strands

As shown in Table 7.3-2 and Figure 7.3-14, at the time of prestressing, the average jacking force for the six strands was 57.2 kips (254.5 kN), while the recorded temperature was between 70 and 76 °F (21 and 24 °C). Due to bulkhead rotation and anchor seating loss, the force in the strands dropped to an average of 54.1 kips (240.7 kN) just after releasing the hydraulic pump. An elongation of 7.2 in (183 mm) in each strand was measured just after releasing the hydraulic pump. An additional 2.0 kip (8.9 kN) of loss per strand was observed from time of jacking to the start of concrete placement.

No significant change in prestressing force was observed at the time of concrete placement. However, after casting the concrete and during the curing period, an increase in temperature was recorded as shown in Figure 7.3-15. The highest recorded temperature was 112 °F (44 °C) and the rate of temperature increase was similar for all strands as shown in the temperature-time curves. During concrete curing, bonded Strands 1, 3, 4 and 6 experienced a rapid descend in the prestressing forces followed by a regain of the lost force. A decrease in the prestressing force curve mirrored the rise in temperature from the time-temperature curve. Nevertheless, the debonded

241

Strands 2 and 5 exhibited a gradual loss in the prestressing force with a slightly noticeable descend at the time of temperature increase but without any signs of prestress regain until the time of prestress release.

As the temperature of the concrete increased, the concrete expanded and stretched the bonded segments of the strands as shown in Figure 7.3-16. This resulted in the load cells, outside the concrete, registering a decrease in the prestressing force. On the other hand, as the concrete cooled down and shrunk, the bonded segments of the strands contracted along with the concrete body, which resulted in the load cells showing a regain in the prestressing force. Neither the registered loss nor the gain of the prestressing force was an accurate representation of the force in the bonded strand segments. In fact, it is nearly opposite.

The increase in temperature during concrete hydration (70 to 114 °F or 21 to 44 °C) would yield a theoretical thermal expansion of concrete body (δ_c) of 0.14 in., (3.6 mm) according to Eqn. 1.

$$\delta_c = \Delta T \cdot \alpha \cdot L_b \tag{1}$$

In Eqn. 1, ΔT is the change in temperature = 41 °F (23 °C); α is the thermal expansion of concrete = $6\times10\text{-}6/$ °F ($10.8\times10\text{-}6/$ °C); and L_b is the total length of three concrete beams in one row = 48 ft (14.6 m). According to the manufacturer, the thermal expansion of CFCC strands in the fiber direction is negligible and the linear coefficient of thermal expansion may be taken as zero.

In the beam setup, CFCC strands extended beyond the concrete body and were coupled with steel strands, while the ends of the steel strands were anchored to the bulkheads. Therefore, the thermal expansion of the concrete body resulted in an elongation of the bonded CFCC strand segments and at the same time resulted in a contraction of the exterior segment of CFCC strands and coupled steel strands between the concrete beams and both bulkheads. The contraction resulted in the loss of force registered in the load cells. The relationship between the contraction and the loss in the force can be expressed as:

$$\delta_c = \Delta P \left(\frac{L}{EA}\right)_{CFCC} + \Delta P \left(\frac{L}{EA}\right)_{Steel} \tag{2}$$

242

In Eqn. 2, L_{CFCC} is the length of exterior CFCC segment = 12 ft (3660 mm); L_{Steel} is the length of coupled steel strand = 10 ft (3050 mm); E_{CFCC} is the elastic modulus of 0.7″ CFCC = 22,600 ksi (156 GPa); E_{Steel} is the elastic modulus of 0.7″ (18 mm) prestressing steel strand = 29,000 ksi (200 GPa); A_{CFCC} is the cross-sectional area of 0.7″ CFCC = 0.23 in.^{2} (151 mm^2); and A_{Steel} is the cross-sectional area of 0.7″ (18 mm) steel strand = 0.29 in.^{2} (189.6 mm^2).

Using Eqn. 2, the theoretical change in prestressing force (ΔP) is estimated as 3.4 kip (15.3 kN) for δ_c of 0.14 in. (3.6 mm), which matches the average force drop registered by the load cells on bonded CFCC strands during concrete hydration (3.6 kip or 16.4 kN).

As shown in Figure 7.3-17, while Strands 2 and 5 (fully debonded) did not expand with the concrete body, they did experience elongation through their heated segments in the form of heat relaxation as discussed using heat relaxation analysis. Using the strain-temperature curve for 0.7″ CFCC strands (Figure 7.3-18), a heat relaxation strain of 121 με was estimated at a temperature of 112 °F (44 °C). Since the heated length of each strand ($L_{h_{CFCC}}$) was equal to the length of the concrete beams (48 ft or 14.6 m), the elongation (ΔL) of the strands due to heat relaxation was estimated as 0.07 in. (1.78 mm) according to Eqn. 3.

$$\Delta L = \varepsilon \cdot L_{h_{CFCC}} \tag{3}$$

The corresponding change in the prestressing force (ΔP) in the debonded CFCC strands can be computed through Eqn. 4

$$\Delta L = \Delta P \left(\frac{L_h}{EA}\right)_{CFCC} + \Delta P \left(\frac{L_{uh}}{EA}\right)_{CFCC} + \Delta P \left(\frac{L}{EA}\right)_{Steel} \tag{4}$$

In Eqn. 4, $L_{uh_{CFCC}}$ is the length of the unheated segment of the debonded CFCC strand = 12 ft (3660 mm) and L_{Steel} is the length of the coupled steel strands = 10 ft (3050 mm). By rearranging Eqn. 4, the change in the prestressing force (ΔP) was computed as 0.5 kip (2.1 kN). This value compared well to the recorded change in the prestressing force for Strands 2 and 5, (average of 0.45 kip or 2 kN).

Table 7.3-2 Important prestress levels in CFCC strands

Stage	Temperature, °F	Prestressing Force, kip					
		Bonded Strand 1	Debonded Strand 2	Bonded Strand 3	Bonded Strand 4	Debonded Strand 5	Bonded Strand 6
Jacking	72.7	57.1	57.6	57.1	57.2	57.2	57.0
Seating	72.7	53.4	54.2	54.4	54.1	54.2	54.1
Concrete placement	70.3	51.2	52.0	52.0	51.9	52.8	52.7
Concrete hydration	112.0	47.6	51.5	48.9	47.1	52.4	49.4
Prestress transfer	72.0	50.0	51.0	51.2	48.4	51.8	51.1
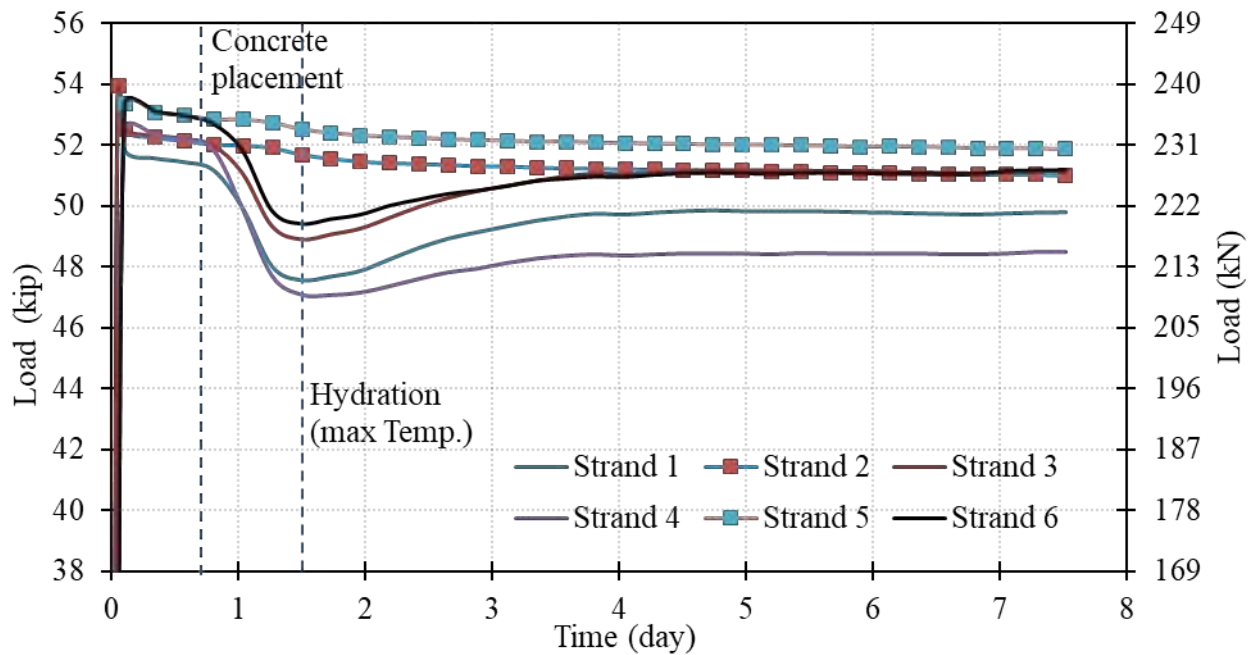
Figure 7.3-14 Prestress reading in all strands during beam construction
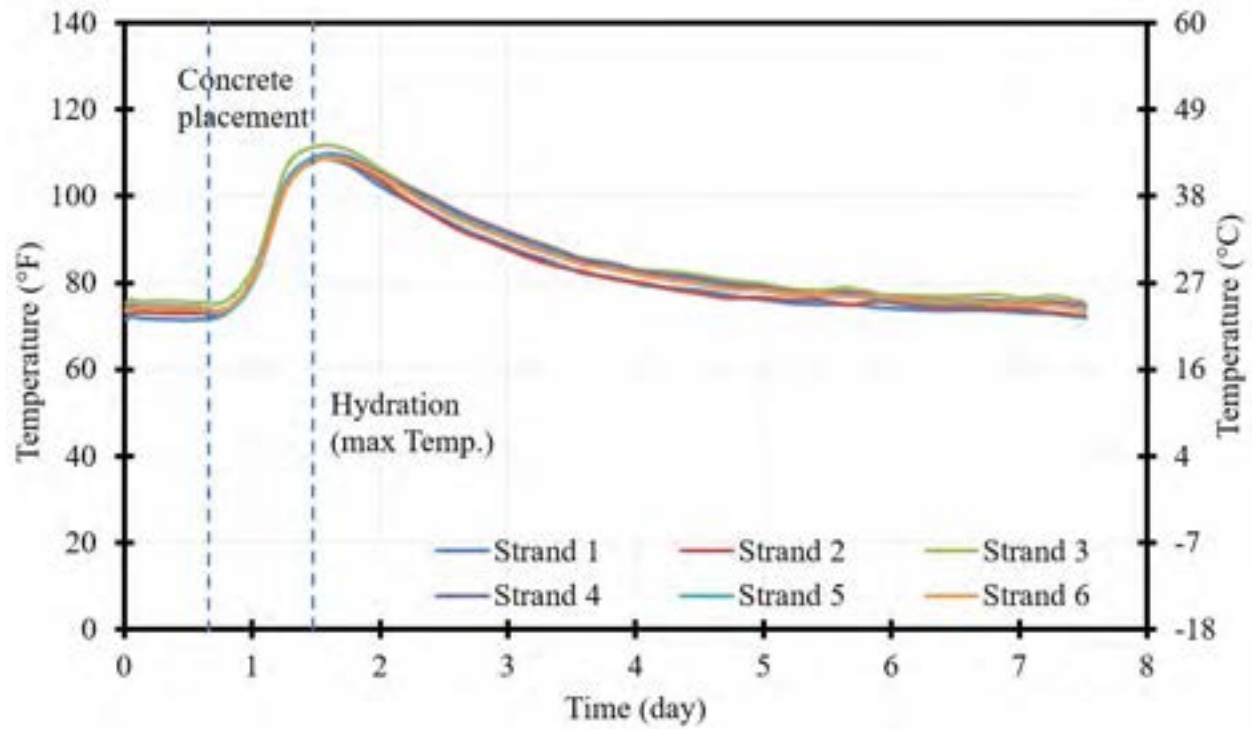
Figure 7.3-15 Change of beam temperature during construction
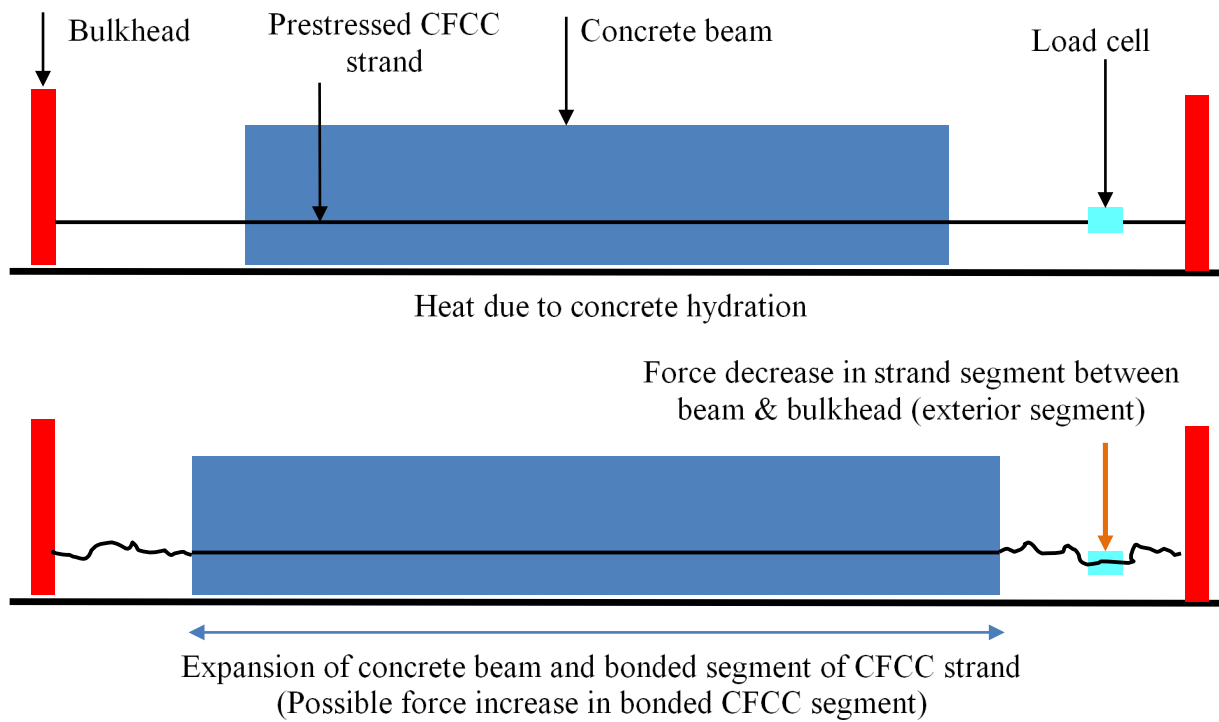
Figure 7.3-16 Change in prestressing force in bonded strands with concrete expansion
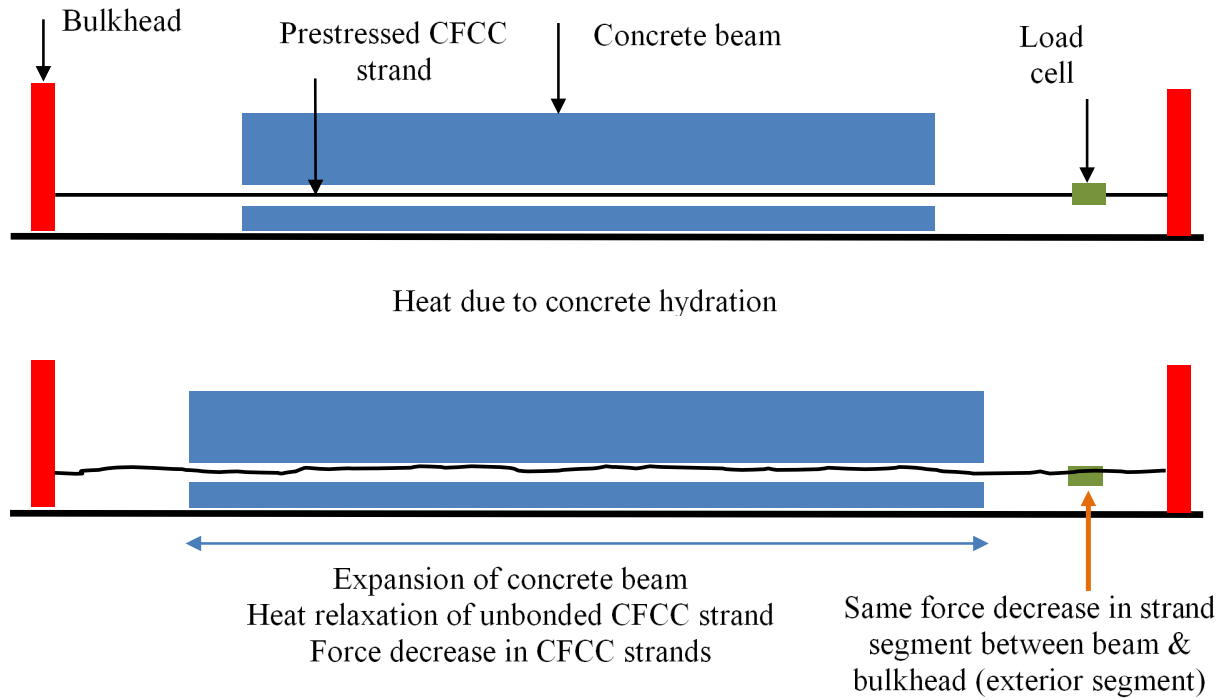
Figure 7.3-17 Change in prestressing force in unbonded strands with concrete expansion
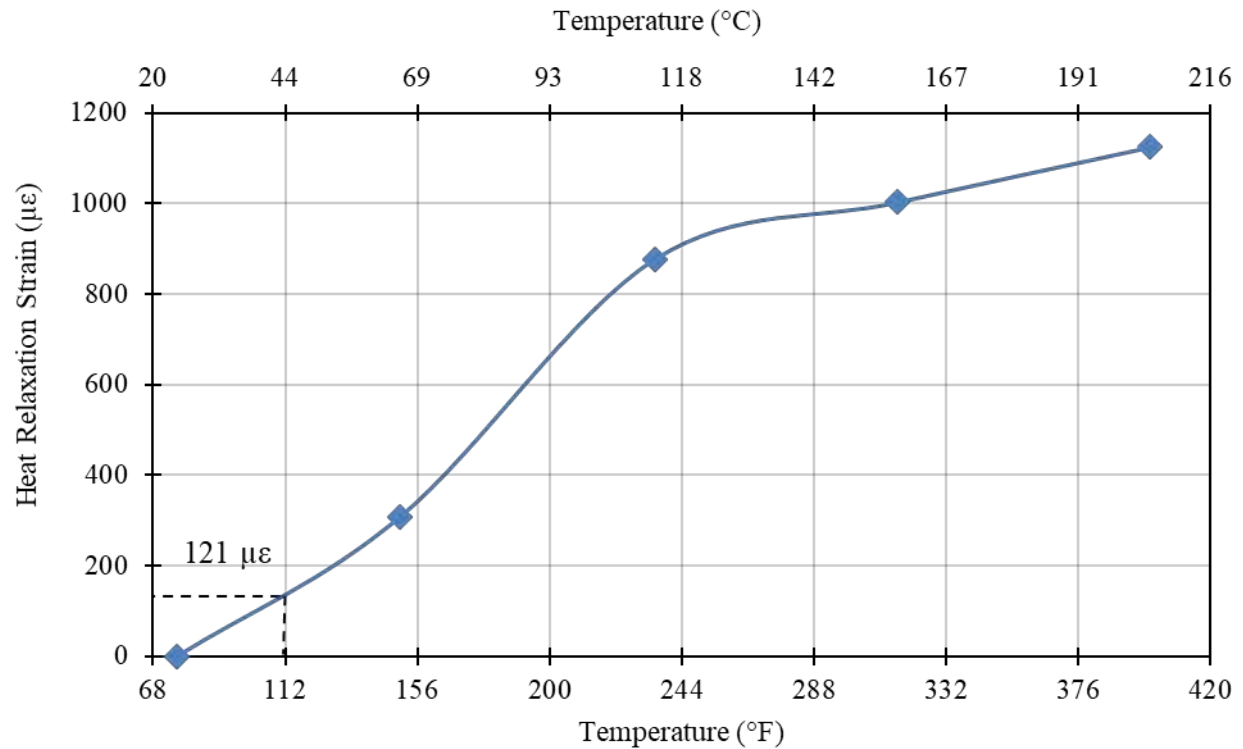
Figure 7.3-18 Correlation between recorded temperature and heat relaxation strain

7.3.3 Seasonal Temperature Change

The coefficient of thermal expansion for concrete is approximately 6×10^{-6} /°F (12×10^{-6} /°C), while CFRP has a coefficient of thermal expansion less than 0.5×10^{-6} /°F (1×10^{-6} /°C). Therefore, concrete beams prestressed with CFRP strands experience a certain loss or gain in the level of prestressing force with the seasonal change in temperature. An experimental study was executed to verify the loss/gain in prestressing level due to thermal changes.

The six decked bulb T beams were loaded under three-point loading over an effective span of 15 ft inside the environmental chamber. Strain gages, load cells, linear variable differential transducers (LVDTs), and linear motion transducers (LMTs) were used to capture the strain, applied load, and deflection of the beams during testing. To monitor the concrete strain, each beam was provided with two strain gages on the top surface at the midspan section. In addition, two strain gages were provided at the bottom surface of the concrete to capture the onset and development of cracks. LVDTs were used to evaluate the strain at different depths at the midspan section.

The main objective of the test was to evaluate the prestressing force in the test beams and evaluate the change of the prestressing force due to the change in temperature. However, there is no feasible way of directly measuring the prestressing force in pretensioned beams since the strands are completely within the concrete. Nevertheless, the effective prestressing force can be evaluated indirectly by observing the cracking and decompression loads while loading the beam in flexure. The cracking load can be used to estimate the effective prestressing force using the stress equation at the soffit of the beam. However, the cracking load is dependent on the modulus of rupture of concrete and can only be used once for each fabricated beam. The decompression load provides a good alternative for calculating the effective prestressing force once the beam is cracked.

After cracking, the decompression load marks the stage where the flexural cracks start to open under the applied loads. The decompression load is the load required to counteract the effect of prestressing force and cause the stresses in the soffit of the beam to reach zero. The decompression load can be identified by attaching a strain gage next to the flexural crack and capture the reading of the strain in the soffit of the beam while loading. The strain will gradually increase with applying

the load. However, as the flexural crack starts to open, the strain peaks and then starts to decrease. The load at the peak strain is approximately equal to the decompression load.

Another method of calculating the decompression load is by observing the load-deflection curves while loading the beam. Before the load reaches the decompression load, the beam behaves as an uncracked beam and the gross-section resists the load. After the load exceeds the decompression load, the cracks start to open and the section acts as a cracked section with a reduced moment of inertia. This can be clearly identified by the change of slope in the load-deflection curve. Before the decompression load, the curve is represented by a straight line with a steep slope, while after the decompression load, the curve is also represented by a straight line but with a much flatter slope. The decompression load, therefore, can be precisely determined from the load-deflection curve by estimating the load at which the curve starts to deviate from its linear uncracked segment.

Out of six beams, two beams were tested under three-point loading setup at ambient temperature (68 °F or 20 °C). The test included loading the beam in cycles of loading and unloading to a maximum load level of 45 kip (200 kN). Since the theoretical loading capacity of the beam was approximately 61 kip (271 kN), the beams were not expected to sustain any permanent damage other than the flexural cracks. Two of the remaining four beams were also tested under the same loading setup but at a temperature of 176 °F (80 °C). After concluding the load cycles at high temperature, the beams were allowed to cool down and the load cycles were repeated at ambient temperature (68 °F or 20 °C). The remaining two beams were tested under the same loading setup but at a temperature of -40 °F (-40 °C). After concluding the load cycles at low temperature, the beams were allowed to warm back up to ambient temperature and then, the load cycles were repeated.

The test beams were labeled as F1, F2, H1, H2, C1 and C2. Beams F1 and F2 were first tested at -40 °F (-40 °C) and then at 68 °F (20 °C). Beams H1 and H2 were first tested at 176 °F (80 °C) and then at 68 °F (20 °C). The control beams were labeled as C1 and C2 and tested only at 68 °F (20 °C). All beams were kept at the assigned temperature for at least 24 hours before conducting the flexural test. The core temperature of each beam was measured using embedded thermocouples and was verified against the air temperature. The flexural test was executed only after the beams reached the steady state with the core temperature matching the surrounding air temperature.

248

7.3.3.1 Beams F1 and F2

Beam F1 was loaded under three-point loading at a freezing temperature of -40 °F (-40 °C) as shown in Figure 7.3-19. The load was applied in cycles of loading and unloading with a load cycle increment of 5 kip (22 kN). The beam was checked for flexural cracks during and after each load cycle. The flexural cracks (Figure 7.3-20) were first observed after the end of the 35-kip (155-kN) load cycle, which suggested a cracking load between 30 (133 kN) and 35 kip (155 kN). The load cycles stopped at a load level of 45 kip (200 kN).

The second phase of testing included loading the beam in multiple load cycles with increments of 5 kip (22.2 kN) to a maximum load cycles to 45 kip (200 kN) at ambient temperature. Since the beam was cracked in the previous phase, no cracking load was observed. However, the decompression load was observed in both phases. The load-deflection curves from both test phases were overlapped for the 35-kip (155-kN) load cycle as shown in Figure 7.3-21. As shown in the figure, there was a slight difference in the decompression load, but this difference is not easily estimated by visual inspection of the graphs. To precisely estimate the decompression load for each case, the slope of the uncracked segment of the curve was estimated. Then, using the estimated slope, a straight line was drawn to overlap the uncracked segment and extended as a linear function. Finally, the deviation of the actual load-deflection curve from this straight line was calculated by subtracting the theoretical linear deflection from the measured experimental deflection. This method of evaluating the decompression load is detailed in Grace et al. (2019). The decompression load recorded at ambient temperature was higher than that recorded at freezing temperature with a difference of approximately 1.6 kip (7.0 kN).

Beam F2 (Figure 7.3-22) was identical in testing conditions to Beam F1. The test was repeated to verify the results through two test specimens. This beam was first saturated at a freezing temperature of -40 °F (-40 °C) and then tested under loading and unloading cycles to determine the cracking (Figure 7.3-23) and decompression loads. Similar to Beam F1, the cracking load was observed at the end of the 30-kip (133-kN) load cycle.

After the freezing phase, the beam was loaded again at ambient temperature to evaluate the decompression load and calculate the change in prestressing due to temperature change. With detailed inspection of Figure 7.3-24, there was a slight change in the decompression load with the

decompression load at ambient temperature higher than that at freezing temperature by approximately 1.2 kip (5.3 kN).

Figure 7.3-19 Beam F1 under three-point loading in the environmental chamber

Figure 7.3-20 Development of flexural cracks in Beam F1 after load cycles
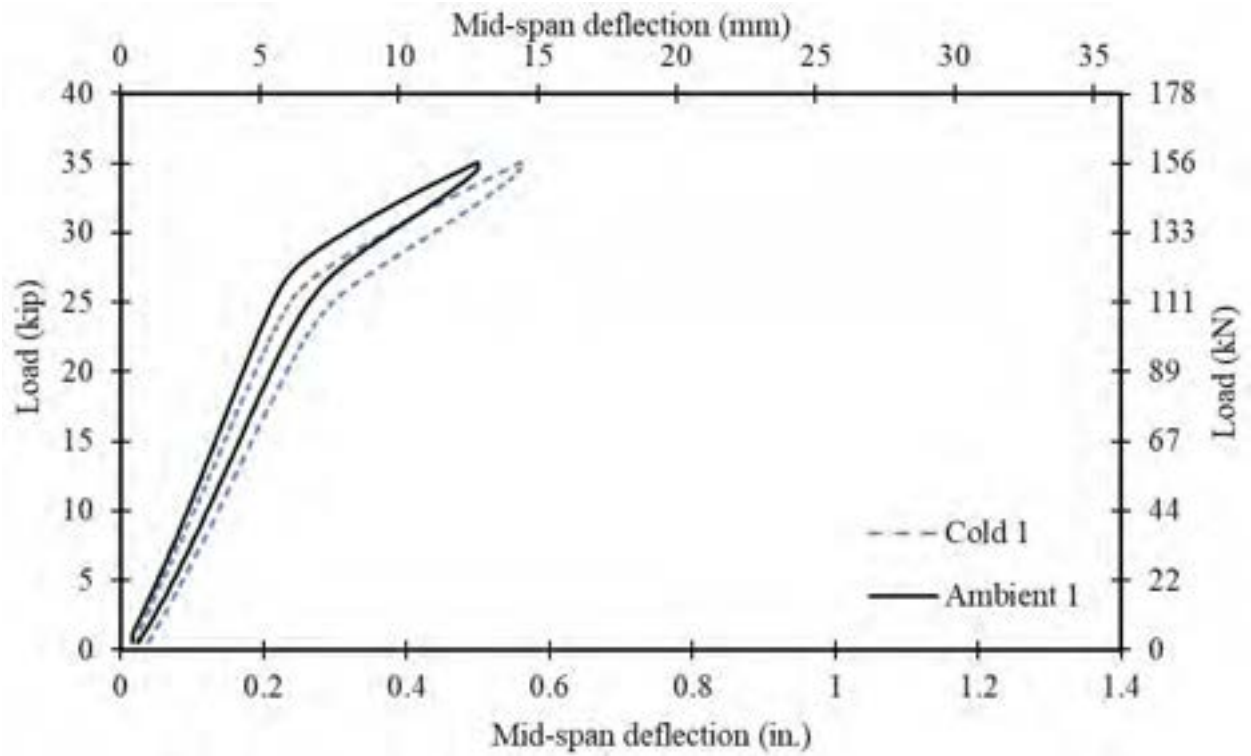
Figure 7.3-21 Change in decompression load with the change in testing temperature in Beam F1

Figure 7.3-22 Beam F2 under three-point loading in the environmental chamber

Figure 7.3-23 Development of flexural cracks in Beam F2 after load cycles
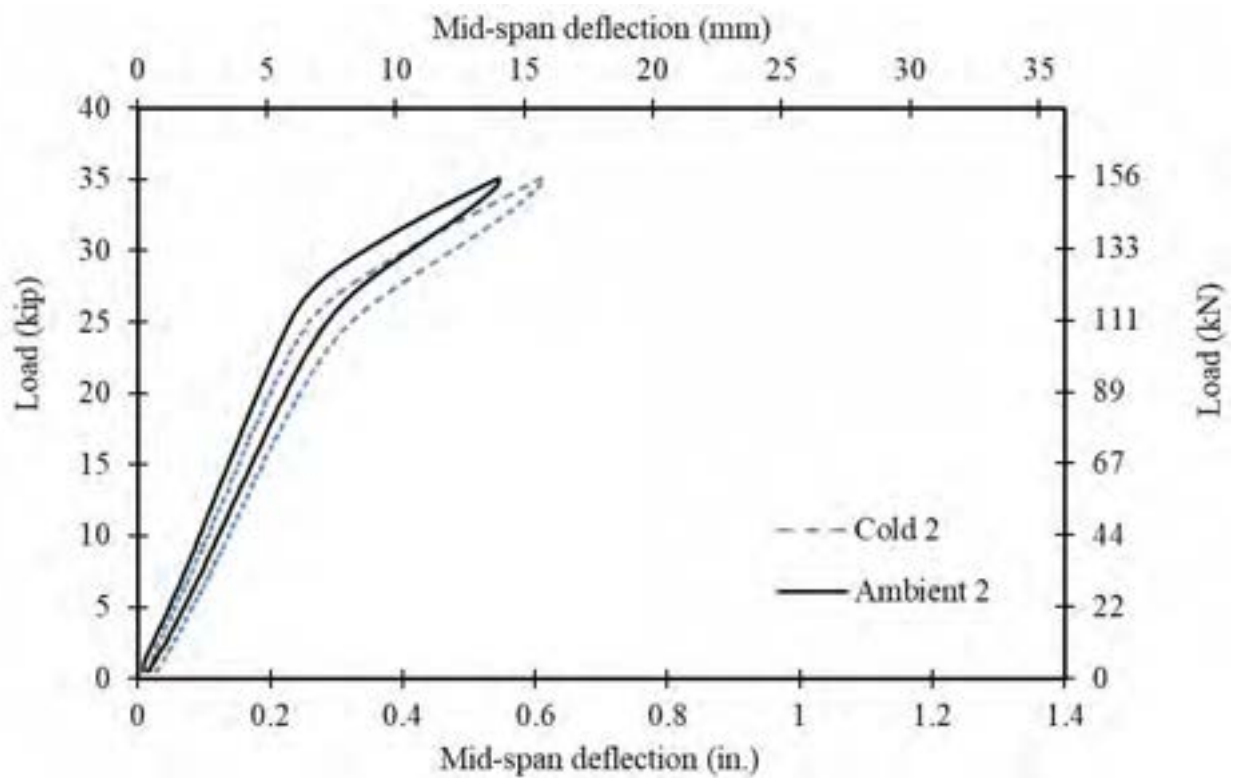
Figure 7.3-24 Change in decompression load with the change in testing temperature in Beam F2

7.3.3.2 Beams H1 and H2

Beam H1 was tested in a similar manner to Beams F1 and F2 except that the first phase of testing was performed at an elevated temperature of 176 °F (80 °C) with a setup as shown in Figure 7.3-25. The beam was allowed to saturate at this high temperature until the core temperature matched the surrounding air temperature. Thereafter, the beam was loaded under three-point loading in loading and unloading cycles to a maximum load of 45 kip (200 kN). The cracking load was observed from the load-deflection curves and was estimated between 30 and 35 kip (133 and 156 kN). Cracking in the beam after the 35-kip (156-kN) load cycle is shown in Figure 7.3-26. After completing the load cycles, the beam was allowed to cool down until it reached the ambient temperature and the load cycles were performed again. The load-deflection curves obtained from the high temperature testing and the ambient temperature testing and for the 35-kip load cycles are compared in Figure 7.3-27. However, a significant change in beam stiffness and drop in the decompression load was observed in the second set of load cycles.

The test and analysis was repeated using Beam H2(Figure 7.3-28 through Figure 7.3-30). Similar results were obtained as shown in Figure 7.3-30 with the decompression load during the second set of load cycles much less than that observed in the first set. The significant change of the decompression load may be an indication of a significant loss in the prestressing force or damage in the beam during the testing at high temperatures, whether the damage is in the concrete, the prestressing strands, or the bond between the concrete and the prestressing strands.

To rule out the damage of CFCC strands due to the increase in temperature and to assess the actual heat relaxation of the strands after exposure to high temperature, three CFCC test specimens were prepared and tensioned in frames as shown in Figure 7.3-31 through Figure 7.3-34. The test specimens followed the same details and dimension of 64-in. (1626 mm) test specimens as discussed earlier in this chapter (Section 7.2). The specimens were tensioned to a target force level of 53 kip (236 kN), similar to the initial force in the strands inside the decked bulb T beams. One specimen served as a control specimen and was maintained in a controlled laboratory environment, while the other two specimens were moved to the environmental chamber, where they were exposed to increase in temperature to 176 °F (80 °C) for 24 hours. The force in the three test specimens was continuously monitored through in-line load cells. As shown in Figure 7.3-35 and Table 7.3-3, the first 24 hours included loading and monitoring the force in the three specimens at

ambient conditions. Afterwards, the temperature of environmental chamber increased to 176 °F (80 °C). As shown in Figure 7.3-35, the increase in temperature resulted in a small increase in the force level, mainly due to the expansion of the steel frames supporting the CFCC strands. This increase in the force was followed by a reduction in the force due to the heat relaxation of the CFCC strands. By the end of the 48-hour period, the heating phase was terminated and the environmental chamber was allowed to cool down naturally to ambient temperature. Another drop in the force level was observed by the end of the heating phase due to the contraction of the supporting steel frames. Finally, the specimens were released from the frames.

The test showed that the CFCC specimens inside the environmental chamber lost, on average, an additional 6.16 kip (27 kN) due to heat relaxation. It should be noted that this loss of the force includes relaxation of the CFCC strands as well as relaxation of the anchor system. From Figure 7.3-18, the estimated heat relaxation strain at 176 °F (80 °C) is approximately 600 με and after accounting for anchorage relaxation, the test results appear to match the estimated heat relaxation of the CFCC strands. This indicated that the reduction in the decompression load of Beams H1 and H2 during the second set of load cycles (at ambient) was most likely due to softening of the concrete material. The increase in temperature along with the high load level (nearly 75 % of the estimated nominal capacity) resulted in unfavorable permanent deformation in the beams. Further testing and evaluation are needed to investigate this deformation.

Figure 7.3-25 Beam H1 under three-point loading in the environmental chamber

Figure 7.3-26 Flexural cracks during loading Beam H1 at 176 °F (80 °C) afte 35-kip (156-kN) load cycle
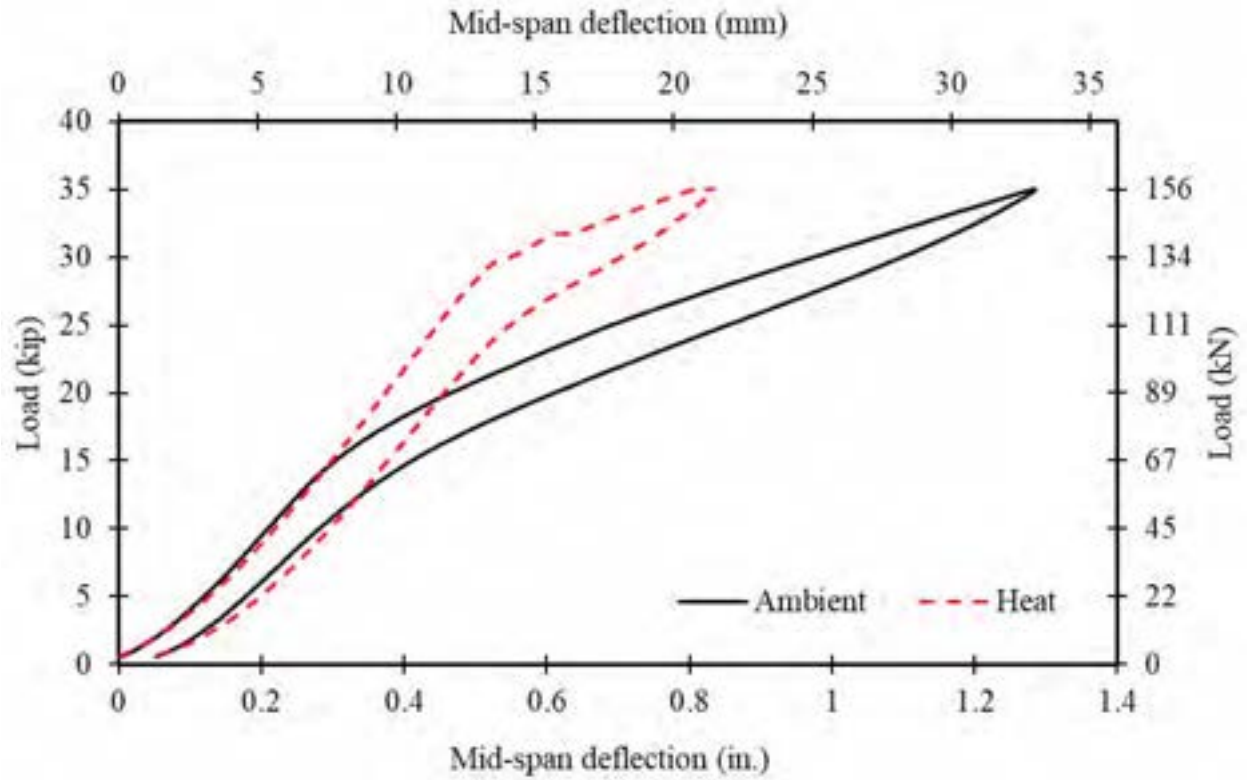
Figure 7.3-27 Change in decompression load with the change in testing temperature in Beam H1

Figure 7.3-28 Beam H2 under three-point loading in the environmental chamber

Figure 7.3-29 Development of flexural cracks in Beam H2 after load cycles
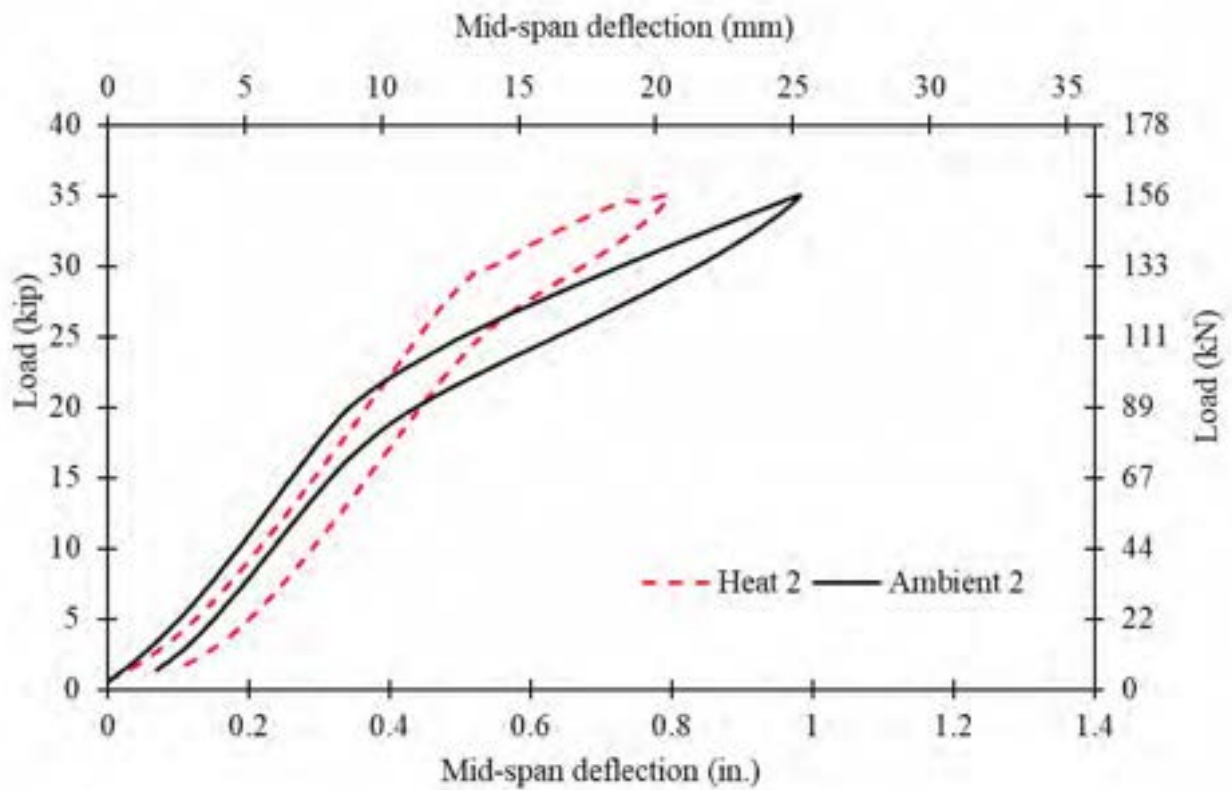
Figure 7.3-30 Change in decompression load with the change in testing temperature in Beam H2

Figure 7.3-31 Preparing unbonded CFCC strands for high temperature evaluation

Figure 7.3-32 Stressing CFCC strands for high temperature evaluation

Figure 7.3-33 Placing two stressed CFCC strands in the environmental chamber to be exposed to a temperature of 176 °F (80 °C) for 24 hours

Figure 7.3-34 Control CFCC strand kept in laboratory environment
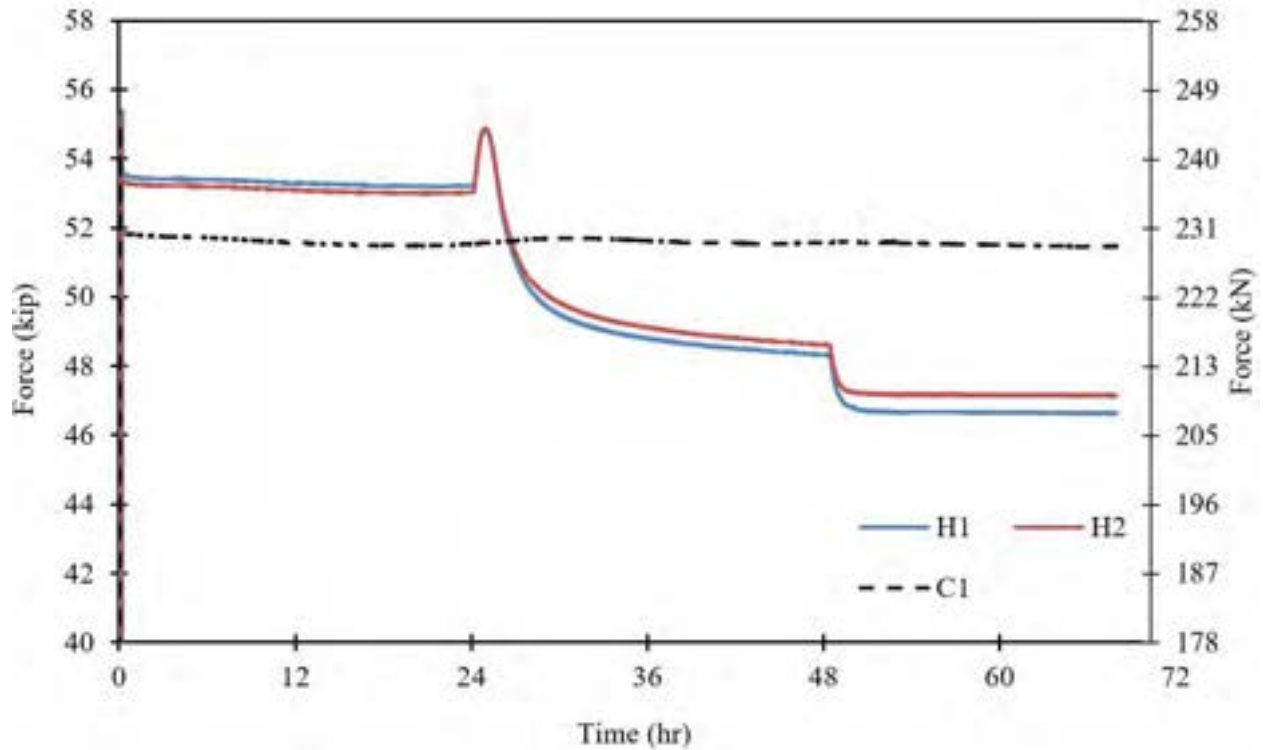
Figure 7.3-35 Change in force in stressed CFCC strands during heating and cooling

Table 7.3-3 Summary of key force levels in the CFCC strands

Prestressing force at each stage, kip	H1	H2	C1
Jacking force	55.36	55.16	54.77
Initial prestressing after seating	53.64	53.44	52.01
Start of heating cycle after initial relaxation	53.19	53.02	51.54
End of heating cycle after heat relaxation	48.32	48.58	51.57
End of cooling	46.63	47.14	51.47

7.3.3.3 Discussion

At the stage of decompression, the stress at the soffit of the beam at midspan (σ_{bot}) is equal to zero. Therefore, the stress equation at the beam soffit can be written as:

260

$$\sigma_{bot} = -\frac{P_e}{A} - \frac{P_e \cdot e}{S_{bot}} + \frac{M_{DL}}{S_{bot}} + \frac{M_{decomp}}{S_{bot}} = 0 \; ksi \; or \; MPa \tag{5}$$

Where:

P_e =   Effective prestressing force (kip or kN)

M_{DL} =   Moment due to dead load = 44.35 kip.in. (5.0 kN.m)

M_{decomp} =   Moment due to the decompression load = $\frac{P_{decomp} \cdot L}{4}$ (kip.in. or kN.m)

P_{decomp} =   Decompression load (kip or kN))

L =   Effective span of the beam = 15 ft (4.57 m)

A =   Cross sectional area of the beam = 126.5 in.^{2} (81,612 mm^2)

S_{bot} =   Section modulus = 468.8 in.^{3} (7,682,255 mm^3)

e =   Eccentricity of prestressing = 7.04 in. (179 mm)

By substituting the aforementioned values, Equation 5 can be rearranged to represent a direct relationship between the effective prestressing force and the decompression load as follows:

$$0 = -P_e \left(\frac{1}{A} + \frac{e}{S_{bot}}\right) + \frac{M_{DL}}{S_{bot}} + \frac{P_{decomp} \cdot L/4}{S_{bot}} \tag{6}$$

$$P_e = \frac{\frac{M_{DL}}{S_{bot}} + \frac{P_{decomp} \cdot L/4}{S_{bot}}}{\left(\frac{1}{A} + \frac{e}{S_{bot}}\right)} = \frac{44.35 + 45 \, P_{decomp}}{11.11} = 4 + 4.05 \, P_{decomp} \tag{7}$$

The change in the effective prestressing force (ΔP_e) can also be directly related to the change in decompression load (ΔP_{decomp}) as:

$$\Delta P_e = 4.05 \, \Delta P_{decomp} \tag{8}$$

With the increase or decrease in temperature, it is expected that the effective prestressing force will increase or decrease accordingly due to the difference in thermal expansion between concrete and CFCC. For instance, assuming the difference in the coefficient of thermal expansion between concrete and CFCC is 6×10^{-6} /°F (12×10^{-6} /°C), the increase in temperature from 68 to 176 °F

(20 to 80 °C) or the decrease in temperature from 68 to -40 °F (20 to -40 °C) (an increase or decrease of 108 °F or 60 °C), would yield a strain increase or decrease of 0.000648. As the total area of prestressing (a_{frp}) is 0.468 in.^{2} (302 mm^2) and the approximate elastic modulus of CFCC (E_{frp}) is 22,480 ksi (155 GPa), this increase or decrease in strain yields an increase or decrease in the effective prestressing force of approximately 6.8 kip (30 kN) per beam, or an increase/decrease in the decompression load by approximately 1.68 kip (7.5 kN).

By comparing this theoretical value with the experimental results of the decompression loads for Beams F1 and F2, it can be concluded that there is reasonable agreement between the experimental and theoretical values and the gain or loss in the prestressing force due to seasonal temperature change can be accurately predicted by estimating the normal temperature range and calculating the prestressing gain/loss due to the temperature change. Beams H1 and H2 were excluded from this analysis until further research assessing their performance becomes available.

Based on the results from the experimental investigation of decked bulb T beams exposed to temperature change, it appears that beams prestressed with CFCC strands experience a loss in the prestressing force with the decrease in temperature. However, this loss in prestressing is recovered when the temperature increases back to the normal range. The loss in effective prestressing force conforms, with a reasonable degree of accuracy, to the theoretical calculations.

7.3.4 Exposure to Freeze-Thaw Cycles

A special tempering tank was constructed inside the environmental chamber to accommodate the four decked bulb T beams so that the temperature along the beam surfaces is constant at each phase of the test. The tempering tank had a length of 17 ft (5.2 m), a width of 48 in. (1.22 m), and a depth of 35 in. (889 mm) and was placed on a wooden platform deck mounted on steel adjustable chairs spaced at 2 ft (610 mm) on center with a height of 10 in. (254 mm). The tank was designed with two access holes at the sides for installing conduits in order to transfer water from the storage reservoir during the thawing phase of the freeze-thaw test. After constructing the tempering tank, the four decked bulb T beams were placed inside the tank (Figure 7.3-36). Meanwhile, four concrete cylinders and five pullout specimens of the same batch of concrete were prepared, labelled and placed inside the tank to evaluate the effects of freeze-thaw cycles on the concrete compressive strength and the bond strength (Figure 7.3-37 through Figure 7.3-39). Air ducts were

arranged inside the chamber and the beams were covered with layers of Styrofoam to ensure constant temperature along the beam length.

The temperature profile of the freeze-thaw test for decked bulb T beams followed the recommendations of ASTM C666 Procedure B, which states that specimens shall be completely surrounded by air during the freezing phase and by water during the thawing phase and that no less than 20 % of the time shall be used for thawing. Also, the temperature of the specimens should be lowered from 40 to 0 °F (4.4 to -18 °C) and then raised from 0 to 40 °F (-18 to 4.5 °C) in a total time not less than 2 hrs. and more than 5 hrs. Therefore, the freezing phase of the test was conducted by lowering the air temperature of the environmental chamber to -50 °F (-45.5 °C) until the core temperature of the beams reached 0 °F (-18 °C) in 2 hrs. and 30 min. The thawing phase was executed by flooding the tempering tank with water and raising the air temperature in the chamber to 50 °F (10 °C) until the core temperature of the beams reached 40 °F (4.5 °C) in one hr. and 50 min. The total duration of each freeze-thaw cycle was set to 4 hrs. and 20 min. Figure 7.3-40 shows the time-temperature variations for freeze-thaw cycles for the prestressed beams, while Figure 7.3-41 shows the arrangement of the beams inside the tank. The 300 freeze-thaw cycles were executed in 54 days with a rate of 5.54 cycles per day. A temperature profile was created using a VS-1 control system to follow the test program. The air temperature was set to change from -50 °F to 50 °F (-45.5 to 10 °C) in sequences to maintain the assigned core temperature. The control system was set to pump the water into the tempering tank with a proper water level in the thawing phase and continue to re-circulate the water through a heat exchanger to maintain the set water temperature of 40 °F (4.5 °C). After the beams were thawed, the system diverted the water back to the holding reservoir and maintained the water at 40 °F (4.5 °C) until the start of the subsequent thaw cycle.

The test was paused after 150 freeze-thaw cycles to gain access and evaluate the conditions of the specimens. While the beams were still intact after 150 freeze-thaw cycles, the concrete cylinders and the pullout specimens significantly deteriorated to the point where further testing was not possible (Figure 7.3-42 and Figure 7.3-43). Additional concrete cylinders and pullout specimens that were cast at the same time as the test beams were placed inside the environmental chamber but on the outside of the tank and the test was resumed for the remaining 150 cycles (Figure 7.3-44).

After completing 300 freeze-thaw cycles on the beams and while monitoring their core temperatures at each cycle, the beams were removed from the tank and were allowed to dry at room temperature (Figure 7.3-45 through Figure 7.3-48). After proper drying, the four decked bulb T beams subjected to 300 freeze-thaw cycles and the two control beams, preserved in controlled laboratory conditions, were moved to the testing facility and were loaded under three-point-load test setup to failure. The concrete cylinders were tested under uniaxial compression test to determine the residual concrete compressive strength.

Figure 7.3-36 Decked bulb T beam placed in the tank for freeze-thaw testing

Figure 7.3-37 Concrete cylinders from the same batch as the beams placed with the beams and exposed to freeze-thaw cycles

Figure 7.3-38 Decked bulb T beams during freezing and thawing cycles

Figure 7.3-39 Decked bulb T beams during freezing and thawing cycles
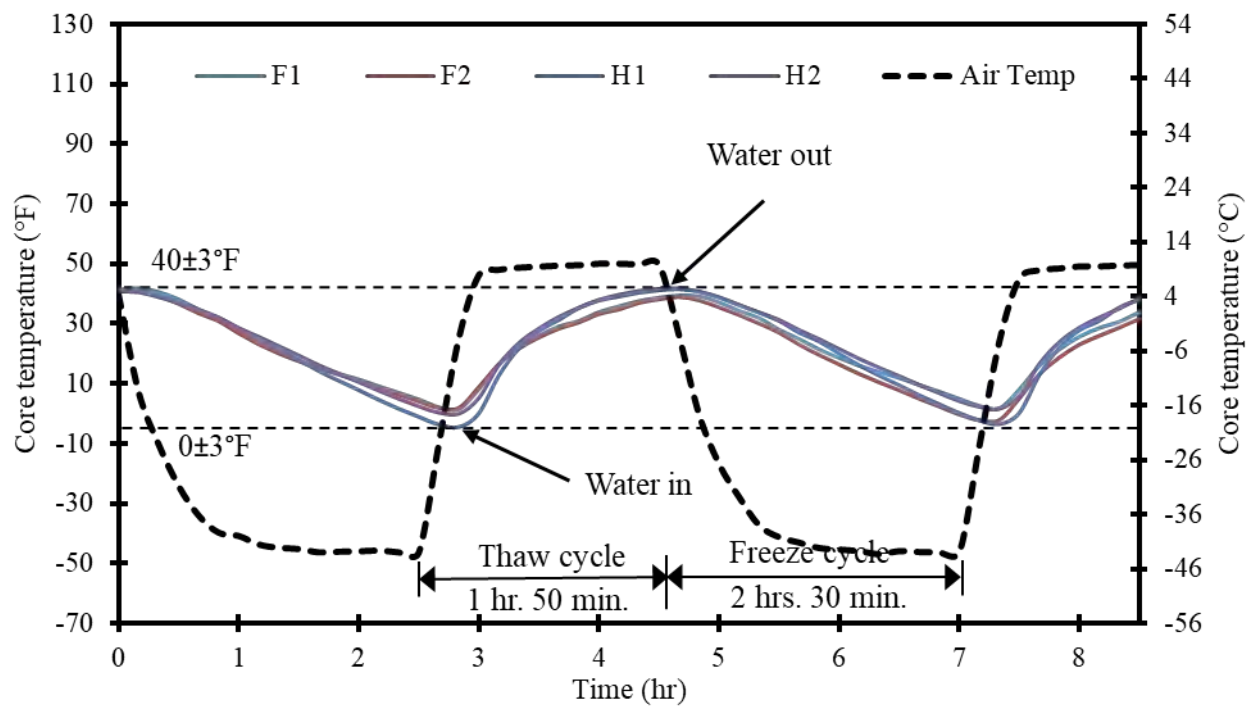
Figure 7.3-40 Air vs. beam core temperature during the freezing and thawing cycles
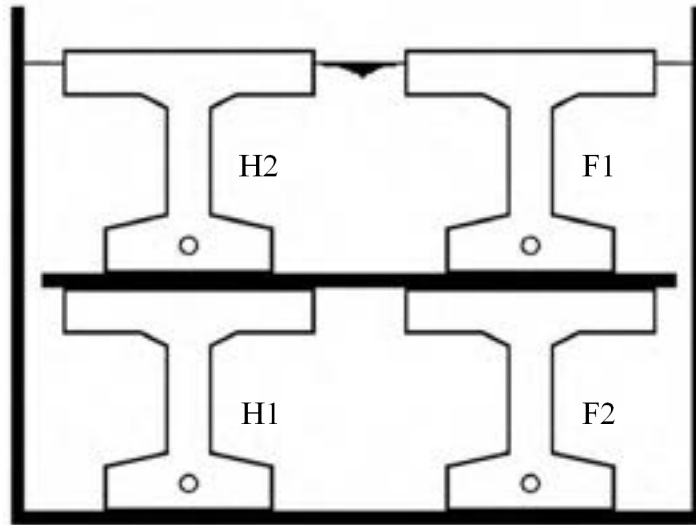
Figure 7.3-41 Arrangement of the test beams in the tank

Figure 7.3-42 Freeze-thaw cycles caused deterioration of the concrete cylinders and pullout specimens (picture taken after 150 cycles)

Figure 7.3-43 Deterioration of pullout specimens after exposure to 150 freeze-thaw cycles

Figure 7.3-44 New cylinders and pullout specimens placed outside the tank after 150 freeze-thaw cycles

Figure 7.3-45 Deterioration of decked bulb T beams after exposure to 300 freeze-thaw cycles

Figure 7.3-46 Concrete corners after exposure to 300 freeze-thaw cycles

Figure 7.3-47 Deterioration of beam edges due to 300 freeze-thaw cycles

Figure 7.3-48 Decked bulb T beams after exposure to 300 freeze-thaw cycles

7.3.5 Residual Flexural Capacity

The flexural test setup included supporting the beams on two elastomeric bearing pads, positioned on two steel stands spaced 15 ft (4.6 m). Two 2 in. (50 mm) linear strain gages were attached on the top concrete surface near the loading point to capture the concrete strain. Two linear motion

transducers (LMTs) were attached to the underside of the beam at midspan to capture the deflection of the beams. Three linear variable differential transducers (LVDTs) were used to evaluate the strain at different depths at the midspan section. A 220-kip (980-kN) MTS hydraulic actuator was programmed to apply a vertical concentrated load at the beam mid-span in a force-control mode with rate of 4 kip/min (100 kN/min). All sensors were connected to a Mars Lab data acquisition system to collect the necessary data needed to perform a detailed analysis. Meanwhile, the concrete cylinders were tested under uniaxial compression load to evaluate the residual concrete strength.

7.3.5.1 Uniaxial Compressive Test of Concrete Cylinders

Figure 7.3-49 through Figure 7.3-51 show the testing and failure of the concrete cylinders under a uniaxial test setup. The freeze-thaw cycles on the prestressed beams and concrete cylinders resulted in deterioration of concrete cylinders inside the tank after 150 cycles. This can be attributed to the water absorption during freeze-thaw cycles. During the thawing phase, the pores of concrete were filled with water and the concrete became fully saturated. In the freezing phase, this water in moist concrete froze and produced pressure on the voids that caused expansion, cracking, and scaling of concrete. The distress to critically saturated concrete from freezing and thawing commenced with the first freeze-thaw cycle and continued throughout the rest of the cycles. It resulted in concrete deterioration that was evident through the disintegration of the concrete cylinders.

Concrete cylinders that were placed outside the tank and exposed to 150 cycles of freezing and thawing in air showed an average compressive strength of 7750 psi (53.4 MPa). On the other hand, the average compressive strength of control cylinders in ambient conditions was approximately 9200 psi (63.4 MPa).

271

Figure 7.3-49 Concrete cylinders after exposure to 150 freeze-thaw cycles (outside the tank)
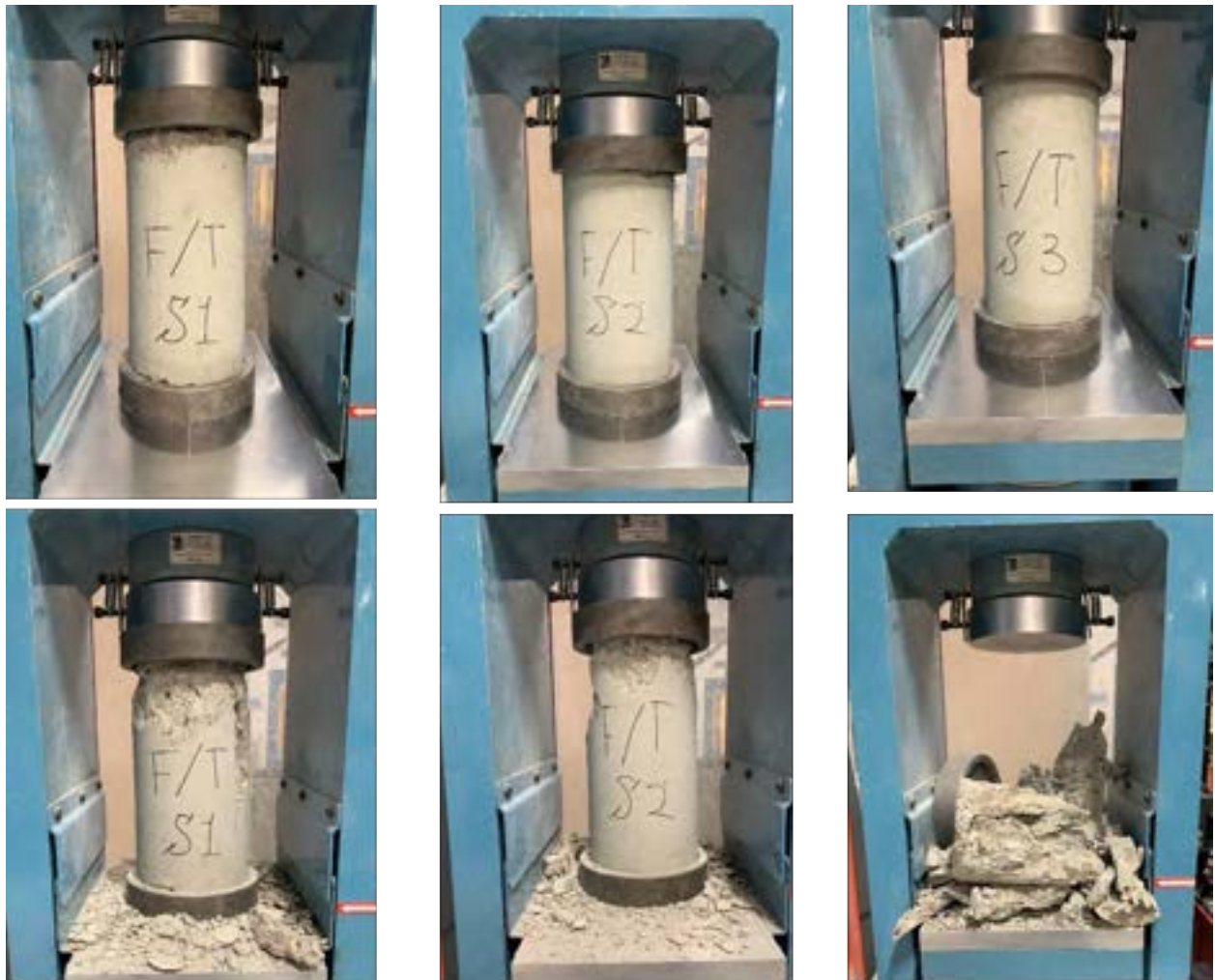
Figure 7.3-50 Testing and failure of concrete cylinders after exposure to 150 freeze-thaw cycles

Figure 7.3-51 Testing and failure of control cylinders

7.3.5.2 Flexural Test of Decked Bulb T Beams

The six decked bulb T-beams, including the control beams, had been previously subjected to multiple load cycles in 5 kip increments up to a maximum load cycle of 45 kips as explained in Section 7.3.3. Therefore, all the beams were cracked before the start of the freeze-thaw test. After freeze-thaw cycles, the beams were loaded under three-point-load test setup in loading-unloading cycles to failure.

The theoretical analysis of the beam cross-section, using the force equilibrium and strain compatibility method, indicated a tension failure by rupture of prestressing CFCC tendons at theoretical load of 61 kip (271 kN). The first beam, Control Beam C1 (Figure 7.3-52 through Figure 7.3-56) failed at a load level of 66.4 kip (295 kN) with a corresponding deflection of 2.8 in.

274

(71 mm). The failure was characterized by slippage of CFCC strands. The maximum recorded concrete compressive strain before failure was approximately 2,604 $\mu\varepsilon$.

Control Beam C2 (Figure 7.3-57 through Figure 7.3-60) failed at a load of 58.3 kip (259 kN) with a corresponding midspan deflection of 2.2 in. (56 mm) and a concrete compression strain of 2,418 $\mu\varepsilon$. Similar to Beam C1, the failure was initiated by slippage of CFCC strands.

Beam F1 (Figure 7.3-61 through Figure 7.3-65) failed at a load level of 49.6 kip (221 kN) with a corresponding deflection of 1.7 in. (43 mm). The maximum recorded concrete compression strain before failure was approximately 1,314 $\mu\varepsilon$. The failure was characterized by slippage of CFCC strands. Beam F2 (Figure 7.3-66 through Figure 7.3-71) was identical in failure mode to Beam F1. Failure initiated by slippage of CFCC strands at a load level of 41.6 kip (185 kN) with a corresponding deflection of 1.4 in. (36 mm) and a maximum recorded concrete compression strain of 1,707 $\mu\varepsilon$.

Beam H1 (Figure 7.3-72 through Figure 7.3-77) failed at a load level of 41.9 kip (186 kN) with a corresponding deflection of 3.2 in. (81 mm) and a maximum recorded concrete compressive strain of approximately 1,457 $\mu\varepsilon$. The failure was characterized by slippage of CFCC strands. Beam H2 (Figure 7.3-78 through Figure 7.3-83) experienced a failure mode similar to that of Beam H1. The beam failed at a load level of 47 kip (209 kN) with a corresponding deflection of 2.9 in. (74 mm) and maximum concrete compression strain at failure of 1,421 $\mu\varepsilon$.

Comparing the load-deflection curves of the control beams with those of Beams F1, F2, H1, and H2 (Figure 7.3-84) revealed that freeze-thaw exposure influenced the flexural strength of the beams by lowering the bond strength between the concrete and CFCC strands. As test results showed that CFCC strands were not negatively impacted by freeze-thaw cycles, the loss in bond strength resulted mainly from the loss of concrete strength. In addition, Beams F1 and H2 were placed on the top of Beams F2 and H1 in the tank during freeze-thaw cycles. As shown in Table 7.3-4, the top beams achieved higher residual capacities than the bottom beams. This can be attributed to a more severe exposure for the bottom beams in the tank due to increased water pressure that pushed the water further into the pores of the bottom beams in addition to the slightly colder temperature at the bottom of the tank.

Figure 7.3-52 Three-point loading of Beam C1 (midspan camber of 0.75 in.)

Figure 7.3-53 Failure of Beam C1 under three-point loading

Figure 7.3-54 Debonding of CFCC strands in Beam C1

Figure 7.3-55 End view showing the slippage of CFCC strands in Beam C1 at maximum load
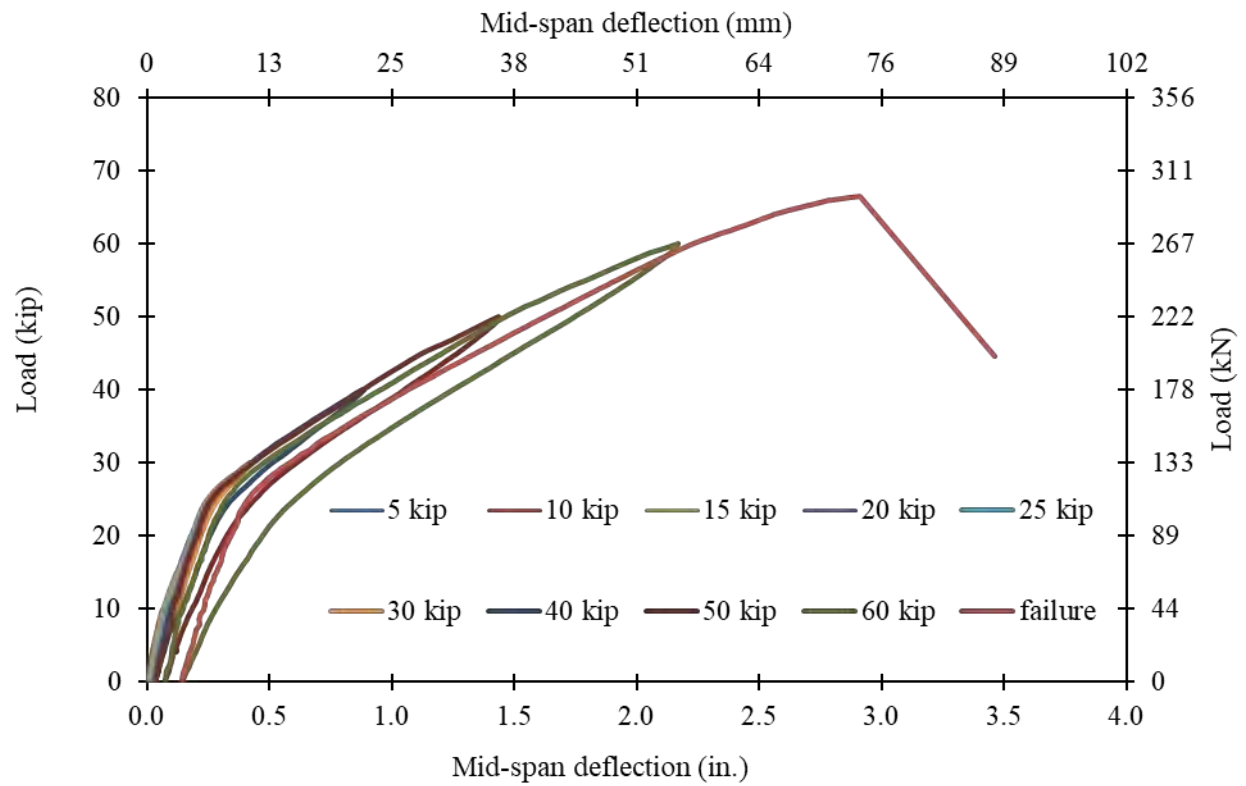
Figure 7.3-56 Load-deflection curves of Beam C1

Figure 7.3-57 Failure of Beam C2 under three-point loading

Figure 7.3-58 Debonding of CFCC strands and spalling of concrete at midspan of Beam C2

Figure 7.3-59 End view showing debonding of CFCC strands in Beam C2 after failure
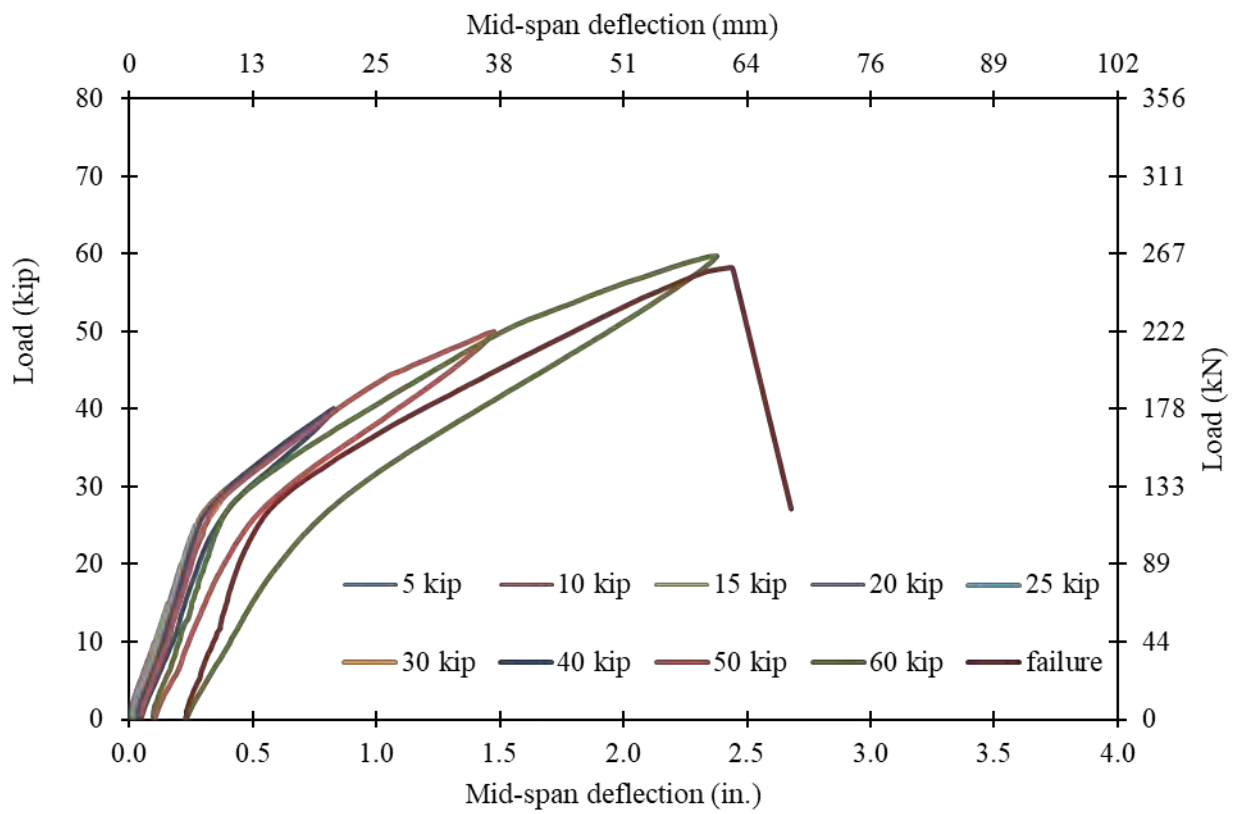
Figure 7.3-60 Load-deflection curves of Beam C2

Figure 7.3-61 Three-point loading of Beam F1

Figure 7.3-62 Midspan camber of 1.0 in. (25.4 mm) in Beam F1 before flexural testing
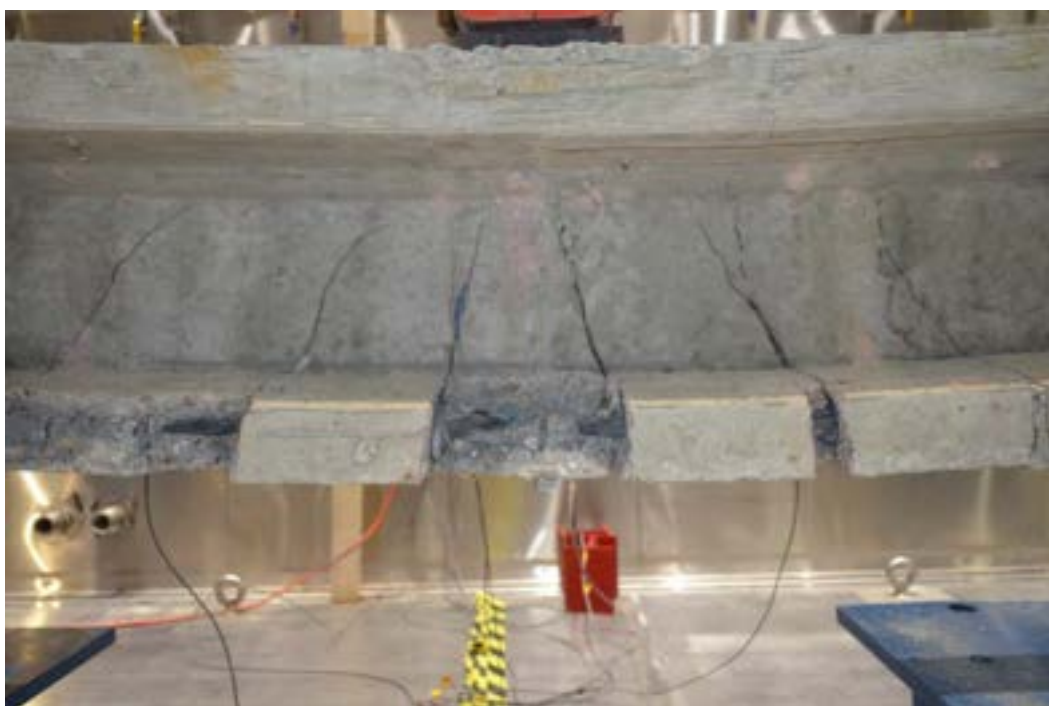
Figure 7.3-63 Debonding of CFCC strands and spalling of concrete at midspan of Beam F1

Figure 7.3-64 End view showing slippage of CFCC strands in Beam F1 at maximum load
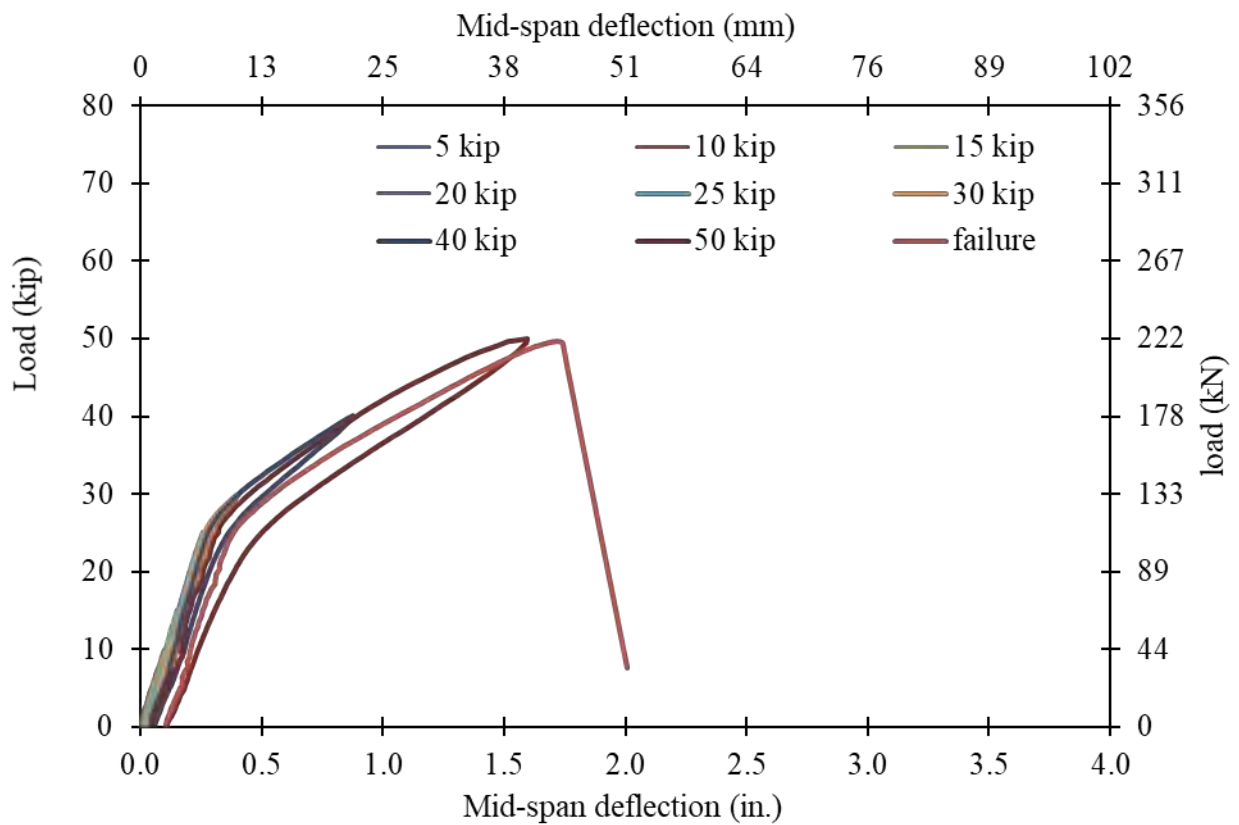
Figure 7.3-65 Load-deflection curves of Beam F1

Figure 7.3-66 Three-point loading of Beam F2

Figure 7.3-67 Midspan camber of 1.0 in. (25.4 mm) in Beam F2 before flexural testing

Figure 7.3-68 Failure of Beam F2 under three-point loading

Figure 7.3-69 Debonding of CFCC strands and spalling of concrete at midspan of Beam F2

Figure 7.3-70 End view showing slippage of CFCC strands in Beam F2 after failure
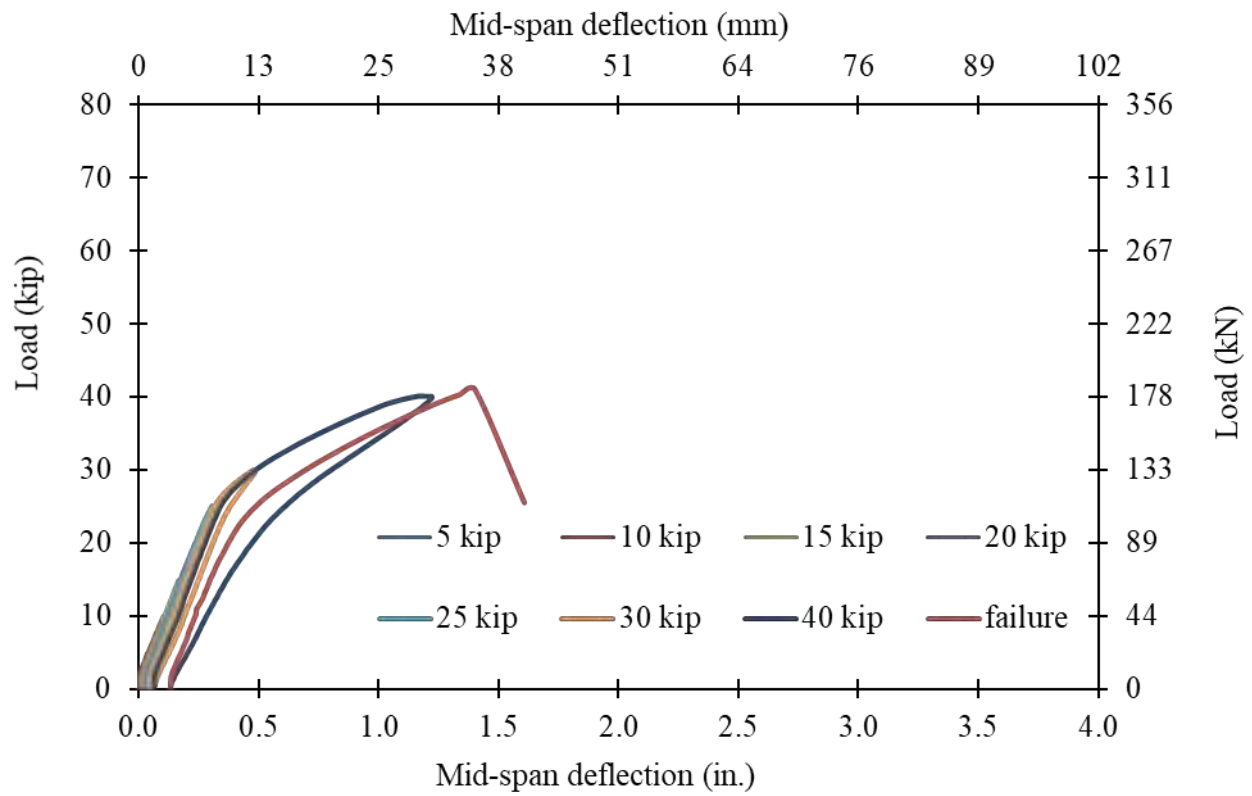
Figure 7.3-71 Load-deflection curves of Beam F2

Figure 7.3-72 Three-point loading of Beam H1

Figure 7.3-73 Midspan camber of 0.75 in. (19 mm) in Beam H1 before flexural testing

Figure 7.3-74 Failure of Beam H1 under three-point loading

Figure 7.3-75 Debonding of CFCC strands and spalling of concrete at midspan of Beam H1

Figure 7.3-76 End view showing slippage of CFCC strands in Beam H1 after failure
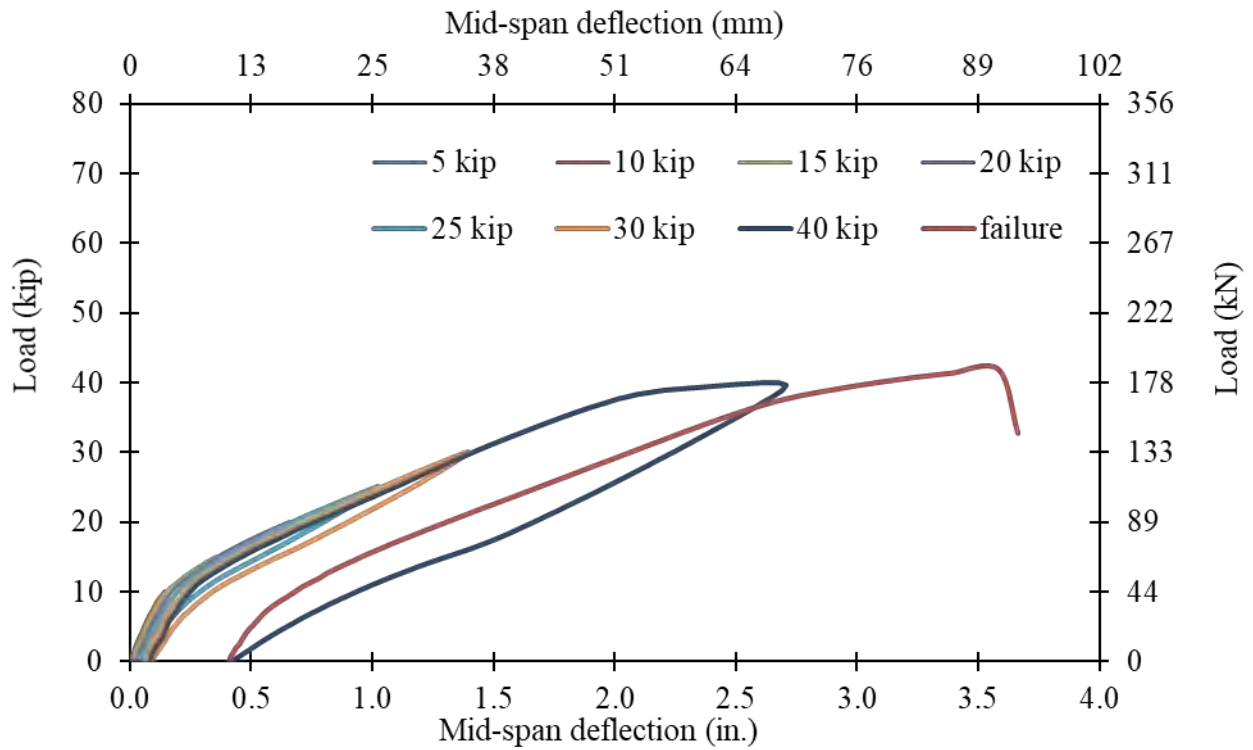
Figure 7.3-77 Load-deflection curves of Beam H1

Figure 7.3-78 Three-point loading of Beam H2

Figure 7.3-79 Midspan camber of 1.0 in. (25.4 mm) in Beam H2 before flexural testing

Figure 7.3-80 Failure of Beam H2 under three-point loading

Figure 7.3-81 Debonding of CFCC strands and spalling of concrete at midspan of Beam H2

Figure 7.3-82 End view showing slippage of CFCC strands in Beam H2 after failure
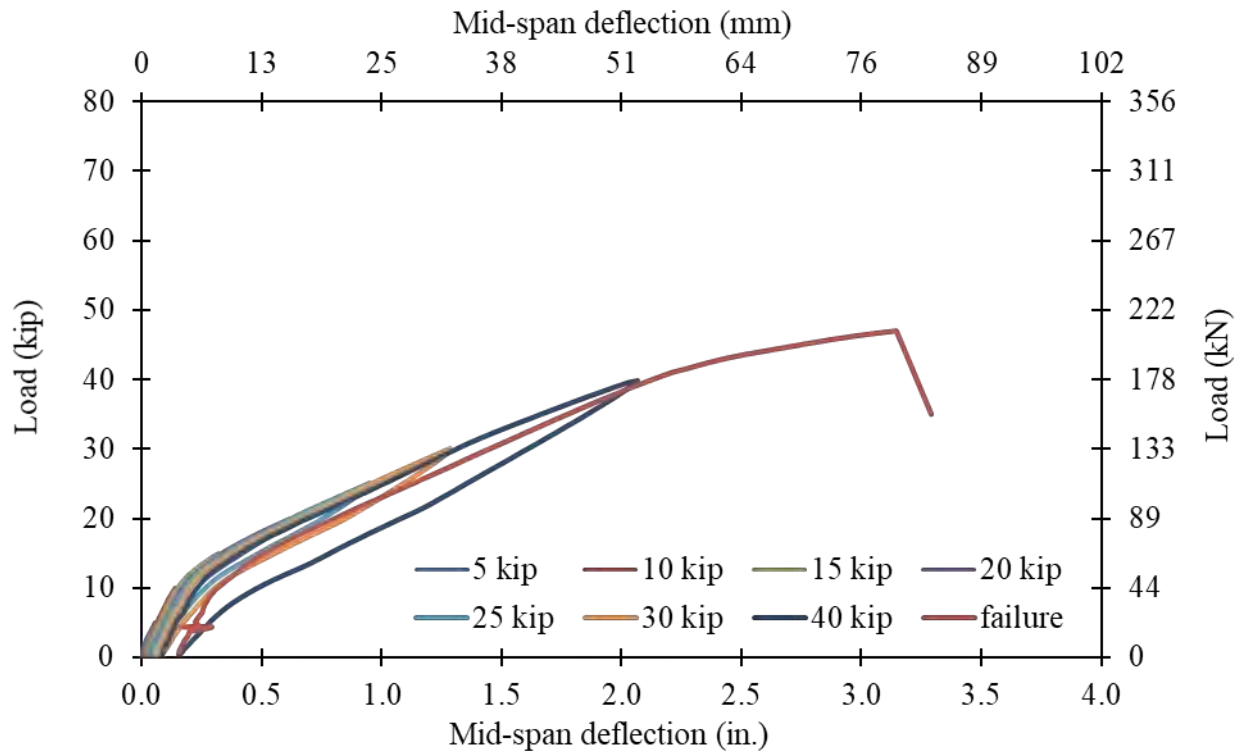
Figure 7.3-83 Load-deflection curves of Beam H2
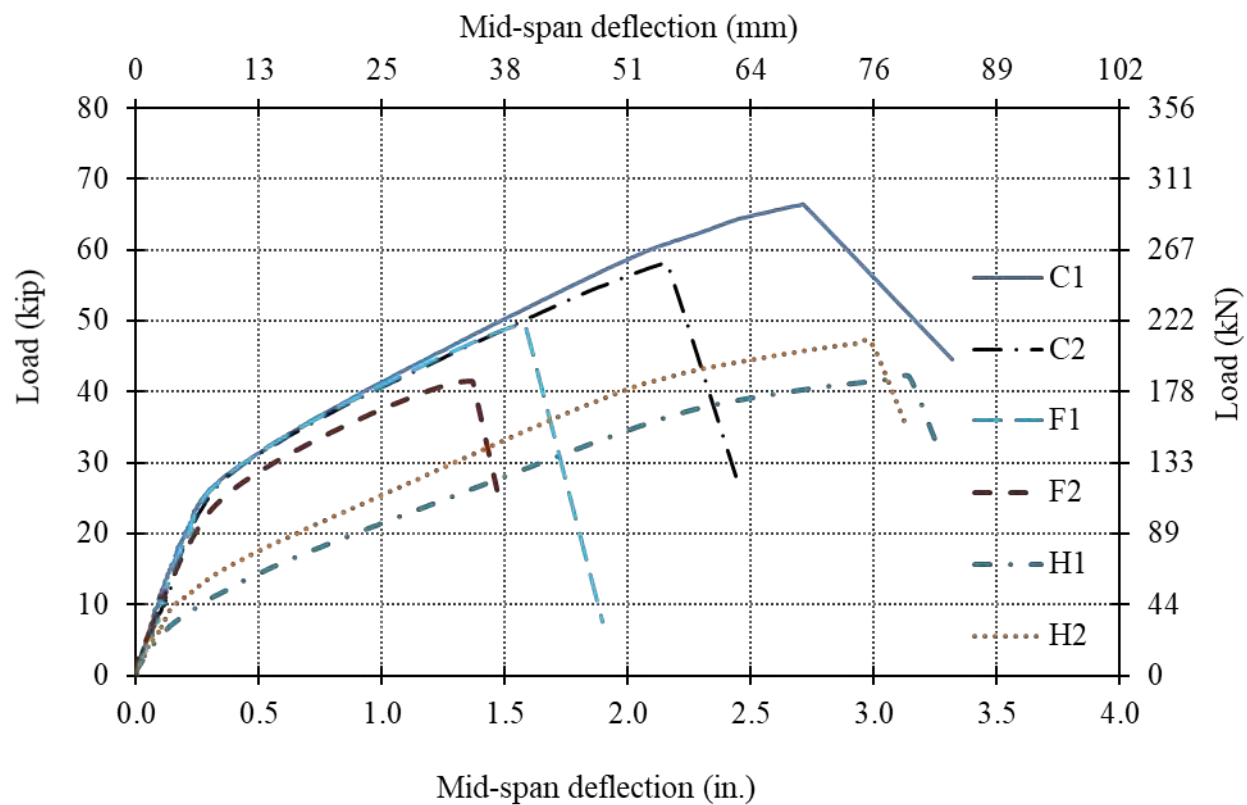
Figure 7.3-84 Comparison between load-deflection curves of all beams

Table 7.3-4 Summary of test results for all beams

Beam ID	Ultimate Load (kip)	Max Deflection (in.)	Conc. strain (με)
C1	66.4	2.8	2604
C2	58.3	2.2	2418
F1	49.6	1.7	1314
F2	41.6	1.4	1707
H1	41.9	3.2	1457
H2	47.0	2.9	1421

7.4 Summary

The decked bulb T beams had a length of 16 ft (4.88 m) with a development length of 8.0 ft (2.44 m) during the three-point-load test. This development length was sufficient for the control beams to achieve their theoretical load carrying capacity. On the other hand, beams exposed to freeze-thaw cycles experienced severe deterioration in concrete strength, which also resulted in a reduction of the bond strength between concrete and CFCC. On average, there was approximately a 28 % drop in the bond strength between concrete and CFCC after exposure to freeze-thaw cycles.

It should be noted that the beams were exposed to freeze-thaw cycles following ASTM C666/C 666M-15 (ASTM 2015) test standards, which states that specimens shall be completely surrounded by air during the freezing phase and by water during the thawing phase and that no less than 20 % of the time shall be used for thawing. Also, the temperature of the specimens should be lowered from 40 to 0 °F (4.4 to -18 °C) and then raised from 0 to 40 °F (-18 to 4.5 °C) in a total time not less than 2 hrs. and more than 5 hrs. Therefore, the freezing phase of the test was conducted by lowering the air temperature of the environmental chamber to -50 °F (-45.5 °C) until the core temperature of the beams reached 0 °F (-18 °C) in 2 hrs. and 30 min. The thawing phase was executed by flooding the tempering tank with water and raising the air temperature in the chamber to 50 °F (10 °C) until the core temperature of the beams reached 40 °F (4.5 °C) in one hr. and 50 min. The total duration of each freeze-thaw cycle was set to 4 hours and 20 min.

The design of the aforementioned freeze-thaw cycle is intended to produce accelerated freeze-thaw effect on the test specimens and does not necessarily represent a typical freeze-thaw cycle during the winter time. Therefore, it can be concluded that that the state of the beams after exposure to 300 freeze-thaw cycles represents the state of the structure near the end of its lifespan. In addition, the freeze-thaw deterioration of the concrete and its bond capacity is prone to happen regardless of the type of the internal reinforcement and prestressing strands. As indicated in Section 7.2, CFCC strands tend to gain strength and stiffness after exposure to freeze-thaw cycles. Therefore, the loss in the bond strength is attributed mainly to the loss of concrete strength.

CHAPTER 8: HALF-SCALE BRIDGE MODEL TESTING

8.1 Introduction

A one-half scale decked bulb T beam bridge model was designed, constructed, instrumented, and tested to evaluate its flexural performance in the Center for Innovative Material Research (CIMR) at Lawrence Technological University (LTU). The bridge model consists of five simply supported precast decked bulb T beams with a total length of 41 ft (12.5 m). The beams are prestressed with 0.7″ CFCC strands and connected together using Ultra High-Performance Concrete (UHPC) shear key joints. A control decked bulb T beam was also constructed and tested to verify the efficacy of the design before the construction and testing of the bridge model. The control beam was tested under four-point loading flexural test setup. The bridge model was tested under different loading configurations including service limit state (pre-cracking stage), post-cracking limit state and strength limit state. Description of construction techniques and materials employed to construct the control beam and the bridge model is provided in the following sections. Instrumentation used to examine the performance of the bridge model is also discussed. Furthermore, test methodology and test results are presented in this chapter.

8.2 Details of Control Beam

Figure 8.2-1 shows an elevation view of the decked bulb T control beam. The decked bulb T beam has a total length of 41 ft (12.5 m) and an effective span of 40 ft (12.2 m). The beam is composed of two end blocks of 17 in. (457 mm) wide and five intermediate diaphragms of 10 in. (254 mm) wide spaced at 6.5 ft (21 m). The dimensions of the beam cross-section, between end blocks and diaphragms, include an 18 in. (457 mm) wide top flange, a 16 in. (406 mm) deep web and a 12 in. (305 mm) wide bottom flange. The cross and longitudinal sections of the decked bulb T beam are shown in Figure 8.2-2. The beam is prestressed with three 0.7″ CFCC strands. To avoid excess tensile stresses at the beam ends after prestress transfer, one out of the three CFCC strands is debonded for a length of 10 ft (3 m) at each end. All CFCC strands in the control beam were tensioned with an initial jacking force of 57-kip (253 kN), which corresponds to a stress level of approximately 72.5 % of the guaranteed strength of 0.7″ CFCC. In addition, the beam was provided with five No. 5 Grade 60 steel rebars in the top flange and transverse reinforcement of No. 3 Grade 60 steel rebars. The beam was designed to fail in tension by rupture of CFCC strands.

294
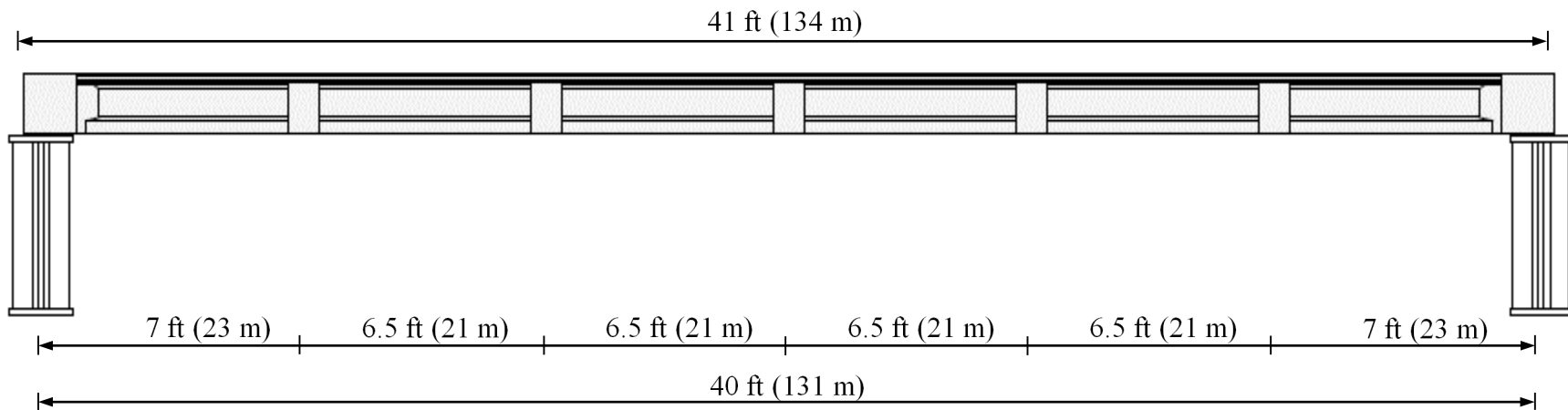
Figure 8.2-1 Elevation view of decked bulb T control beam
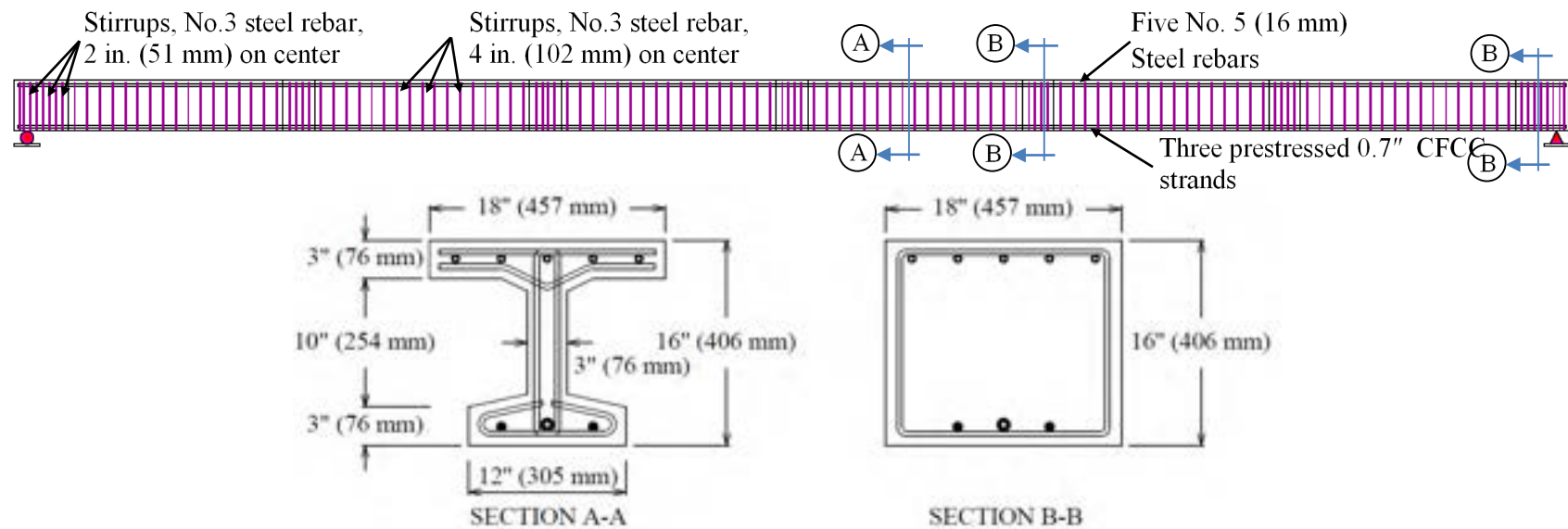
Figure 8.2-2 Cross-section and internal reinforcement details of decked bulb T beam

295

8.3 Materials

All decked bulb T beams were constructed using normal-weight, ready-mix concrete provided by McCoig Materials in Detroit, MI. The concrete mix was designed to achieve a 28-day compressive strength of 7000 psi (48 MPa). The maximum aggregate size was limited to 0.75 in. (19 mm) and a slump of 8 in. (203 mm) or higher was verified before concrete casting.

The flexural reinforcement is composed of Carbon Fiber Composite Cable (CFCC) strands provided in the bottom fibers in the tensile zone of the concrete beam. Whereas, top reinforcement is composed of No. 5 (16 mm) Grade 60 steel rebars. The mechanical properties of CFCC strands are listed in Table 8.3-1, as provided by the manufacturer. Before starting the construction of decked bulb T beams, static tensile tests were carried out on five CFCC specimens according to ASTM D7205/D7205M-06 (ASTM 2016) to evaluate the tensile strength of CFCC. The average tensile strength of 0.7″ CFCC strands was approximately 105.3 kip (469 kN) with a minimum breaking load of 104.7 kip (466 kN) and maximum breaking load of 106 kip (471 kN).

The primary shear reinforcement of the decked bulb T beam was made up of three steel stirrups welded together with tack welds, as shown in Figure 8.3-1 (a). The stirrups were made from No. 3 (9.5 mm) deformed steel bars spaced 4 in. (101 mm) on center. The beam end blocks and diaphragms were provided with rectangular stirrups every 2 in. (51 mm), as shown in Figure 8.3-1 (b).

Table 8.3-1 Mechanical properties of 0.7″ CFCC strand

Strand Configuration	1 x 7
Diameter, in. (mm)	0.682 (17.3)
Guaranteed breaking load, kip (kN)	78.7 (350)
Cross-sectional area, in.^{2} (mm^2)	0.234 (151.1)
Max. breaking load, kip (kN)	104.8 (466)
Min. breaking load, kip (kN)	99.2 (441)
Tensile strength, ksi (GPa)	438 (3.02)
Tensile modulus, ksi (GPa)	22,200 (153)
Elongation, %	1.97

(a) Stirrups between end block and diaphragm   (b) Stirrups for end block and diaphragm
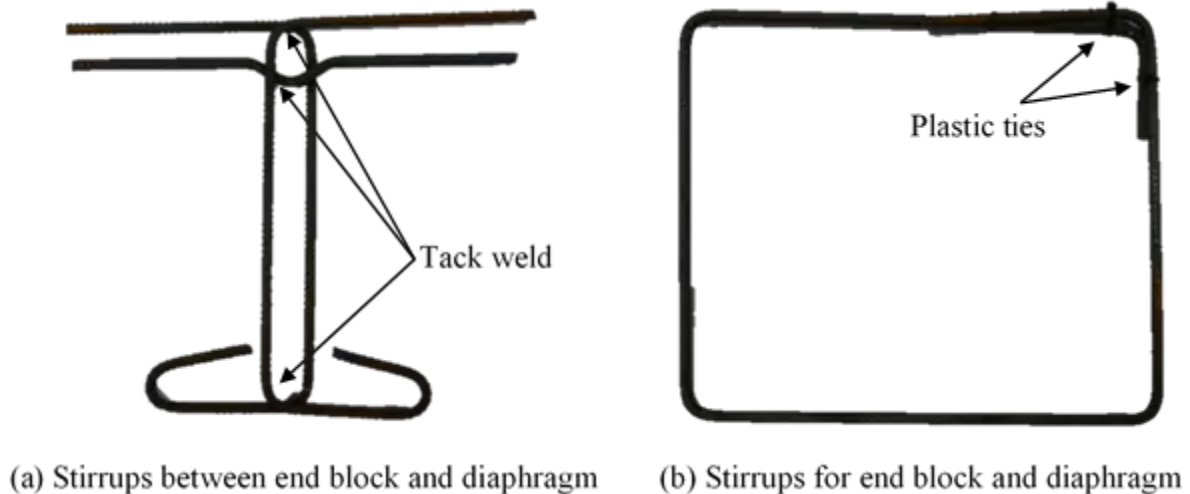
Figure 8.3-1 Steel stirrups for decked bulb T beam

8.4 Construction of Individual Beams

The construction sequence of the decked bulb T beam included setting up the prestressing bed and formwork, building the reinforcement cage, tensioning CFCC strands, placing concrete inside the formwork, curing concrete and transferring the prestressing force to the concrete beams. The formwork consisted of a wooden decking platform and center walls that were constructed from plywood and dimensioned lumber. The sides of the formwork were constructed from layers of plywood and polystyrene (Styrofoam) to form the required bulb T shape and accommodate the end blocks (Figure 8.4-1). These layers of Styrofoam were pre-cut to shape using a table saw and attached to the plywood using adhesive and wood screws. The formwork was confined by a series of wooden braces.

The reinforcement cages were assembled from No. 5 Grade 60 steel rebars and the steel stirrups, as shown in Figure 8.4-2. After assembling the reinforcement cages, CFCC strands were cut to the required length using an air grinder. Thereafter, the prestressing strands were passed through the cages, while debonded CFCC strands were shielded from concrete using a high-density polyethylene pipe, as shown in Figure 8.4-3.

The prestressing process was executed one day before concrete casting through two fixed steel bulkheads. Each strand was prestressed with an initial jacking force of 57 kip (253 kN). To facilitate the prestressing and avoid damaging the CFCC strands, a special coupler system was used to connect the prestressing CFCC strands with conventional 7-wire 0.6″ low relaxation steel

297

strands. After installing the coupler system, the steel strands were tensioned from the live end, while a set of in-line load cells were attached to the prestressing strands at the dead end as shown in Figure 8.4-4. The prestressing was executed using a hydraulic pump and a jacking system, as shown in Figure 8.4-5. A seating loss of approximately 3.5 kip (15.6 kN) was observed immediately after the initial jacking of CFCC strands. The elongation of the strands was measured and was found to be 5.25 in. (133 mm).

Upon the arrival of concrete ready-mix trucks provided by Mc-Coig Concrete Inc., a slump test was performed in accordance with ASTM C143/C143M-05 (ASTM 2005). A slump of 10 in. (254 mm) was verified before pouring concrete. Concrete was placed in the formwork and was compacted using electric pencil vibrators (Figure 8.4-6). In addition, twelve standard concrete cylinders of 6 in. (152 mm) diameter and 12 in. (305 mm) height were cast from the same batch of concrete beams according to ASTM C31/C31M-19 (ASTM 2019). The casting period was approximately one hour. After concrete casting, the beams were covered with wet burlap and plastic sheet to prevent moisture escape and allow for proper curing. Concrete cylinders were tested after 7, 14, 28 and 55 days according to ASTM C39/C39M-20 (ASTM 2020). The average compressive strength after 28 days was reported as 9.7 ksi (67 MPa), while the concrete compressive strength at the day of beam testing, after 55 days, was 9.8 ksi (67.7 MPa). Figure 8.4-7 shows the variation of the concrete compressive strength at different ages.

Prestress release took place seven days after concrete casting and after verifying that the concrete had achieved more than 80 % of its 28-day compressive strength. The prestress release was executed by slowly heating the steel strands using an acetylene/oxygen torch, as shown in Figure 8.4-8. An average camber of 1 in. (25.4 mm) was measured for the control beam at the midspan immediately after prestress transfer. The readings of the attached load cells, from the time of initial jacking, through concrete curing and until prestress release, were plotted as shown in Figure 8.4-9. A total prestress loss of approximately 2.9 kip (13 kN) per strand is observed from Figure 8.4-9 resulting an initial average prestressing force of 50.3 kip (224 kN) at prestress transfer. After prestress release, the beams were removed from the formwork and placed in indoor storage until the testing facility in CIMR was available.

Figure 8.4-1 Setting up the wooden center walls and attaching the Styrofoam to center walls

Figure 8.4-2 Assemblage of the reinforcement cage from steel rebars and steel stirrups

Figure 8.4-3 Passing prestressing CFCC strands inside the reinforcement cage and shielding the debonded strands from concrete using polyethylene pipes

Completed coupler system at live end   In-line load cells installed at the dead end
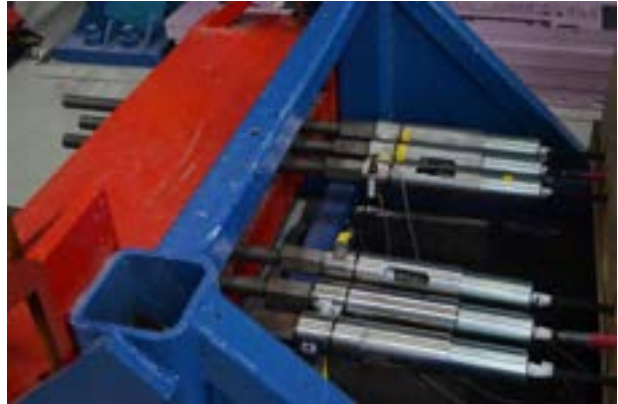
Figure 8.4-4 Connecting end couples and load cells at live and dead ends

Figure 8.4-5 Prestressing CFCC strands by pulling coupled steel strands using hydraulic pump

Figure 8.4-6 Placing concrete into the formwork and compacting using electric pencil vibrators
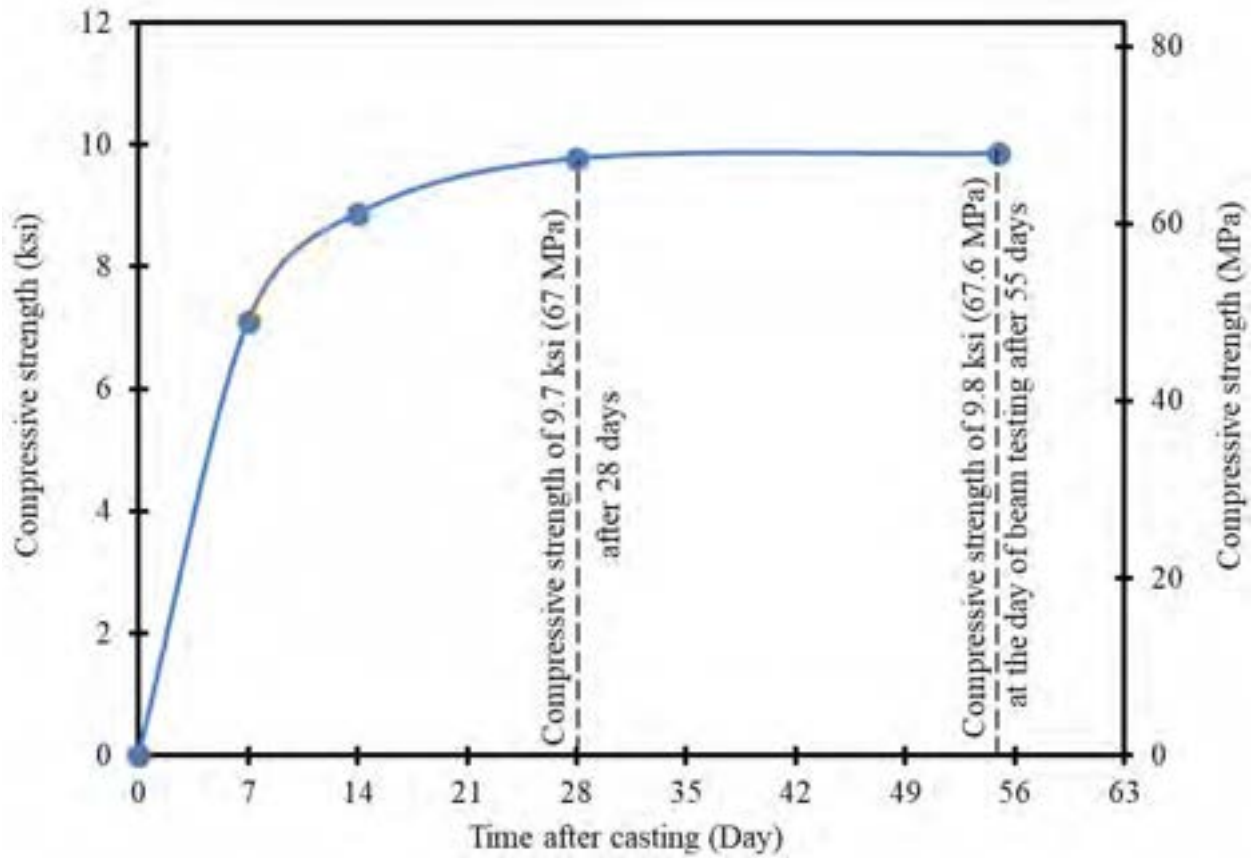
Figure 8.4-7 Average concrete compressive strength at different ages

Figure 8.4-8 Prestress release by heating the steel strands using an acetylene/oxygen torch
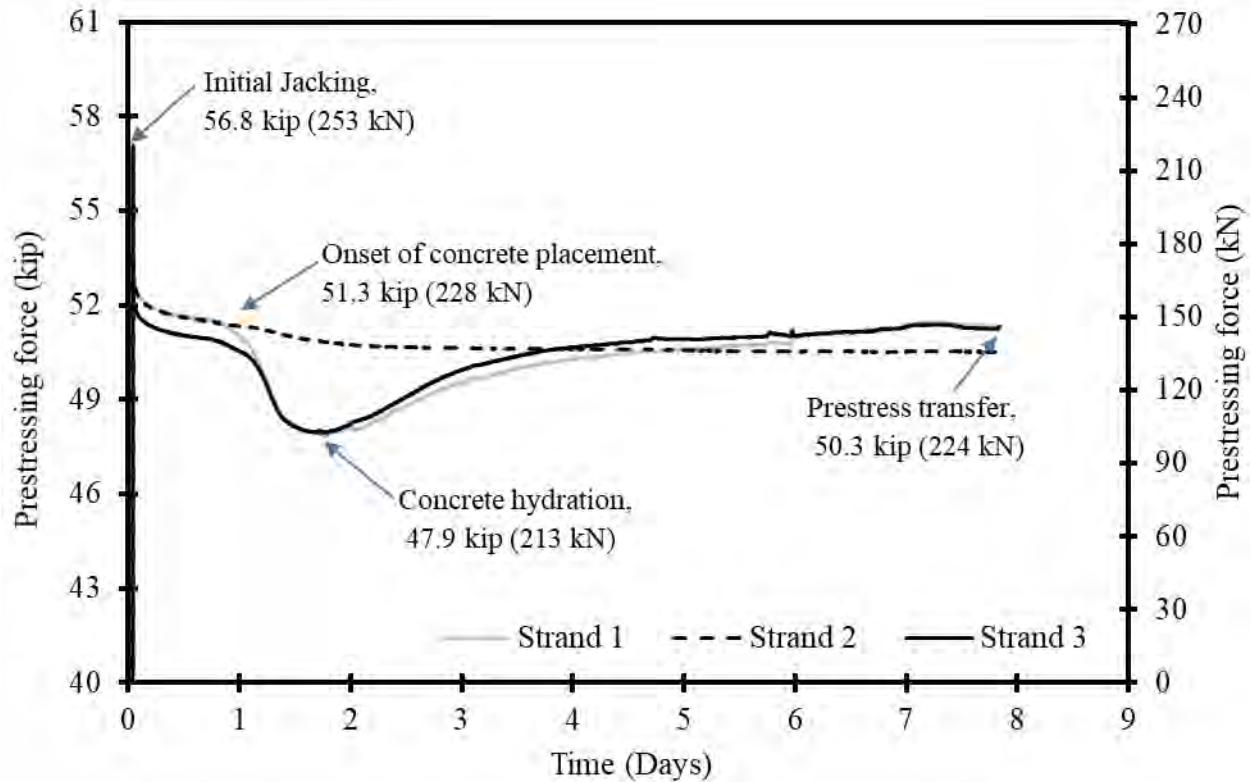
Figure 8.4-9 Prestressing force vs. time from initial jacking to prestress release in control beam

8.5 Details of Bridge Model

The bridge model consisted of five, one-half scale simply supported decked bulb T beams. Similar to the control beam, the bridge model had a length of 41 ft (12.5 m) and an effective span between the supports of 40 ft (12.2 m). The five decked bulb T beams were designed to fail by rupture of CFCC strands (tensioned-controlled sections) similar to the control beam. In addition, each beam was prestressed with three 0.7″ CFCC strands. Like the control beam, the middle strand in each beam was debonded for 10 ft (3 m) at each beam end.

To support the beams in the transverse direction and achieve the structural integrity of the bridge model, two end diaphragms and five intermediate diaphragms in each beam were constructed, where part of the diaphragms were cast along the beams and then, the diaphragms were connected together using UHPC. Figure 8.5-1, Figure 8.5-2 and Figure 8.5-3 show the cross section of the bridge model at three different locations; between diaphragms, at intermediate diaphragms and at end diaphragms, respectively. As shown in the figures, the stirrups at the top flange of the exterior and interior beams were protruded from one or both sides, respectively, in

302

order to form the required reinforcement of the shear key joints. In addition, and as shown in Figure 8.5-2, the intermediate diaphragms were reinforced with 4 No. 3 (9.5 mm) rectangular steel bars and protruded out of the concrete. These bars were spliced at the shear key joints before casting the UHPC.
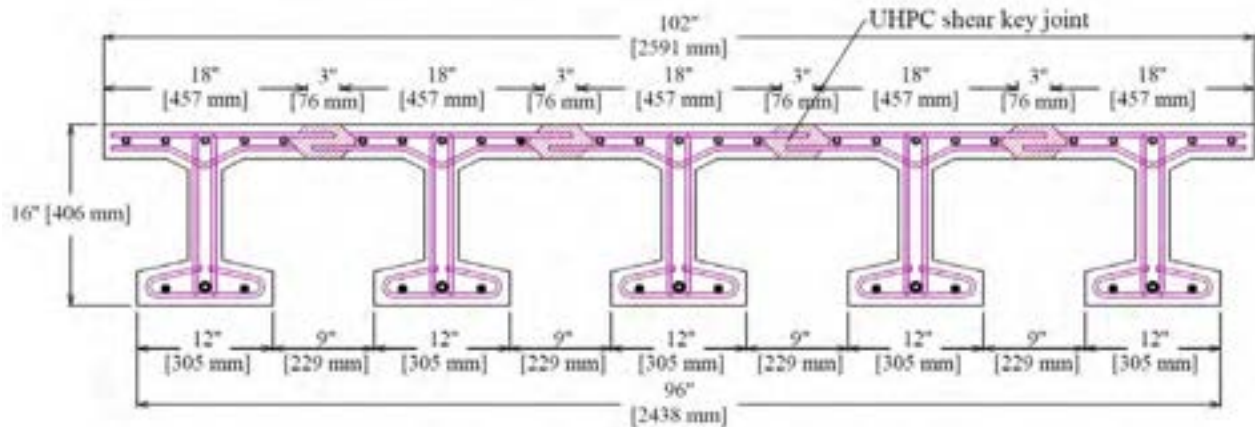
Figure 8.5-1 Cross-section of bridge model between diaphragms
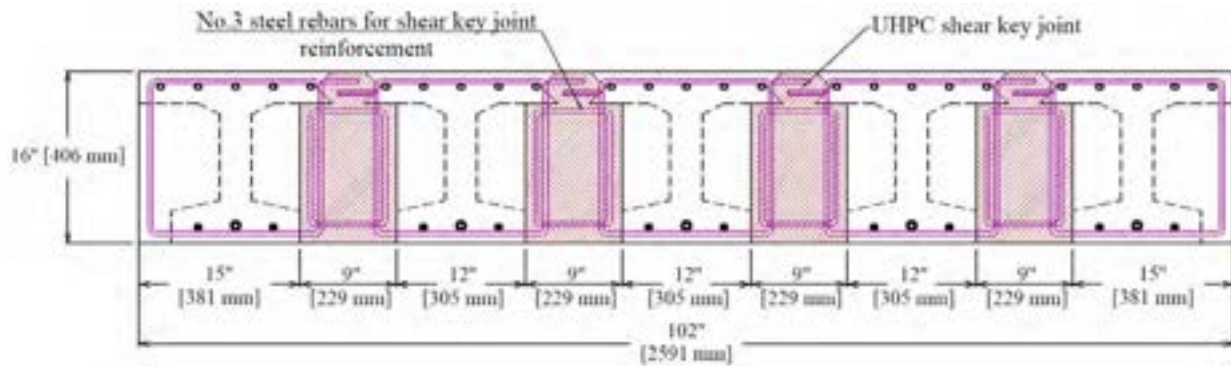
Figure 8.5-2 Cross-section of bridge model at intermediate diaphragms
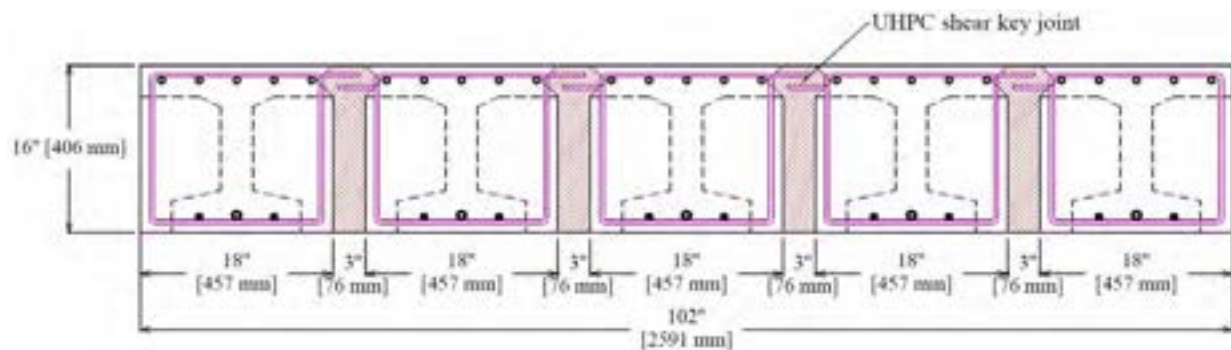
Figure 8.5-3 Cross-section of bridge model at end diaphragms

8.5.1 Construction of Bridge Model

The sequence of the bridge model construction started by constructing five individual decked bulb T beams followed by assembling the bridge model from the individual beams using shear key connections. The decked bulb T beams of the bridge model were identical in dimensions and reinforcement in comparison to the control beam. However, the transverse reinforcement of the diaphragms in addition to the T-shape stirrups at the top flange protruded out of the beams and extended 2.5 in. (63.5 mm) into the shear key joints. The pultrusion of the stirrups for the interior and exterior beams was executed during the construction phase by drilling holes into the center and side walls of the formwork, as shown Figure 8.5-4.

The construction of the individual beams of the bridge model went through the same construction phases of the control beams, which included setting up the formwork, assembling the reinforcement cages, placing the cages inside the formwork, pulling the pretensioning strands, casting the concrete, curing the concrete, removing the sides of the formwork, and finally, transferring the prestress force to the cured concrete beams and removing the beams from the formwork. The details of each construction phase were explained thoroughly in Section 8.4.

Different characteristics of the decked bulb T beams of the bridge model are listed in Table 8.5-1, including the compressive strength at different ages, camber values measured immediately after transfer and the initial prestressing force/strand at prestress transfer. Figure 8.5-5 shows the precast prestressed beams after proper casting and curing.

Figure 8.5-4 Drilling holes in the side walls of the formwork to accommodate for the pultrusion of the T-shape stirrups at the top flange of the beams

Table 8.5-1 Average concrete compressive strengths, cambers, and initial prestress forces for prestressed beams of bridge model

Beam	Compressive Strength, psi (MPa)			Camber, in. (mm)	Initial prestress force per strand, kip (kN)
	7 Days	14 Days	28 Days		
Exterior Beam 1	7096 (48.9)	9770 (67.4)	9855 (67.9)	1 (25.4)	49.6 (220.7)
Interior Beam 1	5657 (39.0)	6282 (43.3)	6453 (44.5)	1.1 (27.9)	51.2 (227.7)
Interior Beam 2 (Intermediate Beam)	5657 (39.0)	6282 (43.3)	6453 (44.5)	1.1 (27.9)	51.4 (228.6)
Interior Beam 3	6562 (45.2)	6974 (48.1)	7923 (54.6)	1.05 (26.7)	52.0 (231.4)
Exterior Beam 2	6562 (45.2)	6974 (48.1)	7923 (54.6)	1.05 (26.7)	52.7 (234.5)

Figure 8.5-5 Individual beams of the bridge model after construction

The bridge model was constructed by placing the individual beams side-by-side over steel supports with a 3 in. (76 mm) gap between the top flanges of the beams, as shown in Figure 8.5-6. To eliminate the differential camber between the beams, two steel beams were connected together at the mid-span of the beams using steel threaded rods, as shown in Figure 8.5-7. After leveling the beams, the formwork for the four longitudinal shear keys was constructed from wooden plywood that extended underneath the shear keys and around the transverse diaphragms to hold the UHPC in place during casting. In addition, wooden strips of 2 in. (51 mm) thick plywood was glued around the shear keys in the longitudinal direction over the top flange of the beams to prevent any UHPC overflow. Transverse reinforcement of four No. 3 (9.5 mm) rectangular steel bars were provided at the shear key joint and spliced to the protruded reinforcements of the intermediate diaphragms. Figure 8.5-8 shows the stages of construction for the shear key joints.

Figure 8.5-6 Lifting and placing the beams on steel supports with 3-in. (76-mm) gaps

Figure 8.5-7 Beam leveling and wooden end plates at the beam ends

Figure 8.5-8 Formwork and reinforcement configuration for shear key joints

8.5.2 Casting UHPC in Shear Key Joints

A total of four notched 3 in. (76 mm) wide longitudinal UHPC shear keys was cast between the beams of the bridge model. The UHPC was supplied by Lafarge North America under a commercial name Ductal® JS1000. Before casting the shear keys, the UHPC was prepared at CIMR by mixing 15 sacks of Ductal premix (340 kg), 37.95 lb (17.2 kg) of water, 10.25 lb (4.6 kg) of superplasticizer (Premia 150) and 53.12 lb (24 kg) of brass-coated steel fibers to form one batch of UHPC mix. Six batches of UHPC were mixed to cast the shear key joints. Figure 8.5-9 shows the components of UHPC (Lafarge North America) used in this study.

A centrifugal concrete mixer was used to mix the components of UHPC for 15 min until the mix become homogenous (Figure 8.5-10). Each batch of UHPC was tested by performing flow table tests according to ASTM C1437-20 (ASTM 2020): "Standard Test Method for Flow of Hydraulic Cement Mortar." The flow of UHPC was assessed by measuring the diameter of the sample after 25 blows, which was found to be approximately 8.5 in. (216 mm) indicating good workability of the UHPC batch. In addition to the flow table tests, eight concrete cylinders of 3 x 6 in. (76 x 152 mm) were cast from the same batch in order to be tested after 28 days and at the day the bridge model was tested. The average compressive strength of UHPC after 28 days was estimated as 26.8 ksi (185 MPa).

Figure 8.5-11 shows the process of filling the shear key joints with UHPC. After pouring UHPC, the shear key joints were cured using plastic sheets and plywood for 5 days. After curing, the surface of the shear key joints near the applied load was grinded using an air grinder and water jet to create a smooth bridge surface.

307

a) Ductal premix powder

b) Superplasticizer (Premia 150)

c) Coated steel fiber

d) Water

Figure 8.5-9 Components of the UHPC

Figure 8.5-10 Mixing UHPC using centrifugal concrete mixer

Figure 8.5-11 Pouring UHPC into shear key joints

8.6 Instrumentation

Sensors were installed at various stages of the experimental program to record strains, deflections, and forces. The sensors used were: strain gauges, load cells, Linear Motion Transducers (LMTs) and Linear Variable Differential Transducers (LVDTs). In addition, a computer with a data acquisition system was used to provide real-time monitoring of the behavior of the beams during the tests.

8.6.1 Instrumentation of Control Beam

In order to measure the strain developed on the concrete top surface of the control beam during testing, Electrical Strain Gages (ESGs) were installed at the midspan section and next to the two loading points of the four-point loading setup, as shown in Figure 8.6-1. In addition to the ESGs, the control beam was provided with Linear Variable Differential Transducers (LVDTs) to capture the strain developed at the prestressing strands during flexural loading. Two LVDTS were mounted externally on the concrete surface at the level of the prestressing CFCC strands in the bottom flange of the decked bulb T beam, as shown in Figure 8.6-2(a). An additional LVDT was attached at the soffit of the beam to capture the strain at the bottom surface. Two Linear Motion Transducers (LMTs) were installed at the midspan of the control beam to measure the deflection, as shown in Figure 8.6-2(b). A Mars Lab Titan Control Software (TCS) data acquisition system was used for converting the analog voltage output from the sensors to digital values. The system is composed of a digital pod and computer software (Figure 8.6-3). All the sensors were directly connected to the digital pod, and subsequently connected to the computer for data monitoring and recording.
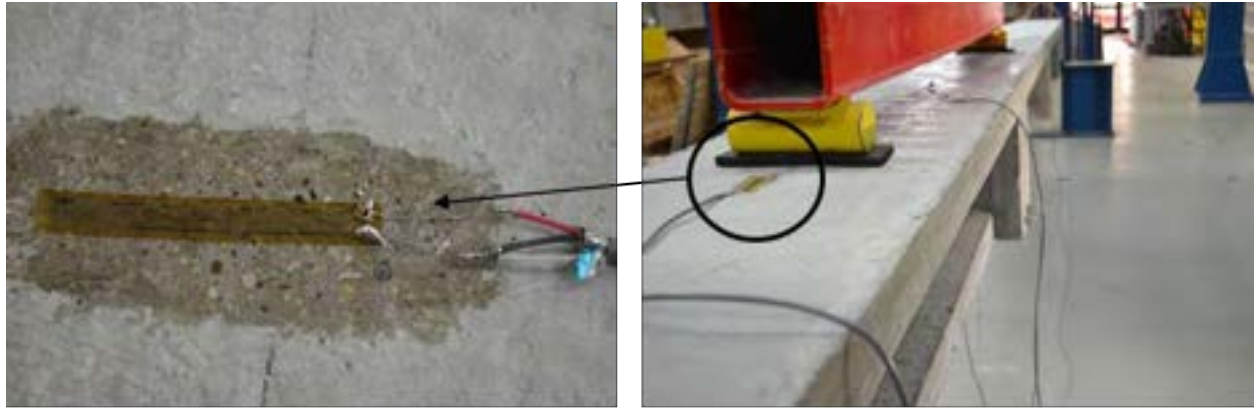
Figure 8.6-1 Electrical strain gages attached to the top concrete surface to capture the strain

a) LVDT for strain measurement   b) LMT for deflection measurement

Figure 8.6-2 Sensors installed at the sides and the soffit of the beam; (a) LVDT, (b) LMT

a) Digital pods for data acquisition   b) Windows 7 software control

Figure 8.6-3 Components of data acquisition system for data monitoring and recording

8.6.2 Instrumentation of Bridge Model

Similar to the control beam, the decked bulb T beams of the bridge model were equipped with the same sensors, but with different arrangement and configuration. To accurately capture the

deflection of each beam during the load distribution test, Linear Variable Inductive Transducers (LVITs) with small range were attached under each of the five beams at the midspan section (Figure 8.6-4). A load distribution test on the bridge model was conducted using a 100-ton hydraulic cylinder with a stroke of 10 in. (254 mm) as shown in Figure 8.6-5.

Strain gages were attached to the top surface of the bridge model to measure the concrete strain during the shear key and the flexural tests. In addition, LVDTs are mounted on the side of the exterior decked bulb T beams to capture the strain at the level of prestressing strands during flexural loading. All the sensors were connected to the data acquisition system.

Figure 8.6-4 Attaching Linear Variable Inductive Transducers (LVITs) at the soffit of the bridge
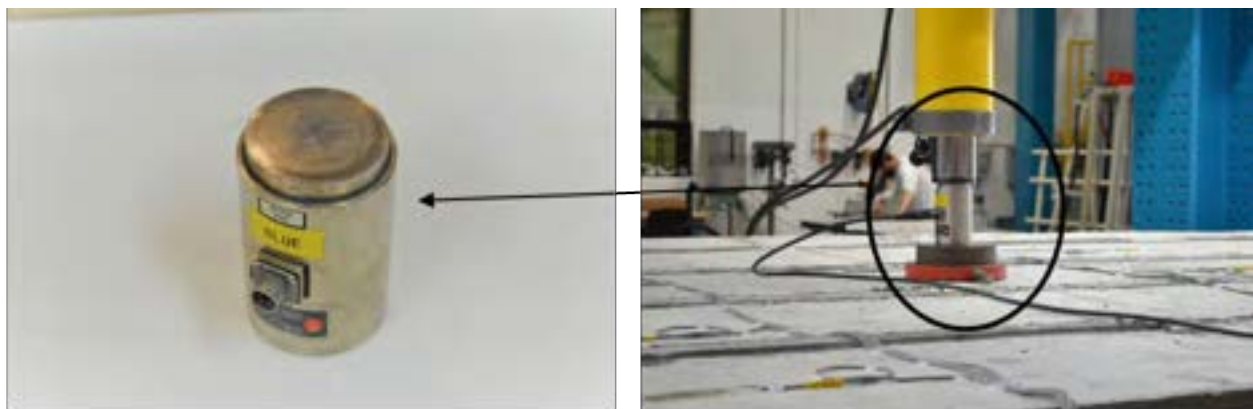
Figure 8.6-5 Load cell attached to the hydraulic cylinder at the location of the point load on the bridge model

8.7 Flexural Testing of Control Beam

The control beam was tested to failure under four-point flexural test setup. The main purpose of the test was to evaluate the flexural behavior of a single decked bulb T beam prestressed with 0.7″ strands before testing the bridge model. The flexural behavior was evaluated by determining the cracking load, decompression load, ultimate failure load and ductility of a single decked bulb T beam. Figure 8.7-1 shows the setup of the control beam. The simply supported beam with an effective span of 40 ft. (12.2 m) was placed on two elastomeric bearing pads of 1 in. (25.4 mm) thickness, positioned on two steel stands. The load was applied to the beam using a steel spreader with two loading points that were 78 in. (2.0 m) apart.

The testing scenario included loading the beam through several loading/unloading cycles in increments of 2 kip (9 kN) until the first flexural crack was observed and in increments of 4kip (18 kN) after cracking to failure. The 220-kip (980 kN) MTS hydraulic actuator was programmed to apply the load cycles with a force control rate of 2 kip/min (18 kN/min). Service limit state testing was performed, where the concrete beam remained uncracked and ended with the initiation of the first flexural crack. The first flexural crack was observed at a load level between 14 and 16 kip (62.3 and 71.2 kN). The load-deflection curves for the service limit state loading cycles are shown in Figure 8.7-2. It should be noted that the change in the slope of the load-deflection curve is attributed mainly to the change in the flexural stiffness of the cross-section due to concrete cracking at the beam soffit. The cracking load was determined as 14.8 kip (66 kN), whereas the decompression load was estimated as 9.5 kip (42.3 kN), which represented an effective prestressing force of 111 kip (494 kN) (prestress loss of 19.5 %).

Figure 8.7-1 Flexural test setup of the control beam
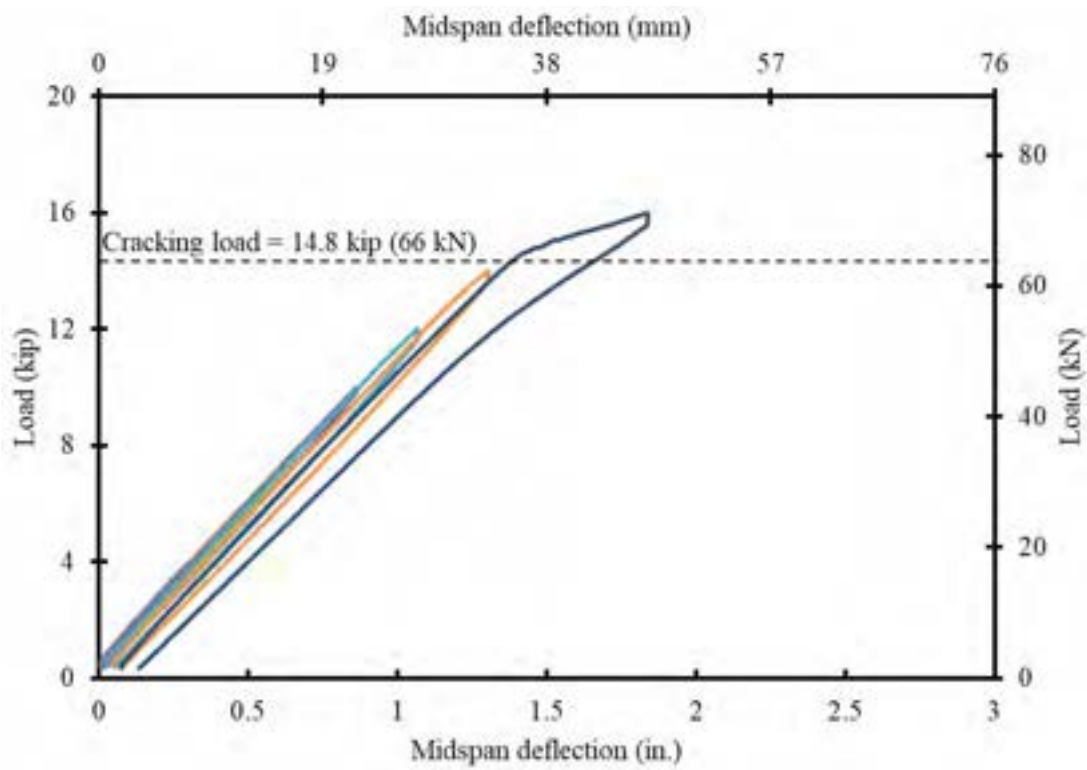
Figure 8.7-2 Service limit state load-deflection curves

Post-cracking stage testing started with the initiation of the first flexural crack and was marked by an apparent change in the slope in the load-deflection curves. Several flexural cracks developed

313

in the beam with increasing the load beyond the cracking load. Consequently, the beam experienced further reduction in its flexural stiffness with each loading/unloading cycle. The cracks were uniformly distributed under the loading spreader and propagated vertically to the top flange. By increasing the applied load, the beam showed gradual increase in the crack pattern and width. In addition, inclined cracks were developed far from the loading points in the form of flexural-shear cracks, as shown in Figure 8.7-3. The post-cracking stage ended by loading the beam to a load level of 24 kip (107 kN). This corresponded to a midspan deflection of 7.4 in. (188 mm) and residual deflection of 0.5 in. (12.7 mm) from previous load cycles. Figure 8.7-4 shows the deflection of the control beam during the 24-kip (107-kN) load cycle. It should be noted that the beam exhibited significant deflection accompanied by spalling of concrete edges. In practice, those signs serve as a visual warning before failure of bridge beams.
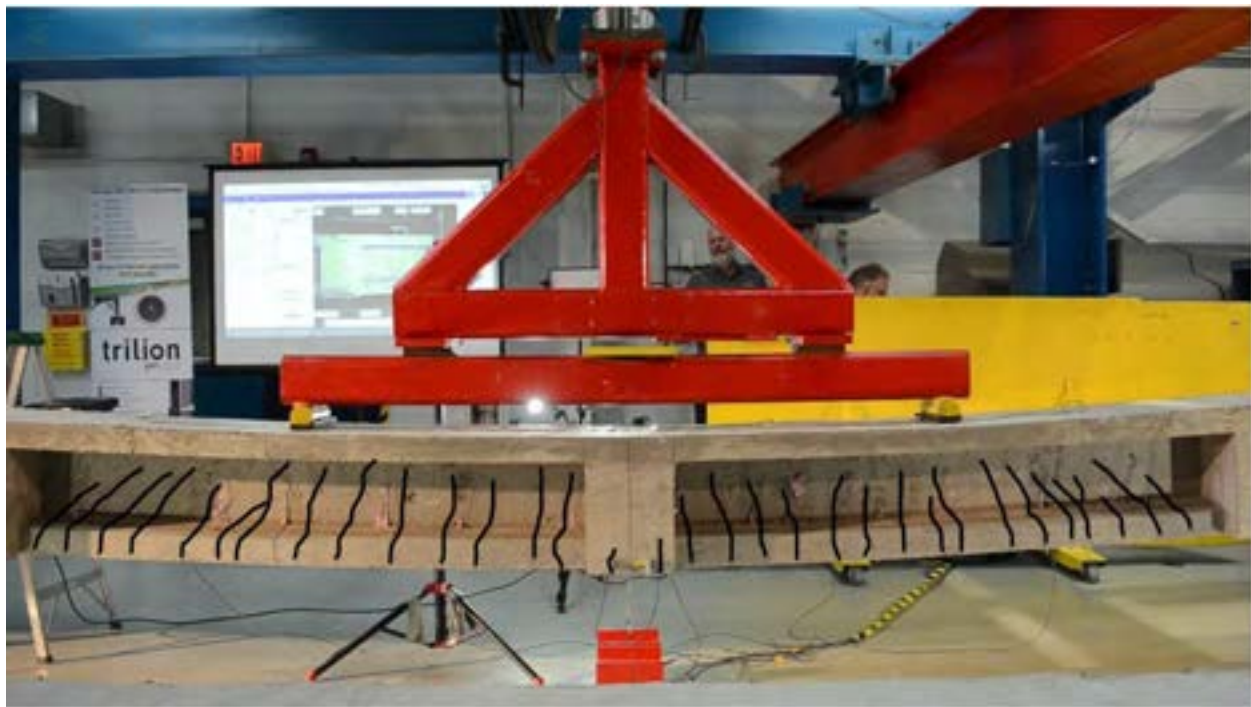
Figure 8.7-3 Crack pattern of control beam at 24-kip (107-kN) load cycle

Figure 8.7-4 Deflection of control beam during 24-kip (107-kN) load cycle

Strength limit state testing was performed after the post-cracking stage by testing the beam monotonically to failure. The failure of the beam took place at a load level of 36.5 kip (162.4 kN) with a corresponding deflection of 18.5 in. (470 mm) not including the residual deflection of 0.5 in. (12.7 mm) from previous load cycles. The maximum recorded strain at the extreme compression zone before failure was approximately 2460 $\mu\varepsilon$. The load-deflection curves and the load-strain curves of the beam during the loading and unloading cycles until failure is presented in Figure 8.7-5 and Figure 8.7-6, respectively. Failure of the control beam was characterized by rupture of CFCC strands in the tension zone accompanied by spalling of the concrete at multiple locations (Figure 8.7-7). In order to calculate the energy absorbed by the control beam, the area under the load-deflection curves from all load cycles including the ultimate load cycle (Figure 8.7-8) was estimated as 472 kip.in. (53.4 kN.m).
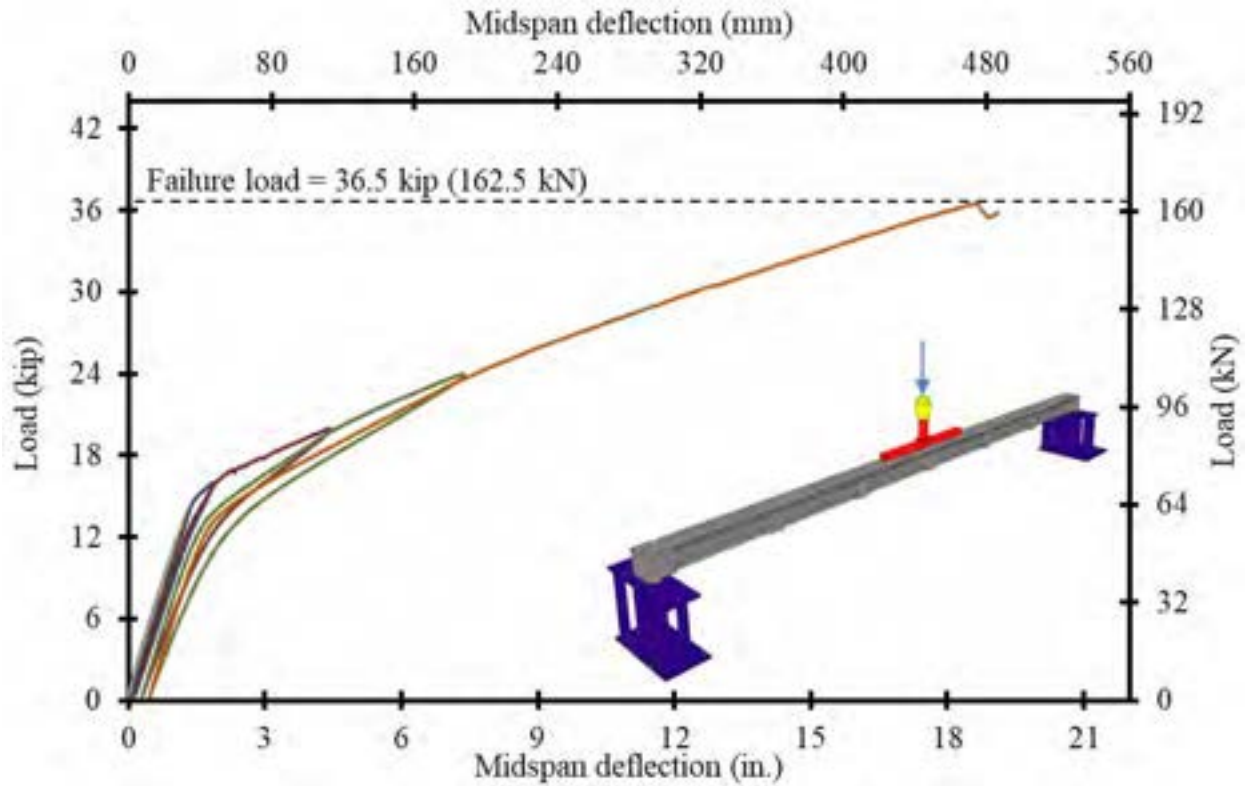
Figure 8.7-5 Load-deflection curves from load cycles performed on control beam until failure
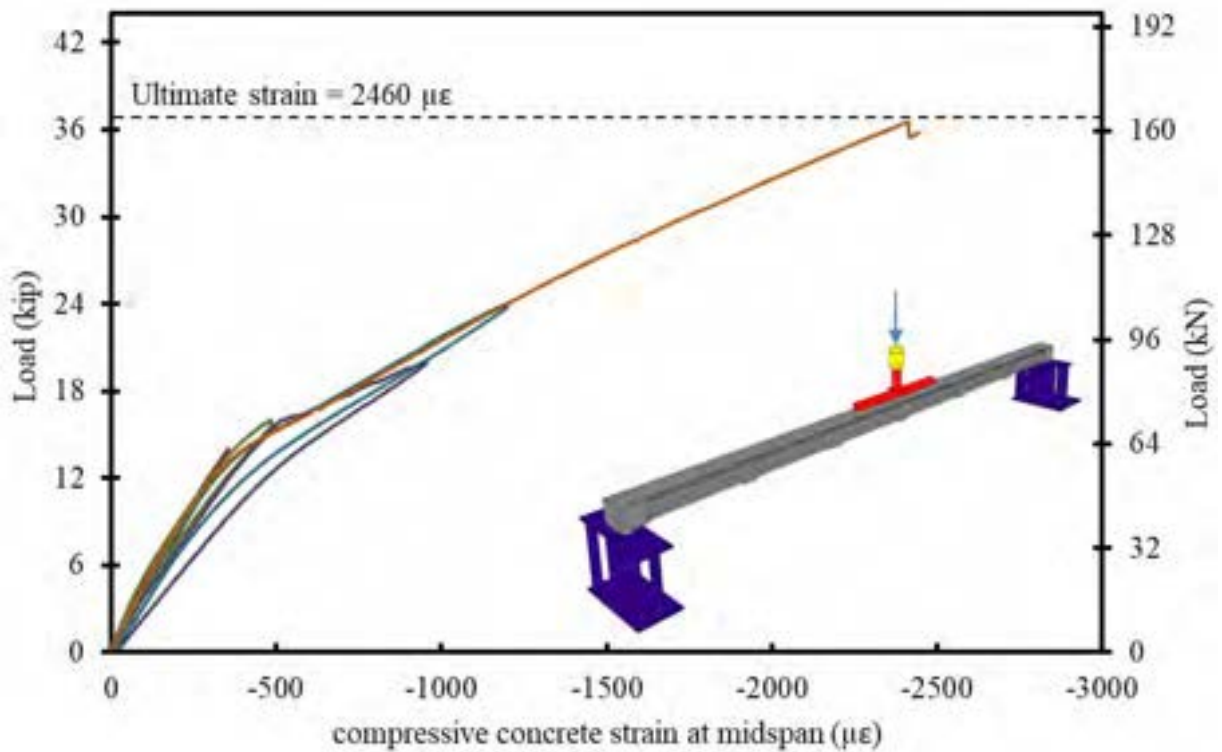
Figure 8.7-6 Load vs. top concrete strain of control beam until failure

316

Figure 8.7-7 Spalling of concrete and rupture of CFCC strands after failure of control beam
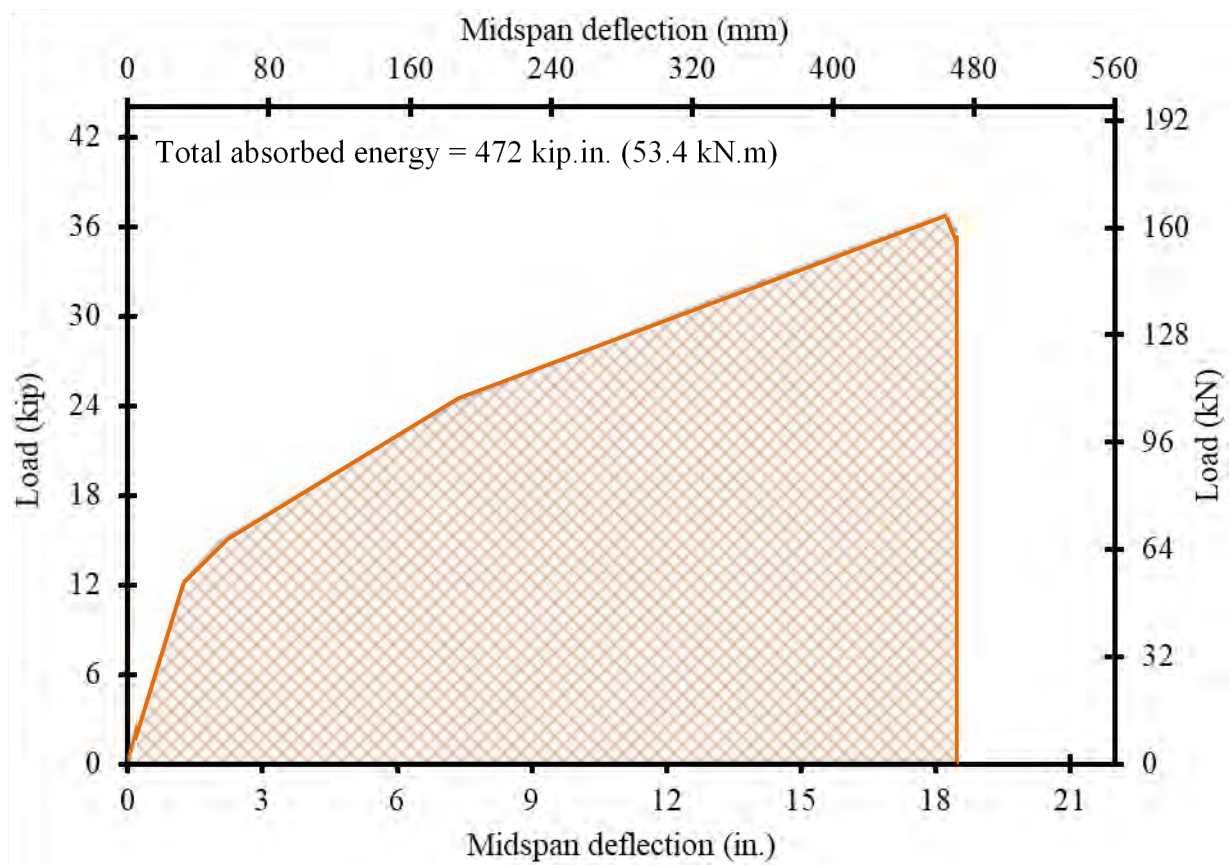
Figure 8.7-8 Estimation of energy absorbed in control beam

8.8 Testing of Bridge Model

The bridge model was tested under different testing configurations. First, service point loads were applied at the mid-span of each beam, which were lower than the anticipated cracking load of the bridge model. Second, the entire bridge model was subjected to loading/unloading cycles, under four-point loading, until the initiation of the first flexural cracks. The post-cracking limit state then commenced by applying a post-cracking point load at the mid-span of each beam to confirm the load distribution factors without inducing any failure in the bridge beam components. Thereafter, one of the exterior beams of the bridge model was loaded under a four-point loading to evaluate the behavior of shear key joints. Afterwards, the load cycling test was continued on the bridge model to approximately 75 % of its ultimate load carrying capacity. Finally, the last testing stage included loading the entire bridge model to failure to evaluate its ultimate failure load at the strength limit state.

8.8.1 Service Limit State Testing

The service limit state is defined as the state where all concrete beams of the bridge model remained uncracked while being tested and it ends with the initiation of the first flexural cracks. The following sections provide a thorough discussion on the tests conducted at this stage.

8.8.1.1 Pre-cracking Load Distribution Test

In order to develop the live load-distribution factors of each beam under service loads, a single point load of 15 kip (67 kN) or 30 kip (134 kN) was applied at the mid-span of each individual decked bulb T beam in the bridge model. Since the theoretical cracking load of the bridge model was anticipated at 60 kip (267 kN), a 15 kip (67 kN) or 30 kip (134) single point load was not expected to induce any flexural cracks in the loaded beams. The point load was applied using a 100-ton hydraulic cylinder connected to a hydraulic pump as shown in Figure 8.8-1. The associated beam deflections were measured using the LMT attached at the midspan of each beam.

Figure 8.8-2 shows a schematic diagram of the sequence of the load distribution test for the bridge model. The load was applied first to the exterior beam followed by the first interior beam, then the second and third interior beams, and finally the second exterior beam. It was observed that the response of the bridge model when loading one side of the bridge model (first exterior, first and second interior beams) was identical to loading the opposite side (second exterior and

third interior beam). Therefore, the deflection curves obtained from loading one side of the bridge are those presented in this discussion, along with deflection curves obtained from loading the center beam. After applying a 15 kip (67 kN) point load at the midspan of each beam, the entire test was repeated using a higher service load of 30 kip (134 kN) in order to validate the load distribution factors.
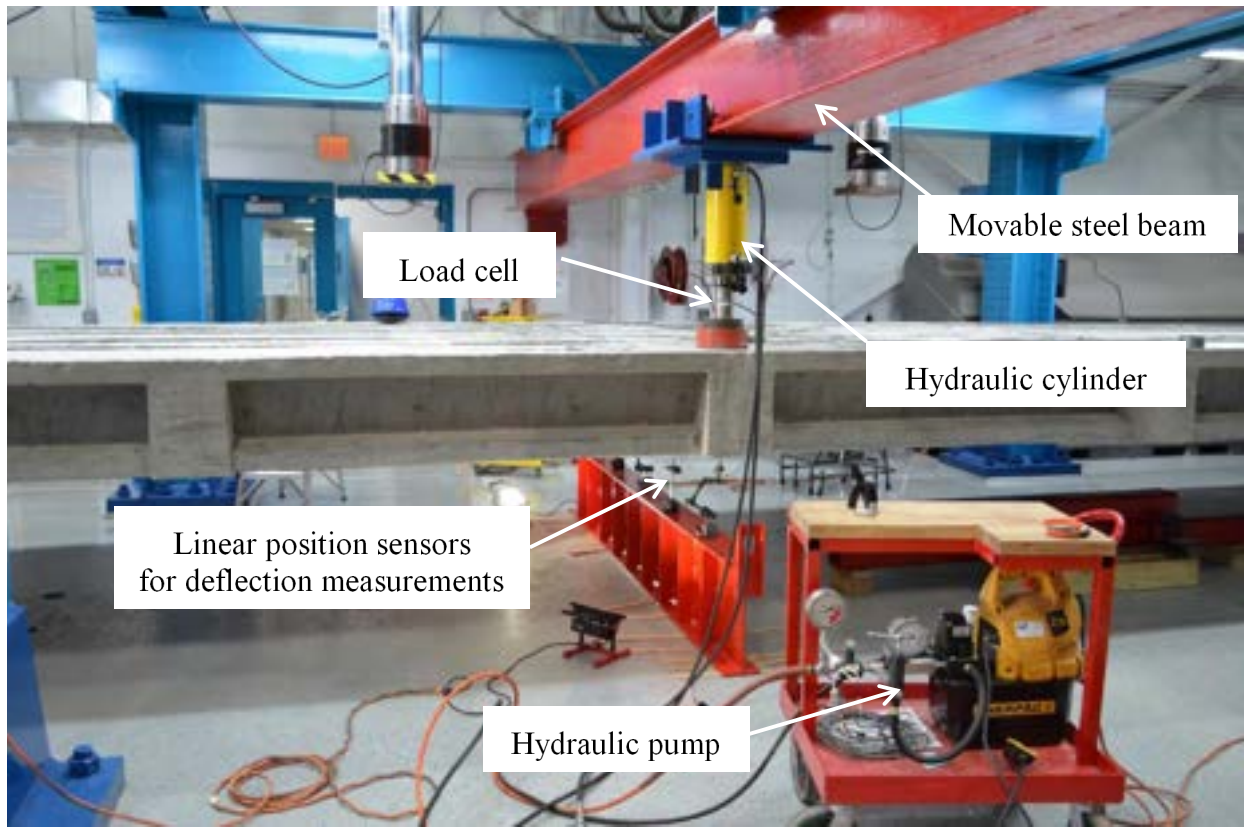
Figure 8.8-1 Load distribution test setup
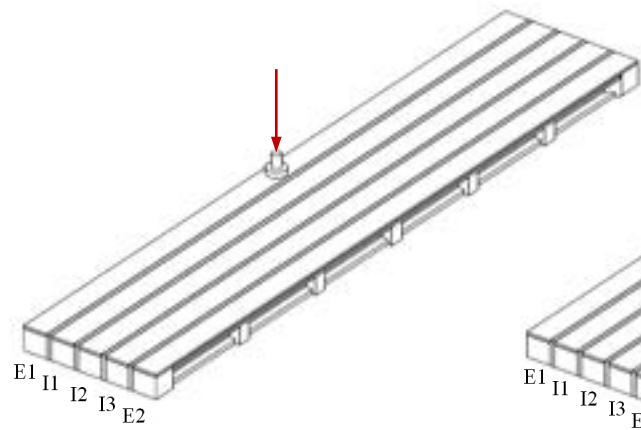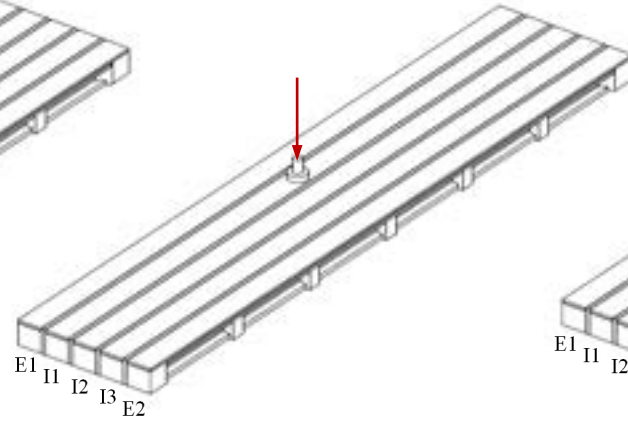
(a) Loading Beam E1   (b) Loading Beam I1   (c) Loading Beam I2
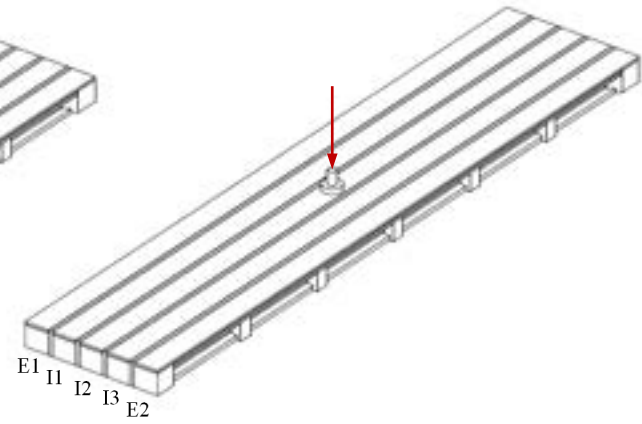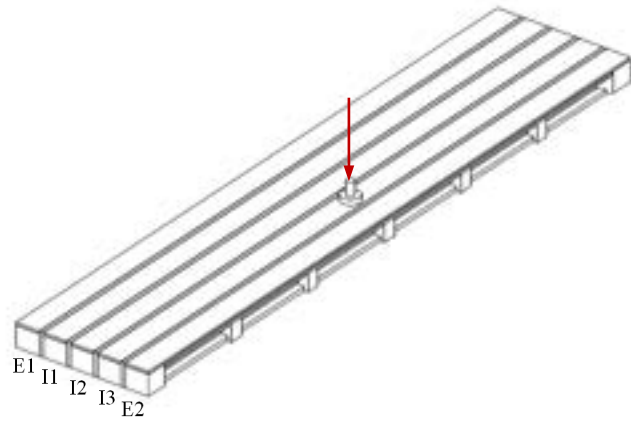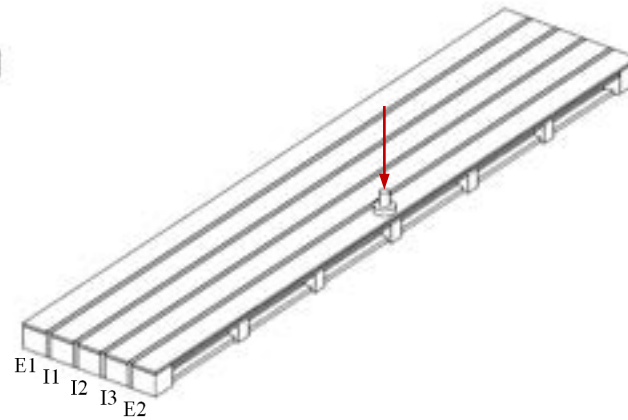
(d) Loading Beam I3   (e) Loading Beam E2

Figure 8.8-2 Sequence of service load application for load distribution test

The deflection curves of the bridge model under service loads of 15 and 30 kip (67 and 134 kN) for different loaded beams are presented in Figure 8.8-3 through Figure 8.8-5. In order to evaluate the response of the bridge model under service loads, load distribution factors among the beams were calculated and compared for different load levels. The load distribution factor was calculated, according to Eqn. 1, by dividing the measured deflection of an individual beam to the sum of the deflections of all five beams in the bridge model. The load distribution factors were computed and listed in Table 8.8-1 and Table 8.8-2.

$$D.F. = \frac{\delta_i}{\sum_{i=1}^{i=5} \delta_i} \tag{1}$$

In Eqn. 1, $D.F.$ is the load distribution factor that is computed for each beam and δ_i is the deflection measured at the midspan of ith beam, in. (mm).

Compared to the deflections of the loaded intermediate and interior beams, the deflections of the loaded exterior beams were higher. Deflections of 0.341 and 0.720 in. (8.66 and 18.29 mm) were observed when the exterior beam was loaded to 15 and 30 kip (67 and 134 kN), respectively. This corresponds to a load distribution factor of approximately 26.5 % for the exterior beam. When the intermediate beam was loaded, it was found that all beams exhibited similar deflection that averaged 0.264 in. (6.73 mm) under a 15-kip (67-kN) point load and 0.544 in. (13.82 mm) under a 30-kip (134-kN) load. This corresponds to a load distribution factor of approximately 20 %. In other words, the service load was distributed equally among the five beams when the intermediate beam was loaded. It should be noted that the structural integrity and composite behavior of the bridge model was maintained in the pre-cracking load distribution tests, where no cracks or sign of shear key distress were observed during the test. Therefore, it can be concluded that the transverse diaphragms along with UHPC shear key joints were able to distribute the service loads among the beams without any crack development and in a pattern similar to that of bridges with cast-in-place deck slab.
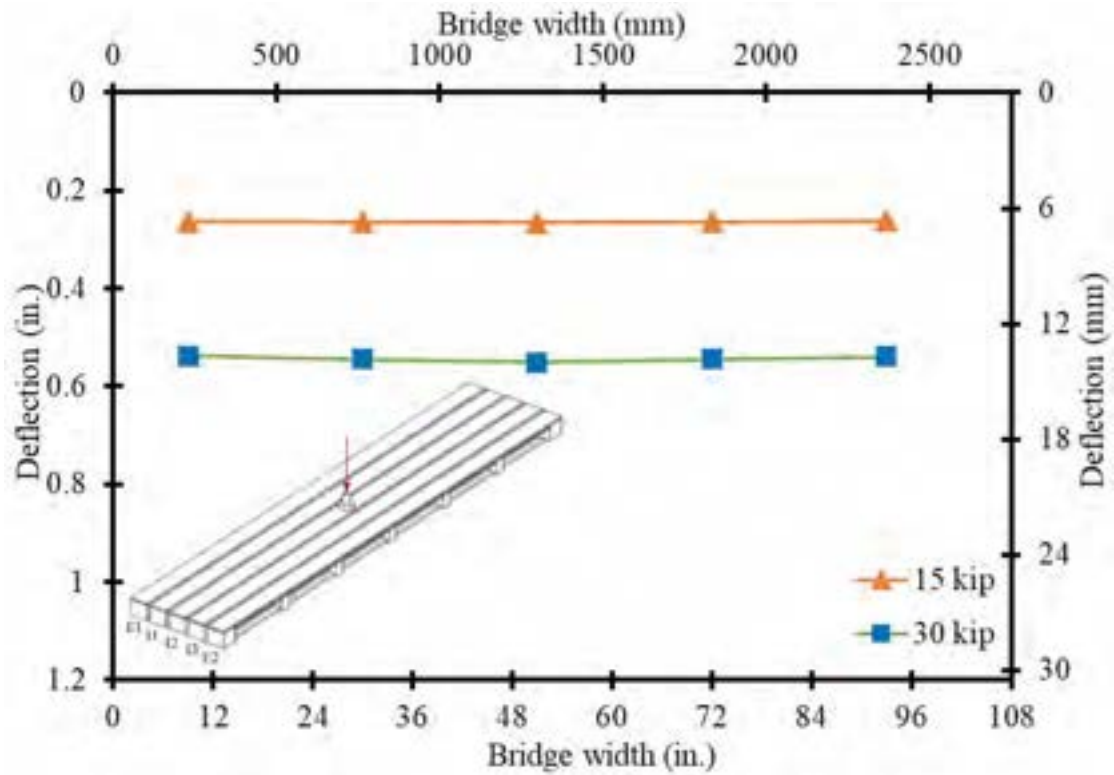
Figure 8.8-3 Deflection curves due to service loads on intermediate beam (I2)
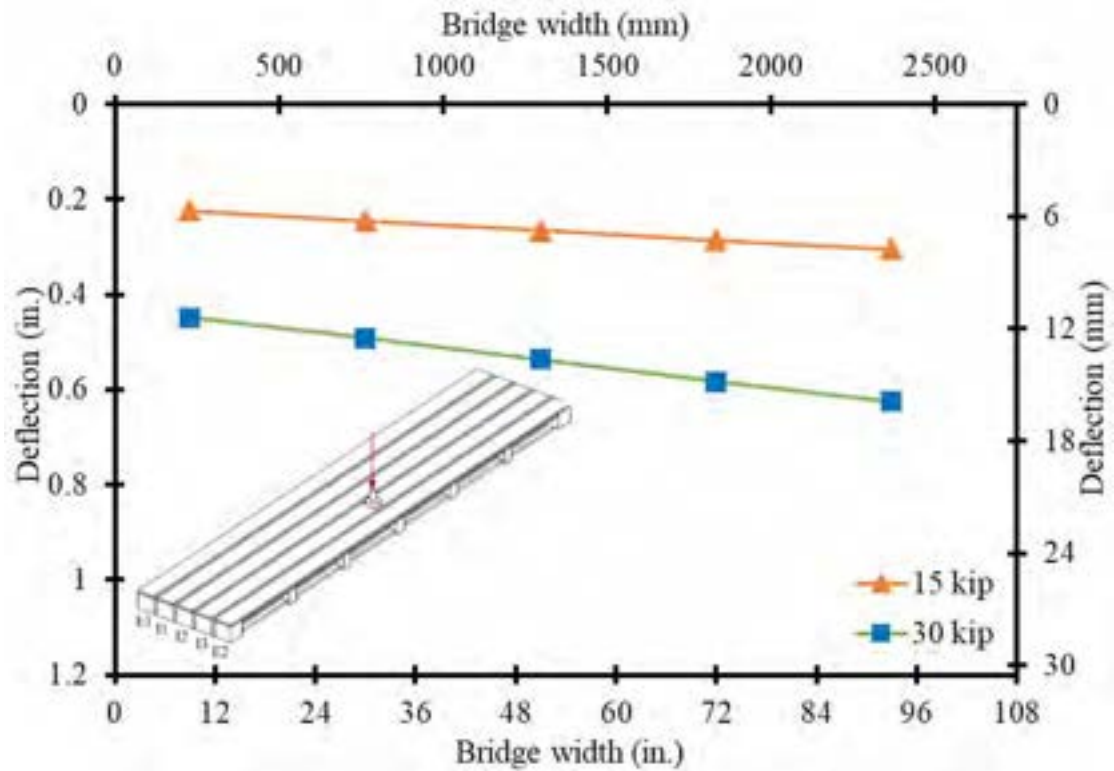
Figure 8.8-4 Deflection curves due to service loads on interior beam (I3)

322
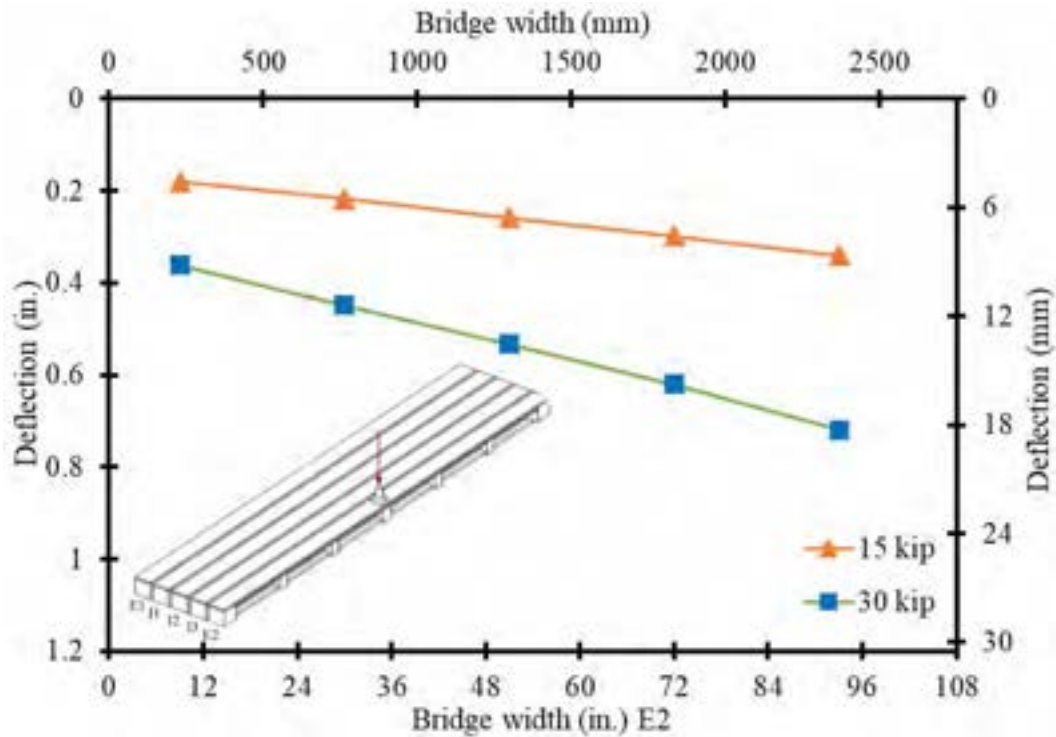
Figure 8.8-5 Deflection curves due to service loads on exterior beam (E2)

Table 8.8-1 Load distribution factors of bridge beams under service loads of 15 kip (67 kN)

	Loaded beam					
	Intermediate Beam I2		Interior Beam I3		Exterior Beam E2	
	δ_i, in. (mm)	D.F.	δ_i, in. (mm)	D.F.	δ_i, in. (mm)	D.F.
Exterior Beam E1	0.263 (6.68)	0.200	0.224 (5.69)	0.169	0.181 (4.59)	0.140
Interior Beam I1	0.264 (6.71)	0.200	0.245 (6.45)	0.185	0.217 (5.51)	0.167
Intermediate Beam I2	0.265 (6.73)	0.201	0.265 (6.73)	0.200	0.259 (6.58)	0.200
Interior Beam I3	0.264 (6.71)	0.200	0.286 (7.26)	0.216	0.298 (7.57)	0.230
Exterior Beam E2	0.262 (6.65)	0.199	0.305 (7.78)	0.230	0.341 (8.66)	0.263

323

Table 8.8-2 Load distribution factors of bridge beams under service loads of 30 kip (134 kN)

	Loaded beam					
	Intermediate Beam I2		Interior Beam I3		Exterior Beam E2	
	δ_i, in. (mm)	D.F.	δ_i, in. (mm)	D.F.	δ_i, in. (mm)	D.F.
Exterior Beam E1	0.538 (13.67)	0.198	0.448 (11.38)	0.167	0.362 (9.19)	0.135
Interior Beam I1	0.545 (13.84)	0.2000	0.492 (12.49)	0.183	0.448 (11.38)	0.167
Intermediate Beam I2	0.551 (13.99)	0.203	0.536 (13.61)	0.200	0.532 (13.51)	0.199
Interior Beam I3	0.545 (13.84)	0.201	0.583 (14.81)	0.217	0.621(15.77)	0.231
Exterior Beam E2	0.539 (13.69)	0.198	0.625 (15.88)	0.233	0.720 (18.29)	0.268

8.8.2 Post-Cracking Limit State Testing

The post-cracking limit state testing started with the initiation of the first flexural cracks by loading the entire bridge model under four-point-loading setup. Then, a load distribution test was conducted using a post-cracking point load to evaluate the response of the cracked bridge model. Moreover, the exterior beam of the bridge model was loaded under four-point loading setup until signs of shear key distress were observed. Lastly, a loading cycling test was performed on the entire bridge model under four-point-loading setup to approximately 75 % of its anticipated ultimate failure load. The following section describes the tests conducted in this stage along with thorough discussion of the test results.

8.8.2.1 Cracking of Bridge Model

To induce the flexural cracks, the entire bridge model was loaded in a four-point loading setup, as shown by the schematic diagram in Figure 8.8-6 and photograph of Figure 8.8-7. The load was applied through two steel spreaders that were placed at a distance of 78 in. (2 m) apart. Moreover, load was applied through loading and unloading cycles using a force control mode at a rate of 2

kip/min (8.9 kN/min). After each load cycle, the bridge was inspected for cracks. The test stopped immediately after spotting the first visible flexural crack at the midspan section.

The bridge model was loaded in cycles from 10 kip (44.5 kN) to a maximum load of 70 kip (312 kN). The first crack was observed during the 70-kip (312-kN) load cycle, as shown in Figure 8.8-8. After evaluating the load-deflection curve, it was determined that the cracking load was 65 kip (289 kN) with a corresponding deflection of 1.2 in. (30.5 mm) and concrete compressive strain of approximately 400 µε at the top flange of the midspan section. The bridge model exhibited nearly elastic behavior during the flexural loading test until cracks were initiated. Then, the development of cracks marked a rapid change in the slope of the load-deflection curve as explained later in this document.
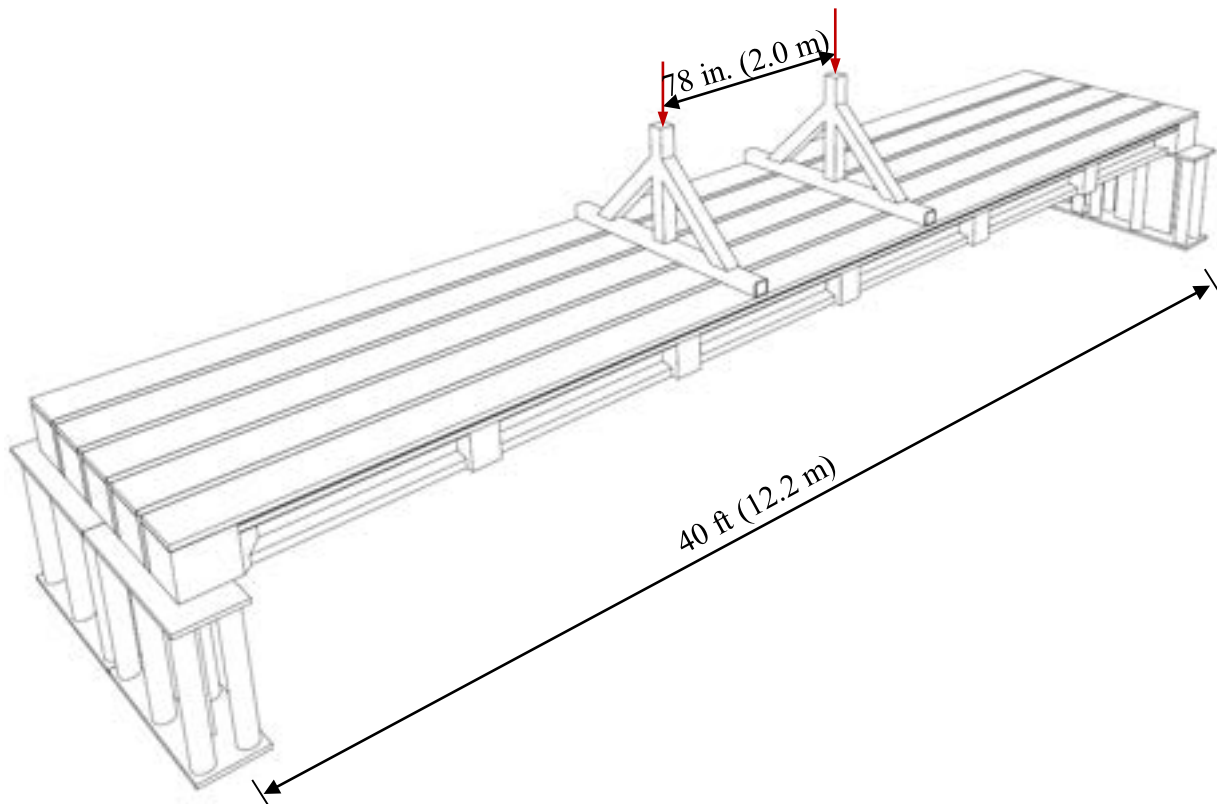
Figure 8.8-6 Schematic diagram showing the four-point load setup for inducing flexural cracks

Figure 8.8-7 Four-point loading of bridge model for inducing flexural cracks

Figure 8.8-8 First flexural crack at the bottom of the bridge model after 70 kip (312 kN) load cycle

8.8.2.2 Post-Cracking Load Distribution Test

After cracking the bridge model, the load distribution test was performed with a point-load of 70 kip (312 kN). The intent of repeating this test was to evaluate the post-cracking load distribution factors and compare them to the values obtained before cracking the bridge.

The deflection curves of the bridge model under a post-cracking load of 70 kip (312 kN) for different loaded beams are presented in Figure 8.8-9. The deflection curves indicated a linear load distribution with no cracks nor shear key distress. The distribution factors were calculated based on the deflection curves and listed in Table 8.8-3. In addition, the load distribution factors obtained from the post-cracking load was compared to that obtained from the service loads of 15 and 30 kip (67 and 134 kN) as shown in Table 8.8-4. In general, the distribution factor did not significantly change even when the load increased from 15 to 70 kip (67 to 312 kN). It should be noted that the recorded deflection values at a service load of 30 kip (134 kN) are nearly double the values recorded at 15 kip (67 kN). However, the deflection values at 70 kip (312 kN) is more than double the values at 30 kip (134 kN). This is due to the cracking and loss of stiffness of the bridge model.
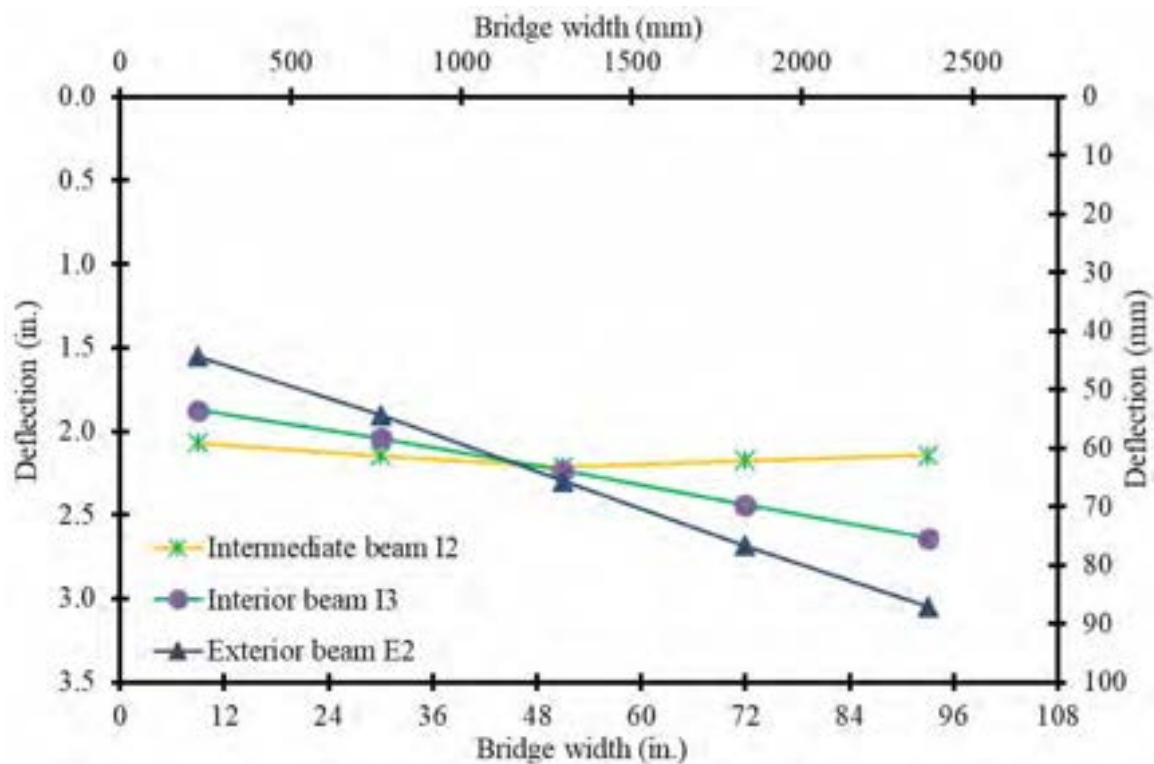
Figure 8.8-9 Deflection curves due to post-cracking loads of 70 kip (312 kN)

Table 8.8-3 Load distribution factors of bridge beams under a point load of 70 kip (312 kN)

	Loaded beam					
	Intermediate Beam I2		Interior Beam I3		Exterior Beam E2	
	δ_i, in. (mm)	D.F.	δ_i, in. (mm)	D.F.	δ_i, in. (mm)	D.F.
Exterior Beam E1	2.070 (52.58)	0.193	1.872 (47.55)	0.167	1.552 (39.42)	0.135
Interior Beam I1	2.147 (54.53)	0.200	2.041 (51.84)	0.182	1.904 (48.36)	0.166
Intermediate Beam I2	2.211 (56.16)	0.206	2.236 (56.79)	0.199	2.297 (58.34)	0.200
Interior Beam I3	2.174 (55.22)	0.202	2.441 (62.00)	0.217	2.685 (68.20)	0.234
Exterior Beam E2	2.143 (54.43)	0.199	2.638 (67.00)	0.235	3.050 (77.47)	0.265

Table 8.8-4 Comparison of load distribution factors under point loads of 15, 30 and 70 kip (67, 134 and 312 kN)

	Loaded beam								
	Intermediate Beam I2			Interior Beam I3			Exterior Beam E2		
	15 kip (67 kN)	30 kip (134 kN)	70 kip (312 kN)	15 kip (67 kN)	30 kip (134 kN)	70 kip (312 kN)	15 kip (67 kN)	30 kip (134 kN)	70 kip (312 kN)
Exterior Beam E1	0.200	0.198	0.193	0.169	0.167	0.167	0.140	0.135	0.135
Interior Beam I1	0.200	0.200	0.200	0.185	0.183	0.182	0.167	0.167	0.166
Intermediate Beam I2	0.201	0.203	0.206	0.200	0.200	0.199	0.200	0.199	0.200
Interior Beam I3	0.200	0.201	0.202	0.216	0.217	0.217	0.230	0.231	0.234
Exterior Beam E2	0.199	0.198	0.199	0.230	0.233	0.235	0.263	0.268	0.265

8.8.2.3 Shear Key Test

The performance of the shear key joints was investigated by loading one of the exterior beams of the bridge model until localized shear key cracks were developed. Figure 8.8-10 and Figure 8.8-11 show the shear key test setup. The exterior beam was loaded using a four-point loading setup with a 78 in. (2 m) distance between the two loading points. Post-cracking loads were applied using a 100-ton hydraulic cylinder in load cycles starting from 70 kip (312 kN) with an increment of 10 kip (44.5 kN). The cracks were inspected after each load cycle. Once the first crack initiated in the shear key connection, the test stopped and the following test was performed.

At a load level of 70 kip (312 kN), minor surface cracks initiated at the top surface of the concrete beams in addition to a limited hairline crack at the shear key joint, as shown in Figure 8.8-12. All cracks developed on the concrete side of the shear key joint and not on the UHPC side. In addition, when the load increased to 80 kip (356 kN), the cracks slightly propagated. Taking into consideration that the failure load of each individual beam in the bridge model was 36.5 kip (162 kN), it can be concluded that the shear key joint resisted more than twice the load carrying capacity of a single beam before cracking. In the case of an interior beam, the load is distributed through two shear key joints instead of one and therefore, it is expected that higher point loads would be reached before cracking the shear key. Since failure of the shear key needed to be omitted for further testing of the bridge model, the test was terminated after reaching a load level of 80 kip (356 kN).

Figure 8.8-13 shows the deflection of the bridge model while the load was applied on the exterior beam. The deflection curves indicated a uniform load distribution among the bridge beams. A maximum deflection of 2.920 in. (74.17 mm) was measured in the exterior beam when loaded to 70 kip (312 kN). In addition, a larger deflection of 3.889 in. (98.78 mm) was measured when the load increased to 80 kip (356 kN) with surface cracks at the connected bridge beam. Overall, the composite unit behavior of the bridge model was maintained under a load level twice the load carrying capacity of each individual beam. Therefore, it can be concluded that the UHPC shear key joints with the transverse intermediate diaphragms can promote the structural integrity of the decked bulb T beam bridge system.
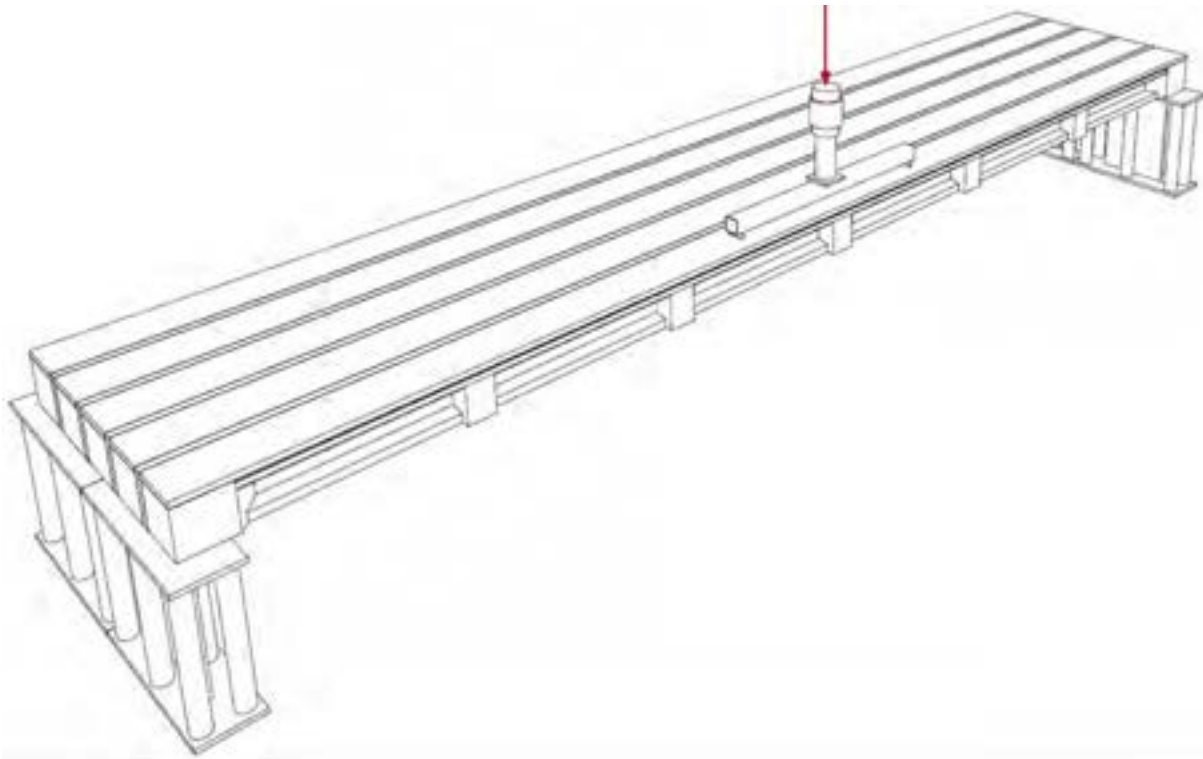
Figure 8.8-10 Schematic diagram of the shear key test

Figure 8.8-11 Test setup for evaluating the shear key joints of the bridge model

Figure 8.8-12 Surface cracks at the concrete side of shear key joints
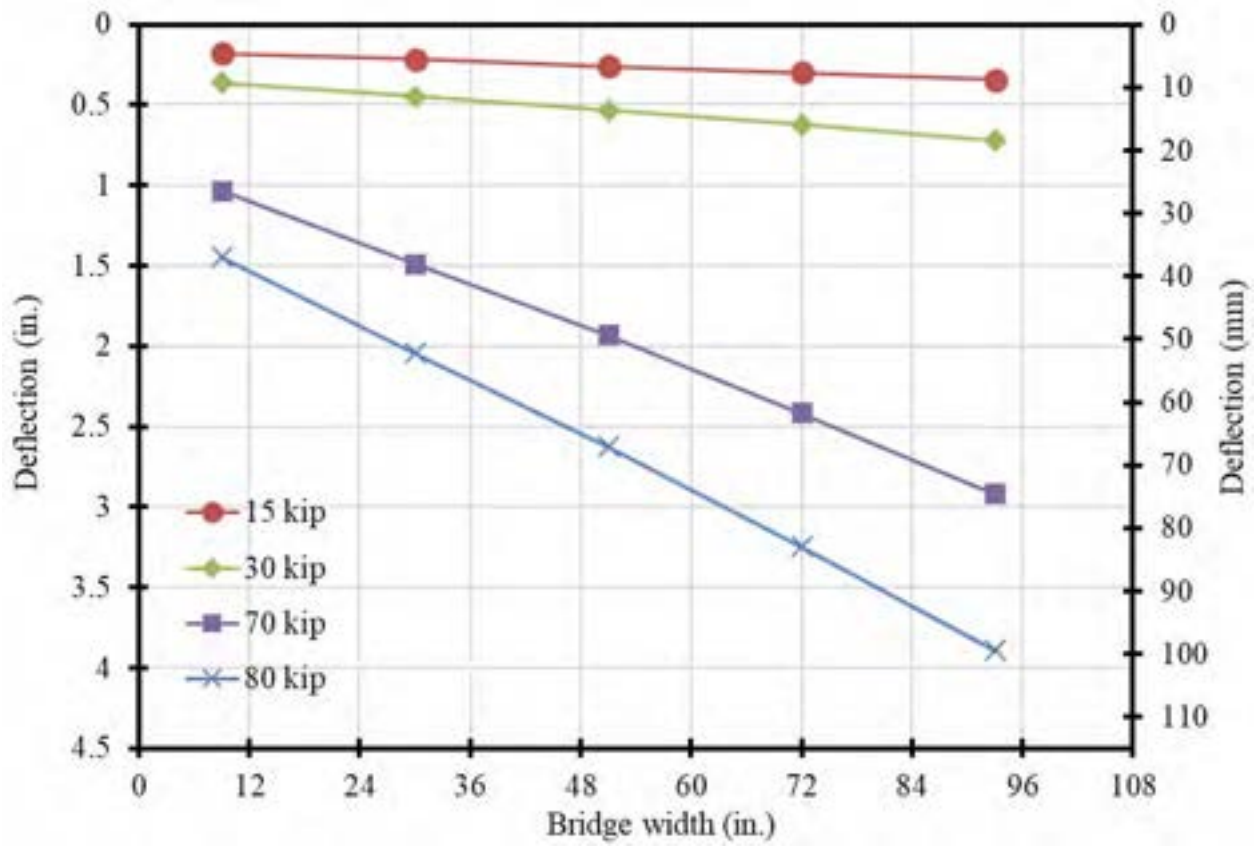
Figure 8.8-13 Deflection curves of bridge model while loading the exterior beam

8.8.2.4 Load Cycles Test

After completing the shear key test, load cycles were applied by loading the entire width of the bridge model under a four-point loading setup. Load cycles of 10-kip (44.5-kN) increments were performed up to 75 % of the expected ultimate capacity of the bridge (130 kip or 579 kN). The main objective of this test was to determine the decompression load from the load-deflection curves and to monitor the cracking pattern of the bridge model. Figure 8.8-14 shows the crack pattern of the bridge model after load cycles. The developed cracks were vertical and concentrated under the loading spreaders near the midspan of the bridge. The load-deflection curves of the bridge model under flexural load cycles is shown in Figure 8.8-15. After conducting each loading and unloading cycle, residual deflection was recorded and added to the succeeding cycles. The corresponding deflection for a load of 130 kip (579 kN) was approximately 9.6 in. (244 mm) with a residual deflection from all loading cycles of 0.6″ (15.2 mm). The decompression load was estimated as 9.5 kip (42.3 kN), which represented an effective prestressing force of 111 kip or 494 kN (prestress loss of 19.5 %).
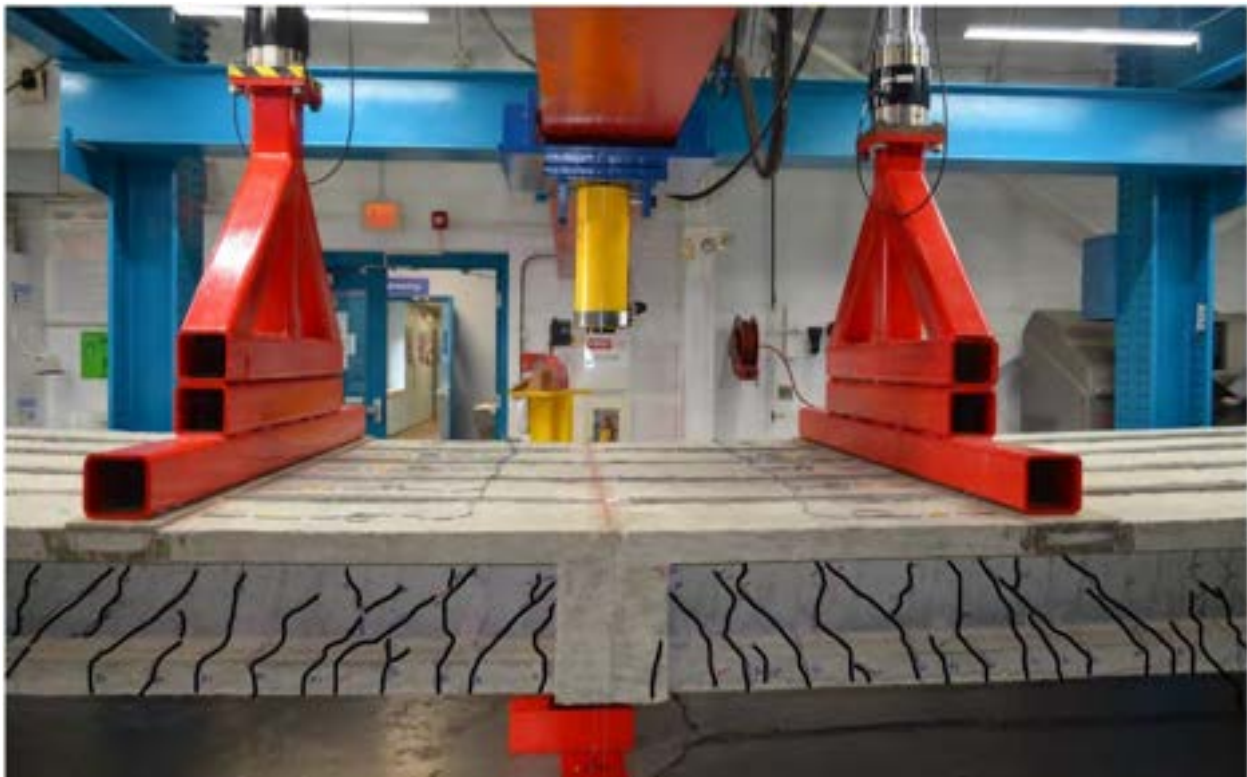
Figure 8.8-14 Crack pattern observed during load cycle test of the bridge model

332
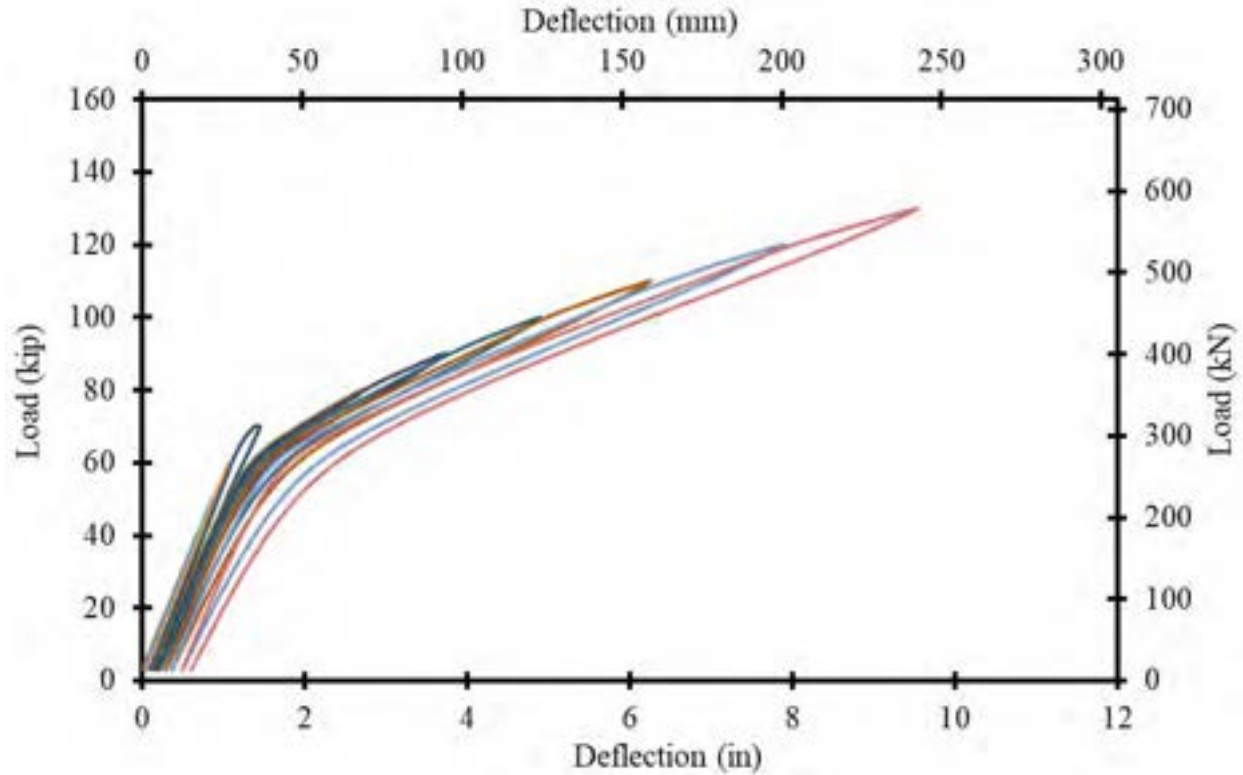
Figure 8.8-15 Load-deflection curves of the bridge model under flexural load cycles

8.8.3 Strength Limit State Testing

After loading the bridge model to approximately 75 % of its anticipated maximum load, the strength limit state testing was performed to determine the load carrying capacity and the mode of failure. The ultimate loading setup is shown in Figure 8.8-16 and Figure 8.8-17, which includes loading only the intermediate beam under four-point loading setup with a 78 in. (2 m) spacing between the two loading points. The objective of this test setup is to assess the capability of the shear key connections along with the transverse diaphragms to transfer the applied load between the decked bulb T beams of the bridge model.

On the testing day, the camber of the bridge model was measured and reported as 1.75 in. (44.5 mm). In addition, concrete cylinders from the same batch of bridge beams and UHPC shear key joints were tested according to ASTM C31/C31M-19 (ASTM 2019). The average compressive strength of the bridge beams and shear key joints was estimated as 8.2 and 31.2 ksi (56.5 and 215 MPa), respectively.

The test started by loading the intermediate beam monotonically, through two MTS actuators, with a force control mode of 5 kip/min (22.3 kN/min). The bridge model experienced a significant deflection before failure accompanied by a dense cracking pattern as shown in Figure 8.8-18. The failure occurred at a load level of 185 kip (823 kN) with a corresponding deflection of 19.5 in. (495 mm) including the residual deflection from previous load cycles. Equal deflections were observed under all five beams of the bridge model, as shown in Figure 8.8-19. The failure of the bridge model was characterized by tendon rupture of CFCC strands at the intermediate loaded beam with partial concrete spalling, as shown in Figure 8.8-20 and Figure 8.8-21. There was no sign of tendon rupture of CFCC strands in the adjacent beams that did not immediately fail, however they continued to support additional load. This demonstrates that the shear key joints in addition to the transverse diaphragm were functional in transferring the load to other bridge beams ever after the failure of the intermediate beam.

The average concrete strain in the top flange of the bridge beams at failure was approximately 2185 $\mu\varepsilon$, which is less than the maximum concrete strain of 3000 $\mu\varepsilon$. This confirms the failure mode of the bridge model since the beams were constructed to fail in tension. To calculate the energy absorbed by the bridge model, the load-deflection curve of the strength limit state test was added to those from previous load cycles and the area under the load-deflection curves from all load cycles, including the ultimate load cycle (Figure 8.8-22) was estimated as 2467.5 kip.in. (279 kN.m).
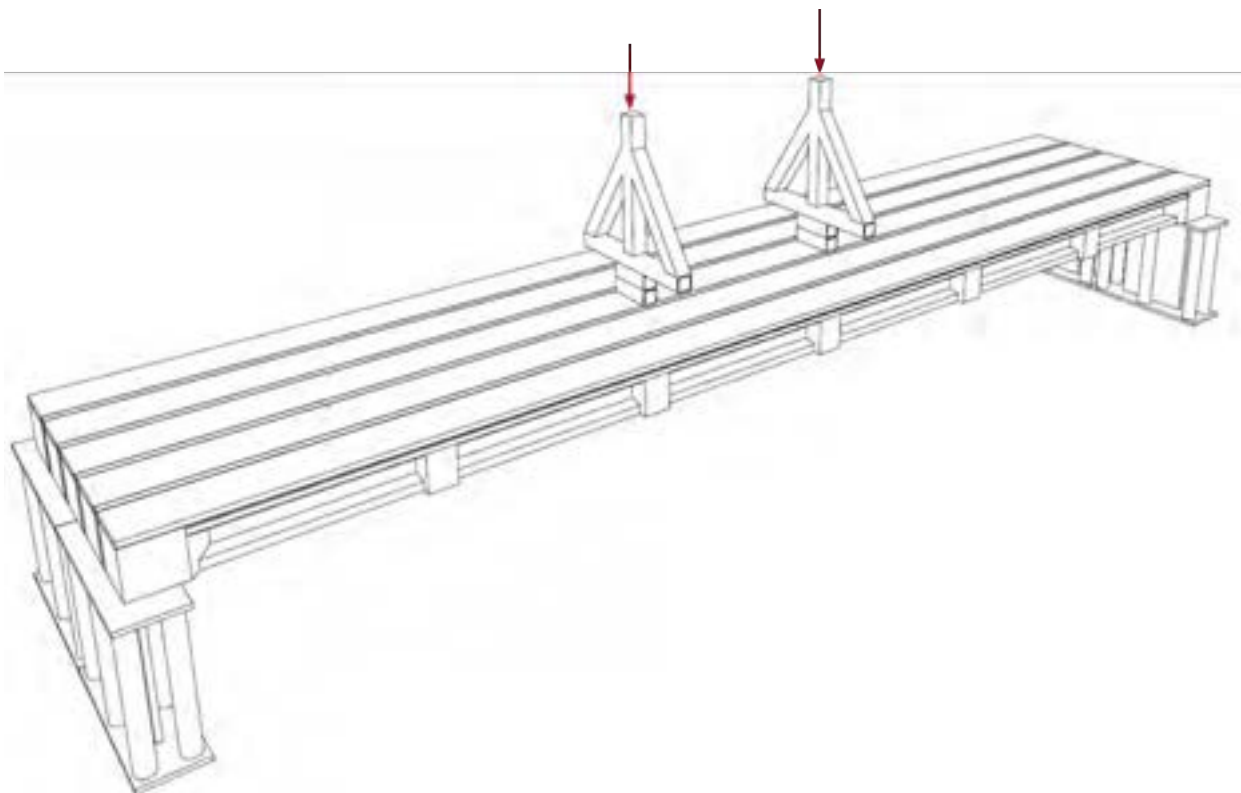
Figure 8.8-16 Schematic diagram showing the strength limit state test

Figure 8.8-17 Four-point loading of the intermediate beam during the strength limit state test

Figure 8.8-18 Deflection of bridge model during strength limit state testing
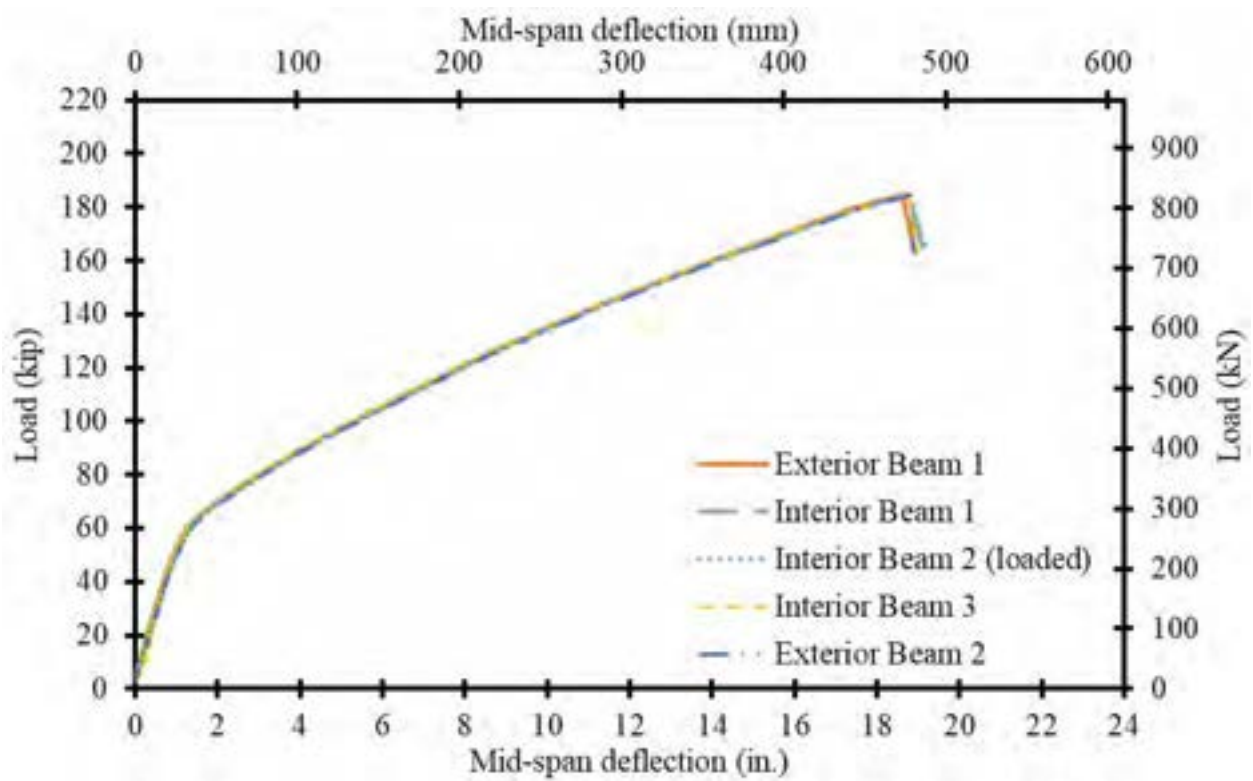
Figure 8.8-19 Load-deflection curves for all beams during ultimate load cycle

Figure 8.8-20 Rupture of CFCC strands accompanied by partial concrete crushing after failure
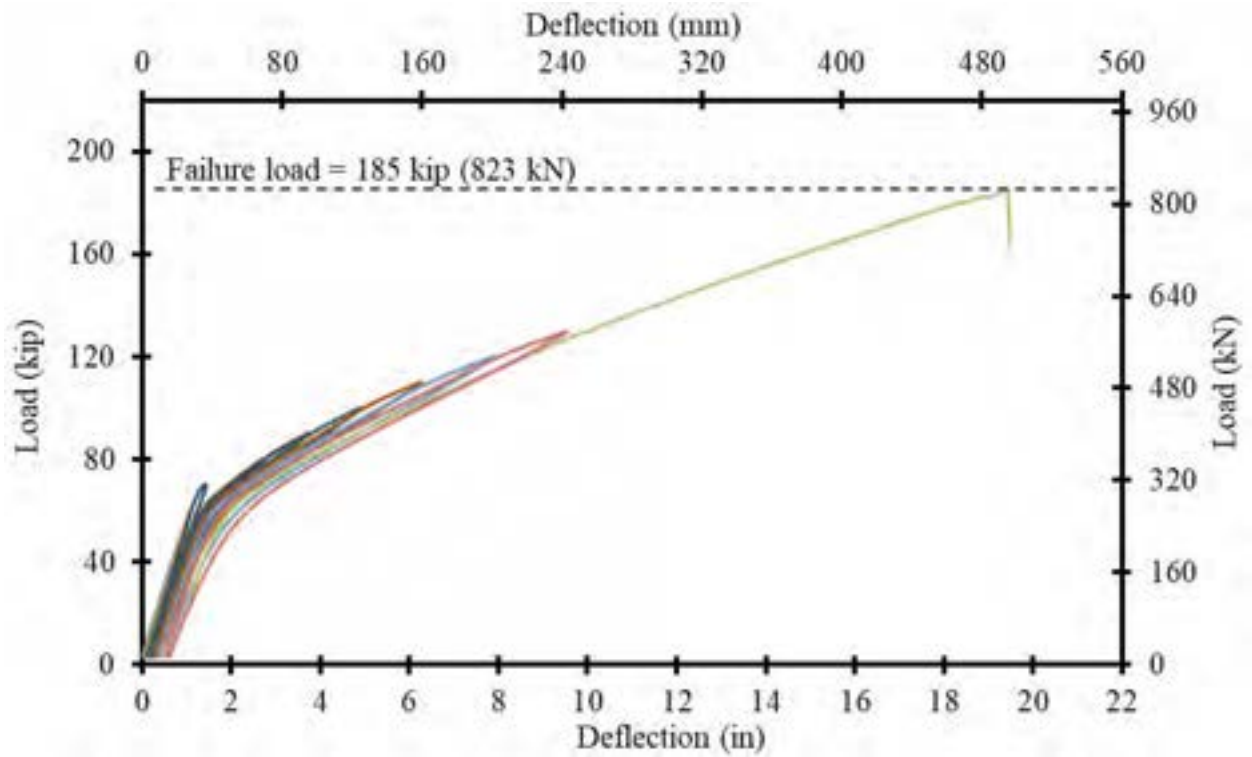
Figure 8.8-21 Combined load-deflection curves including all load cycles until failure
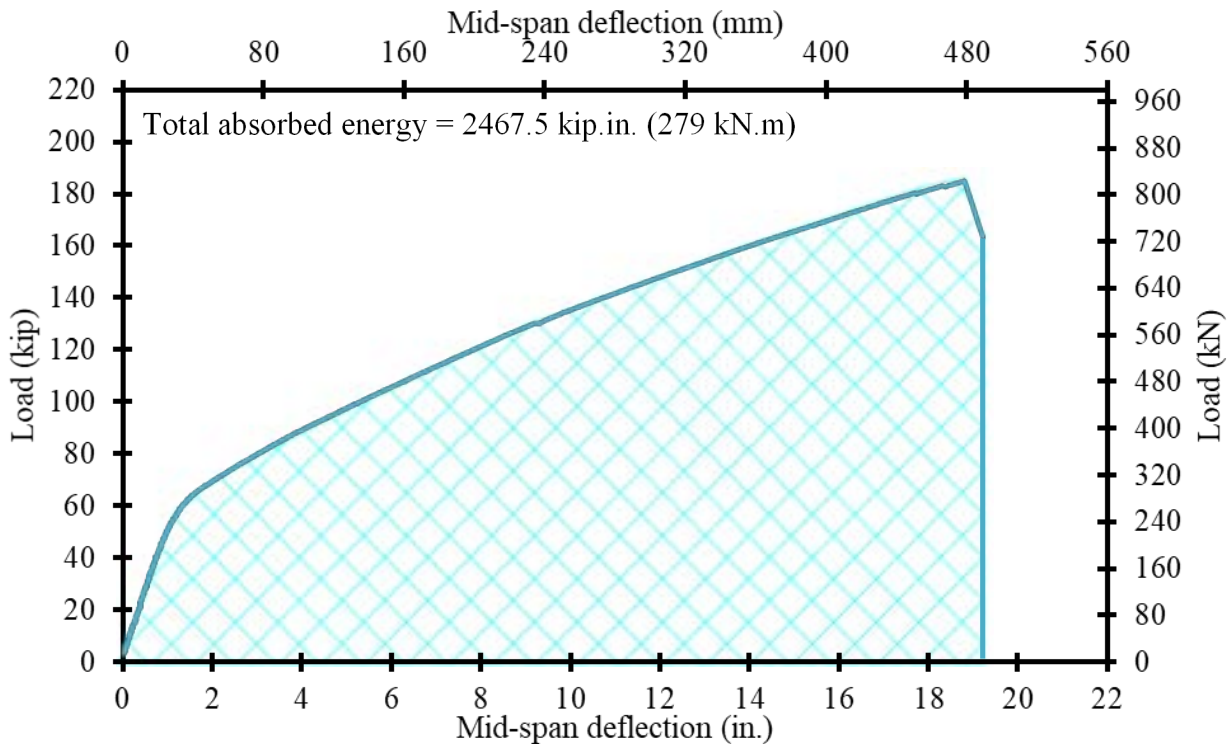
Figure 8.8-22 Total energy absorbed in the bridge model

8.9 Summary

Test results showed that the performance of the bridge model was similar to that of the control beam. The load-deflection curves demonstrated a bilinear relationship with the cracking load marking the change of the slope on the bilinear curve. Also, the failure load in the control beam and bridge model was found to surpass those anticipated by calculations and no premature failure or unpredictable behavior was experienced. The deflection of the bridge model at the ultimate load showed a uniform load distribution between the beams. This demonstrates that the UHPC shear key joints and UHPC transverse diaphragms were sufficient in transferring the load laterally between the beams at all loading stages; service, post cracking and ultimate loading stage, and thus, the structural integrity of the decked bulb T beam bridge was intact.

Finally, the deployment of 0.7″ CFCC strands with higher jacking stress was found to be more efficient and feasible in beam construction as it reduced the number of anchorage devices and improved the beam design by meeting the load-carrying capacity requirements with higher prestressing force per strand and lower number of strands compared to 0.6″ CFCC strands.

338

CHAPTER 9: SUMMARY AND CONCLUSIONS

9.1 Conclusions

Based on the comprehensive investigation and test results that were presented in this report, the following conclusions can be drawn:

1. The uniaxial tensile test of 0.7″ CFCC specimen showed a tensile strength as high as 144 % of the guaranteed strength, which far exceeds the tensile to guaranteed strength ratio for 0.6″ CFCC strands. The additional strength serves as a margin of safety in design.

2. Testing of new 0.7″ CFCC wedge anchorage inside coupler devices, following the manufacturer's guidelines, using old and new buffer systems showed minimal loss in the prestressing force after extended monitoring. Nearly 90 % of prestress loss due to seating of the system took place within the first 24 hours of prestressing. A coupler seating of approximately 0.18 in. (5 mm) was observed after prestressing.

3. A minimum estimate for the one-million-hour creep rupture strength of CFCC strands, based on testing strands with different diameters, is not less than 86 % of the average CFCC tensile strength. For 0.7″ CFCC strands, the minimum one-million-hour creep rupture strength is approximately 98 kip (436 kN), which is higher than the guaranteed strength recommended by the manufacturer (78.7 kip or 350 kN).

4. Similar to 0.6″ CFCC, under sustained loads higher than 95 % of the average tensile strength, 0.7″ CFCC test specimens either ruptured within the first 100 hours of loading or continued to sustain the load without significant signs of creep.

5. The one-million-hour relaxation rate, defined as the expected percentage loss in the force in a CFRP strand over one-million hours, of 0.7″ CFCC strands is approximately 2.2 % based on available test results of strands initially tensioned to a force level of 94 kip (418 kN).

6. By pulling strand specimens with a bond length of 3.5 in. (89 mm) from uncracked concrete with an average 28-day compressive strength of 8.66 ksi (60 MPa), the average pullout strength of 0.7″ CFCC strands was approximately 12.29 kip (55 kN), which was slightly less than the pullout strength of 0.6″ CFCC (13.14 kip or 58 kN). On the other hand, the

pullout strengths of 0.6″ and 0.7″ steel strands averaged 6.28 and 9.30 kip (28 and 41 kN), respectively. However, a difference in the bond mechanism was noted when comparing CFCC to steel specimens.

7. The bond between CFCC strands and concrete is achieved mainly through adhesion at the strand surface. On the other hand, bond between steel strands and concrete seems to develop mainly due to a locking interaction between the twisted strands and the surrounding concrete. This was evident from the significantly larger slippage in the case of steel strands. Due to the difference in the bond mechanism, bond lengths longer than 3.5 in. (89 mm) could yield different bond strength ratios when comparing steel to CFCC strands.

8. The transfer length of 0.7″ CFCC strands with an initial prestressing force of 53 kip (236 kN) is nearly 24 in. (610 mm). This is approximately 35 times the diameter of the strand.

9. Based on the pullout strength of 0.7″ CFCC strands from concrete prisms with different bond lengths and concrete strengths, the minimum bond length that achieved a full development of 0.7″ CFCC strands was approximately 42 in. (1067 mm). However, this length is influenced by different factors such as the compressive strength of the concrete and the state of stress in the concrete surrounding the prestressing strands. In addition, the size of the prism and the presence of lateral confinement appeared to enhance the development of the strands by shortening the required bond length to achieve full development.

10. Through flexural testing of half-scale and full-scale beams, 0.7″ CFCC strands with a bond length of 8 ft (2.44 m) reached their full tensile strength before experiencing bond failure. CFCC strands with a longer bond length achieved their tensile strength without bond failure.

11. Exposure to 300 cycles of freeze-thaw results in deterioration of concrete strength and consequently, a drop in the bond strength between CFCC strands and concrete. On average, there was approximately a 28 % drop in the bond strength between concrete and CFCC after exposure to freeze-thaw cycles.

12. Average tensile strength and elastic modulus of 0.7″ CFCC strands subjected to 150 or 300 cycles of freezing and thawing were slightly higher than the average values obtained from testing strands not exposed to freeze-thaw cycles. The increase in tensile strength was approximately 2.3 and 3.9 % after exposure to 150 and 300 cycles, respectively. An increase in elastic modulus of approximately 5 % was observed after exposure to both 150 and 300 freeze-thaw cycles.

13. Tensile strength of CFCC strands decreases almost linearly with the increase in temperature to 662 °F (350 °C). At the highest temperature, 0.6″ and 0.7″ CFCC strands achieved nearly 49 and 34 % of their ambient tensile capacities, respectively. In addition, a change of mode of failure from brittle rupture to matrix disintegration was observed at temperatures around 437 °F (225 °C) and higher.

14. Exposure to fire resulted in a loss in the bond strength between CFCC and concrete. The loss in the bond strength is attributed to the deterioration of both CFCC and concrete when exposed to elevated temperatures.

15. Fire endurance of a prestressed beam is defined as the time frame in which the prestressed beam continues to effectively support a specific level of service loads in the case of a fire event before any major failure or collapse. The fire endurance of simply-supported full-scale CFCC prestressed beams under three-point loading coupled with a fire event following the standard ASTM E119 time-temperature curve exceeded two hours. This fire endurance was verified for beams with different cross sections provided that major concrete spalling was avoided by proper concrete drying prior to testing,

16. Failure of the CFCC prestressed beams under fire/loading events initiated by debonding of CFCC strands. Loss of prestressing force during the testing was also evident. While the loss in prestressing force resulted in the development of cracks throughout the beam, it slightly extended the fire endurance of the beams by relieving the stress in CFCC strands.

17. After exposure to a fire/loading event for one hour and then subjected to a three-point-load flexural test under ambient conditions, beams prestressed with 0.6″ and 0.7″ CFCC strands failed at lower capacities than their theoretically/experimentally anticipated capacities. The failure of CFCC prestressed beams was characterized by strand slippage. The failure load

was nearly equal to the design load of each beam after accounting for different design strength reduction factors.

18. Stressed CFCC strands subjected to an increase in temperature for the first time exhibit a certain loss in the stress level due to heat-induced relaxation of the strand. The heat relaxation loss will most likely be exhibited during construction at the time of concrete curing, when the temperature of concrete reaches around 150 °F (66 °C). The heat relaxation loss is permanent and is not recovered when the temperature drops back to ambient levels.

19. Heat relaxation loss in CFCC strands takes place only during the first cycle of heating to a certain temperature level. Subsequent heating cycles to the same temperature do not result in any additional relaxation loss.

20. With the exception of prestress loss due to heat relaxation, temperature increase to 400 °F (204 °C) did not seem to have any permanent effect on the mechanical properties of CFCC strands. When heated CFCC specimens were allowed to cool down and then tested to failure at ambient temperature, both elastic modulus and tensile strength were found to be slightly higher than their average values obtained by testing specimens left at ambient conditions. The differences were not statistically significant.

21. At a typical concrete curing temperature of 150 °F (66 °C), the average heat relaxation strain of 0.7″ CFCC strands was estimated as 307 με. Based on the diameter and effective cross-sectional area of the strand, the loss in prestressing force due to heat relaxation was determined as 1.62 kip (7.2 kN) per strand.

22. Flexural testing of full-scale AASHTO I beams showed a significant margin of safety in beams prestressed with 0.6″ and 0.7″ CFCC strands. For instance, an AASHTO I Beam prestressed with 0.7″ CFCC strands achieved approximately 221 % of its analytical design capacity. Likewise, an AASHTO I Beam prestressed with 0.6″ CFCC strands achieved approximately 172 % of its design capacity. On the other hand, an AASHTO I Beam prestressed with 0.6″ steel strands achieved approximately 117 % of its design capacity. The significant margin of safety of beams prestressed with CFCC strands is attributed to the environmental reduction factor (0.9), the strength reduction factor (0.85), and the ratio

between the guaranteed strength and the average tensile strength (0.69 and 0.87 for 0.7" and 0.6" CFCC strands, respectively).

23. Overall, the deployment of 0.7″ CFCC strands, with their higher jacking force, was both feasible and efficient in beam construction as it reduced the number of anchorage devices and improved the beam design by meeting the load-carrying capacity requirements with higher prestressing force per strand and lower number of strands compared to 0.6″ CFCC strands. This was evident through the testing and comparison between two half-scale bulb T bridge models prestressed with 0.6″ and 0.7″ CFCC strands.

24. Based on the test results and comparison with results from testing 0.6" CFCC strands, MDOT CFRP Design Guide Specifications that were developed for use with 0.6" CFCC strands can be extended to 0.7" CFCC strands with no special amendments.

9.2 Construction Specifications

Based on the results and recommendations from the experimental program and the experience gained from field deployment of CFCC in recent highway bridge projects, the following construction specifications and recommendations are provided:

1. Construction of beams prestressed with CFCC strands shall conform to Standard Specifications of Construction approved by the jurisdiction where construction is taking place with the exception of handling, anchoring, and prestressing CFCC strands.

2. Handling of CFCC must adhere to manufacturer's recommendations. Care shall be taken to avoid damaging the strands or scoring the strand surface. CFCC strands have lower shear and compressive strengths compared to their tensile strength. Therefore, CFCC strands shall not be used to support heavy weights along their length such as tools and weight of personnel. Further details for handling are listed in the most-recent version of the manufacturer's handling manual.

3. Care must be taken to avoid exposing CFCC strands to any curvature. Strands must be pulled away from the reel and cut to the required length. Recoiling extra strands shall be avoided whenever possible or shall be performed in such a manner to avoid exposing the strands to a compressive force that might result in kinking the strand. When recoiling

CFCC strands, the minimum radius of curvature shall be forty (40) times the diameter of the strand.

4. Any segment of CFCC strand that is exposed to kinking shall be cut and discarded. Untwisting of CFCC strands is also not allowed. When coupling steel with CFCC strands, care shall be taken to ensure the same twist (lay) direction in both strands.

5. CFCC strands shall not be bent around hard objects such as sharp steel corners.

6. CFCC strands shall be protected from open flames or any heat source (welding sparks, torch flames, etc.) during construction.

7. CFCC strands are susceptible to abrasion, which can damage the strands and reduce their tensile capacity. Therefore, CFCC strands shall not be dragged against hard objects or corners that might scratch the surface. It is recommended that hard surfaces are covered with plastic sheets or protective foam before pulling the strands on them.

8. When not immediately in use, care shall be taken to cover CFCC strands on the reel or in the prestressing bed to avoid extended exposure to direct sun and ultraviolet rays. CFCC strands must be kept free of any oil, grease, chemical substances, or foreign matters.

9. CFCC strands shall be unpacked from the reel only when they are ready for use. CFCC strand segments that show signs of surface damage shall not be used. Damage to the reel or the shipping package may indicate underlying damage in CFCC strands and shall be properly investigated. CFCC shall be stored indoors on the reel and shall be free from dust and protected from damage by proper covering.

10. CFCC reels shall be lifted using slings and the crane of a fork-lift. The lifting device shall only be attached to the wooden reel of the pallets and must not come into contact with the CFCC strands on the reel at any point.

11. When unpacking CFCC strands, the reel shall be positioned so that the strand is pulled from the lower side of the reel and the strand shall be pulled carefully away from the reel. Sudden movement or recoiling shall be avoided. The strand may be cut to length using a cutting wheel or a grinder. After cutting the required length, the end of the remaining CFCC strand spool shall be properly fastened to the reel with a string.

344

12. Initial prestressing force immediately prior to transfer shall be indicated on the shop drawings. The jacking force shall be established by accounting for all anticipated prestress loss/gain from the time of prestressing to the time of prestress release.

13. Thermal corrections for the prestressing force shall be calculated based on the ambient conditions during the time of prestressing, temperature of the concrete, and the type of the prestressing bed. For the purpose of thermal calculations, the coefficient of thermal expansion of the CFCC can be assumed zero.

14. Other prestress losses during construction such as bed shortening and seating of the anchorage and coupler devices shall be calculated accordingly and considered when establishing the jacking force.

15. Anchoring of CFCC strands is continually evolving to eliminate complexity and facilitate the process. Attaching the anchorage devices to CFCC strands shall be conformed to the most-recent manufacturer's recommendations. The main steps of anchoring of CFCC strands are: (a) wrapping the end of the strands with a buffer layer, (b) spraying molybdenum (lubricant) on the inside of the sleeve socket, (c) placing the steel wedges around the strand (d) seating the wedges and the strand inside the sleeve socket, and (e) pushing the wedges and the strand inside the sleeve socket using a hydraulic jack. After anchoring the CFCC strand, it shall be coupled with a steel strand of the same diameter using the completed coupler system.

16. Dimensions and specifications of the sleeve, wedges, and buffer materials vary by the diameter of the CFCC strand. The manufacturer shall review and approve the anchorage system prior to the start of construction.

17. Tensioning of CFCC strands and the cutting sequence are similar to the sequence followed when using steel strands. Tolerances of prestressing force shall conform to steel strand tolerances listed in the Standard Specifications of Construction and approved by the jurisdiction.

18. Layout of the staggered couplers shall be provided and approved prior to construction. Due to the size of the couplers, it is crucial that elongation is calculated accordingly and enough room is given to each coupler to move freely without touching or pushing other couplers

during strand prestressing. Serious accidents and injuries are imminent should the couplers come into contact with each other.

19. The anchorage device shall not be exposed to extreme heat (above 122 °F or 50 °C) and shall not be exposed to steam.

20. It is recommended to use external vibrators when pouring the concrete. If internal vibrators are used, they shall be shielded with polyurethane sheathing to avoid damaging CFCC strands. Curing concrete shall take place at temperatures from 70 to 150 °F (21 to 65 °C) until concrete attains the required strength at release.

21. After placement of concrete and proper curing, the force is released to the beam by torch-cutting the steel strands coupled with CFCC strands in a preapproved sequence. When a series of beams is constructed in one bed, a cutting wheel may be used to cut the CFCC strands between the beams. Wedges and sleeve sockets are removed using a hydraulic jack and stored for future use.

REFERENCES

1. AASHTO, 2017, "AASHTO LRFD Bridge Design Specifications," 8th ed., American Association of State Highway and Transportation Officials, Washington, DC.

2. Abbasi, A. & Hogg, P., 2006, "Fire Testing of Concrete Beams with Fibre Reinforced Plastic Rebar," Composites Part A: Applied Science and Manufacturing. Vol. 37, Issue No. 8, pp. 1142-1150.

3. Achillides, Z. and Pilakoutas, K., 2004, "Bond Behavior of Reinforced Polymer Bars under Direct Loading," Journal of Composites for Construction, Vol. 8, Issue No. 2, pp. 173-181.

4. Akbas, T., Celik, O., Yalcin, C., and Ilki, A., 2016, "Monotonic and Cyclic Bond Behavior of Deformed CFRP Bars in High Strength Concrete," Polymers, Vol. 8, Issue No. 6, doi: 10.3390/polym8060211.

5. Alsiwat, J. and Saatcioglu, M., 1992, "Reinforcement Anchorage Slip under Monotonic Loading," ASCE Journal of Structural Engineering, Vol. 118, Issue No. 9, pp. 2421-2438.

6. American Concrete Institute (ACI), 2004, "Prestressing Concrete Structures with FRP Tendons," ACI 440.4R-04, Farmington Hills, MI.

7. American Concrete Institute (ACI), 2012, "Guide Test Methods for Fiber-Reinforced Polymer (FRP) Composites for Reinforcing or Strengthening Concrete and Masonry Structures," ACI 440.3R-12, Farmington Hills, MI.

8. American Concrete Institute (ACI), 2015, "Guide for the Design and Construction of Structural Concrete Reinforced with FRP Bars," ACI 440.1R-15, Farmington Hills, MI.

9. Ashton, L. and Malhotra, H., 1953, "The Fire Resistance of Prestressed Concrete Beams," Fire Res. Notes (1953), pp. 65.

10. ASTM C143/C143M-05, 2005, "Slump of Hydraulic Cement Concrete," ASTM International, West Conshohocken, PA, USA, www.astm.org.

11. ASTM C31/C31M-19, 2019, "Standard Practice for Making and Curing Concrete Test Specimens in the Field," ASTM International, West Conshohocken, PA, USA, www.astm.org.

12. ASTM C39/C39M, 2020, "Compressive Strength of Cylindrical Concrete Specimens," ASTM International, West Conshohocken, PA, USA, www.astm.org.

13. ASTM D7205/D7205M, 2016, "Tensile Properties of Fiber Reinforced Polymer Matrix Composite Bars." ASTM International, West Conshohocken, PA, USA, www.astm.org.

14. ASTM E119-20, 2020, "Fire Tests of Building Construction and Materials," ASTM International, West Conshohocken, PA, USA, www.astm.org.

15. ASTM E1640-18, 2018, "Assignment of the Glass Transition Temperature by Dynamic Mechanical Analysis," ASTM International, West Conshohocken, PA, USA, www.astm.org.

16. ASTM Standard C666, 2015, "Resistance of Concrete to Rapid Freezing and Thawing," ASTM International, West Conshohocken, PA, USA, www.astm.org.

17. ASTM Standard C1437, 2020, "Flow of Hydraulic Cement Mortar," ASTM International, West Conshohocken, PA, USA, www.astm.org.

18. Barr, P. J., Stanton, J. F., and Eberhard, M. O., 2005, "Effects of Temperature Variations on Precast, Prestressed Concrete Bridge Beams," Journal of Bridge Engineering, Vol. 10, No. 2, pp. 186-194.

19. Bryan, P. E. and Green, M. F., 1996, "Low Temperature Behavior of CFRP Prestressed Concrete Beams," Canadian Journal of Civil Engineering, Vol. 23, No. 2, pp. 464-470.

20. Ceroni, F., Cosenza, E., Gaetano, M., and Pecce, M., 2006, "Durability Issues of FRP Rebars in Reinforced Concrete Members," Cement and Concrete Composites, Vol. 28, No. 10, pp. 857-868.

21. Elbadry, M., Abdalla, H., and Ghali, A., 2000, "Effects of Temperature on the Behaviour of Fiber Reinforced Polymer Reinforced Concrete Members: Experimental Studies," Canadian Journal of Civil Engineering, Vol. 27, No. 5, pp. 993-1004.

22. El-Hacha, R., Wight, R., and Green, M., 2004, "Prestressed Carbon Fiber Reinforced Polymer Sheets for Strengthening Concrete Beams at Room and Low Temperatures," Journal of Composites for Construction, Vol. 8, No. 1, pp. 3-13.

23. Enomoto, T., Harada, T., Ushijima, K., and Khin, M., 2009, "Long Term Relaxation Characteristics of CFRP Cables," Proceedings of the 4th International Conference on Construction Materials (ConMat09), Japan Concrete Institute, Japan, pp. 1205-1210.

24. Grace N., 1999, "Innovative CFRP Continuous Prestressed Concrete Bridges," ACI Concrete International, Vol. 21, No. 10, pp. 42-47.

25. Grace and Abdel-Sayed, 2000, "Behavior of Carbon Fiber - Reinforced Prestressed Concrete Skew Bridges," ACI Structural Journal, Vol. 97, No. 1, Jan.-Feb.

26. Grace, 2000, "Transfer Length of CFRP/CFCC Strands for Double-T Beams," PCI Journal, Vol. 45, No. 5, September/October.

27. Grace, Navarre, Nacey, Bonus, and Collavino, 2002a, "Design-Construction of Bridge Street Bridge-First CFRP Bridge in the United States," PCI Journal, Vol. 47, No. 5, September/October.

28. Grace, N., Enomoto, T., and Yagi, K., 2002b, "Behavior of CFCC and CFRP Leadline Prestressing Systems in Bridge Construction," PCI Journal, Vol. 47, No. 3, May/June.

29. Grace, Singh, Shenouda, and Sunup, 2004, "Flexural Response of CFRP Prestressed Concrete Box Beams for Highway Bridges," PCI Journal, Vol. 49, No. 1, January/February.

30. Grace, N., Enomoto, T., Baah, P. and Bebawy, M., 2012a, "Flexural Behavior of CFRP Precast Prestressed Decked Bulb T Beams," ASCE Journal of Composites for Construction, Vol. 16, No. 3, May/June, pp. 225-234.

31. Grace, N., Jensen, E., Eamon, C., Shi, X., 2012b, "Life Cycle Cost Analysis of CFRP Reinforced Concrete Bridges," ACI Structural Journal, Vol. 109, Issue 5, pp. 697-704.

32. Grace, N., Jensen, E., and Bebawy, M., 2012c, "Transverse Post-Tensioning Arrangement for Side-by-Side Box-Beam Bridges", PCI Journal, Vol. 57, Issue 2, Spring, pp. 48-63.

33. Grace, N., Ushijima, K., Baah, P. and Bebawy, M., 2013a, "Behavior of CFRP Prestressed Decked Bulb T Beam Bridge System," ASCE Journal of Composites for Construction, Vol. 17, No. 4, July/Aug., pp. 497-506.

34. Grace, N., Ushijima, K., Matsagar, V., and Wu, C., 2013b, "Performance of AASHTO-Type Bridge Model Prestressed with Carbon Fiber-Reinforced Polymer Reinforcement," ACI Structural Journal, Vol. 110, Issue 3, pp. 491-501.

35. Grace, N., Jensen, E., Matsagar, V., and Penjendra, P., 2013c, "Performance of an AASHTO Beam Bridge Prestressed with CFRP Tendons," Journal of Bridge Engineering, 18, pp. 110-121, 10.1061/(ASCE)BE.1943-5592.0000339.

36. Grace, N., and Bebawy, M., 2014, "Fire Protection for Beams with Fiber-Reinforced Polymer Flexural Strengthening Systems," ACI Structural Journal, Vol. 111, No. 3, pp. 537-548.

37. Grace, N., Ushijima, K., Rout, S., and Bebawy, M., 2015, "Performance of CFRP Stirrups in Prestressed Decked Bulb T Beams," ASCE Journal of Composites for Construction, 1090-0268/04014061, May/June, Vol. 19, Issue 3.

38. Grace, N., Bebawy, M., Kasabasic, M., Al-Hassan, E., Acharya, A., Abdo, K, and Mohamed, M., 2019, "Evaluating Long Term Capacity & Ductility of Carbon Fiber Reinforced Polymer Prestressing & Post Tensioning Strands Subject to Long Term Losses, Creep, and Environmental Factors, and Development of CFRP Prestressing Specifications for the Design of Highway Bridges," Rep. No. SPR-1690, Southfield, MI, Center for Innovative Material Research.

39. Green, M., Bisby, L., Beaudoin, Y., and Labossiere, P., 2000, "Effect of Freeze-Thaw Cycles on the Bond Durability between Fiber Reinforced Polymer Plate Reinforcement and Concrete," Canadian Journal of Civil Engineering, Vol. 27, No. 5, pp. 949-959.

40. Green, M. F., Soudki, K. A., and Johnson, M. M., 1997, "Freeze-Thaw Behavior of Reinforced Concrete Beams Strengthened by Fiber Reinforced Sheets," In Proc. Annual Conf. of the Canadian Society for Civil Engineering, pp. 31-39, Sherbrooke, Quebec, Canadian Society for Civil Engineering.

41. Hao, Q., Wang, Y., and Ou, J., 2008, "Design Recommendations for Bond Between GFRP/Steel Wire Composite Rebars and Concrete," Engineering Structures, Vol. 30, pp. 3239-3246.

42. Harajli, M. and Abouniaj, M., 2010, "Bond Performance of GFRP Bars in Tension: Experimental Evaluation and Assessment of ACI 440 Guidelines," ASCE Journal of Composites for Construction, Vol. 14, No. 6, pp. 659-668.

43. Harajli, M. H., 2009, "Bond Stress-Slip Model for Steel Bars in Unconfined or Steel, FRC, or FRP Confined Concrete under Cyclic Loading," ASCE Journal of Composites for Construction, Vol. 135, No. 5, pp. 509-518.

44. Japanese Society of Civil Engineers (JSCE), 1995, "Test Method for Creep Failure of Continuous Fiber Reinforcing Materials," JSCE, Tokyo, Japan.

45. Japanese Society of Civil Engineers (JSCE), 1995, "Test Method for Long-Term Relaxation of Continuous Fiber Reinforcing Materials," JSCE, Tokyo, Japan.

46. Kanakubo, T., Yonemaru, K., Fukuyama, H., Fujisawa, M., and Sonobe, Y., 1993, "Bond Performance of Concrete Members Reinforced with FRP Bars," Proc., Int. Symp. on Fiber Reinforced Plastic Reinforcement for Concrete Structures: ACI SP-138, A. Nanni and C. W. Dolan, Eds.

47. Katz, A., Berman, N. and Bank, L., 1999, "Effect of High Temperature on Bond Strength of FRP Rebars," Journal of Composites for Construction, Vol. 3, No. 2, pp. 73-81.

48. Kim, Y., Hossain, M., and Chi, Y., 2011, "Characteristics of CFRP–Concrete Interface Subjected to Cold Region Environments Including Three-Dimensional Topography," Cold Regions Science and Technology, 67(1), pp. 37-48.

49. Kodur, V. K. and Bisby, L. A., 2005, "Evaluation of Fire Endurance of Concrete Slabs Reinforced with Fiber-Reinforced Polymer Bars," Journal of Composites for Construction, Vol. 131, No. 1, pp. 73-81.

50. Kodur, V., Bisby, L., and Foo, S., 2005, "Thermal Behavior of Fire-Exposed Concrete Slabs Reinforced with Fiber-Reinforced Polymer Bars," ACI Structural Journal, Vol. 102, No. 6, pp. 799–807.

51. Maluk, C., Bisby, L., Santa Maria, H., Terrasi, G. and Green, M., 2010, "Effects of Elevated Temperatures and Fire on Bond Strength of Prestressed Steel and Carbon FRP Bars in High Performance Self-Consolidating Concrete," Proceedings of the 2nd

Postgraduate Engineering Students' PUC Congress, May 28, Pontificia Universidad Católica de Chile, Santiago, Chile.

52. Malvar, L. J., 1994, "Bond Stress-Slip Characteristics of FRP Rebars," Rep. TR-2013-SHR, Naval Fac. Engrg. Service Ctr., Port Hueneme, California.

53. Rafi, M., Nadjai, A., and Ali, F., 2007, "Fire Resistance of Carbon FRP Reinforced Concrete Beams," Magazine of Concrete Research, Vol. 59, No. 4, pp. 245-255.

54. Robert, M. and Benmokrane, B., 2010, "Behavior of GFRP Reinforcing Bars Subjected to Extreme Temperatures," ASCE Journal of Composites for Construction, Vol. 14, No. 4, pp. 353-360.

55. Saadatmanesh, H. and Tannous, F., 1999, "Relaxation, Creep and Fatigue Behavior of Cardon Fiber Reinforced Plastic Tendons," ACI Material Journal, Vol. 96, Issue No. 2, pp. 143-153.

56. Saafi, M., 2002, "Effect of Fire on FRP Reinforced Concrete Members," Composite Structures, Elsevier, Vol. 58, No. 1, pp. 11-20.

57. Saiedi, R., Green, M., and Fam, A., 2013, "Behavior of CFRP-Prestressed Concrete Beams Under Sustained Load at Low Temperature," Journal of Cold Regions Engineering, Vol. 27, No. 1, pp. 1-27.

58. Sasaki, I. and Nishizaki, I., 2012, "Tensile Load Relaxation of FRP Cable System During Long-Term Exposure Tests." In Proc., 6th Int. Conf. on FRP Composites in Civil Engineering, 1–8, Rome, Italy: CICE.

59. Sayed-Ahmed, E. Y., and Shrive, N. G., 1999, "Smart FRP Prestressing Tendons: Properties and Prospects," Proc., Second Middle East Symp. on Structural Composites for Infrastructure Applications, A.H. Hosny, I. Mahfouz, and S. Sarkani, eds., pp. 80–93.

60. Shoukry, S., William, G., Downie, B., and Riad, M., 2011, "Effect of Moisture and Temperature on the Mechanical Properties of Concrete," Construction and Building Materials, Vol. 25, No. 2, pp. 688-696.

61. Subramaniam, K., Ali-Ahmad, M., and Ghoson, M., 2008, "Freeze-Thaw Degradation of FRP-Concrete Interface: Impact on Cohesive Fracture Response," Engineering Fracture Mechanics, Vol. 75, pp. 3924-3940.

62. Swenson, T. and French, C., 2015, "Effect of Temperature on Prestressed Concrete Bridge Beam Strand Stress During Fabrication," Research Report No. MN/RC 2015-50, Minnesota Department of Transportation.

63. Tastani, S., and Pantazopoulou, S., 2010, "Direct Tension Pullout Test: Experimental Results," ASCE Journal of Structural Engineering, Vol. 136, pp. 731-743.

64. The National Institute of Standards and Technology (NIST), 2014, "Freeze-Thaw Cycles: Expansions and Contractions Cause Potholes," https://www.pothole.info/2014/12/freeze-thaw-cycles-expansions-and-contractions-cause-potholes/, (Dec. 05, 2014).

65. Williams, B., Kodur, V., Green, M. and Bisby, L., 2008, "Fire Endurance of Fiber-Reinforced Polymer Strengthened Concrete T-Beams," ACI Structural Journal, Vol. 105, Issue No. 1, pp. 60-67.

66. Zhang, G., Kodur, V., Hou, W., and He, S., 2017, "Evaluating Fire Resistance of Prestressed Concrete Bridge Beams," Structural Engineering and Mechanics, Vol. 62, pp. 663-674.

67. Zhang, G., Kodur, V., Xie, J., He, S., and Hou, W., 2017, "Behavior of Prestressed Concrete Box Bridge Beams Under Hydrocarbon Fire Condition," Procedia Engineering, Elsevier, Vol. 210, pp. 449-455.

APPENDIX A: DESIGN EXAMPLES